Doctoral Thesis

Cross-scale properties of pulsating auroras based on low-altitude satellite and ground-based observations

Takanori Nishiyama

Department of Geophysics
Graduate School of Science
Tohoku University

Thesis Committee Members

Associate Professor Takeshi Sakanoi (Supervisor)
Professor Takahiro Obara (Chair)
Professor Takayuki Ono
Professor Yasumasa Kasaba
Associate Professor Yuto Katoh
Associate Professor Hiroaki Misawa

2012

博士論文

低高度衛星ならびに地上観測に基づくパルセーティングオーロラのスケール横断特性

東北大学大学院理学研究科
地球物理学専攻

西山尚典

論文審査委員

坂野井　健　准教授　（指導教員）
小原　隆博　教授　　（主査）
小野　高幸　教授
笠羽　康正　教授
加藤　雄人　准教授
三澤　浩昭　准教授

平成 24 年

Acknowledgments

The present thesis has been achieved in doctoral course of Geophysical Department of Geophysics in Graduate School of Science, Tohoku University, and I have countless people to thank for a number of supports. I would like to express my heartfelt thanks to a supervisor, Associate Professor Takeshi Sakanoi, for his introducing this study, and a number of supporting and persistent encouragements. I would also express my thanks to Dr. Shoichi Okano for his kind consideration and precious advice on study in all aspects.

Associate Professor Yoshizumi Miyoshi has been supporting me throughout this work. I wold like to appreciate so much for grateful discussions, suggestions, and encouragements. I would also express my gratitude to Associate Professor Yuto Katoh for precious discussions and advice on this work. Dr. Donald L. Hampton supported the ground-based observations at Science Operation Center in Poker Flat Research Range (PFRR), Fairbanks, Alaska, the United States in winter for 2010-11 and 2011-12. I really appreciate for his kind considerations in all aspects during the observations. I am so grateful to Professor Masahumi Hirahara, and Dr. Kazushi Asamura for their precious advice and great encouragements on the study based on Reimei observations. I would like to thank Dr. Ryuho Kataoka to give precious and specific advice on analysis methods.

Professor Natuso Sato and Professor Akira Kadokura made helpful advice and discussions on this study. I would like to express my thanks to their considerations. I had grateful discussions with Associate Professor Keisuke Hosokawa, Associate Professor Yasunobu Ogawa, and Associate Professor Yusuke Ebihara, and I appreciate so much for their constructive suggestions on this study. This study also has been based on the development and continuing operations by the Reimei technology team and the Reimei science team, and I would like to appreciate so much for their grateful supports. I am grateful National Insitute of Polar Research to provide opportunity to make experiments with an integration sphere system. I thank B. Lawson, K. Abnett and all members of PFRR staff for their helpful support during observations.

I am grateful to Professor Takahiro Obara, Associate Professor Hiroaki Misawa, Drs. Fuminori Tsuchiya, Michiko Morooka, Masato Kagitani, and Professor Emeritus Akira Morioka for their helpful suggestions through the discussions in regular seminars of Planetary Plasma and Atmospheric Research Center (PPARC). I also express my gratitude to the secretaries of PPARC, Ms. Kanno, Ms. Fukui, Ms. Yamamoto, and Ms. Imai, nee Sato for their continuing supports. Ms. Otomo, nee Koiwa, gave me a great help to the ground-based observations at PFRR in 2011-12, development of a software for a photometer and the install of the instruments to PFRR. I appreciate so much for the grateful cooperations to this study.

I would like to express my thanks to Professors Takayuki Ono, Yasumasa Kasaba, Associate Professors Atsushi Kumamoto, Naoki Terada, and Isao Murata, Dr. Hiromu Nakagawa for their advice and suggestions through associated seminars of Space physics and Planetary science group of Tohoku University.

I spend a month in Planetary and Space group of Hokkaido University after the earthquake occurred on 11 March 2011, and I would like to express my gratitude for thier hosipitality, in particular Professor Shigeto Watanabe, Dr. Mitsuteru Sato, and Professor Yukihiro Takahashi.

T. N. has been supported by Grants-in-Aid for Japan Society for the Promotion of Science (JSPS) Research Fellowship for Young Scientists (K1232151) from the Ministry of Education, Science, Sports, Technology, and Culture of Japan, and the Global COE program “Global Education and Research Center for Earth and Planetary Dynamics” of Tohoku University. This work was also carried out by the joint research program of the Solar-Terrestrial Environment Laboratory, Nagoya University. I would appreciate so much for these aids to this study.

The Dst and AE indices were provided by the World Data Center for Geomagnetism (WDC-C2) at Kyoto University. The IMF and solar wind data were obtained from the GSFC/SPDF OMNIWeb interface at http://omniweb.gsfc.nasa.gov/. IDL Geopack DLM povided by Dr. Haje Korth, which is a Dynamic Link Module (DLM) for the Interactive Data Language (IDL), was used for the calculation of geomagnetic field based on the model by Dr. N. A. Tsyganenko. I acknowledge NASA contract NAS5-02099 and V. Angelopoulos for use of data from the THEMIS Mission. Specifically for S. Mende and E. Donovan for use of the ASI data, the CSA for logistical support in fielding and data retrieval from the GBO stations, and NSF for support of GIMNAST through grant AGS-1004736, and for data provided by the Geophysical Institute Magnetometer Array operated by the Geophysical Institute, University of Alaska.

Six-years academic life in PPARC has been one of my greatest assets. I would like to my deep gratitude to all members of PPARC for their kindness and encouragement, especially, Dr. Mizuki Yoneda, Mr. Satoshi Kurita, and Mr. Hajime Kita for their kind considerations on this study.

Finally, I would like to genuinely express gratitude to my family for their continuing supports and encouragements over the years.

Abstract

Pulsating aurora (PA) is characterized by the periodically changing emission amplitudes with on-off pulsations of less than 1 s to a few tens of seconds [*Røyrvik and Davis*, 1977; *Oguti et al.*, 1981; *Yamamoto*, 1988]. PA is also well-known as its patchy structure with the horizontal size of 10-200 km. A number of rockets and low-altitude satellites have provided observations of precipitating electrons, which generate PAs, and the characteristics such as 3-Hz modulations [*Bryant et al.*, 1971; *Sandahl et al.*, 1980; *Yau et al.*, 1981] and energy-time dispersions [*Sato et al.*, 2004; *Miyoshi et al.*, 2010]. The energy of precipitating electrons ranges from one to a few tens of keV. The electron precipitation that generates PA is thought to result from pitch angle scattering due to wave-particle interactions near the magnetic equator. In particular, the whistler mode waves are widely accepted as one of the drivers for PA on the basis of result from theoretical studies [*Johnstone*, 1983; *Davidson*, 1990], and it is suggested that whistler mode chorus wave taking into account non linear process plays an important role in the generation of PA [*Demekhov and Trakhtengerts*, 1994; *Trakhtengerts*, 1999].

Recently, *Nishimura et al.* [2010, 2011] found a one-to-one correspondence between the intensities of PA and amplitudes of whistler mode chorus near the equator. Similarly, electron cyclotron harmonics (ECH) with enough wave amplitudes to scatter electrons into a loss cone were observed synchronizing with switch-on and switch-off of PA [*Liang et al.*, 2010]. It is expected that ULF waves control the excitation of both the whistler mode chorus and ECH by the modulation of the local plasma density [*Liang et al.*, 2010; *Li et al.*, 2011]. However, an important problem, identifying which mechanism is the most dominant, remains unsolved. In addition, the observational evidence focusing on small-structures of PAs and their relationship among other properties of PAs such as the on-off periods and the rapid modulations has not been reported except for *Samara and Michell.* [2010]. Since PA has the distinctive properties in a variety of spatial and temporal scales, we should investigate such multi-scale properties statistically to further understandings of the generation mechanism of PA.

The purpose in this study is to reveal the precise spatial-temporal properties and a generation mechanism for the property of PA using two different approaches: micro-scale electron precipitations typically less than 1 second and identifications of source regions of the precipitating electrons obtained from the Reimei satellite, and further precise spatio-temporal properties in a two-dimensional plane using ground-based EMCCD camera with a wide field-of-view (FOV) and 100-Hz sampling rate. We will establish the generation mechanism for the properties of PA including unclear characteristics such as the small-scale structures (10-30 km) and rapid temporal variations (3-Hz modulations) based on observations and statistics.

We investigated the generation process of the electron precipitations and identified the source region of the electrons with applying the two TOF analysis models to 29 PA events. Reimei has a three-channel monochromatic auroral camera (MAC) with a narrow FOV and top-hat electrostatic electron and ion energy spectrum analyzers (ESA/ISA) with energy ranges from 10 eV/q to 12 keV/q. Time resolutions of the two instruments are 8 frames per second and 40 msec for a full scan of the energy range, respectively,

which make it possible to measure the micro-scale electron precipitations associate with PAs. The source region obtained from the standard TOF model (TOF-A) was distributed almost continuously in magnetic latitude ranges from -20 to 50°. On the other hand, the source region obtained from the new TOF model (TOF-B), which takes into account the interaction electron and whistler mode wave [*Miyoshi et al.*, 2010], ranged from the magnetic equator to low-latitudinal region (∼ -11°). The source regions obtained from the TOF-B analysis generally corresponded to the regions in which whistler mode chorus waves are frequently observed in the previous studies, suggesting that the micro-scale precipitation of electrons caused by the cyclotron resonance with propagating whistler mode waves is a plausible mechanism for the production of PAs.

The result from the Reimei observation data and the TOF analyses implies that the micro-scale electron precipitation constitutes temporal variations of PA. For expanding our scope of the investigation on the property of PA, the ground-based optical observation was carried out during the period from November 2010 to March 2011 and from November 2011 to March 2012. We used an EMCCD camera with wide a FOV (49 × 49°) and a high sampling rate of 100 frames/s. Firstly, we focused on meso- and small-scale PAs appeared at the early recovery phase of the substorm on March 4, 2011. Three independent pulsating patches (PA1-3) with different periods from 4 to 7 seconds were observed in the FOV of 100 ×100 km at the altitude of 110 km. The typical scale of the patch was estimated to be 2000 km in the magnetic equator, and it is comparable with the estimations based on recent in-situ observations. We examined the modulations of PAs in the frequency range higher than 1.0 Hz and their spatial distributions in detail. The results revealed that the modulation had a peak frequency around 1.5 Hz, with a narrow frequency width of 0.30 Hz. On the other hand, the adjacent PA2 and PA3 did not have dominant modulation and coherency at the frequency around 1.5 Hz. We also conducted the cross spectrum analysis and the result revealed that the modulations around 1.5 Hz inside PA1 were almost in phase. Moreover, it was found that the low frequency variations from 0.2 to 0.5 Hz inside PA1-3 propagated as a group of flows with consistent directions. The estimated fast flow velocities inside PA2 ranged from 50 to 120 km/s at the auroral altitude. They were corresponding to the horizontal velocities between 1800 and 2700 km/s at the magnetic equator, and almost equal to the Alfven speed at $L \sim 6$. The result suggests that compressional waves may drive control the growth rates of whistler mode waves, which can generate precipitation associated with PA, and drive the dynamics inside a patch.

Further, the PA observed on 1st December, 2011 also showed the typical cross-scale properties of PA in space and time. A southward propagating aurora patch exhibited the meso-scale structures composed of a few sub-structures. The temporal variations of the PA contained clear 3.0-Hz temporal modulations superimposed on on-off pulsations of the period of 8-10 seconds. While the large-spatial scale of the whole patch was estimated to be 1500 km mapped onto the magnetic equator, the spatial scale of the sub-structure was 800 km. Additionally, the strong 3.0-Hz modulations were excited only in the sub-structures. The minimum width of sub-structures was estimated to be 410 km at the magnetic equator. On the other hand local proton gyro radius was estimated to be smaller (≈ 100 km) than the width, which suggests that the sub-structures would be mainly maintained by MHD forces. However, a kinetic effect, such as ion finite Larmor radius effects, may also contribute to form the complicated sub-structures [*Hiraki and Sakaguchi*, 2010], because the minimum scale was still close to local proton gyro radius.

Finally, the statistical study on the cross-scale properties were presented based on 53 events during the period from December 1st, 2011 to March 1st, 2012. The observed modulation frequency ranged from 1.5 to 3.3 Hz, and it is almost consistent with well-known 3 ± 1 Hz modulations in previous studies [*Røyrvik and Davis*, 1977]. The occurrence probability was slightly concentrated on the frequency range between 2.0 and 2.5 Hz. Although recent result with ground-based observations showed rapid variations in higher frequency range of 10-30 Hz, any strong modulations were not seen in frequency range higher than about 3 Hz in our study, which may suggest that the TOF of electron makes the time-smoothing effect on the rapid variations higher than 3 Hz. Moreover, the frequency of modulation showed relatively strong correlation to auroral intensity with the correlation coefficient of 0.52, and it can be explained with non linear wave growth theory suggesting that higher modulation frequency with larger wave amplitude of whistler mode chorus. In contrast to the rapid modulations, the on-off pulsations showed no significant correlations with any of other properties of PA. This result implies that the on-off periods may be determined by the balance of a variety of factor. In contrast to the rapid modulations, the on-off pulsations showed no significant correlations with any of other properties of PA. This results imply that the on-off periods may be determined by the balance of a variety of factor. In addition to the wave-particle interactions corresponding to loss rate of electrons in a flux tube, long-term variations of the cold plasma density caused by compressional mode waves would play more important role in control wave-particle interactions in the temporal scale of the on-off pulsation periods. The enhancement of rapid variations was seen inside sub-structures in many cases. However, no clear correlations between the modulation frequency and the spatial size of the whole and sub-structures were found statistically. The reason still remains an open question and should be addressed to investigate in near future.

As a conclusion of this study, we propose a possible generation mechanism of PAs that explains the spatial and temporal cross-scale properties presented in this study. A group of energetic electron with energy ranges from a few to a few tens of keV are supplied into a flux tube with a drift velocity. The electrons with sufficient anisotropy immediately excite whistler mode chorus element with a time scale less than 1 second based on non linear wave growth theory, and the electrons are almost simultaneously scattered into small pitch angles. The electrons scattered into a local loss cone result the micro-scale electron precipitation with a duration time of several hundreds of milli-seconds. As long as the supply of fresh electrons into the flux tube continues or the cyclotron resonance conditions are changed by temporal variations of cold plasma density due to compressional mode waves, both the chorus elements and the micro-scale precipitations of electrons are generated repeatedly. Consequently, the on-phase of PA modulated at the frequency of a few-Hz can be observed with ground-based optical instruments. Expanding a scope of the property in equatorial plane, a compressional mode wave may drive the dynamics inside a patch, such as expansion-contraction and streaming, via modulation of the flux tube. Force balance between magnetic tension and plasma pressure triggers the development of complicated spatial patch structures governed by instabilities taking into account kinetic effects on a time scale longer than a few minutes.

This model for the generation process gives us comprehensive understandings of the cross-scale properties of PA in space and time. Quantitative evaluation of the model combined with simultaneous ground-based and in-situ observations would be an essential, and the visualization of wave-particle interactions and related instabilities with a high-speed imaging technique is quite useful for further understandings of microscopic space plasma physics including PAs.

Contents

Chapter 1

Introduction

Our planet, the Earth, is the only one planet where many different kinds of life coexist as far as our knowledge. Life in the Earth has been going on with evolution under the protection of the Earth's atmosphere, ground and sea. If once life goes out of the protection, harsh space environments, which consist of radiations, high energy cosmic rays and so on, would not allow us to keep surviving. Similarly, the Earth couldn't keep the atmosphere and sea without the magnetosphere because of direct solar wind blowing to the Earth. Since the first Earth-orbiting artificial satellite, Sputnik 1, was launched in 1957, a number of satellites have observed the space environment in the vicinity of the Earth. Consequently it is revealed that the magnetosphere and internal plasma vary considerably under the solar activity. In addition, it is known that the influence reaches the upper-atmosphere and interesting phenomena often happen there such as auroral phenomena. Because observations of auroras make it possible to visualize spatial and temporal variations of physical processes inside the magnetosphere, it can be regarded as an effective method for monitoring the magnetospheric dynamics. This thesis concerns on auroral phenomena, in particular, pulsating auroras using a variety of observational data obtained from a low-altitude satellite and ground-based instruments.

1.1 Magnetosphere of the Earth

The Earth is one planet of our solar system that has an intrinsic magnetosphere. Its geomagnetic field can almost be assumed to be dipole field, whose magnetic moment is known to be 8.05 $\times 10^{22}$ Am^2, as long as it is not too far from the surface of the Earth. Getting away from the Earth, external magnetic field derived by magnetospheric currents is gradually intensified. The three-dimensional structure of the magnetosphere is actually more complicated than dipole magnetic field, because the solar wind pressure compresses the front side of the magnetosphere and make extended anti-sunward tail of the magnetosphere: besides the geographical axis is tilted not only for the geomagnetic axis in about 10 degrees but also for the ecliptic plane in 23.4 degrees. Figure 1.1 shows the magnetospheric structure and typical regions categorized with properties of internal plasma. Most of the magnetospheric plasma regions and the surrounding interplanetary space are characterized by their large conductivity. Under such conditions the plasma is strongly coupled to the magnetic field, as if magnetic field lines were frozen in the plasma fluid. The plasma entering the magnetosphere through a variety of instabilities at the magnetopause is transported inward with adiabatic heating. The plasma of inner magnetosphere is not uniformly distributed, but localized in each different region characterized as a group of plasma with different bulk energies and densities (e.g., radiation belt, plasma sheet, ring current, plasmasphere, etc.) [e.g. Kivelson and Russell, 1995] because the redistribution of plasma energy by collisions does not happen under collisionless plasma conditions.

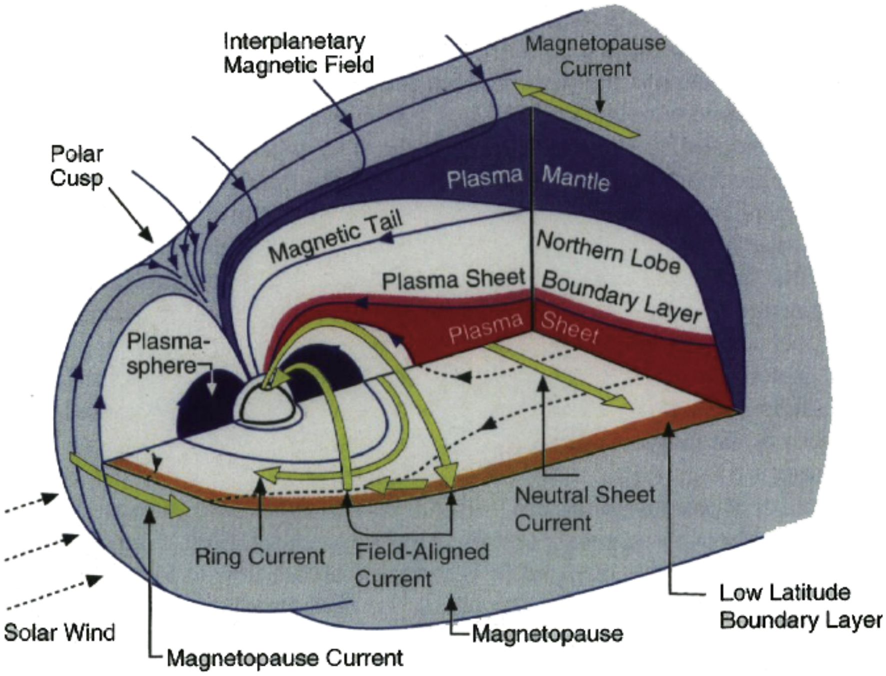

Figure 1.1: The structure of the magnetosphere and the main current systems. Adapted from *Kivelson and Russell* [1995].

However, during a magnetic storm or a substorm, a number of hot plasma are supplied into the inner magnetosphere, and many plasma processes take place for particle acceleration, transport, and loss. These processes include a radial diffusion, a variety of wave-particle interactions, injections of plasma as source populations, and global electric and magnetic field configuration changes in the inner magnetosphere (Figure 1.2). In particular, the wave-particle interactions play an essential role in local particle acceleration and loss, because particles redistribute the energies with each other through excitation and damping of various plasma waves such as whistler mode waves in ELF and VLF ranges, electro-magnetic ion cyclotron (EMIC) waves and ULF waves. As a result, the particles accelerated in a relativistic energy contribute to the formation of inner radiation belt. On the other hand, the velocity distribution functions of particles in a broad energy range is changed due to pitch angle scatterings. The pitch angle scattering causes the following processes: one is particle escaping to interplanetary space from the magnetopause in the process of transportation to dayside through their drift motion, which is known as magntopause shadowing [e.g., *Saito et al.*, 2010]. and the other that the particles are putted into local loss cone angle resulting in precipitations into terrestrial upper-atmosphere, and subsequently they generate auroral emissions.

1.2 Aurora phenomena

Auroral emission localized in specific magnetic latitudes and MLT sectors are known to compose of the global distribution called "aurora oval". Figure 1.3 shows an example of aurora oval obtained from FUV imaging of the IMAGE satellite in its apogee. A number of ground-based and satellite observations revealed the characteristics of aurora as follows:

- While auroras are mainly concentrated around magnetic latitude 67 degrees in night side, the day side auroras appear in higher latitudes reaching 70 degrees. Therefore, their occurrence regions are seen as an oval.
- The distribution of aurora oval depends on geomagnetic activities. During geo-

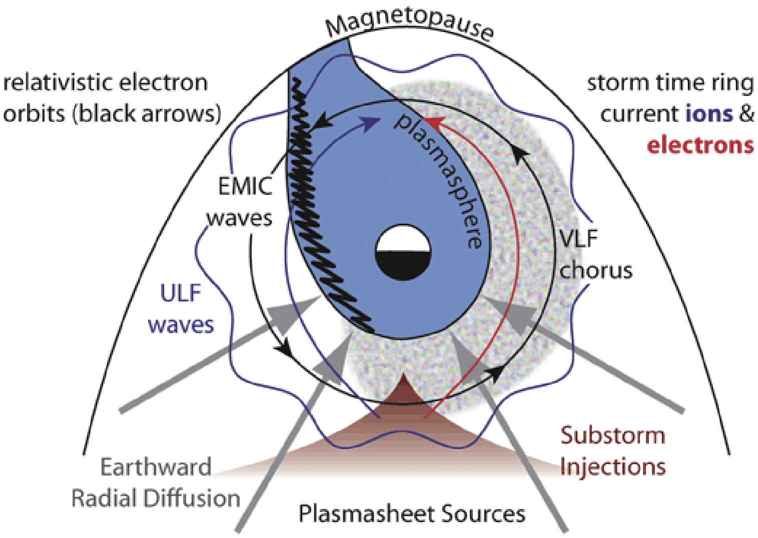

Figure 1.2: Schematic diagram showing the MLT distribution of plasma waves in the equatorial plane which can interact with electrons with an energy higher than keV. Red and dark blue arrowed lines show the convective injection trajectories of ring current ions and electrons, respectively. Ring current electrons excite whistler mode chorus waves. Interaction of ring current ions with high-density cold plasmaspheric plasma and regions of plume in the dayside plasmasphere excites EMIC waves. The wavy line denotes ULF waves. Black arrowed line shows the circular trajectory of the relativistic electrons in the radiation belt [*Reeves*, 2007].

magnetically disturbed period, the aurora oval is shifted to lower latitudes with expanding its latitudinal width.

- The aurora oval is fixed in the magnetic latitude and magnetic local time (MLT) coordinate, and therefore, the Earth rotates under aurora oval fixed in the Sun-Earth coordinate.

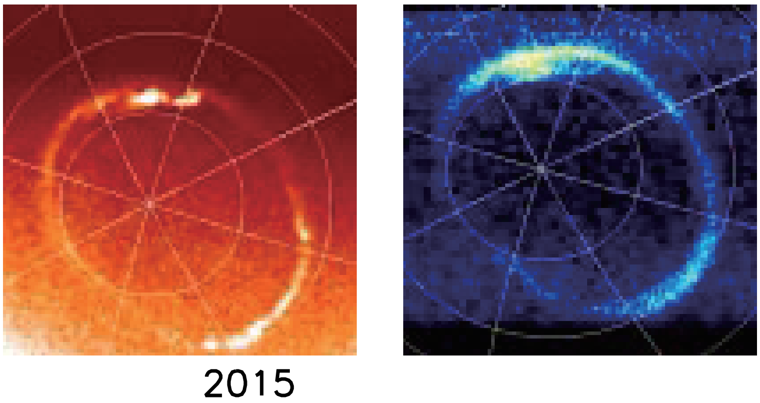

Figure 1.3: Global auroral structures obtained by IMAGE FUV at 2015 UT on June 28th, 2000. They are mapped onto the geographic latitude/local-time grid and the latitudinal circles indicate 75, 60 and 45 degrees. The WIC image (left) and the SI12 image (right) were observed with 140-170 nm and Doppler shifted Lyman alpha, respectively. Noon-midnight is very closely aligned with the vertical of the page (midnight is approximately at the top) [*Mende et al.*, 2001].

In addition, the aurora oval does not show spatially uniform distribution of auroral intensity but contains a variety of auroral signatures inside. For instance, intense auroral emission and fast motion are observed more frequently in the night side than the day side.

The aurora oval is normally classified into two regions as follows: the higher latitude side oval in which bright discrete aurora (described in Section 1.2.1) are seen, and the lower latitude side in which diffuse auroras (described in Section 1.2.2) and pulsating auroras (described in Section 1.3) appear. Since the globally inhomogeneous distribution of auroral characteristics such as brightness, structure and movement can reflect the magnetospheric properties, they are useful to understand a variety of spatial and temporal characteristics in different regions of the magnetosphere.

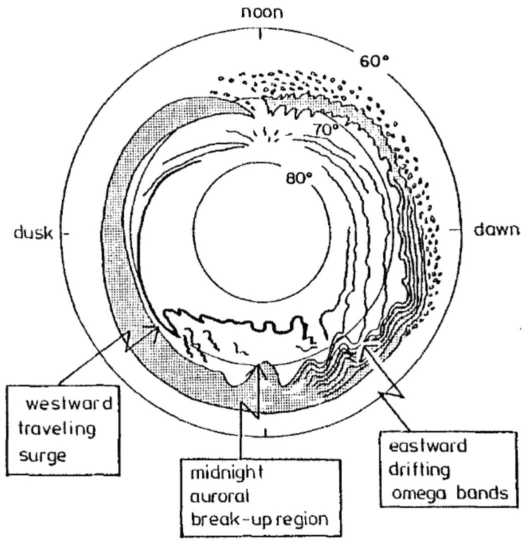

Figure 1.4: Schematic representation of main global auroral features given by *Akasofu* [1976]. Indicated are features corresponding to ionospheric current systems. After *Akasofu* [1981], complemented *Untiedt and Baumjohann*, [1993].

Once an aurora breakup that shows auroral emission suddenly starts to be intensified and simultaneously the expansion of bright regions occurs, the intense fluctuations of geomagnetic field sometimes reaching 1000 - 2000 nT is observed. This is because the ionospheric current flows azimuthally at the altitude of 100-120 km called the auroral jet current and it is a part of a whole current system connecting to the magnetosphere. Figure 1.5 shows a schematic view of upward and downward field-aligned currents (FACs) which compose of the 3-D magnetosphere-ionosphere coupling current system.

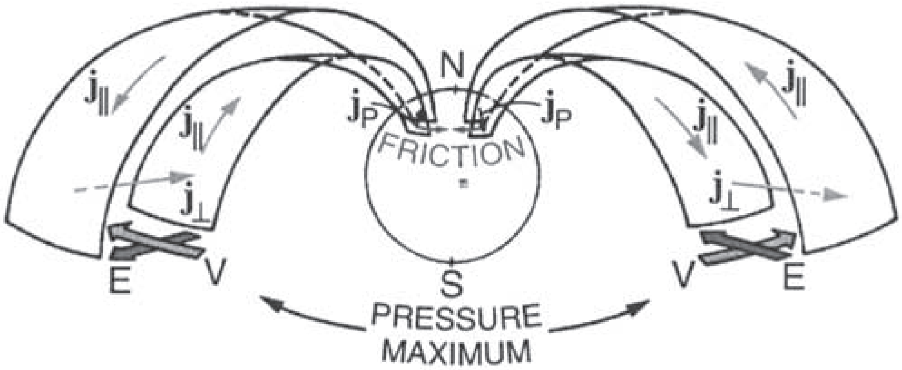

Figure 1.5: The Type II current system after *Boström* [1964] in the midnight sector [*Haerendel et al.*, 2007].

These large-scale currents are called "Birkeland currents" and classified into two types as follows: the poleward system called Region 1 and the equatorward system called Region 2. The Region 1 current flows near the polar cap boundary, into the ionosphere in the post-midnight sector and out from the ionosphere in the pre-midnight sector. This current system is generally expected to originate from the plasma sheet. The total current of this circuit is estimated to be 1-2 MA. The Region 2 current flows equatorward of Region 1 in the opposite direction: the current flows out from the ionosphere in the post-midnight sector and into the ionosphere in the pre-midnight sector. At high-altitudes, the Region 2 current merges with the ring current in the inner magnetosphere. The total current in the Region 2 circuit is slightly smaller than that in the Region 1 current circuit, typically less than 1 MA.

The field-aligned current is mainly carried by electrons because of their small mass. While cold ionospheric upgoing electrons contribute to downward current, hot magnetospheric electrons mainly carry the upward current. If the current density is small, the thermal flux of electrons is enough for the carrier of the current. However, during active periods when the magnetospheric plasma flows are fast, the current densities become too large to be carried by thermal particles. This is why electric field along a field line is generated in order to provide current continuity and maintain charge neutrality except for the very small difference in electron and ion densities that makes the electric fields. On account for the electric field, the magnetic field lines is no longer equipotentials, violating the frozen-in condition. These parallel electric fields are observed in both the upward and downward current regions. In particular, the bright aurora such as discrete aurora is primarily due to downward electrons accelerated by the parallel electric field in the upward field-aligned current region.

1.2.1 Discrete aurora

Discrete aurora, often called an auroral arc, is a typical aurora frequently observed during substorms, and it is well-known to appear with the shape of a curtain extending to a few hundreds or thousands km in the longitudinal direction; besides, the latitudinal width is about 10 km. It is also characterized by its brightness typically exceeding 10 kR. The auroral arc has been known to be produced by the precipitating electrons related to upward field-aligned currents from many in-situ observations.

Figure 1.6 is an example of discrete auroral emission and the associated electron flux (note that it is not downward-going electron flux) obtained from in-situ observation by the FAST satellite. In the energy-time (E-t) spectrum in Figure 1.6, several increases of electron flux with energy ranges from a few keV to ten keV, named “inverted-V” after its shape, are seen. The signatures indicate that electrons are accelerated by the electric field potential along a field line as described in the preceding section, and they show a one-to-one correspondence to discrete auroras in almost cases. Additionally, it is known that the discrete aurora sometimes appears as multiple arc structures accompanying fast and complicated motions known as a shear motion and vortex.

1.2.2 Diffuse aurora

Diffuse aurora is observed in the lower latitude regions of aurora oval, and it appears spreading uniformly over a wide region with almost no internal structure. Its luminosity is fairly low (a few kR) and seldom exceeds 10 kR. It is thought that precipitation of the plasma sheet electrons is responsible for the diffuse aurora, because a distribution function of precipitating electrons is agreed with Maxwellian distribution, as well as that of plasma sheet electrons. Figure 1.7 shows an example of precipitating electrons observed by the FAST satellite associated with diffuse auroras. In the top panel of electron E-t spectrum, two populations overlap between 20:09:08 UT and 20:09:37 UT and they are corresponding to diffuse aurora identified by ground-based observations. As Figure 1.7 shows, the precipitation is characterized by uniform electrons with energies more than a few keV.

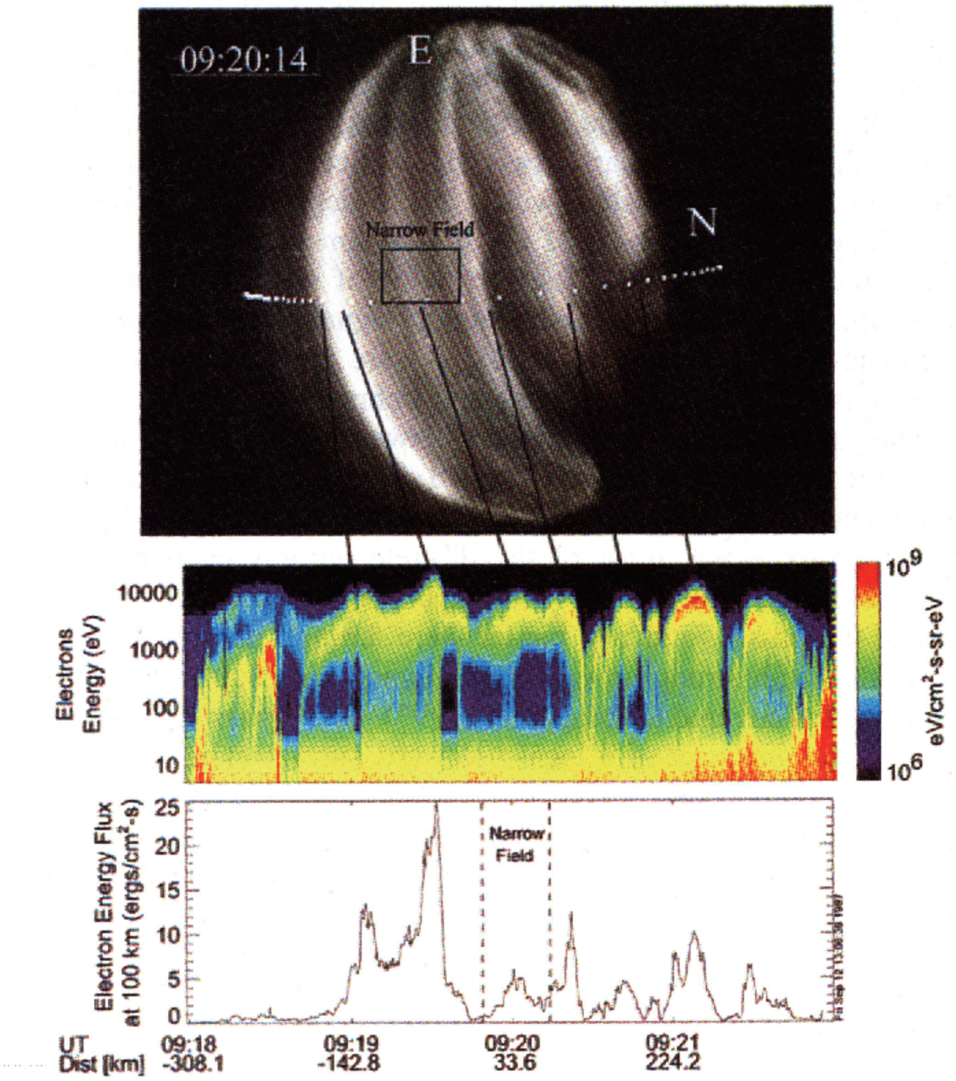

Figure 1.6: Multiple arcs as seen in the all sky image and by FAST. The 110 km conjugate is shown at 10 s intervals as FAST passed across from left to right. The center panel is the electron energy-time (E-t) spectrum integrated over all pitch angles and show a number of inverted-V structures. The bottom panel is the energy flux of precipitating electrons on a linear scale. The narrow auroral arcs are clearly displayed here. The pass was near 21:20 magnetic local time. [*Stenbaek-Nielsen et al.*, 1998]

The mechanism generating the precipitating electrons responsible for diffuse aurora has been discussed for a few decades, and there are mainly two candidates as follows: one is the pitch angle diffusion due to the interaction between electrons and electrostatic electron cyclotron harmonic (ECH) waves [*Kennel and Petscheck*, 1966], the other is the pitch angle scattering by whistler mode waves [*Kennel et al.*, 1970; *Lyons*, 1974; *Horne and Thorne*, 2000]. Considering that the diffuse aurora covers a wide area and exists almost permanently, this electron precipitation contributes to major loss of magnetospheric electrons at $\sim$ keV energy range [*Lyons et al.*, 1999] and, therefore, the diffuse aurora indicates that plasma waves play an important role in productions of precipitating electrons in the inner magnetosphere. Additionally, since it would be expected to reveal spatial distribution and intensity of wave-particle interactions from the ground, the diffuse aurora is said to be an interesting phenomenon and worth investigating in order to understand the process of particles diffusion and excitation of various plasma waves.

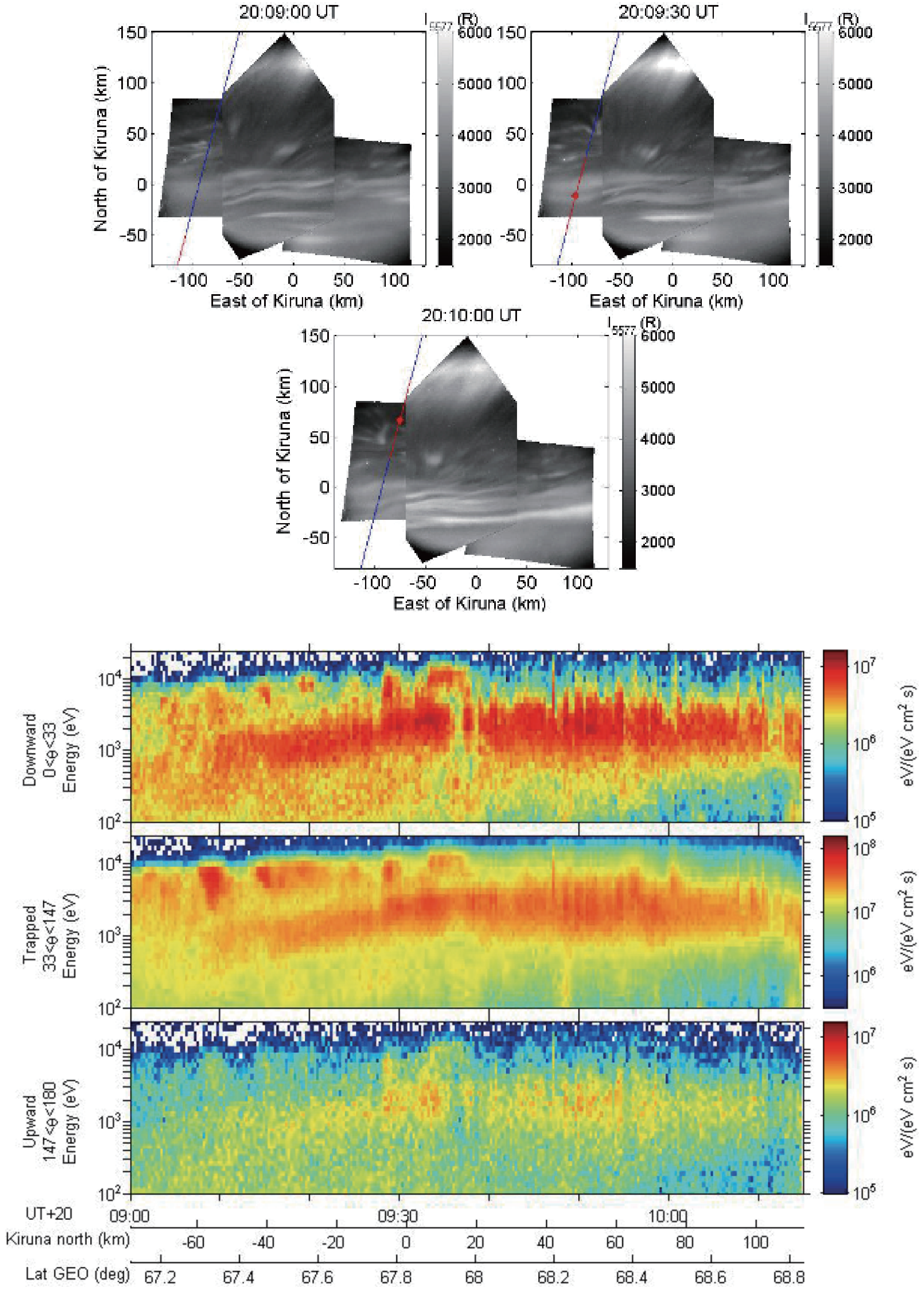

Figure 1.7: ALIS auroral images obtained at Abisko, Nikkaluokta, and Silkkimuotka projected to an altitude of 107 km and the electron differential energy flux as a function of time and energy for the time interval 20:09:00-20:10:27 UT. The blue lines show the FAST footprint. Red asterisks indicate the position of FAST at the moment when the image was taken. Red lines indicate the time interval ± 15 s around the center time. In the E-t spectrogram, the upper panel presents the fluxes integrated over the pitch angle interval of $0 < \alpha < 33$ (downward), the middle panel the interval of $33 < \alpha < 147$ (trapped), and the bottom panel the interval of $147 < \alpha < 180$ (upward). [*Sergienko et al.*, 2008]

1.3 Pulsating aurora

1.3.1 General properties

Pulsating aurora (PA) is characterized by the periodically changing emission amplitudes with rectangular pulses of less than 1 s to a few tens of seconds [*Røyrvik and Davis*, 1977; *Oguti et al.*, 1981; *Yamamoto*, 1988], and this characteristic is aptly described by the terms "switch on" and "switch off" [*Scourfield and Parsons*, 1969]. Figure 1.8 shows the temporal variations of pulsating auroral intensity, characterized by switch "on" and "off", and the histograms of pulsation "on" time, "off" time, repetition period are shown in Figure 1.9. PA tends to appear in the recovery phase of a substorm between midnight and dawn sectors in low-latitudinal region of auroral oval, and it is one of typical auroral phenomena categorized into diffuse aurora. PA is also well-known as its patchy structure with the horizontal size of 10-200 km, and it sometimes appears with east-west elongated bands or segments on spatial scale of 100 to 1000 km (See Figure1.10). Drift motions of each patch in the horizontal plane on global scales are corresponding to E × B drift in the

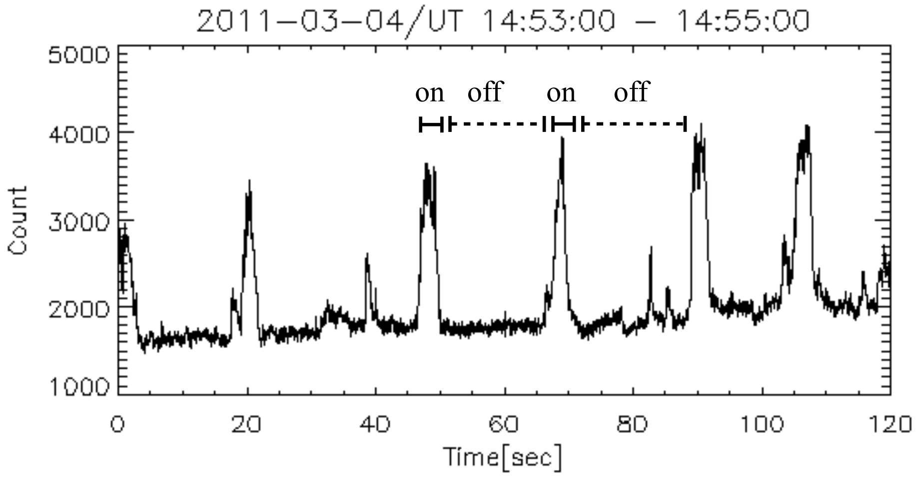

Figure 1.8: Auroral intensity variations as function of time for 2 minutes. We can see intermittent enhancements of auroral intensity as switch "on" and "off".

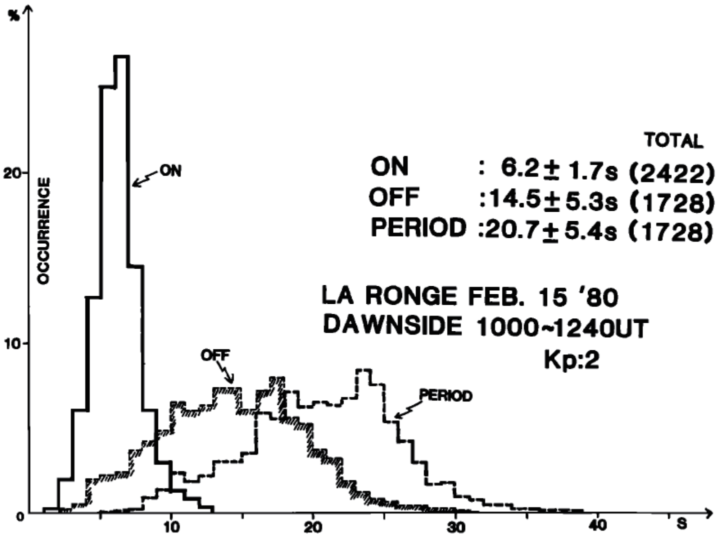

Figure 1.9: Histograms of pulsation "on" time, "off" time and repetition period observed at La Ronge on February 15 during 0200-0440 MLT [*Yamamoto*, 1988]

magnetosphere [*Nakamura et al.*, 1987]. While a population of cold plasma is expected to show E *times* B drift motion, magnetic drift, i.e, grad - B and curvature drifts are also taken into account for the horizontal motions of energetic electrons. Therefore, each patch is thought to show the spatial structure of cold plasma (See Figure1.11). Moreover, it is suggested that the cold plasma density controls the conditions for a wave-particle interactions by theories and in-situ observations. (described later in detail). PA often exhibits distinctive dynamics inside a patch known as streaming, fast auroral wave [*Røyrvik and Davis*, 1977], and expansion. *Yamamoto and Oguti* [1982] investigated luminosity propagating velocities in patches, corresponding to "streaming" motion, using an all-sky TV camera. The speeds of propagations were estimated to be several tens of km/s, which suggests that the propagation inside patches were driven by electrostatic waves or compressional mode wave. However, a model for a specific generation process of the dynamics inside pulsating patches is not established. It is well known that the morphology of PAs significantly depends on the local time sector, phase of substorm, and the position in the aurora oval, and the details were given in *Røyrvik and Davis* [1977]. *Jones et al.* [2011] also reported the temporal evolutions of PAs and the difference of spatial features between the pre- and post-midnight sectors. This may imply that the generation mechanism and morphology of PA are closely related to a substorm phase and the local time in the auroral oval.

Figure 1.10: Patchy structures of PAs appeared near the magnetic zenith taken at Fort Vermilion in Canada on February 22, 2012

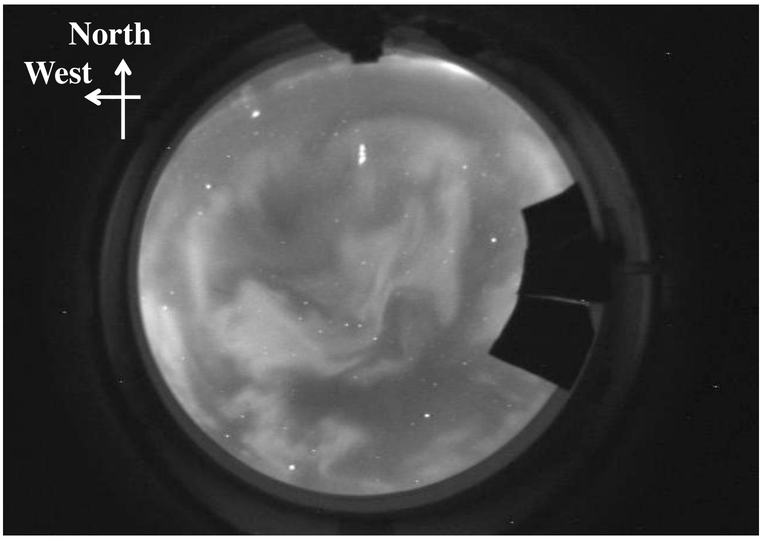

Figure 1.11: Large-scale patchy structures of PAs obtained from an all-sky camera in Poker Flat Research Range at 14:32:28 UT on February 19, 2012. This event occurred in the dawn sector in MLT, and each patch exhibited eastward drift motion.

A number of rockets and low-altitude satellites have provided observations of precipitating electrons, which generate PAs, and the precise characteristics such as 3-Hz modulations [*Bryant et al.*, 1971; *Sandahl et al.*, 1980; *Yau et al.*, 1981] and energy-time dispersions [*Sato et al.*, 2004; *Miyoshi et al.*, 2010]. The energy of precipitating electrons ranges from one to a few tens of keV, which is higher than the typical electron energy associated with diffuse aurora. *Nemzek et al.* [1995] demonstrated that such high-energy electrons (>20 keV) were supplied by substorm injection and correlated with the appearance of PAs. Typical examples of observed downward electrons associated with PAs are presented in Figure 1.12 and 1.13.

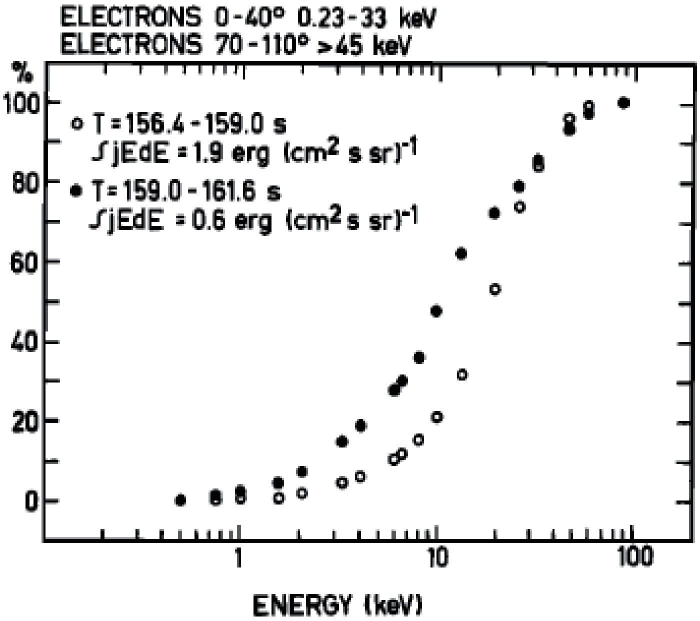

Figure 1.12: Normalized integral directional energy flux as a unction of electron energy E_0 for one pulsation maximum and the adjacent minimum by the rocket experiment [*Sandahl et al.*, 1980]. Open symbols represent the maximum and filled ones are the minimum, respectively. The normalized integral directional energy flux for the specific electron energy E_0 is defined as

$$\int_0^{E_0} j(E,\alpha)\cdot EdE \bigg/ \int_0^{\infty} j(E,\alpha)\cdot EdE$$

1.3.2 Generation mechanism

Since PAs usually appears in the dawn of the auroral oval and in the recovery phase, the electron precipitation that generates PA is thought to result from pitch angle scattering due to wave-particle interactions near the magnetic equator, similar to diffuse auroras. In particular, the whistler mode waves are widely accepted as one of the drivers for PA on the basis of result from theoretical studies [*Johnstone*, 1983; *Davidson*, 1990]. Moreover, the backward wave oscillator theory [*Demekhov and Trakhtengerts*, 1994; *Trakhtengerts*, 1999] suggests the non linear growth of whistler mode waves, i.e., whistler mode wave chorus, plays an important role in the generation of periodic precipitations. Some simultaneous optical and VLF wave ground observations also supported these ideas; however, it was demonstrated indirectly [*Tsuruda et al.*, 1981; *Hansen and Scourfield*, 1990; *Ozaki et al.*, 2012]. On the other hand, many simultaneous observations at geomagnetically conjugate points indicate the conjugate PAs often show differences in shape, luminosity and period [*Stenbaek-Nielsen et al.*, 1973; *Sato et al.*, 1998; *Watanabe et al.*, 2007]. However, there also exists the instance that the PAs appear with the almost same shape in the geomagnetically conjugate stations [*Fujii et al.*, 1987].

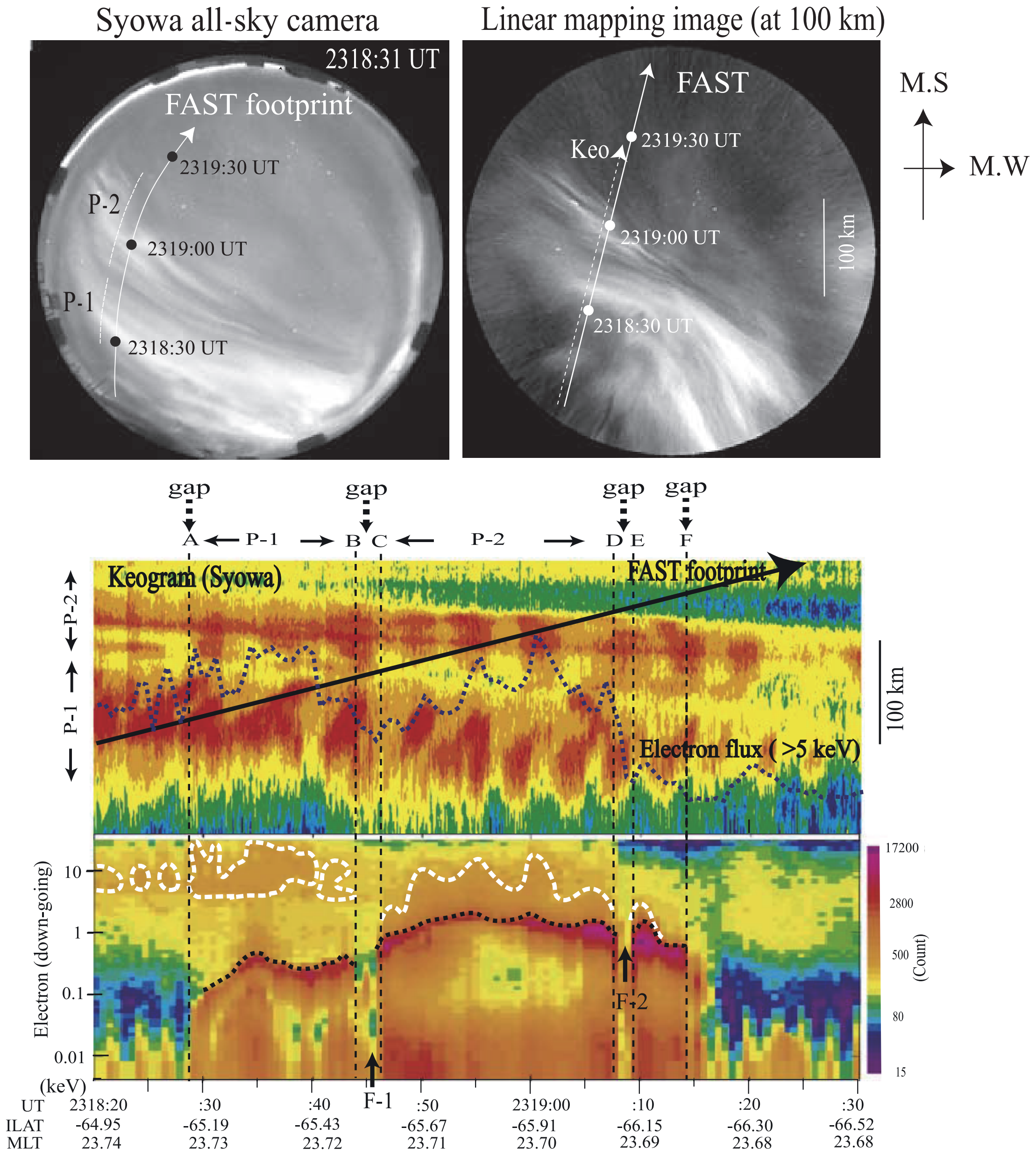

Figure 1.13: The top two panels show a white-light snapshot image from the Syowa all-sky camera at 2318:31 UT on 30 September 2000. The footprint of FAST mapped to 100-km altitude is marked in the images. Both images were reversely remapped in the east-west direction relative to the original all-sky images. The middle panel shows the auroral Keogram reproduced from the Syowa all-sky TV camera data along the FAST footprints, together with the total energy flux variations of downgoing electrons with energies larger than 5 keV obtained by FAST. The E-t spectrum of the downgoing electrons is illustrated in the bottom panel [*Sato et al.*, 2004].

Recently, several simultaneous ground-based and in situ observations have directly demonstrated specific generation mechanisms of PAs. Using the data with Time History of Events and Macro-scale Interactions during Substorm (THEMIS) spacecraft and All-Sky Imagers (ASIs) installed at THEMIS ground-based observatories (GBOs), *Nishimura et al.* [2010, 2011] found a one-to-one correspondence between the intensities of PA and amplitudes of whistler mode chorus near the equator, which means that the excitation of the chorus leads electrons to precipitate into the atmosphere. Figure 1.14 is a summary plot shown in *Nishimura et al.* [2010], and the panel D of this figure demonstrates strong correlation between auroral intensity and chorus wave magnetic field intensity integrated over 0.05 to 0.5 f_c during this period, where f_c is the local cyclotron frequency. Similarly, electron cyclotron harmonics (ECH) with enough wave amplitudes to scatter electrons into a loss cone were observed synchronizing with switch-on and switch-off of PA [*Liang et al.*, 2010]. It is expected that ULF waves control the excitation of both the whistler mode chorus and ECH by the modulation of the local plasma density [*Liang et al.*, 2010; *Li et al.*, 2011]. As examples of PAs not related with wave activities at the magnetic equator, time-varying field-aligned potential near the Earth was proposed as shown in Figure 1.15 on the basis of conjugate ground optical and the FAST satellite observations [*Sato et al.*, 2004]. *Nakajima et al.* [2012] also reported a PA event by conjugate observations between THEMIS and an all-sky imager. The THEMIS satellite confirmed the periodic enhancement of the field-aligned 1-10 keV electrons corresponding to the period of PA observed from the ground. It is suggested that the field-aligned electrons may have resulted not from wave-particle interactions but Fermi-type acceleration accompanied with earthward plasma flow. However, the most of these results showed a mechanism for only one event; an important problem, identifying which mechanism is the most dominant, remains unsolved.

Figure 1.16 shows the possible generation mechanisms recently proposed by simultaneous ground-based and in-situ observations and the positional relationship in the magnetosphere. Wave-related generation mechanisms, whistler mode chorus and ECH, are expected to work close to the magnetic equator. The radial distances where these mechanisms work are quite different: whistler mode chorus were observed simultaneously with PAs at the radial distance of 5.3 to 9.2 R_E [*Nishimura et al.*, 2011], on the other hand, ECH was observed at $L \sim 11$ although only one case was demonstrated in *Liang et al.* [2010]. Moreover, the one-to-one correspondences between PA and whistler mode wave were found in the ground-based observation data at L-values less than 6. These observational results imply that whistler mode chorus waves contribute to generation of PA in the inner magnetosphere. During the PA event associated with Fermi-type acceleration reported in *Nakajima et al.* [2012], the THEMIS satellites were located around at radial distance of 12 R_E. The modulation regions estimated in *Sato et al.* [2004] ware located rather close to the Earth, ranging from 2 to 6 R_E. It should be noticed that the magnetic field line connected FAST calculated by Tsyganenko model [*Tsyganenko*, 2002a, 2002b, 2003] was stretched out during this period, and the magnetic equator seemed to be located at 15 R_E. Therefore, it can be thought that whistler mode chorus works dominantly in the regions with L less than 6, and other mechanisms reported as a case study may work in the region of high L-value. However, it is rather difficult to clarify such a complicated property of PA in space and time based on event study using satellite data combined with ground-based experiments. Thus, we suppose that continuous observation of a variety type of PAs with ground-based instruments is also necessary to understand the mechanisms make different properties of PA, such as periodicity and morphology.

1.3.3 Rapid variations and small-scale structures

From many in-situ measurements of electrons related to PA with rockets and low-altitude satellites, the 3-Hz modulations of downward electron flux are widely known [*Bryant et al.*, 1971; *Sandahl et al.*, 1980; *Yau et al.*, 1981]. In contrast, only a few studies on the 3-Hz modulation using ground-based instruments, and the possible generation process of the modulation has been not discussed well. *Samara and Michell* [2010] carried out ground-based optical observations with a 14 × 14 ° field-of-view (FOV) camera, which is appropriate for investigations of PA. They reported relatively broad modulations with many peaks in the range of 0.5 to 15 Hz in one event (Figure 1.17), and discussed the relationships among the modulations up to 15 Hz, spatial structures, and auroral intensities in the context of whistler mode chorus. However, the FOV is still too narrow to cover

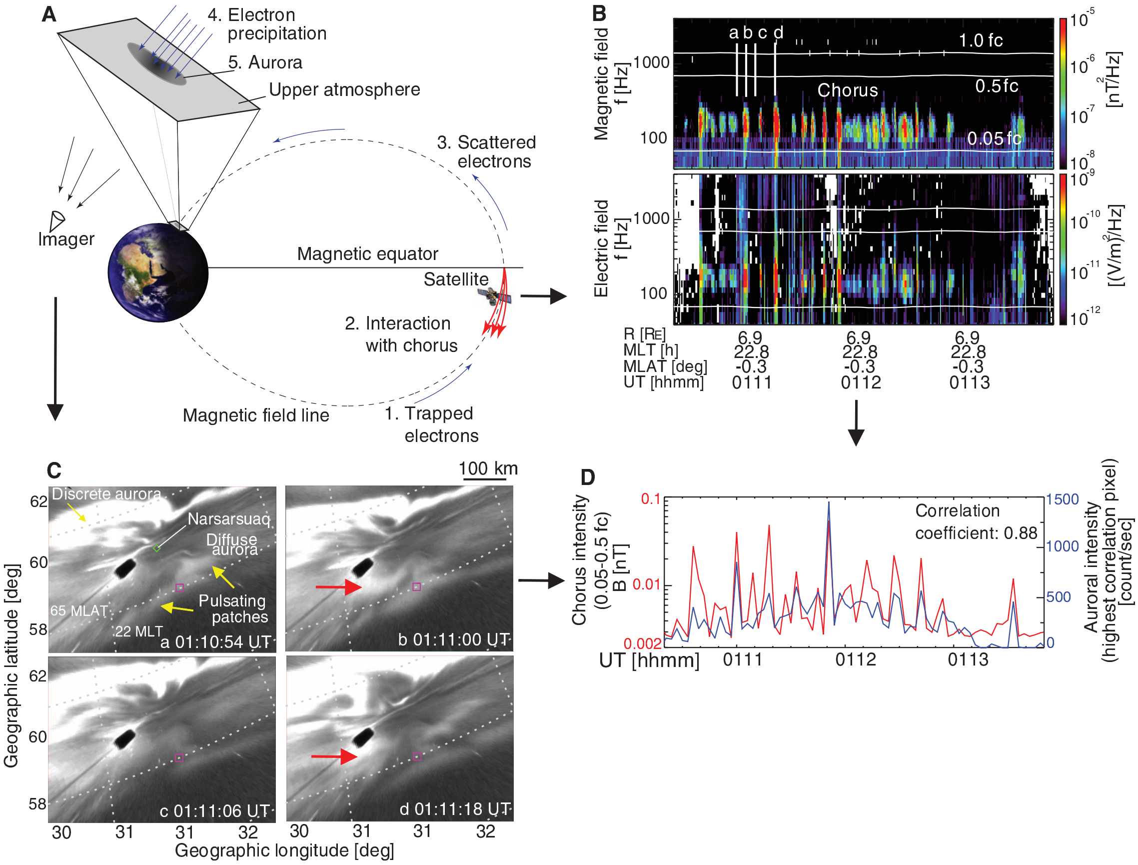

Figure 1.14: Coordinated observation of PA with the Narsarsuaq all-sky imager (ASI) and the THEMIS-A spacecraft during 01:10:20 UT to 01:13:50 UT on 15 February 2009. (A) Schematic diagram showing the geometry of chorus wave propagation (red arrows), electron precipitation (blue arrows), and PA. (B) THEMIS-A observation of bursts of lower-band chorus shown in electromagnetic field spectra. The white lines indicate 0.05, 0.5, and 1.0 f_c using the measured magnetic field, where f_c is the local cyclotron frequency. (C) Snapshots of imager data projected onto the geographic coordinates at 110-km altitude. The pulsating patch correlating with chorus is indicated by the red arrows. ASI snapshot times are also marked in (B) by white vertical lines. The pink square shows the magnetic footprint of the THEMIS-A spacecraft using the Tsyganenko 96 magnetic field model (the model was used only for a rough estimation of the footprint, and the choice of the model is arbitrary). The spacecraft footprint was located close to the center of the imager field of view (green square in panel a). Dashed lines give magnetic coordinates every 3° in latitude and 1 hour in local time. The black spot near the center of each image is an artificial object. (D) Correlation of lower-band chorus integrated magnetic field intensity over 0.05 to 0.5 f_c (red) and auroral intensity (blue) at the highest cross-correlation pixel [*Nishimura et al.*, 2010].

the adjacent patches of PA, and an observation with a higher sampling rate is required to understand rapid temporal variations.

In addition, electron microbursts are well known as short-duration bursts of precipitating electrons from satellite data: the duration is typically shorter than 1 second, and the energy ranges from a few tens of keV [*Anderson and Milton*, 1964] to above a few hundreds of keV [*Imhof et al.*, 1992; *Lorentzen et al.*, 2001]. Although the electron energy of precipitation associated with PA is one or two order of magnitudes lower than that of typical microbursts, a few similarities between them are seen: temporal scales of both, modulations superimposed on the on-phase of PA and the duration of a microburst, are shorter than 1 second, and proposed generation mechanism of both PAs and microbursts are considered to be related to whistler mode chorus. Recently, a one-to-one correspondence between the

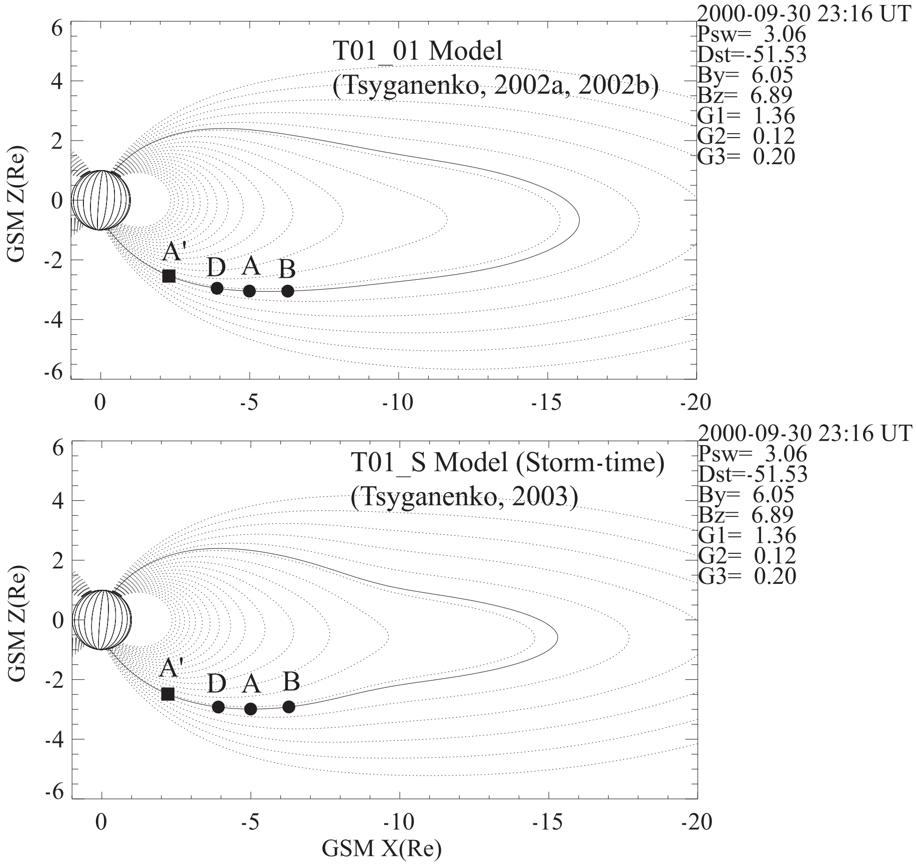

Figure 1.15: The source positions of precipitating electrons associated with the PA mapped onto the model magnetospheres. See details in *Sato et al.* [2004]

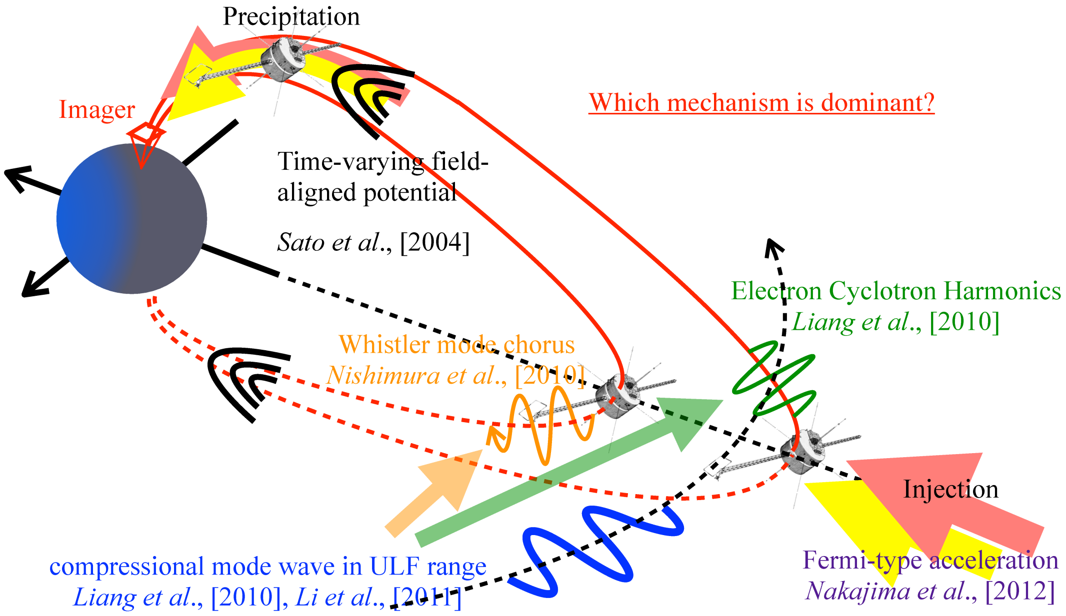

Figure 1.16: A schematic illustration showing the possible generation mechanisms by simultaneous ground-based and in-situ observations and the modulation regions of electrons in the magnetosphere.

electron microbursts and the generation of discrete chorus elements were demonstrated in a numerical simulation based on a self-consistent full-particle method [*Hikishima et al* 2010], which supports the non linear wave growth theory of chorus emissions by *Omura et*

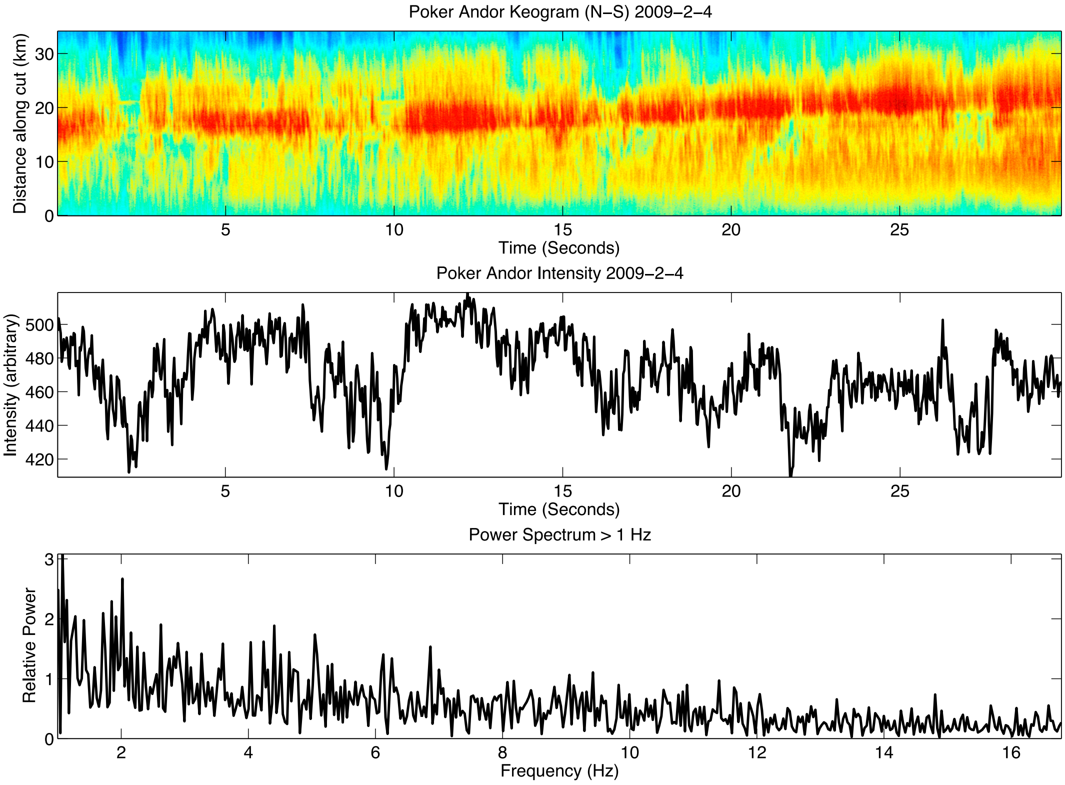

Figure 1.17: (Top) North-south keogram from successive 14 × 14 deg FOV images, taken near 13:25 UT on 04 February 2009. North is up and the horizontal lines are stars. (Middle) Intensity profile taken along the center of the keogram. (Bottom) FFT of the intensity [*Samara and Michell.*, 2010].

al. [2008, 2009]. Therefore, rapid variations of precipitating electrons as 3-Hz modulations in PAs may be coupled with the generation process of microburst-like electron precipitation. Images of PA with ground-based observations can help us to obtain the coherent spatial size of high-energetic electron precipitation.

Fine-scale structures of the aurora have recently been measured with remarkable improvement in image pickup devices. Many cases of fine-scale structures in discrete auroras were demonstrated by both spacecraft investigations and ground-based observations concerning on Alfvenic auroras [*Semeter et al.*, 2008; *Frey et al.*, 2010] and on flickering auroras [*Gustavsson et al.*, 2008; *Whiter et al.*, 2008, 2010; *Yaegashi et al.*, 2011]. While diffuse aurora has been generally regarded as uniform and not discrete structures, small-scale structures were also reported as ∼ 30 km width [*Wallis et al.*, 1979], ∼ 10 km width [*Pedersen et al.*, 2007]. Simultaneous optical instruments on the ground and the FAST electron spectrometer data demonstrated thin auroral stripes extended along the geomagnetic latitudinal directions with a width of about 5 km in dim background luminosity [*Sergienko et al.*, 2008]. In this paper, precipitating and trapped electrons obtained from the particle measurement data showed two different peak energies and anisotropy between downward and trapped electrons with higher energy, which suggested that the auroral stripes and background may be generated by the upper band chorus and ECH, respectively (See also Figure 1.7). Additionally, the narrow field of view imagers on the Reimei satellite captured "smokelike auroras" images with a width of 0.6 km (FWHM) estimated by using simultaneous particle measurements as shown in Figure 1.18 [*Ebihara et al.*, 2010]. Panels on the right side of Figure 1.18 compares the brightness of the auroral emissions at 557.7 nm taken along the magnetic footprints and precipitating particles. The brightness of the emission (a) shows fairly well correlation with the energy flux of

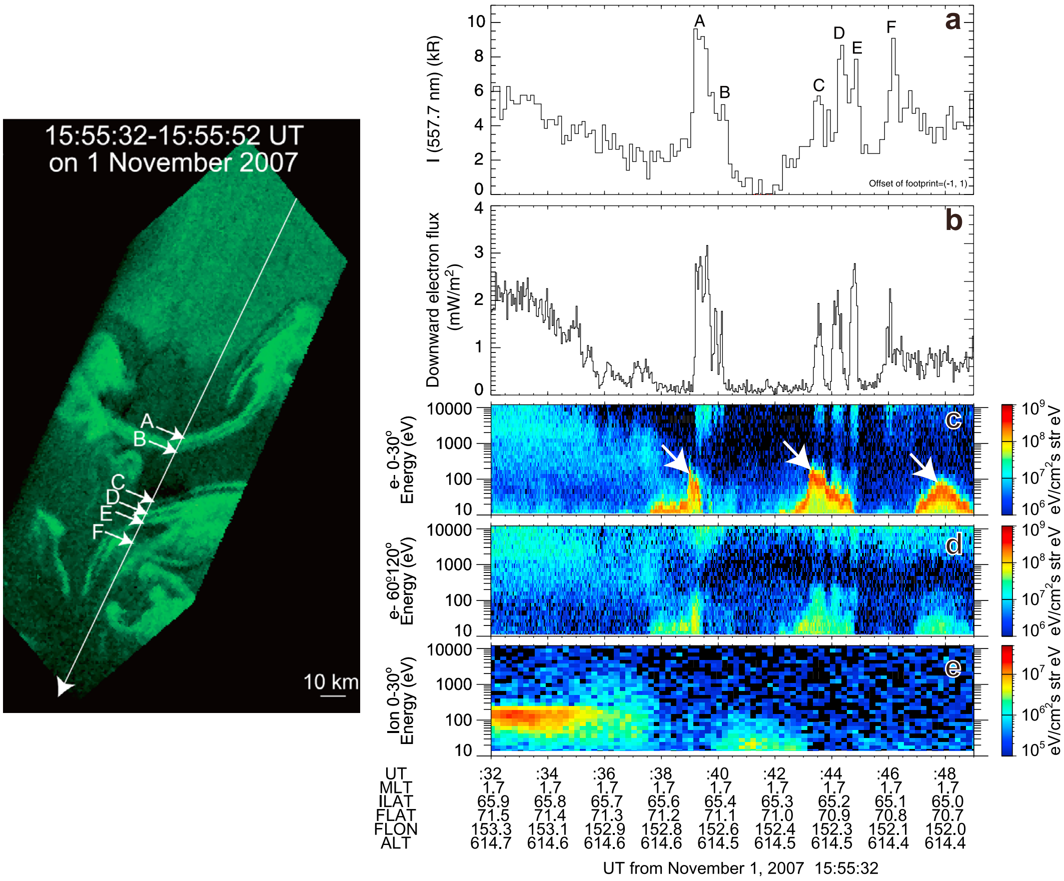

Figure 1.18: (Left) Collage of auroral images captured by the Reimei satellite at 557.7 nm at 15:55:32-15:55:52 UT on 1 November 2007. The white line indicates the footprints of magnetic field threading the satellite. The images are mapped to the geographic coordinates at 110 km altitude. The geographic north is at the top. (Right) (a) Auroral luminosity at wavelength of 557.7 nm represented as intensity of radiance in kilo-Rayleighs (kR) as a function of time. The letters A-F represent the position indicated by the corresponding arrow. (b) Energy flux of downgoing electrons. (c) Energy and time spectrogram of downgoing electrons (pitch angles of 0-30°). (d) Energy and time spectrogram of trapped electrons (pitch angles of 60°-120°). (e) Energy and time spectrogram of downgoing ions [*Ebihara et al.*, 2010].

precipitating electrons (b), and E-t spectrum of precipitating electrons (c) demonstrates that energetic electrons ($>$ 1 keV) mainly contributed to the highly-structured auroras. The spatial feature probably resulted from the interchange instability maintained mainly by pressures of high-energy electrons and pitch angle scattering by whistler mode waves generated in the tenuous plasma region. In particular, the energetic and non-accelerated electrons with energy range of 8 keV are thought to be responsible for highly-structured auroras [*Sergienko et al.*, 2008; *Samara et al.*, 2010]. As already described above, PA can be considered as quite similar phenomenon to diffuse auroras in their morphology and generation process. However, the observational evidence focusing on small-structures of PAs and their relationship among other properties of PAs such as the on-off periods and the rapid modulations has not been reported except for *Samara and Michell.* [2010], we should investigate the property of the meso-small scale structures of PA statistically to further understandings.

1.4 Purpose

The purpose in this study is to reveal the precise spatial-temporal properties and a generation mechanism for the property of PA using two different approaches: micro-scale electron precipitations typically less than 1 second and identifications of source regions of the precipitating electrons obtained from the Reimei satellite (Chapter 2), and further precise spatio-temporal properties in a two-dimensional plane using ground-based EMCCD camera with a wide FOV and 100-Hz sampling rate (Chapter 3). We will establish the generation mechanism for the properties of PA including unclear characteristics such as the small-scale structures (10-30 km) and rapid temporal variations (3-Hz modulations) based on observations and statistics. The detailed purposes in each chapter are summarized as follows.

Study with the Reimei satellite data

Simultaneous ground-based and in-situ (e.g., rocket and satellite) observations have been useful to elucidate the causal relationship between aurora phenomena and precipitating particles in detail. However, completely conjugacy between the two observations is rare, and the opportunity is inherently limited. The study presented in Chapter 2 will focus on identifying the source region and generation mechanism of PA using the image-particle data obtained from the Reimei satellite. This data is particularly useful because Reimei can simultaneously observe aurora images and the precipitating particles, and statistical analyses are possible using the data for a number of simultaneous image-particle observations. Moreover, the high spatial and temporal resolution data make it possible to investigate a pulsation patch and an energy-time dispersion signature in precipitating electrons with a timescale of a few 100 ms. Therefore we can obtain statistical results using a number of simultaneous image-particle observation data. In Chapter 2 we will conduct statistical analysis of the energy-time dispersions associated with PA. Two TOF analyses, the standard TOF and a new TOF recently proposed by *Miyoshi et al.* [2010], are applied to the same auroral events, and the adequacy of each model for PA is discussed. We also investigate the plasma density and wave frequency that can be derived from the TOF analysis of *Miyoshi et al.* [2010].

Study with a ground-based EMCCD camera

Although ground-based all-sky observations of PAs have been made so far for decades, a quantitative characteristics on the meso- and small-scale (10-100 km) and dynamical motion of PA such as streaming and fast auroral wave were rarely discussed. In particular, the fast temporal variation of auroral luminosity, corresponding to 3-Hz modulations of electron precipitations, have not been studied using ground-based optical instrument data because of the limited temporal resolutions and sensitivities. Since such a few Hz modulation of electron precipitation is probably caused by wave-particle interactions in the magnetosphere, precise investigation of PA helps us to understand the spatial and temporal evolution of related wave-particle interactions in the magnetic equatorial plane. This has not been achieved yet by using multi-spacecraft observations and simulations. We carried out ground-based observations using multiple instruments at Poker Flat Research Range during the period from November 2010 to March 2011, and from November 2011 to March 2012, in order to investigate the spatial meso-small scale structures, the dynamics inside a patch, and the temporal variations in the frequency range from a typical pulsation periods (a few - a few tens seconds) to a few Hz modulations or faster. Here, we present such spatial and temporal cross-scale properties of PA on two case studies and statistical analysis of total 53 events.

Finally, we discuss a possible generation mechanism of PA and limitation of this study based on observational evidences from two approaches, and propose future plans for further understanding of space plasma physics related to the generation process of PA.

Chapter 2

Reimei observations

In order to achieve the scientific goal mentioned in the previous chapter, we have statistically analyzed image and particle data associated with PAs obtained from Reimei satellite. In this chapter, the details of the Reimei satellite including operations system, scientific instrumentations and observation modes are described at first. Secondary, we present a course of analysis process focusing on two types of Time Of Flight (TOF) methods: Standard method [e.g., *Yau et al.*, 1981; *Hardy et al.*, 1990] and a new TOF model proposed by *Miyoshi et al.* [2010]. Finally, statistical characteristics of the modulation region identified by the two TOF methods for 29 PA events are shown, and we discuss the plausible generation mechanism of PAs that can explain the spatial distribution of modulation regions obtained from our analysis.

2.1 Reimei/INDEX

2.1.1 General description

The Reimei satellite is the first Japanese scientific micro-satellite, whose size and weight are 724 × 626 × 609 mm and about 70 kg, mainly developed by JAXA/ISAS in order to investigate mechanisms of auroral fine-scale structures (Figure 2.1). More particular scientific targets are presented in *Sakanoi et al.* [2003] and *Asamura et al.*, [2003], some of them are enumerated as follows:

- One-to-one correspondence between the fine-scale auroral structures and precipitating particles,
- Temporal variations of aurora phenomena such as Alfvenic auroras and PAs, and their relationships to precipitating particle signatures,
- Distributions of auroral emissions as a function of altitudes by taking images in the limb direction,

As the mission named INDEX (INnovative-technology Demonstration EXperiment) shows, Reimei has an aspect that it gives a demonstration of advanced satellite technologies. In particular, it is unique and distinguished that Reimei, despite its size, realizes the three-axis bias momentum attitude control with three magnetic torques and a reaction wheel. Main advanced technologies including it are shown as below [*Saito et al.,* 2001]:

- Three-axis attitude control system in a small satellite,
- Solar-concentrated deployable solar panels with thin film reflector,
- Lithium ion rechargeable battery using lithium manganate as a main satellite battery,

- GPS receiver with all-sky antenna-coverage,
- Compact S band receiver and transmitter,
- Compact ground tracking station based on PCs for general use.

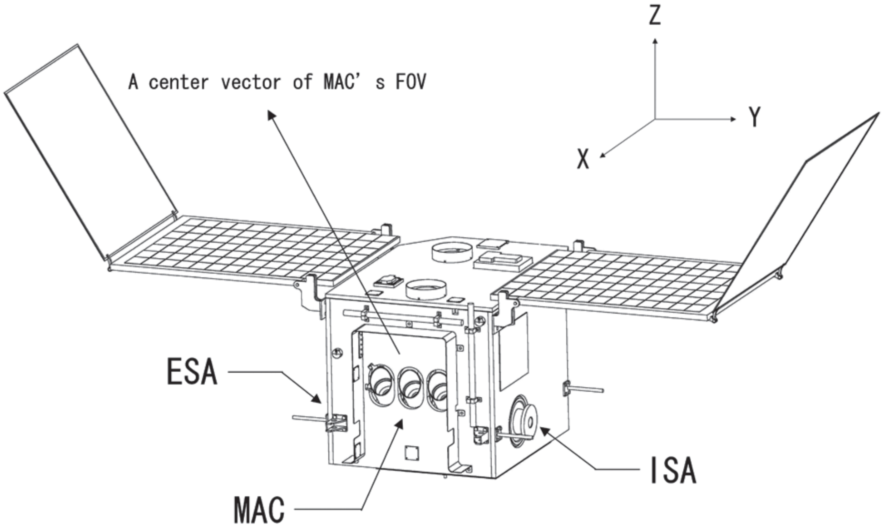

Figure 2.1: Schematic view of the Reimei satellite and positions of the main scientific instruments. MAC and ESA/ISA are installed in a Y-Z plane and a Z-X plane of the satellite coordinates, respectively. A center vector of the MAC's field of view has an inclination of 45 degrees in a Z-X plane [*Obuchi et al.*, 2008].

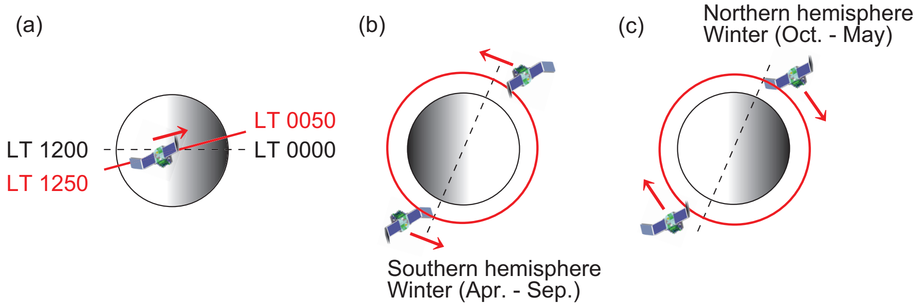

Figure 2.2: Schematic illustrations of the Reimei orbit. (a) The sun-synchronous polar orbit of Reimei viewed from the northern hemisphere mapped onto an equatorial plane. It is confined to local noon and midnight. (b)-(c) The sun-synchronous polar orbits of Reimei mapped onto a meridian plane in winter of southern and northern hemisphere, respectively.

Reimei was launched from Baikonur Space Center as a piggy-back satellite and inserted into a sun-synchronous polar orbit (inclination: 98.6 deg) at an altitude of approximately 630 km on 23 August 2005. The orbital meridian is on a 0050-1250 local time and it takes about 98 minutes to go around the Earth (Figure 2.2). During the development and at the beginning of operation, Reimei was officially planned to be able to operate only for one winter in the northern hemisphere. Although it has experienced twice fatal troubles with electron and ion sensors in August 2008 and January 2012, respectively, it still keeps observations for auroral emissions, airglows and sprites using multiple imagers.

2.1.2 Operation system

Flexible and compact operation system can be also given as one of Reimei advantages. Since such an operation system is one of the subjects of demonstration of advanced technologies, some attempts to simplify the operation itself were made. In addition, the flexible system for making observation plans enables us to collaborate easily with ground-based measurements such as EISCAT radar, THEMIS GBOs, and so on. A main operation station is located at JAXA/ISAS Sagamihara campus (Figure 2.3). It is composed of one room with several PCs installed in Windows OS and a communication antenna system with diameter of 3 m on the roof of a building. Various operations as command uplink for observations and data downlink are basically carried out in this simple and small station. The operations are performed usually 4 or 5 passes every day, since two opportunities of passing over Sagamihara come around every local noon and midnight, due to its sun-synchronous orbit. In the case of an emergency at Sagamihara, the operations can be conducted in alternative station of JAXA/ISAS at Uchinoura. There are also two ground-stations only for conducting data downlink at Svalbard Satellite station in Norway and Syowa station in Antarctica.

A plan of Reimei observation is fixed based on judgments as to whether a planed observation satisfies the safe condition of electric power supply, attitude control, data storage and so on [*Obuchi et al.,* 2008]. If a plan for observation fulfills the requirements, it is registered with Reimei through operations. Figure 2.4 shows the schematic flow chart of the operation. Based on an observation plan for 2 or 3 days, the operation plan that consists of several commands for uplink and downlink procedures, Stored Command (SC) including observation plan and Binary Command (BC) accompanied by SC is produced. It is sent to the command PC from the command server, and the PC for antenna control reads a forecast Reimei orbit over the station. After a confirmation that Reimei getting into the range of communication by the station and stable tracking for Reimei, we start to establish interactive telecommunication between Reimei and the station by sending Uplink command from the Command PC to Reimei. The downlink data received by the telemetry is continuously transferred to PC for Quick Look (QL) of Reimei status via Server. Prepared commands before the operation are sent to Reimei, with monitoring Reimei status such as electric power of batteries on board and errors of attitude control, and we confirm whether the commands are successfully registered on command PC one by one. When either completing this sequence of operation or Reimei getting out the communication range of the station, the operation should be ended. The duration of operation for Reimei can range from 5 to 10 minutes depending on its orbit. In addition, automatically operation is partly introduced into the system as experiments to put it into practical use in near future.

Figure 2.3: (Left) A look inside Reimei operation room. Several PCs for sending a variety of commads and displaying satelitte status are putted into the room. (Right) Communication antenna with diameter of 3 m imstalled on the roof of ISAS building at Sagamihara .

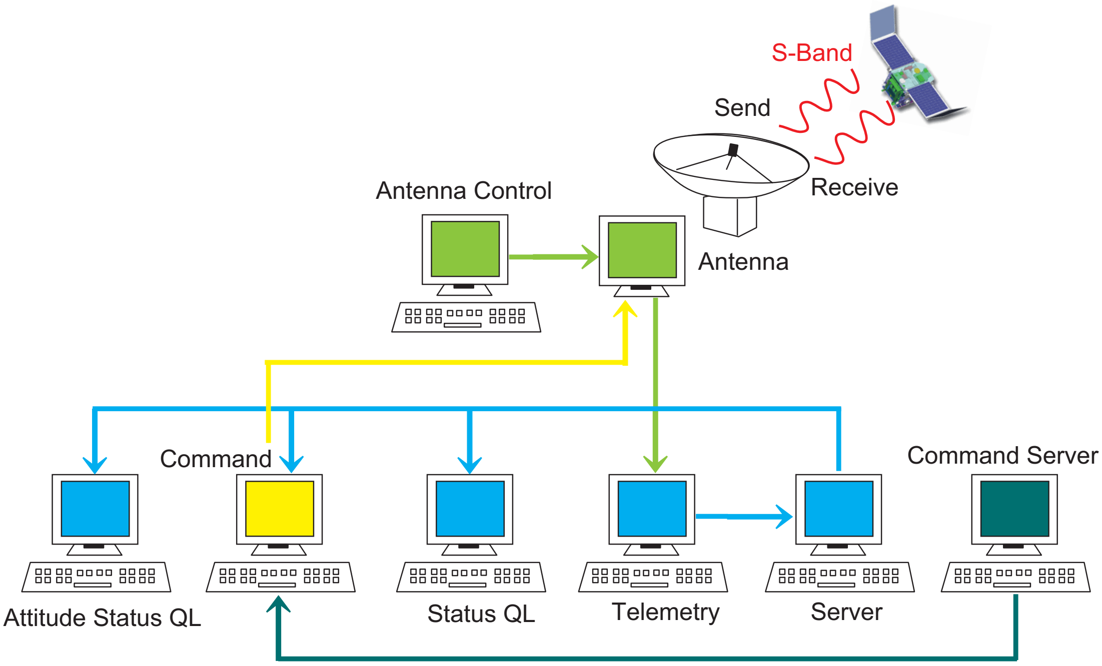

Figure 2.4: A schematic diagram of the operation system in ground-based station of Reimei. Arrows indicate flow of informations during an operation.

2.1.3 On-board scientific instruments

Reimei has five scientific instruments. Above all, three main instruments were developed for the purpose of aurora observation in high temporal and spatial resolutions: a multi-spectral auroral camera (MAC) with three-CCD channels [*Sakanoi et al.*, 2003; *Obuchi et al.*, 2008] and top-hat type electron and ion energy spectrum analyzers (ESA/ISA) [*Asamura et al.*, 2003, 2009]. Additionally, a plasma current monitor (CRM) composed of three Langmuir probes and magnetic field sensor (GAS) used for deriving attitude vector of satellite are also on board. All scientific instruments are controlled by Science-Handling-Unit (SHU), which supplies electric power and sends control signals to each instrument. The observation data and status of each scientific instrument are sent and concentrated in SHU temporally. SHU is under the control of Integrated Control Unit (ICU) of Reimei.

Multi-spectral Auroral Camera

MAC consists of three-channel monochromatic CCD imagers based on the concept that auroral fine structures and their rapid variations can be measured with high spatial and high temporal resolutions. Its body and other parts are made from aluminum for reduction in size and weight (about 4.6 kg). Figure 2.5 shows appearance of MAC developed as a flight model. MAC takes auroral images simultaneously at three wavelengths: 427.8 nm (N_2^+ 1st Negative Band), 557.7 nm (O Green line) and 670.0 nm (N_2 1st Positive Band). Power requirement at maximum is 29.4 W operating with three channels at the same time. The FOV of each channel is 7.6 × 7.6°, and it corresponds to a spatial scale of approximately 70 km × 70 km assuming that an altitude is 110 km. Table 2.1 shows the main specifications of MAC. Note that its spatial and temporal resolutions depend on observation modes (described later).

Figure 2.5: A flight model of MAC [*Obuchi et al.*, 2008]

Since three optical systems of MAC are independent of each other, MAC can simultaneously measure auroral emissions at three wavelengths. Auroral emissions at 427.8 nm and 670.0 nm are known as permitted lines whose lifetime are so short that it is appropriate for an observation of rapid variations. On the other hand, although an auroral emission line at 557.7 nm is a typical forbidden line with a lifetime of 0.74 sec, its excitation process is thought to be related to N_2 1st Positive Band emission. Therefore, it can help us to understand well physical and chemical process associated with precipitation generating a variety of aurora phenomena using the ratio between auroral intensities

Table 2.1: Specifications for MAC [*Obuchi et al.*, 2008]

MAC	
Optics design	Refracting monochromatic imager
Channel	3 (3 sets of optics, band-pass filters, and CCDs)
Wavelength	427.8 nm (N_2^+ 1N), 557.7 nm (OI), 670.0 nm (N_2 1P)
Focal length	50 mm
F number	1.5
FOV	7.6° × 7.6°
CCD	
Type	Interline transfer and surface irradiation type
Pixel number	1024 × 1024 pixels
Quantum efficiency	$\sim$ 0.6 @ 558 nm
Band-pass filter	
Center wavelength	FWHM/Transmittance (center of bandwidth)
427.8 nm	2.50 nm / 0.46
557.7 nm	1.57 nm / 0.55
670.0 nm	38.23 nm / 0.90
Lens	
Center wavelength	FWHM/Transmittance(center of bandwidth)
—	— / 0.8

with each wavelength. MAC is designed as fast optics ($F = 1.5$) with little aberration for the investigation of auroral fine-scale structures. It consists of synthetic silica lenses, an interference filter, and a radiation shield plate made of synthetic silica (Figure 2.6). Its transmittance of the whole optical system, without the band-pass filter of each channel, is 0.80. MAC uses a CCD which is the interline transfer and surface irradiation type with full pixel of 1024 × 1024 (each pixel size is 6.4 μm × 6.4 μm), and its quantum efficiency at 427.8 nm, 557.7 nm and 670.0 nm are about 0.53, 0.62 and 0.56, respectively. Suitable pixel binning on the CCD chip is performed according to the observation modes, and the binning size determines spatial resolutions of each observation mode. Additionally, the exposure time is variable in the stored commands sent from ground operations after launch. The exposure time can be selected in the range from 130 μsec to 3 sec. Although the exposure time is variable, the exposure cycle is basically fixed for each observation mode. They are 120, 1000, 4040, and 480 msec for Mode-0, 1, 2, and 3, respectively and more detailed description is given later.

Electron/Ion energy Spectrum Analyzers

Electron and Ion energy Spectrum Analyzers (ESA/ISA) measure flux of electrons and ions associted with auroral phenomena (Figure 2.7). They are so-called top-hat type electrostatic analyzers, whose mass is 1.4 kg and electric power requirement is 2.5 W in each sensor. Electrons and ions with energy per charge ranges from 10 eV/q to 12 keV/q in a logarithmic step, but ISA cannot distinguish ion species by the mass. It takes 1.25 msec to detect particles on each one energy step and, therefore, one scan for all 32 energy steps needs no more than 40 msec. Since the satellite velocity is $\sim$ 7.5 km/s, temporal resolution of ESA/ISA is corresponding to a horizontal spatial scale of 300 m at the altitude of 110 km. ESA/ISA has field of view covering 300° in the polar angle direction, divided into 30 sectors. During image-particle simultaneous observation mode, the Reimei attitude is controlled so as to keep the geomagnetic field direction within the disk-like FOV of ESA/ISA, so that particle distributions with full pitch-angle coverage can be obtained

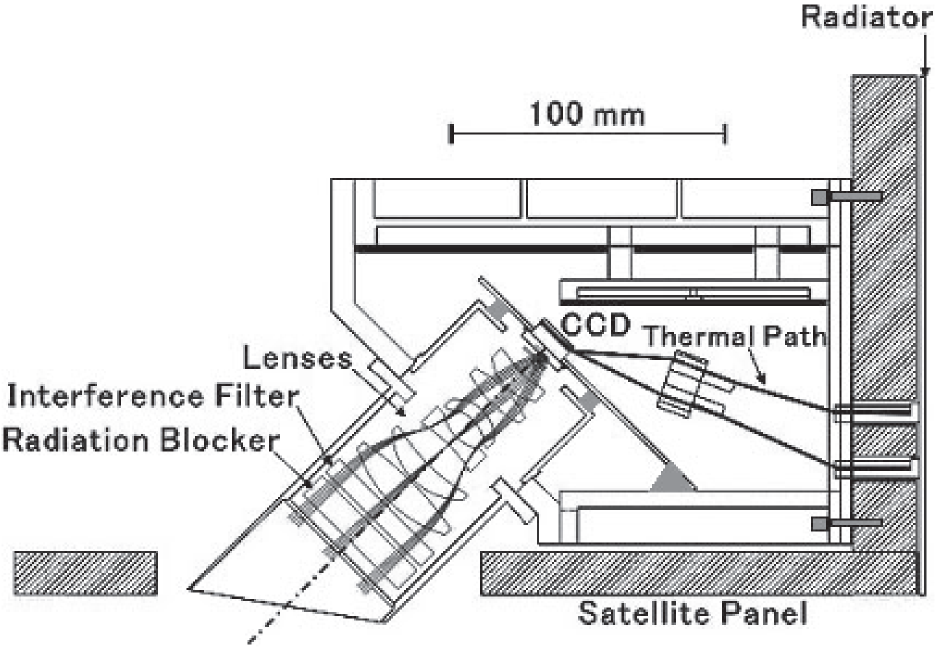

Figure 2.6: Schematic overview of cross-sectioned MAC and its surroundings. Three CCDs are connected to the radiator, which is attached to the outside of the satellite panel, with thermal paths [*Sakanoi et al.*, 2003].

in temporal resolution equal to an internal of one energy scan (40ms). Table 2.2 shows specifications of ESA and ISA.

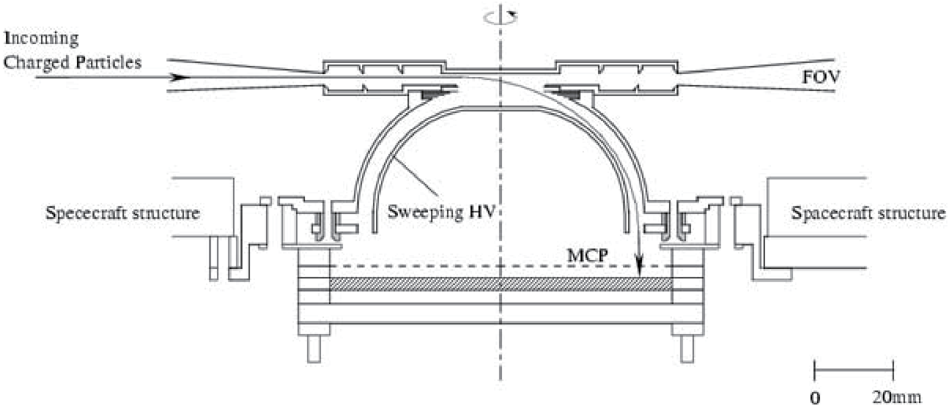

Figure 2.7: Schematic overview of cross-sectioned ESA/ISA [*Asamura et al.*, 2003].

Table 2.2: Specifications for ESA and ISA. [*Asamura et al.*, 2003]

ESA/ISA	
Design	Top-hat type electrostatic analyzer
Energy range (ESA)	12 eV - 12 keV
Energy range (ISA)	10 eV/q - 12 keV/q
Energy step	32 (logarithmic)
Energy resolution ($\Delta E/E$)	15% (FWHM)
Temporal resolution	40 msec/32 energy steps (1.25 msec/one energy step)
FOV	4 degree × 300°
Angular resolution	30 bins in polar angle direction
Geometry factor (ESA)	2.8×10^{-4} [cm^2 sr eV/eV/10°]
Geometry factor (ISA)	4.9×10^{-4} [cm^2 sr eV/eV/10°]

2.1.4 Observation mode

As mentioned in Chapter 2.1.1, Reimei realizes the three-axis attitude control. Consequently, it can observe in various attitudes under the conditions that the solar panel is pointed at the sun within 25 degrees for sufficient power supply. In addition, Reimei has several sensors in order to improve three-attitude attitude determination: a star tracker, a spin sun sensor, a non-spin sensor, an optical fiber gyro, and magnetic field sensor. As a result, Reimei attain complicated observation mode required high accuracy of attitude determination. There are four observation modes for MAC: Mode-0, Mode-1, Mode-2 and Mode-3 (Table 2.3). Mode-0, called Mode-S, is for the image-particle simultaneous measurement, and the detail of this mode is described later. Both Mode-1 and Mode-3 are usually used for measurement of aurora height distributions by pointing MAC's field-of-view (FOV) at the limb of the Earth. Assuming that MAC measures an aurora 2000 km distant from the satellite, the spatial resolutions in Mode-1 and 3 are 4.1 km and 2.0 km, respectively. Though Mode-3 allows to measure with a higher spatial resolution, it needs longer exposure time due to small pixel binning. Recently, Reimei has observed the height distribution of airglow and sprites in the mid-latitude regions in Mode-1. On the other hand the precise auroral distribution is measured with a higher spatial resolution in Mode-3. In Mode-2, Reimei obtains the data used for calibration such as the angles between FOV and the three axes of the satellite coordinates.

Table 2.3: Specifications of each observation mode. [*Obuchi et al.*, 2008]

Mode	Aim	Pixel binning	Temporal resolution	Spatial resolution
Mode-0	Footprint	16 × 16 pixels	120 msec	1.2 × 1.2 km [1]
Mode-1	Limb of the earth	16 × 16 pixels	1 sec	4.1 × 4.1 km [2]
Mode-2	Calibration stars	2 × 2 pixels	4.04 sec	—
Mode-3	Limb of the earth	8 × 8 pixels	480 msec	2.0 × 2.0 km [2]

Mode-S: Image and particle simultaneous observation

Reimei can conduct simultaneous observation of aurora image and particle flux by the three-axis attitude control that makes it possible to point the FOV of MAC at a footprint of magnetic field line threading Reimei (Figure 2.8). This observation mode is called Mode-S, and we have mainly used the data obtained during Mode-S in this study. Since 16 × 16 pixels are binned in Mode-S, MAC data is composed of 64 × 64 bins in each frame. The spatial resolution mapped on the magnetic footprint at an altitude of 110 km

---

[1] Assuming Reimei observes downward an auroral structure of altitude 110 km.

[2] Assuming Reimei observes an auroral height distribution distant from 2000 km.

results in about 1.2 × 1.2 km. Taking velocity of Reimei itself and the spatial resolution into account, an interval of each imaging that includes typical exposure time of 60 msec is set to be 120 msec.

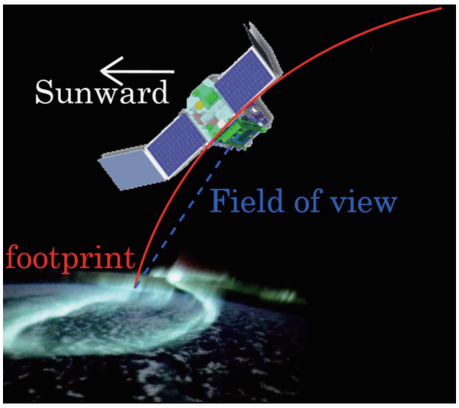

Figure 2.8: An illustration of the Reimei satellite during the measurements with Mode-S. (aurora image; http://images.jsc.nasa.gov/index.html)

2.2 Analysis

2.2.1 Typical PA event on October 18, 2007

We first present a typical PA event observed by Reimei in Mode-S over Alaska state in the United States from 11:35:12 UT to 11:35:59 UT on October 18, 2007. Note that this event has been reported by *Miyoshi et al.* [2010] as a case study. During this observation, the magnetic footprint of the Reimei satellite moved along the 0.7 magnetic local time (MLT) at invariant latitudes ranging from 65.9 to 62.7° (L = 6.00-4.75), corresponding to latitudes between 65.3 and 62.5° and east longitudes between 213.0 and 210.8° in the geographical coordinates. Figure 2.9 shows energy-time spectrograms for electron and ion based on measurement by Reimei/EISA between 11:35 UT and 11:36 UT. Intermittent precipitation with energy larger than a few keV can be clearly seen in the spectrogram for downward electrons with pitch angle of 0-30° (top panel in Figure 2.9). On the other hand, trapped electrons with pitch angle of 60-120° continuously existed during this period and they seemed to have no significant structures (second panel in Figure 2.9). Such a discrepancy between downward and trapped electrons suggests that strong pitch angle scattering enough to fulfill the loss cone immediately occurred above Reimei altitude along the filed line. *Sato et al.* [2002] reported an anti-correlation between downward flux of electrons and ions, therefore, a field-aligned potential may generate PA. However, no significant flux of ions for all components were observed by Reimei/ISA in this event. Moreover, the image-particle data obtained from the observations in Mode-S shows one-to-one correspondence between on-off switching of PAs and electron precipitation during this period. Here, Figure 2.10 indicates summary plots of the data from simultaneous Reimei/ESA and MAC observations. Figures 2.10 (a) and (b) are energy-time spectrograms for the downward electron flux with a local pitch angle of 0-30° during the Mode-S observations. Reimei passed over several regions characterized by intermittent precipitating electrons with energies of more than a few keV. These precipitating electrons had 3-4 Hz modulations and they appeared especially in higher-energy channels for 8.7 and 12 keV (not shown). Such quasi-3 Hz modulations have been reported in the previous studies [e.g., *Sandahl et al.*, 1980; *Sato et al.*, 2004]. Figures 2.10 (c) and (d) show images exhibiting bright and extended aurora in the north-south direction. Figure 2.10 (e) shows no significant aurora emissions although most of the imaged area overlaps that in Figure 2.10 (d), which means that MAC data can be used to identify the temporal variation in a PA. Note that Figures 2.10 (c) and (d) correspond to the on-phase and Figure 2.10 (e) corresponds to the off-phase and that the quasi-periodic emission had a recurrence period of about 3-4 s. The quasi-periodic precipitations of electrons with energy of more than a few keV from 11:35:20 UT to 11:35:50 UT were similarly related to PAs.

As indicated by the red arrow in Figure 2.10 (b), typical fine-scale structures of electron precipitation showing an energy-time dispersion with a lower energy limit of about 2 keV can be clearly seen at around 11:35:14 UT. Since TOF analysis requires the energies and time delays of a particle arriving at the detector, as described later, we carried out following analyses to estimate the values of time delay precisely. Figure 2.11 (a) shows the normalized count of electrons for each energy channel (12, 8.7, 6.8, 5.3, 4.2, 3.2, and 2.4 keV) as a function of time corresponding to the energy-time dispersion starting at 11:35:14 UT, corresponding to the dispersion indicated by the red arrow in Figure 2.11 (b). The normalized counts of higher energies have a better signal-to-noise (S/N) ratio because of their higher count rate. To obtain a better S/N ratio for the lower energy electrons, we applied an exponentially weighted moving average to the count data at each energy channel. For a weighted moving average, we used three data intervals, which correspond to 120 msec. This method makes it possible to gain the S/N ratio while retaining the original waveforms. The results are shown in Figure 2.11 (b). In this analysis, an initial increase of energy-time dispersion should satisfy the condition that the flux is larger in

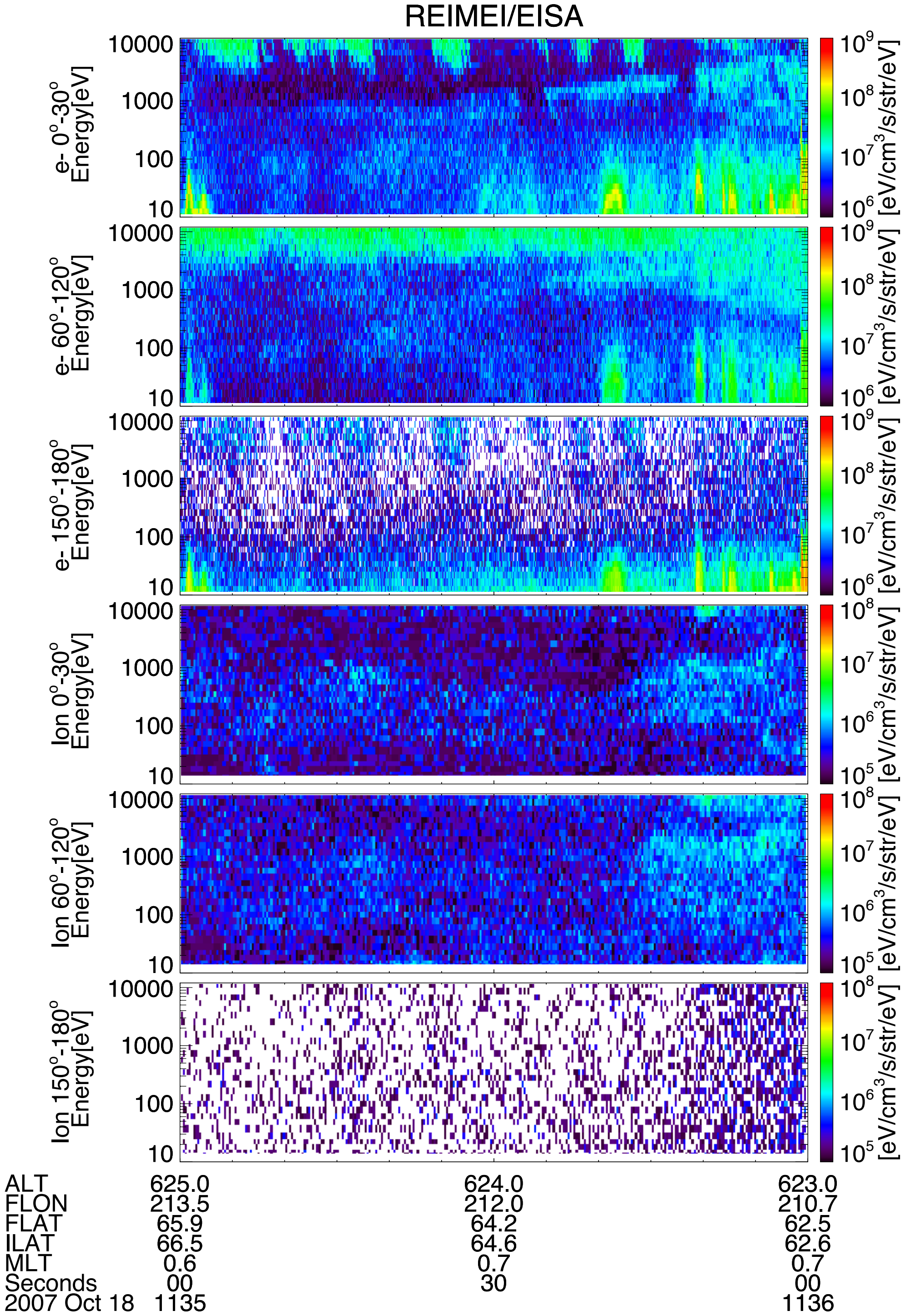

Figure 2.9: Energy-time spectrograms obtained from Reimei/EISA measurement from 11:35 UT to 11:36 UT on October 18, 2007. Top three panels show differential energy flux of electrons as a function of time and energy ranges 12 eV to 12 keV, for downward ($0° < \alpha < 30°$), trapped ($60° < \alpha < 120°$), upward ($150° < \alpha < 180°$) components, where α is the pitch angle. Similarly, bottom three panels show differential energy flux of ions as a function of time and energy per charge ranges 10 eV/q to 12 keV/q, for downward ($0° < \alpha < 30°$), trapped ($60° < \alpha < 120°$), and upward ($150° < \alpha < 180°$) components, as well.

one order than previous background flux. The initial increase of 12 keV electrons was identified around 11:35:14.3 UT. Next, cross-correlation analysis was conducted, and the time delays among the variations in the different energy channels were estimated. The

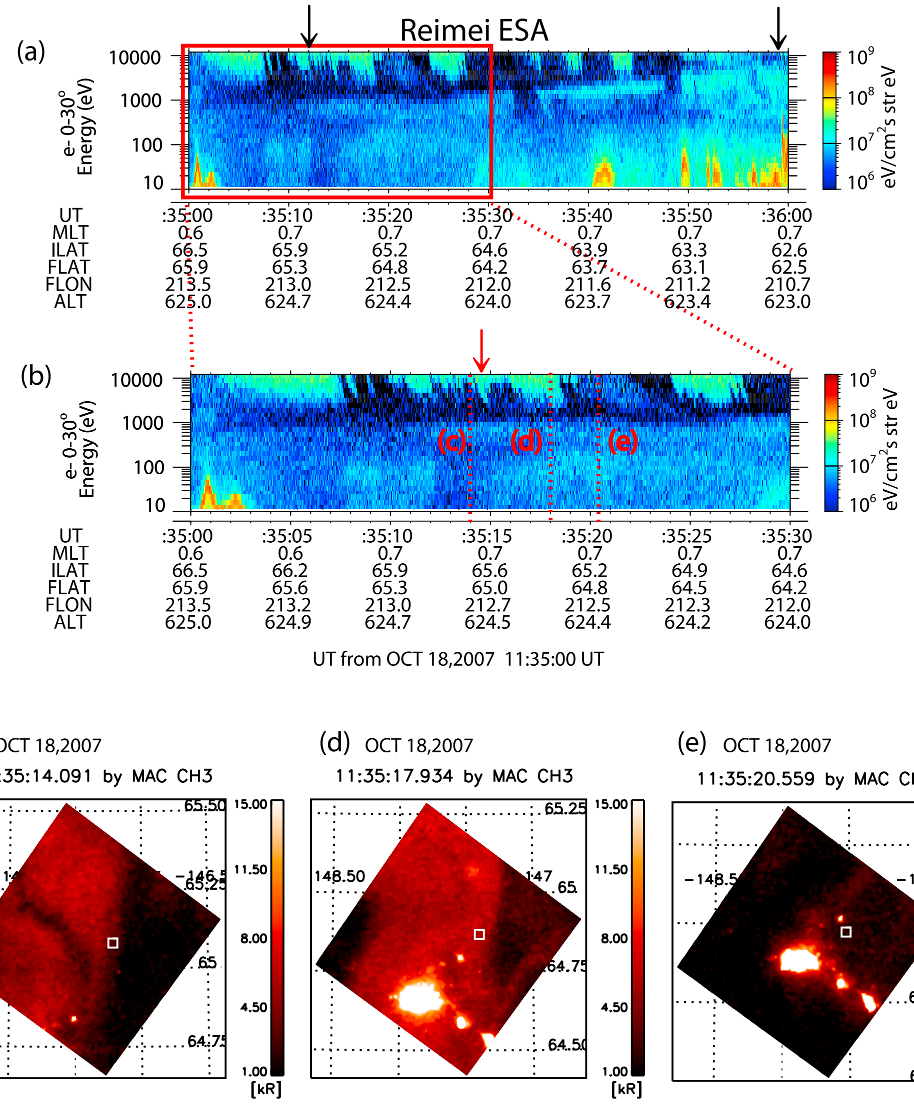

Figure 2.10: Summary plots of Reimei data for a PA event on October 18, 2007, showing energy-time spectrograms of precipitating electrons for (a) 11:35:00 UT to 11:36:00 UT and (b) 11:35:00 UT to 11:35:30 UT, respectively. Black arrows in (a) indicate the start and end of Mode-S observation, and red arrow in (b) around 11:35:14 UT indicates energy-time dispersion of precipitation. (c-e) Successive auroral images at 670.0 nm emission are plotted in geographical coordinates showing spatial and temporal variations of PA during on-phase in (c) and (d) and off-phase in (e). White square in each image represents the location of ionospheric footprint of the magnetic field line threading Reimei.

2.4 keV electrons, for example, were found to have an estimated time delay of 480 msec compared to the 12 keV electrons.

2.2.2 Time of flight analysis method

We can calculate the distance between the observation location and source position from the TOF analysis assuming that electrons with different energies start precipitating simultaneously from the same source position. With this standard TOF model, distance to electron source L is given by

$$L^{-1} = \left(v_i^{-1} - v_j^{-1}\right) \Big/ (t_i - t_j) \quad (v_i < v_j \quad and \quad t_j < t_i) \tag{2.1}$$

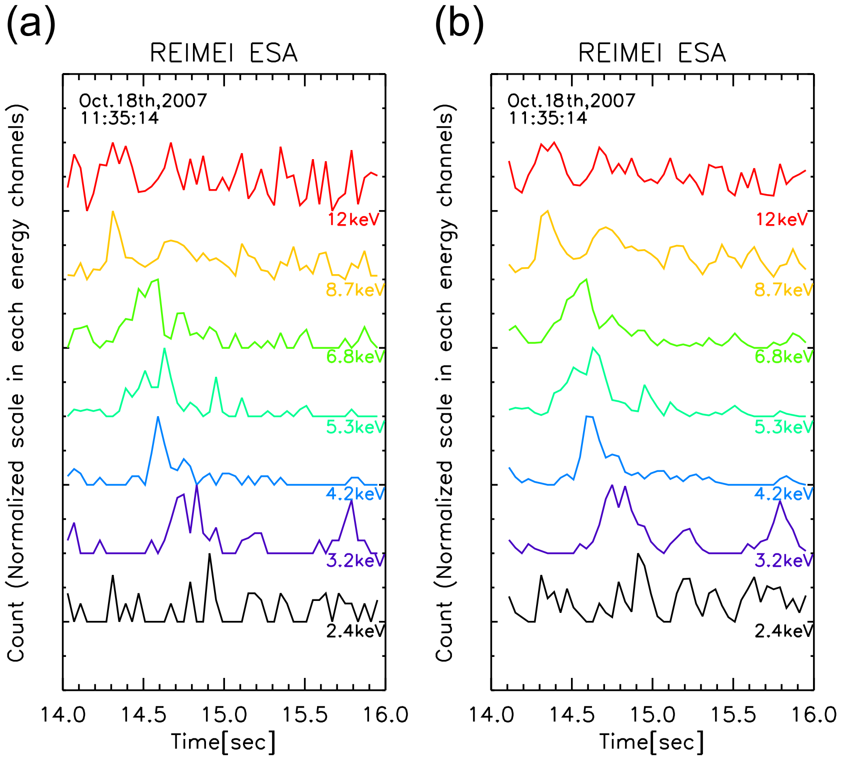

Figure 2.11: (a) Normalized count of electrons for each energy channel (12, 8.7, 6.8, 5.3, 4.2, 3.2, and 2.4 keV) as a function of time starting at 11:35:14 UT for auroral event on October 18, 2007. (b) Normalized count on exponentially weighted moving average chart for each energy channel.

where v and t are electron velocity and detection time, respectively [*Hardy et al.*, 1990; *Sato et al.*, 2004]. The distance to the electron source is obtained by fitting a line to the observed data. The source in the magnetosphere can be mapped by tracing the field line from the satellite position using the realistic magnetic field model of *Tsyganenko and Sitnov* [2005]. The solar wind parameters used for the magnetic field model were obtained from the OMNI database (http://omniweb.gsfc.nasa.gov/).

2.2.3 Time of flight model: wave-particle interactions between electrons and propagating whistler mode waves

We also carried out an alternative TOF analysis taking into account whistler mode wave propagation and wave-particle interactions [*Miyoshi et al.*, 2010]. It is based on the idea that whistler mode wave packet originating at the magnetic equator propagates toward higher latitudes and resonates with electrons, when the resonance conditions are satisfied. Previous studies revealed that chorus waves are generated at the magnetic equator and propagate away from it [e.g., *Santolik et al.*, 2003]. Figure 2.12 shows the schematic sequence of this process adapted from *Miyoshi et al.* [2010]. At first, whistler mode wave is generated, and it resonates with the electron with the lowest energy of precipitations at the magnetic equator. Then the whistler mode wave propagates to the high latitudes along the field line. The propagating whistler mode wave can resonate with the higher-energy electrons at the high latitudes. This model has two key features. One is that the source region of a PA observed in the Southern (Northern) Hemisphere continues northward (southward) along the field line from the equator. This is because an electron interacts via cyclotron resonance $\omega - k_{||}v_{||} = n\omega_{ce}/\gamma$, where $\omega < \omega_{ce}$ ($n = 0, \pm 1, \pm 2...$) with a whistler mode wave that propagates to the opposite directions. The second key feature is that the higher energy electrons arrive at the ionosphere earlier even though the resonance of higher-energy electrons occurs after that of lower-energy electrons and the higher-energy electrons travel a longer path, which reproduces the observed energy-time dispersions.

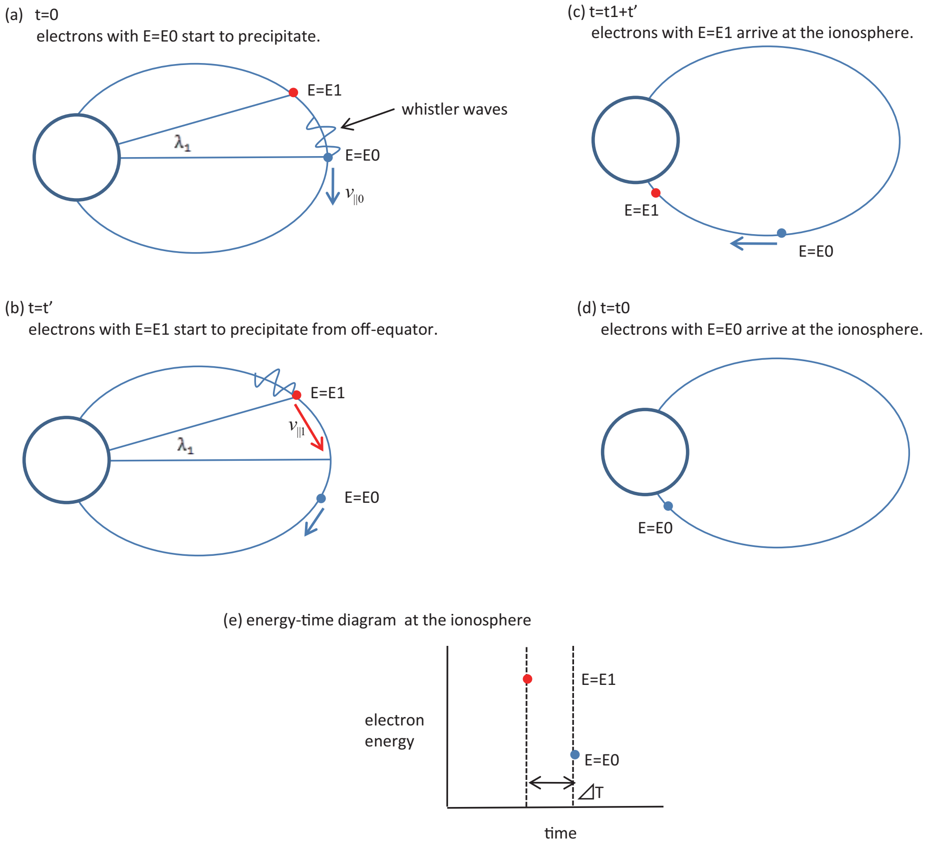

Figure 2.12: Schematic diagrams showing (a-d) a sequence of pitch angle scattering of electrons with propagating whistler mode waves and (e) expected energy-time diagram at ionospheric altitude (adapted from *Miyoshi et al.* [2010]).

The basic process of obtaining theoretical energy-time dispersion is as follows. If the cyclotron resonance occurs between electrons whistler mode waves and in the course of propagation, the first-order resonance energy of electron is given by *Kennel and Petschek* [1966]

$$E_{res} = \frac{B^2}{2\mu_0 N_c} \frac{\omega_{ce}}{\omega} \left(1 - \frac{\omega}{\omega_{ce}}\right)^3 \tag{2.2}$$

where B is the ambient magnetic field intensity, μ_0 is the permittivity of a vacuum , ω is the frequency of whistler mode wave, and ω_{ce} is the local cyclotron frequency. N_c is the cold plasma density, and it can be assumed to be uniform along the field line. Figure 2.13 shows an example of calculation. Since E_{res} is a function of magnetic field intensity, E_{res} becomes larger at regions distant from the equator as Figure 2.13 demonstrate. A part of electrons resonated with whistler mode waves falls into a local loss cone by pitch angle scattering and precipitates into the ionosphere. From a conservation of the first adiabatic invariant, the local loss cone angle at a point, s, along a filed line, $\alpha_{loss}(s)$, can be derived as;

$$\alpha_{loss}(s) = \arcsin\left(\sin\alpha(s_{ionosphere}) \cdot \sqrt{\frac{B(s)}{B(s_{ionosphere})}}\right) \tag{2.3}$$

where $\alpha(s_{ionosphere})$ and $B(s_{ionosphere})$ are the pitch angle of electron and the magnetic

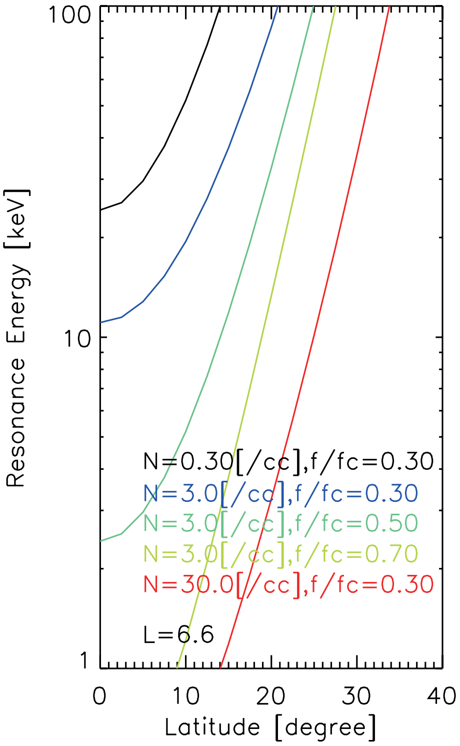

Figure 2.13: Electron resonance energy of the first order based on [*Kennel and Petschek*, 1966]. In this calculation, cold plasma density, N_c, and normalized frequency by the local cyclotron frequency, ω/ω_{ce}, are free parameters and L-value, L, is assumed to be 6.6.

field intensity in the ionosphere. $B(s)$ is the magnetic field intensity at the point of s. Regarding downward electrons with pitch angle of 0-30° observed by Reimei/ESA as electrons associated with auroras, data for electron with pitch angle within 30° and the magnetic field at Reimei altitude are used for the condition at the ionosphere. As a result, we can obtain pitch angle of electrons at any places connected to Reimei by the field line. Next, whistler mode wave grows at the magnetic equator s_0 and resonates the electron with the lowest energy E_0. Then, the electron starts to precipitate into the upper atmosphere in the opposite hemisphere. The travel time of the electron is obtained as;

$$\begin{aligned} t_0 &= \int_{s_0}^{s_{ionosphere}} \frac{ds}{v_{\parallel 0}(s)} \\ &= \int_{s_0}^{s_{ionosphere}} \sqrt{\frac{m_e}{2E_0}} \frac{ds}{\sqrt{1 - \sin^2 \alpha_{loss}(s_{ionosphere}) \dfrac{B(s)}{B(s_{ionosphere})}}} \end{aligned} \tag{2.4}$$

where m_e is the mass of electron. The whistler mode wave propagates to higher latitudes and resonates with the electron of higher energy E_1. Traveling time of waves to propagates from the equator to a point at latitude λ_1 is given as;

$$t' = \int_{s_0}^{s_{\lambda_1}} \frac{ds}{v_g} = \int_{s_0}^{s_{\lambda_1}} \frac{ds}{\partial\omega \big/ \partial k} \tag{2.5}$$

where k is the wave number. The electron with energy E_1 is delayed by a finite time of t' to start to precipitate. In this case, the traveling time of the electron is similarly written as;

$$\begin{aligned} t_1 &= \int_{s_1}^{s_{ionosphere}} \frac{ds}{v_{\|1}(s)} \\ &= \int_{s_1}^{s_{ionosphere}} \sqrt{\frac{m}{2E_1}} \frac{ds}{\sqrt{1 - \sin^2 \alpha_{loss}(s_{ionosphere}) \frac{B(s)}{B(s_{ionosphere})}}} \end{aligned} \tag{2.6}$$

and the difference of arrival time at the ionosphere between electrons with energy of E_0 and E_1 is finally given as below;

$$\Delta T|_{E_0,E_1} = |t_1 + t' - t_0|. \tag{2.7}$$

A theoretical energy dispersion curve can be calculated by repeating these steps for a variety of electron energies, i.e. a variety of points along the field line.

2.2.4 Fitting to observed energy-time dispersion

In this thesis, the two TOF analyses are hereafter referred to as "TOF-A" (described in 2.2.2) and "TOF-B" (described in 2.2.3), respectively. We carried out the TOF-A and TOF-B analyses by using the energy-time dispersion of the downward electrons causing the PA observed by Reimei. We estimated the distance from the source region by linear fitting to the inverse electron velocity as a function of time in the TOF-A analysis. Figure 2.14(a) shows the results of linear fitting using the TOF-A analysis; the estimated distance to the modulation region was about 30,000 × (1 ± 0.034) km, corresponding to magnetic latitude of 25.0°. The TOF-B model assumes that an element of whistler mode chorus wave with a typical rising tone of 7.6 kHz/s [*Santolik et al.*, 2008] and finite frequency ranges ($0.10 < \omega/\Omega_{ce} < 0.50$, $0.50 < \omega/\Omega_{ce} < 0.70$) [e.g., *Santolik et al.*, 2005b]. Note that ω_{ce} means equatorial cyclotron frequency. We assume that whistler mode chorus waves propagate along a field line with keeping their initial frequencies at the equator $\omega = a\Omega_{ce}$, where $0.10 < a < 0.70$ [*Santolik et al.*, 2003]. Each frequency component of a rising tone starts to propagate from the equator with a time delay corresponding to the frequency drift, and each frequency component should interact with electrons.

In the analysis, an adjustment for thermal plasma density N_c (0.10-30.0 cm^{-3}) and whistler mode wave frequency is needed to fit the theoretical dispersion curve to the measured energy dispersion. Figure 2.14(b) is the results of the fitting. The red points represent energy of each ESA channel, and black solid lines indicate an energy-time dispersion of precipitating electrons corresponding to each frequency component of a rising tone. The line that first appeared in the E-t spectrum resulted from wave-particle interactions with the minimum frequency component launched from the equator, and sub- sequent energy-time dispersions can be seen due to the precipitations caused by higher-frequency component. There may be inconsistency between ESA measurements and precipitations expected from the model at the energies between 2 and 1 keV, probably because of a few count rates at this lower energy. We estimated a plausible combination of N_c and ω/Ω_{ce} was 9.7 cm^{-3} and $0.40 < \omega/\Omega_{ce} < 0.45$ by fitting of the energy-time dispersion measured by ESA. This best combination was identified by a chi-square test between the data points of ESA measurements and a curve that corresponded to the minimum resonance frequency. Figure 2.14(c) shows the density and frequency dependence of the energy-time dispersion curve. Error bars of the density and frequency can be estimated to be about ±1.5 cm^{-3} and less than 0.02 Ω_{ce}.

2.2.5 Identification of modulation region

We can identify modulation region of electrons associated with PAs based on the two TOF methods described in 2.2.4 and the empirical magnetic field model. Concerning

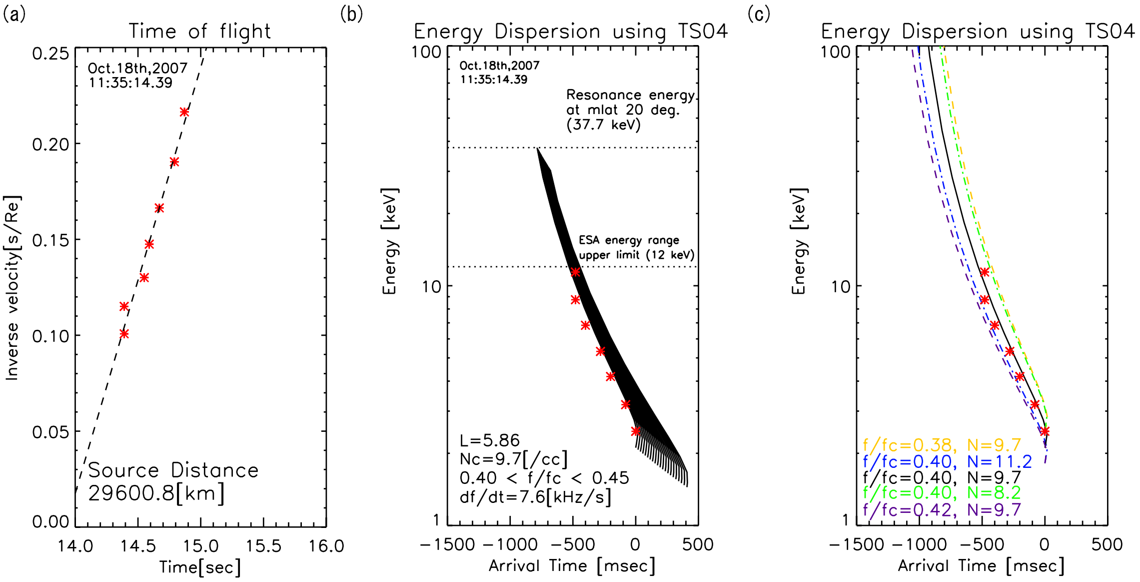

Figure 2.14: (a) Inverse velocity of measured electrons at 11:35:14.39 UT on October 18, 2007. Dashed line indicates linear fitting of data for seven ESA channels. Calculated distance between source region and Reimei satellite was 29,600 km. (b) Result of best fitting between theoretical dispersion curve and observed energy-time dispersion. Red points represent energies of ESA channels. Observed dispersion (red points) fits theoretical dispersion curve very well assuming N_c and ω/Ω_{ce} are 9.7 cm^{-3} and $0.40 < \omega/\Omega_{ce} < 0.45$, respectively. (c) The density and frequency dependence of the calculated dispersion curve. N_c and ω are changed into (9.7 ± 1.5) cm^{-3} and (0.40 ± 0.02) Ω_{ce}, respectively. This result indicates that error bars of the density and frequency could be estimated to be about ±1.5 cm^{-3} and less than 0.02 Ω_{ce}, since the calculated dispersion curves are included by error bars of energy (not shown) in each ESA channel.

TOF-B analysis, the energy of precipitating electrons depends on the latitudes where the cyclotron resonance occurs, and therefore the latitudinal range of the modulation region can be estimated. In this event, the energy of electron ranged from 2.4 to 11 keV. This energy range corresponded to the region between the magnetic equator and magnetic latitude of -14.3°. Figure 2.15(a) shows the modulation region as a point source mapped on the meridinal plane in the GSM coordinates, identified by the TOF-A analysis. The solid line in indicated the field line connecting Reimei position in the ionosphere. The source position is located at mid-magnetic latitude of 26.0° that is far from the equator in this event, and this result is agreed with the precedence result in *Sato et al.* [2004]. On the other hand, Figure 2.15 (b) shows the identified modulation region extended southward mapped onto GSM coordinates. Since the energy of precipitating electrons depends on where the cyclotron resonance occurs, the range of source regions can be identified from their energy ranges. However, we cannot exclude the possibility that electron with energy higher than 11 keV, which are generated in far higher latitudes, precipitated simultaneously during this event. Assuming that the electrons with an energy of 25 keV precipitate observed in this event, the source region is extended to -18.1° in magnetic latitude.

2.3 Results and discussion

2.3.1 Statistical results

The TOF-A and B analyses were carried out for the 29 auroral events in 11 satellite paths that showed the electron energy dispersion clearly in the E-t spectrum As a result, statistical distributions of the modulation regions were identified based on both TOF anal-

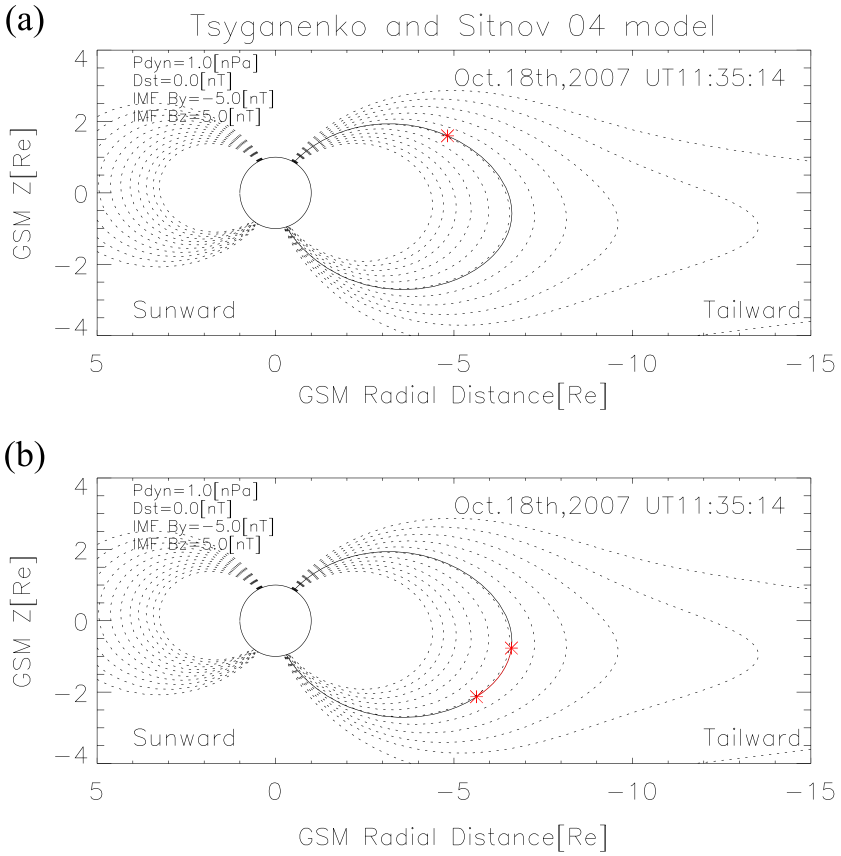

Figure 2.15: (a) The point source identified by the TOF-A analysis mapped on the meridional plane in the GSM coordinates. The magnetic field lines are calculated from the model of *Tsyganenko and Sitnov* [2005] and a solid line indicates the field line connecting to the Reimei position. (b) The source distribution identified by the TOF-B analysis mapped on the meridional plane in the GSM coordinates. Two red marks represent magnetic equator and the end of high latitude limit of the source region.

yses. The data sets were obtained from Mode-S observations in the northern hemisphere (L = 5.13-6.34) during winter in 2005-2008. Dataset used for statistical analysis in this study is listed in Table 2.4.

Figure 2.16(a) shows the source regions estimated by the TOF-A analyses mapped onto coordinates for which the horizontal axis corresponds to the magnetic equator of the field lines for each event. Though a few sources estimated by the TOF-A analyses were in the southern hemisphere, most of the sources were distributed in the Northern Hemisphere (86% of total events). In addition, this statistical result revealed the important fact that the modulation regions were not localized near the Earth but distributed continuously from the equator to the high latitude regions of about 50°. Figure 2.16(b) shows the source regions obtained from the TOF-B analysis. Each red line corresponds to the estimated interaction regions for the observed energy range of electrons. Since all of the PAs in this study were observed in the northern hemisphere by Reimei, the observed precipitating electrons interact with whistler mode waves that propagate from the magnetic equator to the southern hemisphere. Note that the magnetic equator was defined as the location of the minimum magnetic field along a field line in this study. Whistler mode chorus waves have been known to often propagate from the off-equator [*Santolik et al.*, 2005a], and the distance from the equator was estimated to be a few thousand kilometers. This distance corresponds to latitudinal distribution of the source region within 2-3°. Such latitudinal offset on the modulation region does not cause any significant impact on the result because the difference of the local cyclotron frequency along the field line can be

Table 2.4: Dataset used for statistical analysis in this study. All data were obtained from observations in northern hemisphere during Mode-S.

Dataset					
Date	UT	ILat / *L*-value	MLT	*AE* (1h mean)	*Dst*
NOV 30, 2005	00:52:32	66.6 / 6.34	3.3	161 nT	19 nT
	00:52:45	65.9 / 6.00	3.2		
JAN 29, 2006	02:09:17	66.6 / 6.34	3.0	35 nT	13 nT
	02:09:19	66.5 / 6.29	2.9		
	02:09:21	66.4 / 6.24	2.9		
FEB 21, 2006	04:38:28	65.7 / 5.91	2.6	152 nT	-20 nT
OCT 18, 2006	04:06:05	66.4 / 6.23	3.1	91 nT	-15 nT
	04:06:08	66.2 / 6.14	3.1		
FEB 16, 2007	08:10:20	66.1 / 6.09	0.6	62 nT	-20 nT
	08:10:21	66.1 / 6.09	0.6		
SEP 02, 2007	05:21:13	65.6 / 5.86	2.3	301 nT	-22 nT
	05:21:16	65.4 / 5.77	2.3		
	05:21:20	65.3 / 5.73	2.2		
	05:21:23	65.1 / 5.64	2.2		
OCT 18, 2007	11:35:14	65.6 / 5.86	0.7	553 nT	0 nT
	11:35:24	65.0 / 5.60	0.7		
	11:35:39	64.0 / 5.20	0.7		
	11:35:42	63.8 / 5.13	0.7		
NOV 14, 2007	16:44:30	65.4 / 5.77	2.0	279 nT	-8 nT
	16:44:41	64.8 / 5.51	2.0		
	16:44:48	64.4 / 5.35	2.0		
	16:44:51	64.2 / 5.27	1.9		
FEB 11, 2008	10:29:40	65.3 / 5.72	0.1	335 nT	-12 nT
	10:29:56	64.3 / 5.32	0.1		
MAR 11, 2008	08:12:22	64.6 / 5.44	0.6	251 nT	-25 nT
	08:12:25	64.4 / 5.36	0.5		
	08:12:34	63.9 / 5.17	0.5		
MAR 27, 2008	09:55:23	64.2 / 5.28	0.2	474 nT	-30 nT
	09:55:25	64.0 / 5.20	0.2		

negligible around the magnetic equator. Moreover, the maximum growth of chorus waves is expected to occur at the equator by the simulation study [e.g., *Katoh and Omura*, 2007], and therefore, it is plausible to assume that the chorus waves propagate from the magnetic equator.

Figures 2.17(a) and (b) show the latitudinal distributions of the sources calculated from the TOF-A analysis and the off-equator boundaries of the modulation region calculated from the TOF-B analysis, respectively. Figure 2.17(a) shows that the modulation regions are distributed almost continuously from magnetic latitude ranges -20 to 50° and are slightly concentrated from 15 to 25°. Figure 2.17(b) shows that the boundaries of the source regions are located around -12°. The red broken line shows the distribution of the calculated off-equator boundaries assuming precipitation of higher-energy (25 keV) electrons (not measured by Reimei). In this case, these boundaries extend to -15°.

The region where Reimei observed the 29 PAs ranged from 63.8 to 66.6° (L = 5.13-6.34) in the invariant latitude. This region is close to the plasmapause that exists typically at L = 4-6. Since the cold plasma density is an important parameter for wave-particle interactions, the relative position of the PA source to the plasmapause is essential for understanding of the generation process. Figure 2.18 shows the relationship between the

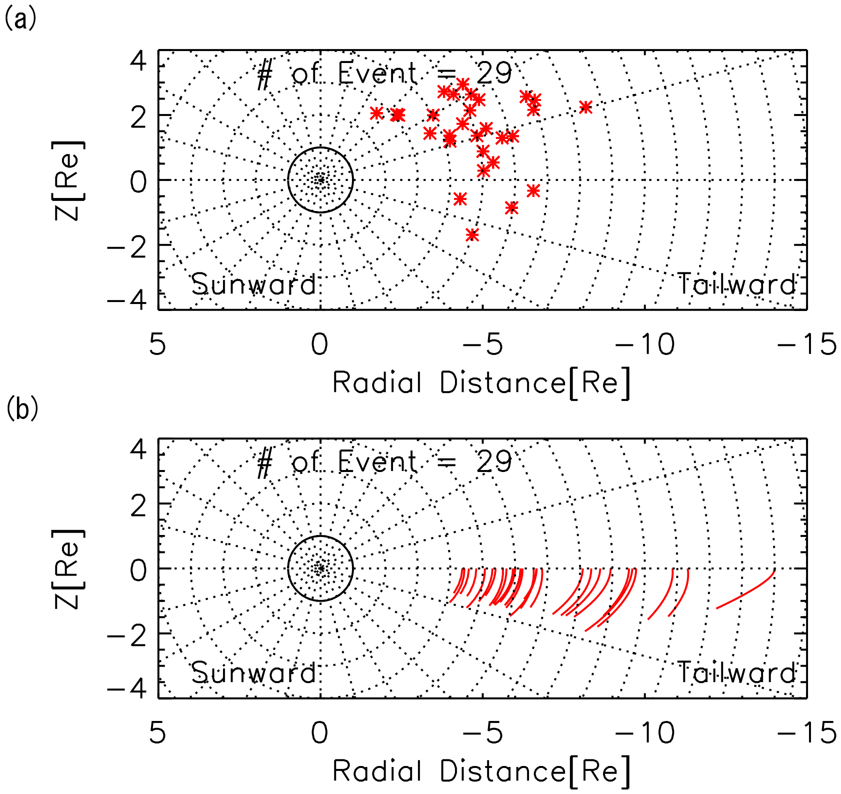

Figure 2.16: (a) Statistical distribution of 29 modulation regions identified by TOF-A analysis mapped onto coordinates in which horizontal axis corresponds to magnetic equator of field lines for each auroral event (not GSM coordinates). Dotted lines indicate magnetic latitudes at 0, 15, 30, 45, 60, 75, and 90°. Red points represent point sources. (b) Statistical distribution of modulation regions identified by TOF-B analysis; red solid lines represent the regions, where wave - particle interactions occurred between whistler mode chorus waves and electrons.

modulation region and plasmapause location estimated from an empirical model [*O'Brien and Moldwin*, 2003]. The four dash-dotted lines indicate the L values of the empirical plasmapause in each MLT sector as a function of the maximum of the AE index for the preceding 36 h. The diamonds represent the L values and AE indices when Reimei observed PAs in these MLT sectors. As shown in Figure 2.18, all of the 29 auroral events occurred outside the empirical plasmapause. The cross-correlation coefficient between $\log_{10}(AE)_{max}$ and L was -0.46. The modulation regions of the PAs also tend to move closer to the Earth as the AE index increase, that is, the plasmapause moves earthward.

The cold plasma density and whistler mode wave frequency can be estimated from the TOF-B analysis. As well as an example of Figure 2.14(c), errors of the density and frequency in all events can be estimated to be about ± 1.5 cm^{-3} and less than 0.02 Ω_{ce}, respectively. Figure 2.19 shows the distributions of the cold plasma density and whistler mode wave frequency plotted in the GSM coordinates, invariant latitudes, and MLTs. Figures 2.19(a) and (b) show the source locations of the PAs mapped onto each of the magnetic equatorial planes determined by the empirical model of *Tsyganenko and Sitnov* [2005]. The colors represent the cold plasma densities and whistler mode wave frequencies. Figures 2.19(c) and (d) are the same as Figures 2.19(a) and (b) except for mapping by the invariant latitudes and MLTs. These positions were calculated from the magnetic footprint of Reimei at the altitude of the 110 km using the international geomagnetic reference field (IGRF) model. The color scales of density and frequency (normalized by the equatorial cyclotron frequency) range from 0.10 to 30.0 cm^{-3} and from 0.10 to 0.70, respectively. The estimated cold plasma densities are consistent with the those of empirical models

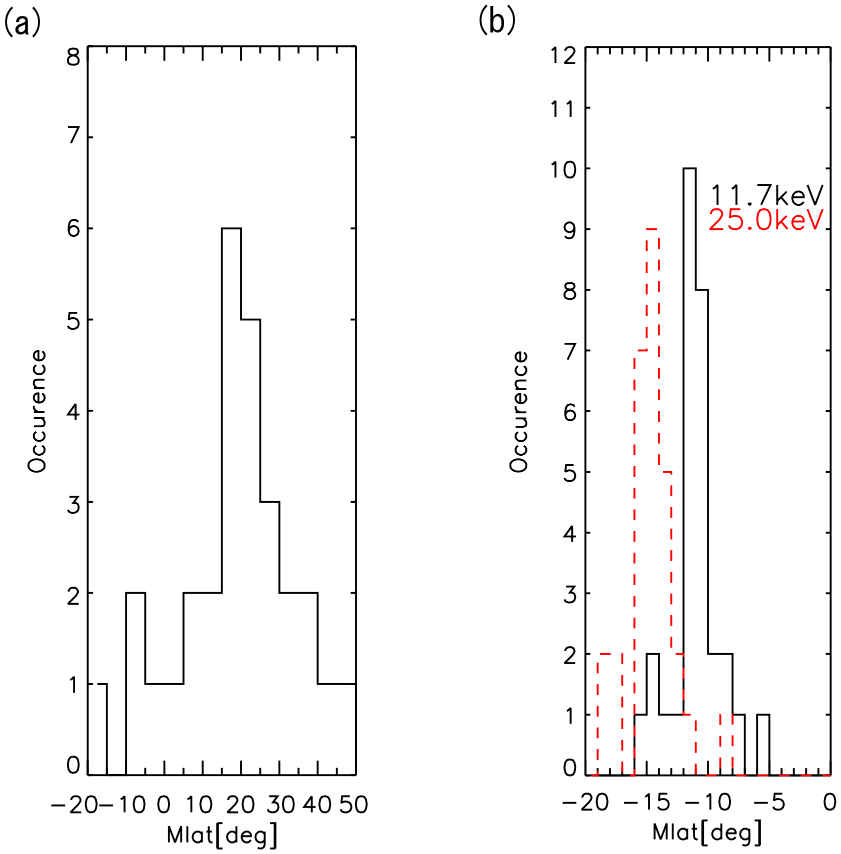

Figure 2.17: (a) Latitudinal dependence of source positions obtained from the TOF-A analysis. (b) Latitudinal dependence of high-latitude boundaries of identified source regions obtained from TOF-B analysis. Black solid line and red broken line in Figure 2.17(b) represent upper limit energies of precipitating electrons with energies of 11.7 and 25.0 keV, respectively.

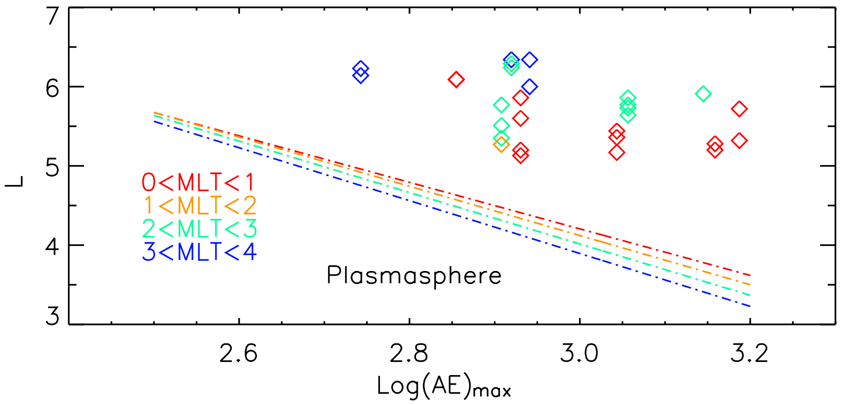

Figure 2.18: Relationship between source region of PA and location of plasmapause. Four dash-dotted lines indicate locations of plasmapause given by empirical model [*O'Brien and Moldwin*, 2003] for four MLT sectors (0-1 h, 1-2 h, 2-3 h, 3-4 h). Diamonds represent L values and AE indices when Reimei observed PA in the same four MLT sectors.

[*Carpenter and Anderson*, 1992; *Sheeley et al.*, 2001], except for only one case where the density reached 21.7 cm^{-3}. As shown in Figure 2.19(a), the density tends to increase as the radial distance from the Earth decreased. The density also increased in the midnight region compared to that in later MLTs (Figure 2.19(c)) although there were also low density (1.0-2.0 cm^{-3}) regions. The higher-frequencies can be obtained in the regions near the Earth and the midnight as shown in Figures 2.19(b) and (d), respectively. It is

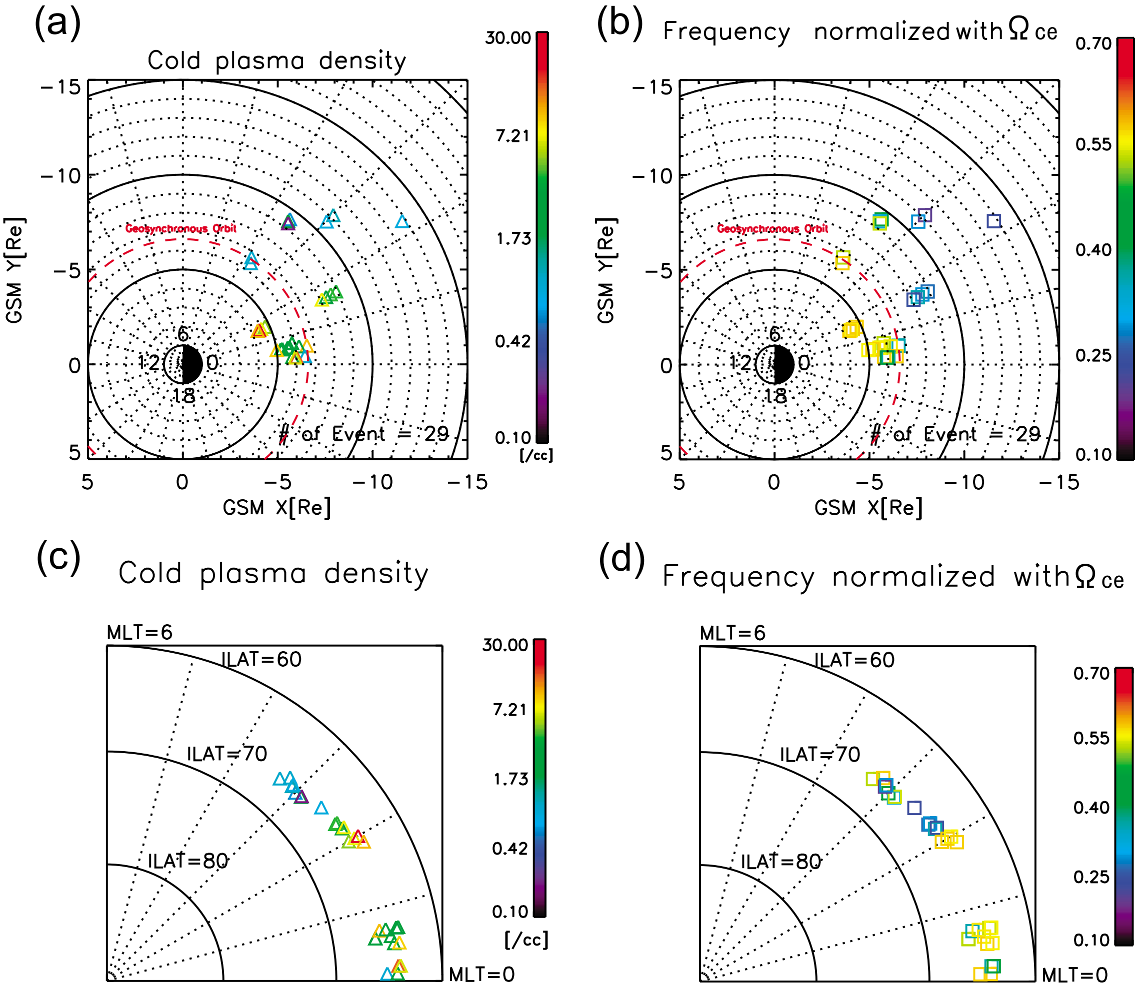

Figure 2.19: (a-b) Source positions of PA events mapped onto magnetic equator using model of *Tsyganenko and Sitnov* [2005]. Colors represent cold plasma density and whistler mode wave frequency. (c-d) Same as (a) and (b) except for mapping with invariant latitude and MLT at magnetic footprint.

important to note that the estimated wave frequency covers from the lower to the upper band chorus.

To investigate in detail the characteristics of the cold plasma density and wave frequency, we plot the dependences of density and wave frequency against the radial distance for the 29 events. As shown in Figure 2.20 (top), the estimated densities at 10-15 R_E were lower (<1.0 cm^{-3}) than that of empirical model [*Carpenter and Anderson*, 1992], and fluctuate widely ranging from 0.20 to 21.7 cm^{-3} in the inner region (4-10 R_E). The estimated density tends to increase as the source region moves toward the Earth although the density distribution has a large variance (correlation coefficient of -0.47.). As shown in Figure 2.20 (bottom), the normalized wave frequencies ranged from 0.22 to 0.65, i.e., covering both lower band chorus and upper band chorus. Compared with the density distributions, the whistler wave frequency increased and eventually corresponded to the upper-band chorus as the source region moves toward the Earth (correlation coefficient of -0.80.). Three green broken lines in Figure 2.20 (bottom) indicate limitation of the detectable frequency range assuming dipole magnetic field, when we consider the upper limit of ESA energy range (12 keV) in cold plasma density of 0.10, 5.0, and 20 cm^{-3}, respectively.

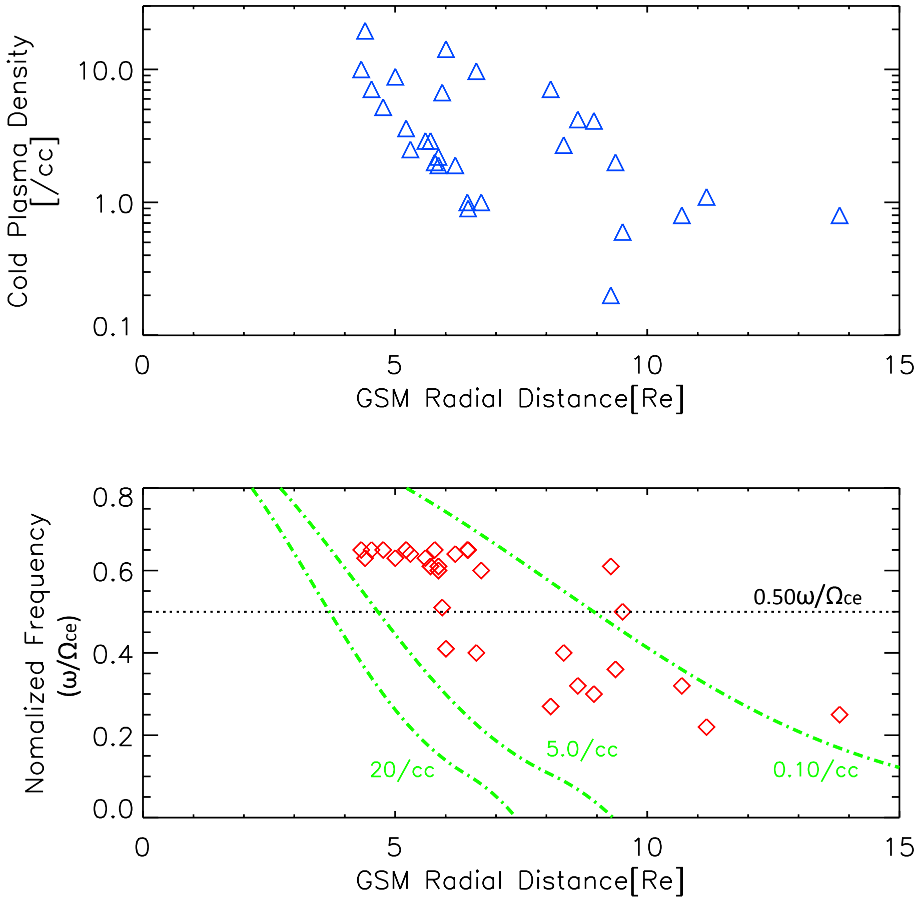

Figure 2.20: (top) Cold plasma density and (bottom) initial frequency of whistler mode chorus wave dependence on radial distance of 29 auroral events. Vertical lines represent range 0.1-25 cm^{-3} in logarithmic scale and normalized wave frequencies ω/Ω_{ce} at 0.10-0.80. Three green broken lines in bottom panel indicate limitation of the detectable frequency range assuming dipole magnetic field and correspond to upper limit of ESA energy range (12 keV) in cold plasma density of 0.10, 5.0 and 20 cm^{-3}, respectively.

2.3.2 Generation mechanism

TOF-A

Since the TOF-A analysis is based on the assumption that electrons with all energies start to precipitate simultaneously from the same point, the generation mechanism should satisfy this assumption about the pitch angle modulation as well as distributions of estimated source region. One possible generation mechanism is a quasi periodic oscillation of the field-aligned electric field in the modulation regions near the Earth [*Sato et al.*, 2002, 2004]. They explained the anti-correlated modulation of electron and proton flux observed by FAST based on this model. However, downward ions were detected in only a few cases by Reimei/ISA, when PAs were observed with Reimei/MAC in our study. Moreover, the on and off phases were not clearly seen in the downward ions. Therefore the characteristics of the PA may be different between our study and *Sato et al.* [2002, 2004]. The PA discussed by *Sato et al.* [2002, 2004] appeared with east-west-aligned multi-band shapes, and FAST electrons data showed not only high-energy precipitations (>5 keV) associated with PAs but also an inverted-V structure (<1 keV). Since inverted-V structure overlapped with non-accelerated precipitation related to PA these is rarely seen in the Reimei observations, it seems that a number of PAs measured by Reimei did not result from the quasi periodic modulation of parallel electric field. According to the fact discussed above, we suggest that the interaction processes assumed in the TOF-A model were not a dominant mechanism for generation of PAs measured by Reimei.

TOF-B

In contrast, the TOF-B analysis, which assumed that whistler mode waves cause the precipitation of electrons during their course of propagation along a field line, revealed that the sources were distributed from the equator to the off-equator. Statistical results from the in situ satellite observations demonstrated that whistler mode waves with large amplitudes are enhanced in the equatorial region of the inner magnetosphere to the extent of ±(10-15)° [*Meredith et al.*, 2003; *Li et al.*, 2009b] (See Figure 2.21 and Figure 2.22). Moreover, the whistler mode chorus waves are typically generated outside the plasmapause [*Meredith et al.*, 2001; *Miyoshi et al.*, 2003]. Our estimated properties of whistler mode waves based on the TOF-B model are consistent well with the characteristics of whistler mode chorus waves from the in situ observations, which suggests that the PA events observed by Reimei can be explained by the TOF-B model. We assumed that chorus was propagated along a magnetic field line in this study. However, ray tracing studies have shown that chorus propagates from the equator with a wave normal angle and its ray path crosses the field line [*Chum et al.*, 2007; *Bortnik et al.*, 2007, 2008]. In order to take into account the effects of both oblique wave normal angles and rays crossing a range of L shells, the time of flight analysis combined with ray-tracing analysis is important to improve the estimations of the source locations and wave frequencies, and this would be a subject in the future study.

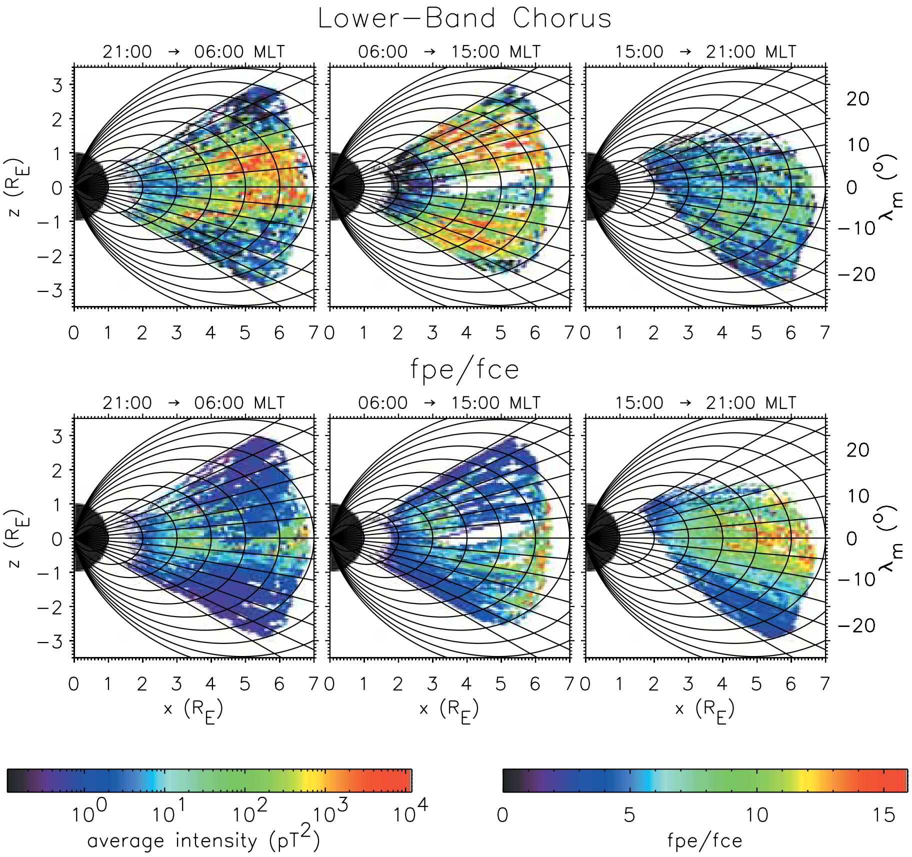

Figure 2.21: The ratio ω_{pe}/ω_{ce} (lower panels) and the lower-band chorus magnetic field intensities (upper panels) for three different local time sectors during active conditions as a function of x and z [*Meredith et al.*, 2003]

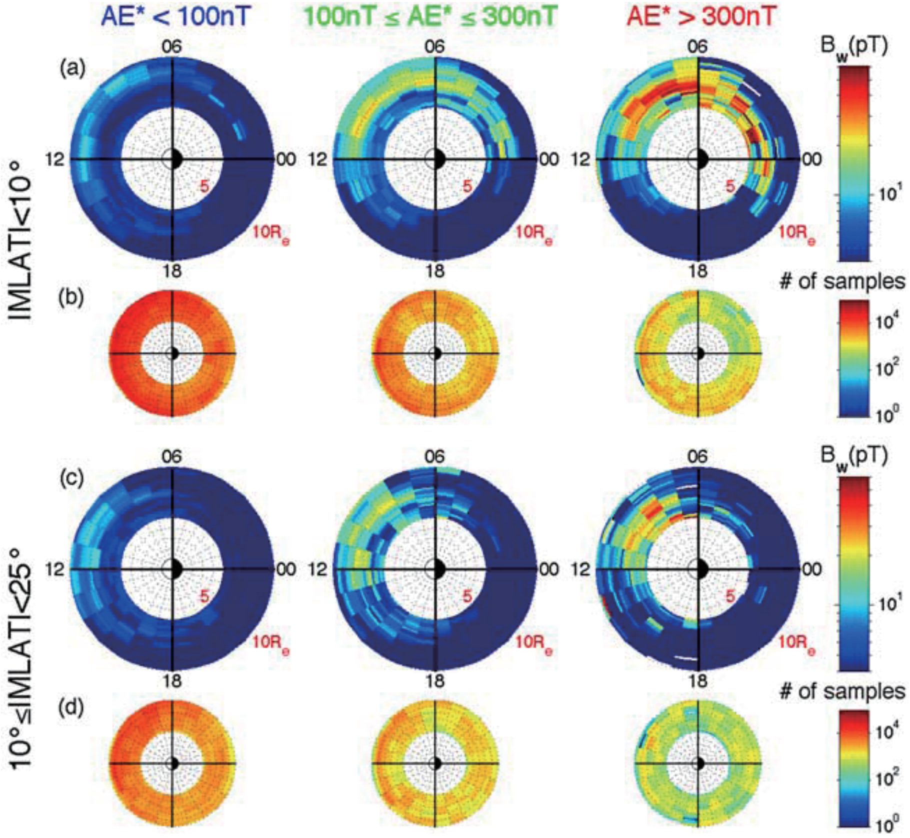

Figure 2.22: Global distribution of chorus observed at the L-shells between 5 and 10 categorized by different AE^* in the (a and b) near equatorial ($|\text{MLAT}| < 10°$) and (c and d) mid-latitude regions ($10°$ $|\text{MLAT}| < 25°$). The larger plots (a and c) show RMS chorus wave amplitudes (pT) and the smaller plots (b and d) indicate the number of samples in each bin. [*Li et al.*, 2009]

2.3.3 Radial and MLT dependence

In this study the cold plasma density ranged from 0.20 to 21.7 cm^{-3} and this agreed with the results from empirical models except for the case in which it reached 21.7 cm^{-3}. Using magnetically conjugate measurements at geosynchronous orbit, *Nemzek et al.* [1995] estimated the upper limits for low-energy plasma density when PAs were observed with a ground-based all-sky video camera to be 1-2 cm^{-3}. Since 12 (41%) of the total events in this study showed the cold plasma density of less than 2.0 cm^{-3}, our results were roughly consistent with those obtained by *Nemzek et al.* [1995]. In the other cases, the PAs possibly occurred in relatively larger density regions. Moreover, the estimated density tended to increase as the source region moved toward the Earth although the density fluctuation is large. Both cold and hot plasma density are important factors in the growth, propagation, and periodicity of whistler mode waves [*Demekhov and Trakhtengerts*, 1994; *Trakhtengerts*, 1999], suggesting that the periodicity of a PA could depend on cold plasma densities in the source regions.

The frequencies of whistler mode waves at the magnetic equator normalized by Ω_{ce} ranged from 0.22 to 0.65, corresponding to the frequency range of lower-band chorus and upper-band chorus. The frequencies increased and eventually reached to the upper-band chorus range as the estimated source region moved to the Earth. As indicated by the Cluster and THEMIS observations, while the lower-band chorus is distributed in a broader L shell (up to $L \approx 8$), the upper-band chorus is observed closer to the plasmapause [*Santolik et al.*, 2005b; *Li et al.*, 2009a]. The upper-band chorus plays an important role in precipitating plasma sheet electrons, especially those with energies up to a few keV [*Ni* *et al.*, 2008]. This suggests that not only the lower-band chorus but also the upper-band chorus contributes to generate the electron precipitation associated with PA, especially near the plasmapause ($L \approx 5$). Since the resonance energy increases as the source region moves closer to the Earth, we discuss the upper and lower limit of the frequency coverage of the TOF-B analysis, which are determined by the energy range of the ESA instrument. We estimated the detectable frequency range assuming a dipole magnetic field as plotted in Figure 2.20 (bottom). The three green broken lines indicate the frequencies corresponding to the upper limit of the ESA energy range (12 keV) at cold plasma densities of 0.10, 5.0, and 20.0 cm^{-3}. The result for the case of 20 cm^{-3} suggests that the lower band chorus ($\omega/\Omega_{ce} > 0.30$) can resonate with electrons of 12 keV under the condition of 20.0 cm^{-3} in the vicinity of the Earth (< 5 R_E). In other words, under the high thermal plasma density condition, energy-time dispersions (< 12 keV) can be generated by the interaction with the lower-band chorus in the region close to the Earth. However, comparing the accuracy of fitting results, theoretical dispersions with upper band chorus can reproduce the observed energy-time dispersions better than those with lower-band chorus. If upper-band chorus waves are responsible for the electron precipitation (< 12 keV), lower band chorus waves are expected to simultaneously cause precipitations in a few tens of keV or over in lower L shell regions ($L <$ 4-5). Reimei cannot measure them due to the energy range of ESA, and it is difficult to conclude exclusively whichever chorus waves actually contributed to the precipitation in the energy range from a few keV to ten keV associated with PA. It is interesting to apply the TOF-B model to observations of precipitating electrons in the energy range up to a few tens keV with high temporal resolution, in order to distinguish the roles of lower and upper band chorus waves on the generation process of the PA, particularly in the region closer to the Earth. As discussed in the present study, since the kinetic energy of the precipitating electrons associated with PAs is directly related to the characteristics of waves in resonance, we can investigate the ambient plasma environment and resonance conditions in the modulation region based on the results of the TOF-B analysis. These results also imply that the generation mechanism of PAs strongly depend on radial distance and MLT of modulation regions, which may have an affect on basic property of PAs such as repetition period and morphology. These subjects are beyond this study and should be investigated in the future.

2.4 Brief summary

Applying the two TOF analysis models to the 29 events data from simultaneous image-particle observations by Reimei in the northern hemisphere, we investigated the generation mechanism for PAs and identified the source region of the electrons. The main results of this study are as follows:

1. The source regions obtained from the TOF-A model were distributed almost continuously from magnetic latitude -20 to 50°, and this is similar to the results in previous studies. On the other hand, the source regions obtained from the TOF-B model that takes into account the interaction electron and whistler mode wave ranged from the magnetic equator to low-latitudinal region in the opposite hemisphere (∼ -11°).

2. The source regions obtained from the TOF-B analysis generally corresponded to the regions in which whistler mode chorus waves are frequently observed in the previous studies, suggesting that the precipitation of electrons by propagating whistler mode waves is a plausible mechanism for the production of PAs.

3. All PA events measured by Reimei occurred outside the plasmapause and the source regions move closer to the Earth with the shrinking of the plasmapause during geomagnetically disturbance periods.

4. The cold plasma densities at the magnetic equator estimated from the TOF-B analysis were mostly consistent with the results of empirical models and ranged from 0.20 to 21.7 cm^{-3}, indicating that the density tends to increase with large fluctuations as the source region moves closer to the Earth.

5. The estimated frequencies (normalized by Ω_{ce}) of whistler mode waves from the TOF-B analysis ranged from 0.22 to 0.65, which corresponded to the lower-band and upper-band chorus. The frequencies became higher when the modulation regions are closer to the Earth, reaching to the upper-band chorus range. These results suggest that different chorus wave bands contribute to the PAs, which depends on the radial distance of the modulation region.

Chapter 3

Ground-based observations

We demonstrated that the electron precipitation associated with PAs is composed of fine-scale downward electrons with energy-time dispersions based on the Reimei observations and it is probably generated by the cyclotron resonance with whistler mode chorus element in Chapter 2. Next, we would like to focus on spatial and temporal characteristics of individual pulsating patches in cross-scale that is difficult to distinguish by low-altitude satellites like Reimei. To investigate such characteristics still remain unclear, the ground-based observations at Poker Flat Research Range have been conducted over two years. At first, an outline of the ground-based observation including scientific purposes, an observation site, and instrumentations are described, and analysis methods for revealing spatio-temporal properties of PAs are explained. Detailed case studies and statistical results for cross-scale property are shown and, finally these results are discussed in the context of generation mechanisms.

3.1 Observations

3.1.1 Scientific purposes

A number of ground-based observations for aurora phenomena have been carried out with a variety of instruments for a variety of purposes. However, imaging observations with narrow FOV and an Electron Multiplying CCD (EMCCD) recently revealed auroral fine-scale structures, in particular for Alfvenic aurora at auroral breakup [e.g., *Semeter et al.*, 2008]. On the other hand, continuous ground-based observation optimized to property of PAs in meso-small scale (smaller than 100 km) has been rarely carried out because it is difficult to measure the small-scale structures (10-30 km) and rapid variations (faster than 1 second) of PAs using conventional ground-based instruments. So, we developed a wide field monochromatic camera with an EMCCD and conducted continuous ground-based observations in winter seasons of 2010-11 and 2011-12 for the specific purposes as follows:

- Rapid variations of PAs corresponding to quasi-3Hz modulations of precipitating electron flux, and spatial distributions of the intensity variations,

- Fine-scale structures of PAs and its relationship to the whole patchy structure in meso-scale,

- Auroral dynamics inside individual pulsating patches such as streaming and fast auroral waves,

- Temporal evolution of PAs during a period of few hours, and the relation with the magnetospheric condition in global scale.

The wide field camera optimized to spatial and temporal scales of PAs with EMCCD and high speed imaging technique was mainly used in this study to achieve these scientific goals. The instrumentation of thecamera and other instruments is described in 3.1.3 in more detail.

3.1.2 Poker Flat Research Range

Poker Flat Research Range (PFRR) is located in the suburbs of Fairbanks and at magnetic latitude (MLAT) of 66.77° (L-value 6.42) where the aurora oval usually exists. PFRR is an integrated observation site that has vast grounds and a variety of instruments including a rocket launcher and an incoherent scattering radar (PFISR). Science Operation Center (SOC) is one of buildings on the top of the hill with the altitude of about one hundred meter in PFRR, and it is main observatory for installation and operation of optical instruments. Ground-based observations for radio and plasma wave in the range of ELF, VLF, and MF are also conducted around SOC, in addition to optical observations.Our instruments were installed in the East Dome of SOC. We stayed at Fairbanks for 1-2 weeks at the beginning of our observations each year, and we did operation and monitoring of our instruments via Internet after leaving the site.

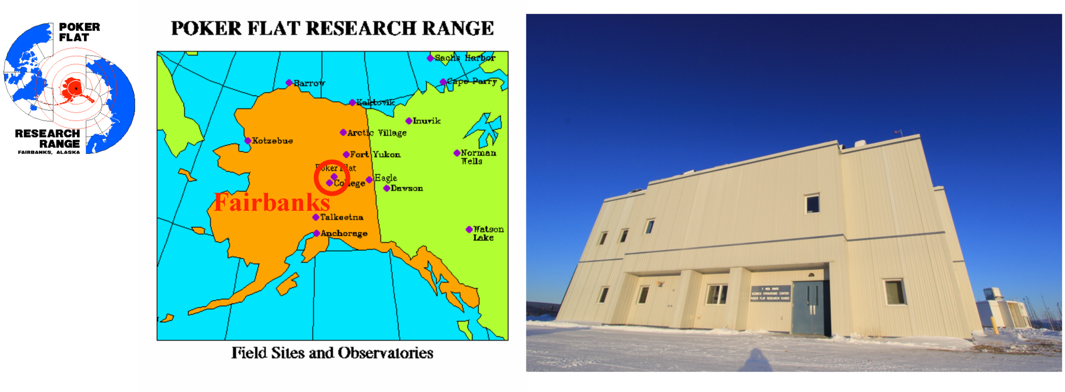

Figure 3.1: (Left) Logo of Poker Flat Research Range and a map shows the location of Fairbanks. Poker Flat Research Range is located in the suburbs of Fairbanks. (Right) The picture of Science Operation Center that has several optical domes, an optical calibration room and a workshop.

3.1.3 Instruments

Three kinds of optical instruments were installed at the East dome of SOC: the wide filed EMCCD camera, an all-sky video camera and narrow filed photometer. We can simultaneously compare auroral phenomena in global scale and auroral signatures in meso-small scale (See the datail in Figure 3.2 and its caption). Rapid variations of PA intensity as reported in *Samara and Michell* [2010] can also be detected by the wide field EMCCD camera (described the detail later). Specification of main instruments are shown in Table 3.1. It is noted that some settings of the instruments were slightly changed between 2010-11 and 2011-12 season. Furthermore, several instruments were additionally used to operate the instruments and record the data: a workstation and a laptop for operations of these instruments, a precise clock using GPS, signal generator for an external pulse triggering operation sequences of the EMCCD camera, and data storages ($\sim$ 8 TB) for recording a huge amount of image data. Additionally, we have been measuring continuously H and D components of magnetic field variations in the frequency range of ELF using two searchcoils since December 2009 [*Yaegashi et al.*, 2011], and the range was expanded to VLF range of 500 Hz since November 2010. Since 500 Hz corresponded to about 0.1 times a cyclotron frequency of electrons at the equator connected to PFRR by the field line, we can expect to use these data to monitor activities of both whistler mode waves and ELF waves.

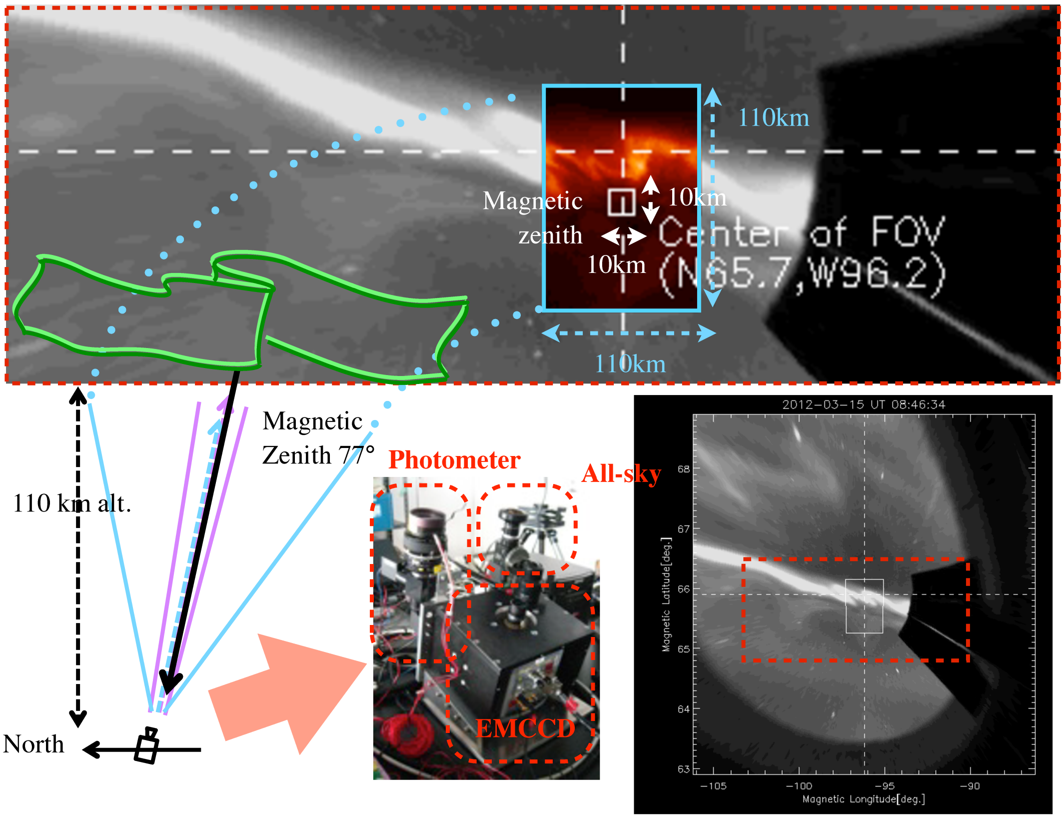

Figure 3.2: An image taken by the EMCCD camera is superimposed on an all-sky image in the geomagnetic coordinates. Schematic illustration for FOV of the EMCCD camera and the photometer, and light blue and white squares represent FOV of them at the altitude of 110 km. We also show the picture of three optical instruments and the all-sky image mapped onto the geomagnetic coordinates. It is noted that this configuration is based on the observation in 2011-2012 season.

Table 3.1: Specifications for instruments used in our ground-based observations

November 2010 - March 2011				
	Sampling	FOV	Target	Pointing
EMCCD camera	100 Hz	49 × 49°	mainly N_2 1st Positive	Zenith
Video camera	1/10 Hz	all-sky	panchromatic	Zenith
Photometer	1 kHz	0.22 × 0.22°	N_2 1st Positive	Magnetic zenith
November 2011 - April 2012				
	Sampling	FOV	Target	Pointing
EMCCD camera	100 Hz	49 × 49°	mainly N_2 1st Positive	Magnetic zenith
Video camera	1/6 Hz	all-sky	panchromatic	Zenith
Photometer	10 Hz	5.7 × 5.7°	N_2 1st Positive & O 844.6 nm	Magnetic zenith

Wide field EMCCD camera

We developed the high-speed and sensitive camera with wide FOV using an EMCCD camera (Andor iXon^{EM} DU-897E-CS0-#BV, Figure 3.3). Since an EMCCD enables charge to be multiplied on each pixel of detector before readout, it can relatively reduce readout noise. Consequently it is possible to gain a signal-to-noise ratio even if the sensor is driven with fast readout (typically less than 1 second). The detector is a 512 × 512 back-illuminated type of frame transfer CCD with 16 × 16 μm in size. The quantum efficiency (QE) of this CCD as a function of wavelengths in the range of 200-1100 nm is shown in Figure 3.4. This EMCCD also has a electrical cooling system, and the CCD is nomally cooled at -80°C during observation.

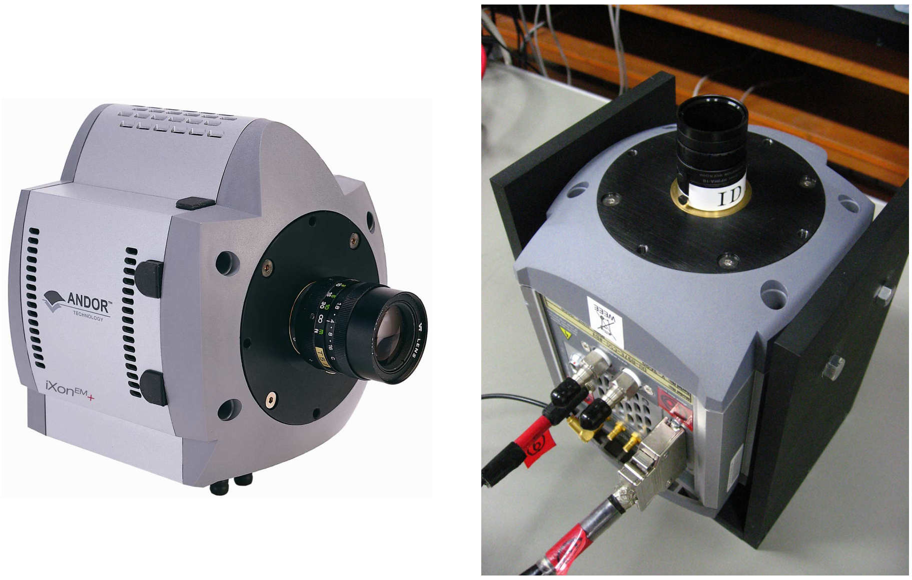

Figure 3.3: (Left) An image of an EMCCD camera and (Right) a picture of our EMCCD camera composed of an EMCCD, a wide FOV objective lens and a sharp cut filter.

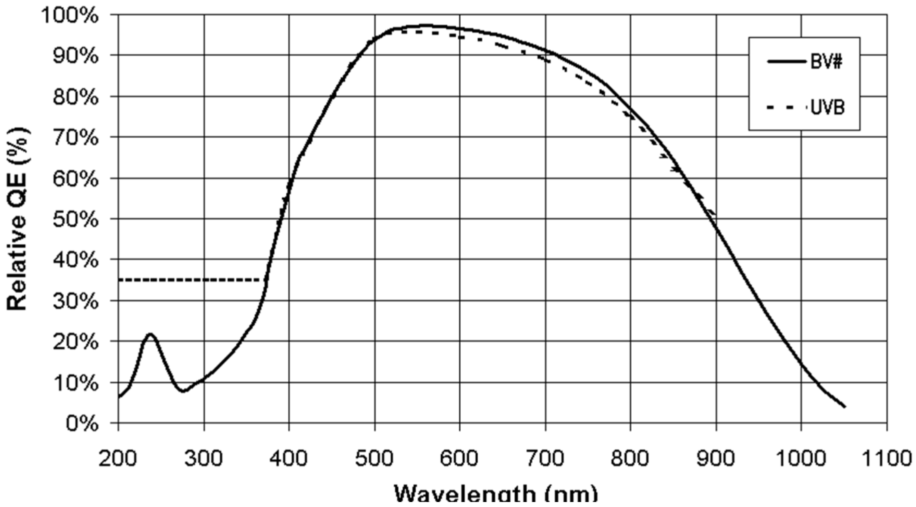

Figure 3.4: Quantum Efficiency of the CCD sensor as a function of wavelengths in the range of 200-1100 nm. A black solid line shows relative QE of CCD used in this study.

The optical parts that constitute our EMCCD camera are only two: an objective lens and a sharp cut filter. A fast and wide FOV lens with a F-number of 1.4 (f=8mm) was used for measuring weak emissions of PAs (∼ a few kRs) and its temporal variations. The FOV is 49 × 49°, which is determined by the focal length of the objective lens and the CCD size. This FOV is selected to be preferable to measure typical pulsating patches at the auroral altitudes of 110 km, we can investigate spatio-temporal properties of individual pulsating patches in detail. As mentioned in 3.1.1, one of our scientific purposes is to detect the rapid variations of PAs in a few-Hz or higher-frequency range, and therefore, the measurements of auroral emissions at permitted lines was strongly required. We adopted a sharp cut filter that is a kind of low-pass filter, and it has a transparency the light in the wavelengths range from ~ 650.0 nm to near infrared. Figure 3.5 shows the transmittance curve as a function of wavelengths. Taking into account the QE characteristics of the CCD shown in Figure 3.4, we can measure mainly prompt auroral emissions of the N_2 1st positive band with combining EMCCD and this filter. This filter has an advantage that the transmittance characteristics do not so much depend on incident light angles, and therefore we can simplify the optical system without a collimator, even for our wide FOV camera. Since the filter does not exclude any emissions in the wavelengths longer than ~ 670.0 nm, airglow emissions such as OH Minel band, could lead to contaminate the data. However, such contamination can be negligible because the auroral intensity integrated over N_2 1st positive band is much greater than the airglow emissions in the most cases. We show spectra obtained from a ground-based observation of type-B aurora, enhanced red aurora at the altitude of 80-150 km, using a CCD television spectrograph in Figure 3.6 as an example of spectrum for N_2 1st positive band [*Hallinan et al.*, 1998]. Figure 3.6 demonstrates that N_2 1st positive band can be considered as dominant auroral emissions in the wavelengths range from 600.0 to 900.0 nm.

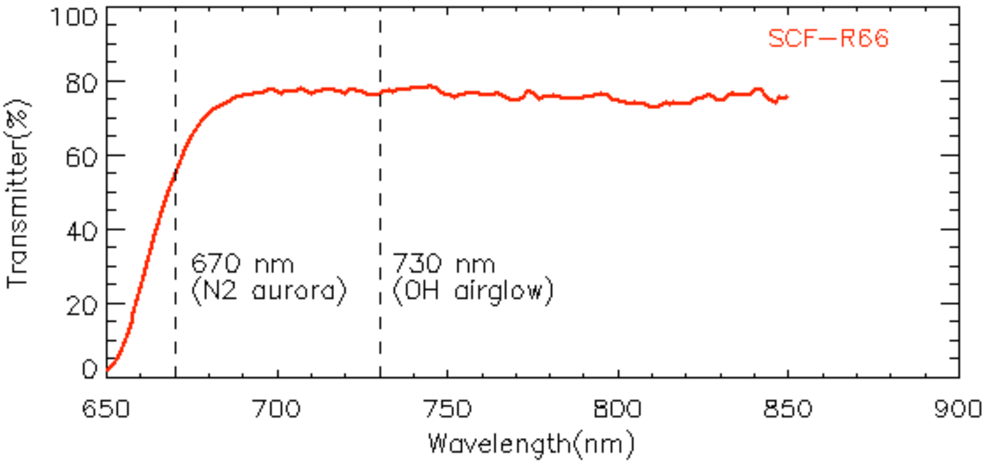

Figure 3.5: Relative transmittance of the sharp cut filter used in this study. The transmittance of this filter reaches 50% at 670.0 nm, and get close to almost constant (≈ 80%) at wavelengths longer than 700.0 nm

An actual observation mode of EMCCD camera was determined based on the balance between performance of the EMCCD and the workstation. One cycle with a duration of 600 seconds consists of a set of total image exposure and data record was programed, and it was repeated during observations. On each cycle, the EMCCD camera took images with 100 Hz sampling and the data was transferred to the memory of workstation for the first 582 seconds. Then totally 58200 images (100 frame/s × 582 s) were recorded in the storage as one FITS file[1]. After an interval of 18 seconds including the time for recording the FITS data, the EMCCD camera restarted the measurements triggered by a pulse from the signal generator synchronized with GPS clock. The detailed setting parameters of EMCCD camera is shown in Table 3.2. The number of binned pixels was determined to be 8 × 8 in order to achieve high sampling rate of 100 Hz, and consequently spatial resolution of EMCCD camera was 1.6 or 1.7 km.

---

[1] A digital file format for scientific image data commonly used in astronomy as Flexible Image Transport System. (http://fits.gsfc.nasa.gov/)

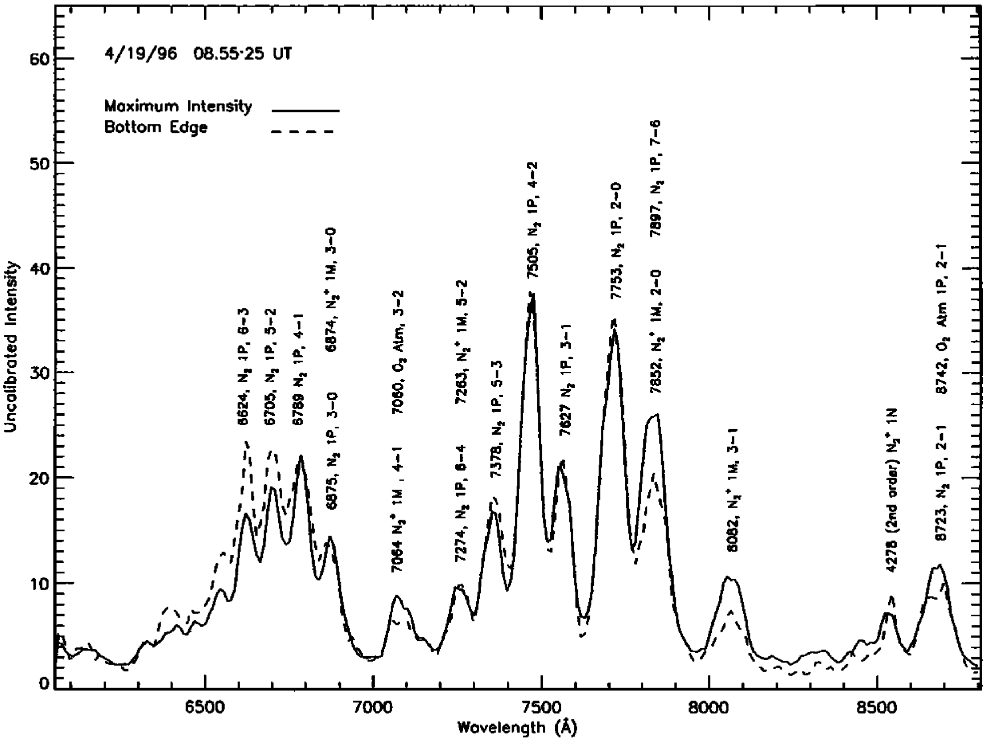

Figure 3.6: Spectra at the altitude of peak emission and along the bottom edge of an extremely bright rayed arc (0.5-second integration time). The intensities have been scaled to match at 7500 Å. The spectra have not been corrected for the spectral response of the detector. A black solid line is the uncalibrated intensity at the altitude of maximum intensity, and a broken line is that at the altitude of the bottom edge of observed type-B aurora [*Hallinan et al.*, 1998].

Table 3.2: The detailed settings of EMCCD camera during observations

EMCCD camera	
	Nov. 2010 - Mar. 2011 / Nov. 2011 - Apr. 2012
Dynamic range	0-16,000 counts
Pre-amplifier gain	5.2
EM gain	20-100 / 100
Readout rate	10 MHz at 14-bit
Vertical pixel shift speed	0.3 μs
Binning	8 × 8 pixels
Exposure	0.00984 s
Sampling rate	100 Hz
FOV	49 × 49°, (100 × 100 km / 110 × 110 km)
Spatial resolution	1.6 km / 1.7 km
Pointing	Zenith / Magnetic zenith
Target	mainly N_2 1st Positive band (> 660.0 nm)

Photometer

The photometer used in this study has been modified between 2010-11 and 2011-12 season, according to a change in specific purposes for measurements. In the 2010-11 observations the photometer was used to find temporal variations of PA in the high frequency range up to 1 kHz. On the other hand, in the 2011-12 observations we carried out the simultaneous measurement of auroral emissions in two wavelengths, N_2 1st positive band (650.0-700.0 nm) and O 844.6 nm, using two photometers. In this section, specifications for the photometer in the 2011-12 season are described.

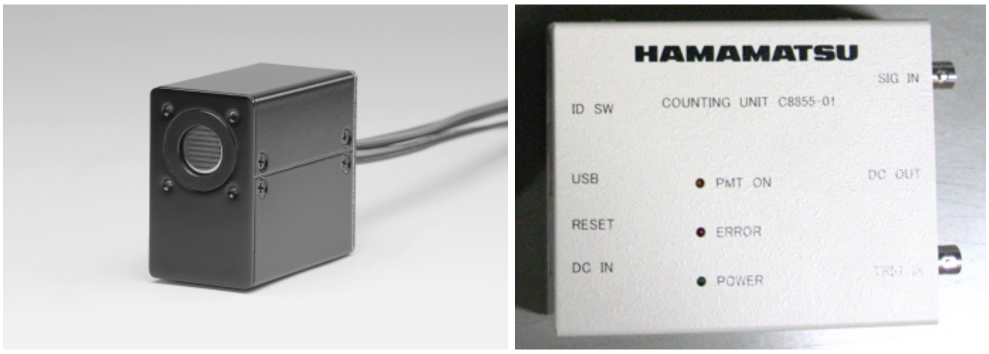

Figure 3.7: (Left) A photon counting head device consisting of a metal package photomultiplier tube and (Right) a counting unit with a USB interface

Figure 3.7 shows the two main electronic devices used in our photometer: A photon counting head device (Hamamatsu H10682-01) and a counting unit (Hamamatsu C8855-01). This counting head device, H10682-01, consists of a metal package photomultiplier tube and has a high speed photon counting circuit and a high-voltage power supply circuit. The high voltage supply for photomultiplier tube and the discrimination level are preset to optimum values, allowing photon counting measurement by just connecting a +5 V supply. A multialkali photocathode used in the counting head has high-sensitivity for the range between 230 nm (UV) to 870 nm (near IR), and the effective area is 8 mm in diameter. The C8855-01 is a counting unit with a USB interface and can be used as a photon counter when combined with a photon counting head. The counter has two counter circuits (double counter method) that allow to count input signals with no dead time. Combining these two devices, we conducted measurements for auroral intensity variations with the photon counting method.

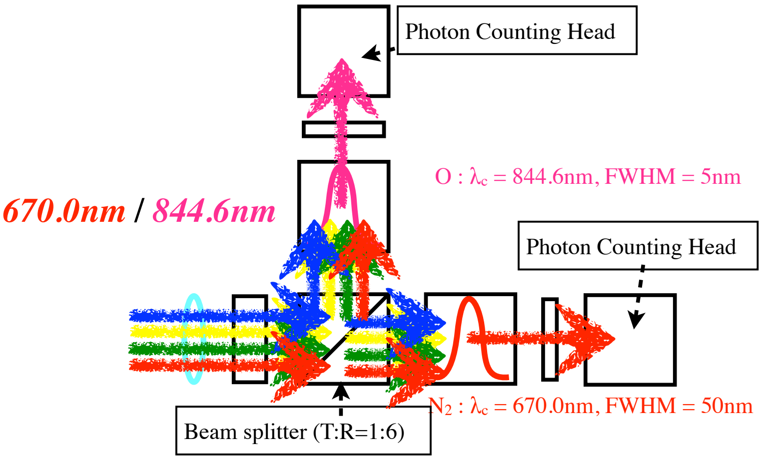

Figure 3.8: Schematic illustration indicates the optics constitute the photometer used in the 2011-12 season. It can measure auroral intensity variations simultaneously in two wavelengths of N_2 1st Positive band and O 844.6 nm emissions.

Table 3.3: Specifications for the optical devices of the photometer used in the 2011-12 season

Lens	
F-number	1.2
Focal length	50 mm
Beam splitter	
Transmittance @ 670.0 nm	0.13
Reflection @ 844.6 nm	0.77
Filters	
Center wavelength	Band width / Transmittance
670.0 nm	50 nm / 0.79
844.6 nm	5.0 nm / 0.55

We designed the photometer used in the 2011-12 season to measure two auroral intensities simultaneously with two channels corresponding to the wavelengths of N_2 1st positive band (Ch1) and O 844.6 nm emission (Ch2). Figure 3.8 is a schematic illustration showing a concept of two channel counting heads, and Table 3.3 shows the detailed specifications of the two channel photometer. Incident light through the objective lens was separated into transmitted (13% of incident light) and reflected (77% of incident light) light by the beam splitter [1]. Two separated lights go through the filters, respectively (See Figure 3.9), and they were finally focused on the photo counting heads. We show Spectra for auroral emissions in the wavelengths range from 4500 Å to 9500 Å taken along a filed line by a ground-based imaging spectrometer. A dashed and solid curve indicate spectra for a arc generated soft electron precipitation and hard electron precipitation, respectively, in Figure 3.10 [*Swenson et al.*, 1998]. Shaded regions by red and pink show the wavelength ranges of the filter, and auroral emissions of N_2 1st positive band (7-4, 6-3, 5-2, 4-1, and 3-0) and O 844.6 nm are seen in these wavelength ranges. It is noted that the enhancement of O 844.6 nm emission occurred at soft electron precipitation, which means this emission is strongly related to electron precipitation with relatively low energy. In order to evaluate the performance of the photometer, we carried out a calibration experiment for the sensitivity of two channels using an integration sphere system installed at National Institute of Polar Research. The result of the calibration is shown in Figure 3.11. Figure 3.11 shows sensitivity variations as a function of inputted luminosity. Note that the sensitivity is normalized with incident luminosity and exposure time. We can see flat characteristics of the sensitivity for inputted luminosity. It demonstrates that the sensitivity of the two channels can hold their linearity for a wide luminosity ranges from a few hundreds Rayleigh to a few tens of kR. This range is enough to measure the temporal variations of PA intensities.

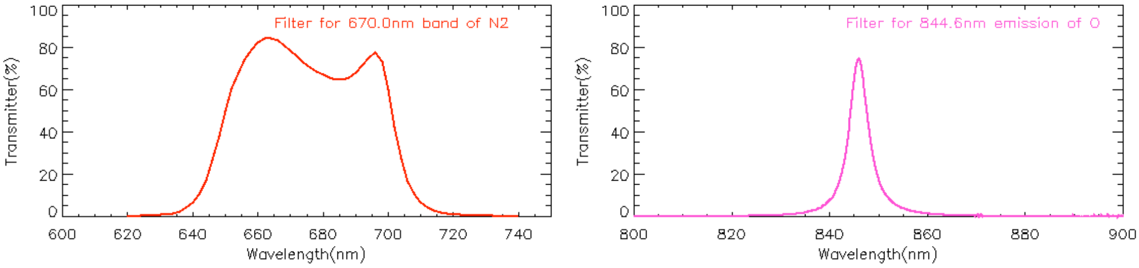

Figure 3.9: Two filter transmittance as a function of wavelenghths for N_2 1st Positive band (Left) and O 844.6 emission (Right)

Figure 3.12 shows pictures of the photometer installed in the east dome of SOC. Since

---

[1] about 10 % of total intensity is lost

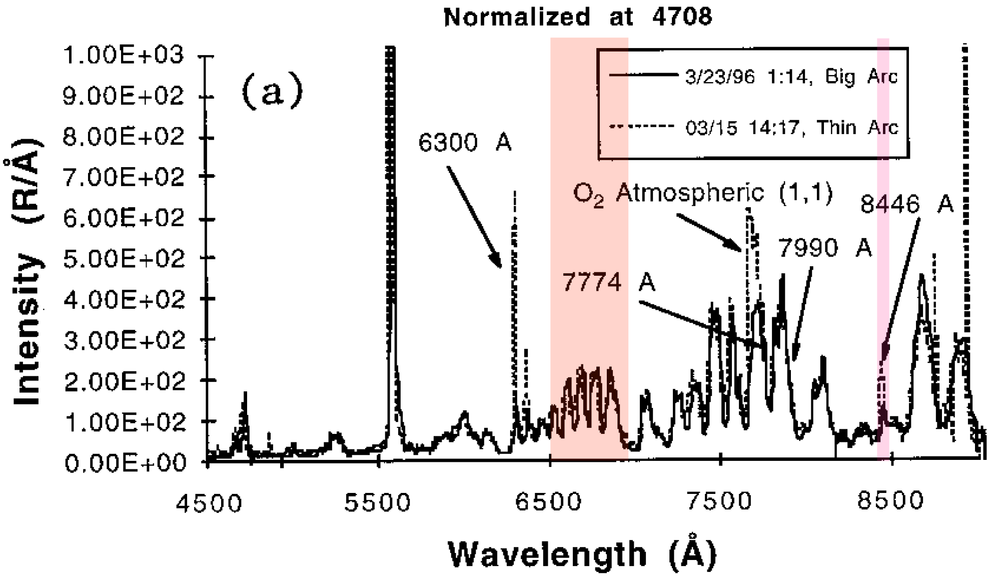

Figure 3.10: Spectra for auroral emissions in the wavelengths range from 4500 Å to 9500 Å taken along a filed line by a ground-based imaging spectrometer. A dashed and solid curve indicate spectra for a arc generated soft electron precipitation and hard electron precipitation, respectively. The two spectra are normalized for energy flux i.e., for the N_2^+ 4708 Å [*Swenson et al.*, 1998].

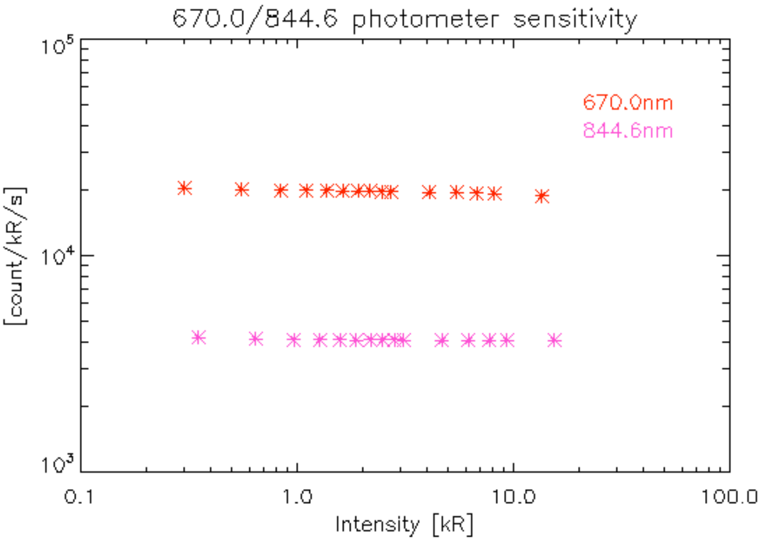

Figure 3.11: Sensitivity variations as a function of incident luminosity on two channels. Red and pink asterisks represent Ch1 (N_2 1st positive band) and Ch2 (O 844.6 nm emission), respectively. Note that the sensitivity for each channel is normalized with incident luminosity and time. Broadly flat characteristics of the sensitivity for the luminosity are seen, which demonstrates that the sensitivity of the two channels can hold their linearity for luminosity ranges a few hundreds Rayleigh to a few tens of kR.

energy flux of precipitating electrons can be estimated from auroral intensities at N_2 1st positive band and O 844.6 nm emission [e.g., *Ono and Morishima*, 1994], we can discuss the relationship between energy flux of precipitating electrons and auroral signatures. The FOV of the photometer is 5.7 × 5.7° corresponding to 10 × 10 km at the altitude of 110 km, and the center of the FOV pointed to the local magnetic zenith as well as the EMCCD camera in the 2011-12 season. It is expected that the sensitivity calibration of the EMCCD camera can be made by using the photometer data. In the 2011-12 season, the continuous operation of photometer started from November 2011 with 10 Hz sampling, and it suddenly stopped simultaneous measurements of two channels in the beginning of February 2012 due to some trouble in connecting between the counting unit of Ch1 and the laptop computer. Therefore, only Ch2 was restarted and operated after the trouble.

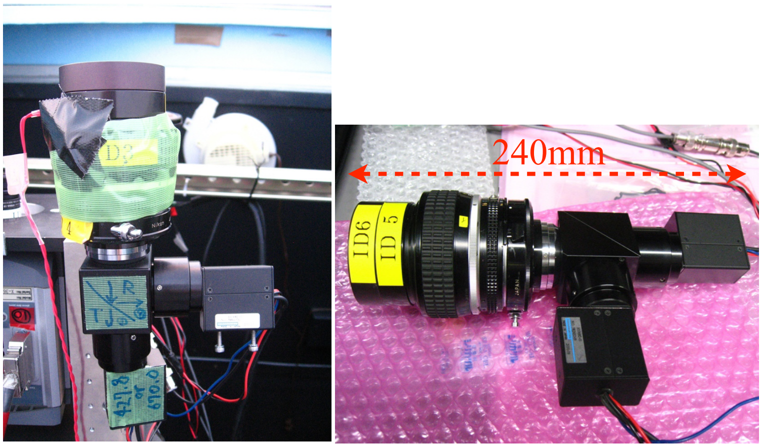

Figure 3.12: Pictures of the photometer installed in the east dome of SOC (Left) and in a laboratory (Right). The photometer is a few tens of centimeters in size.

3.2 Results and discussion

3.2.1 A few-Hz modulations derived from the EMCCD camera

At first we show an typical PA event appeared around 14:55 UT (~ 4 MLT) on March 4th, 2011. Figure 3.13 (a) and (b) show two images obtained from the EMCCD camera at 14:55:03 and 14:55:07 UT. We can see two individual patches next to each other. Auroral intensities on two selected pixels as a function of time from 14:54:30 UT to 14:55:30 UT are shown in Figure 3.13 (c). Light green and blue lines are corresponding to the variations on the two pixels indicated by stars in the same color in the images of Figure 3.13 (a) and (b). Note that light green and blue lines are plotted with 1s-averaged data from raw data obtained from 100 Hz sampling represented by black and red lines. Auroral intensity variations showed rectangular pulse-like temporal variations with repetition periods of 5-10 seconds, and two patches seem to repeat appearing and disappearing independently. Next, rapid variations of the PA in on-phase and the data analysis process for the variations are presented in Figure 3.14. Figure 3.14 (a) is an expanded plot of Figure 3.13 (c), and the period of Figure 3.14 (a) corresponding to that of the period shaded by light red in Figure 3.13 (c). We can identify two kinds of temporal variations: long time scale"on-off" variations and rapid modulations during the on-phase. We can obtain the rapid variations (a light green line in Figure 3.14 (c)) by subtracting long-term variations of 0.5s-

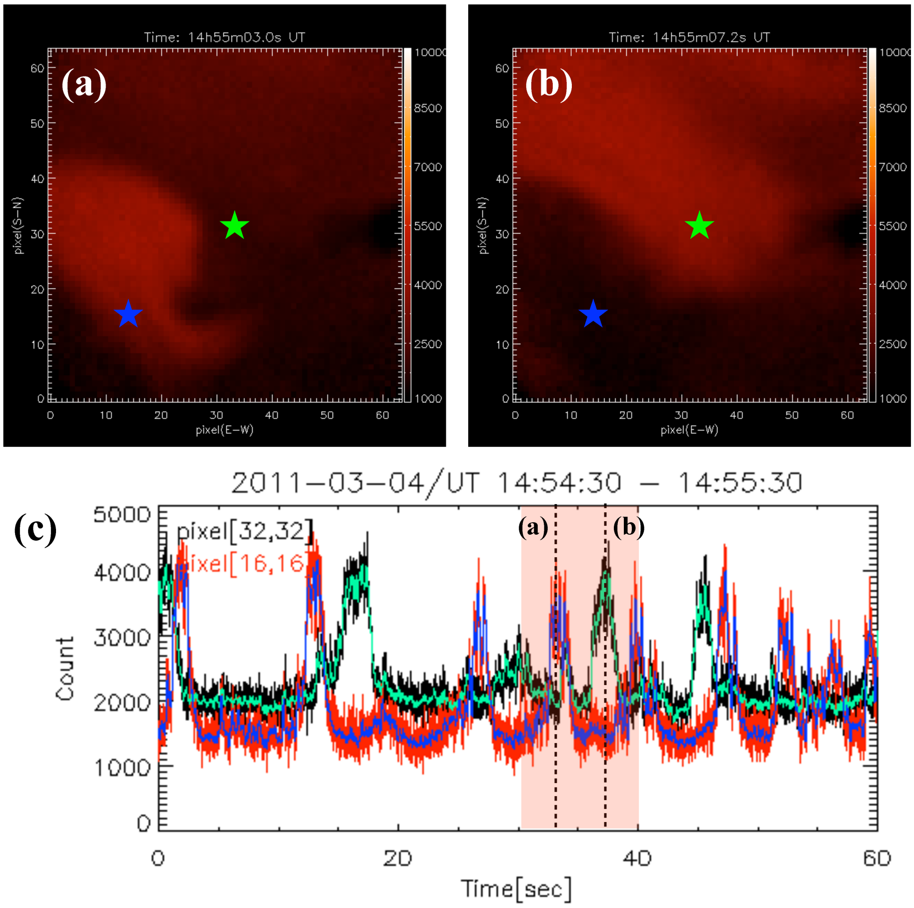

Figure 3.13: (a) and (b) Two images obtained from the EMCCD camera at 14:55:03 UT and 14:55:07 UT in horizontal scale of 100 × 100 km. (c) Auroral intensities on two selected pixels as a function of time from 14:54:30 UT to 14:55:30 UT. Light green and blue lines show the variations on two pixels indicated by two stars in the same color in the images of Figure 3.13 (a) and (b). Note that light green and blue lines are 1s-averaged data and black and red lines are original data obtained from 100 Hz sampling.

averaged data (a blue line in Figure 3.14 (b)) from the original data. After multiplying the component of rapid variations by a function of Hanning window (a red line in Figure 3.14 (c)), the Fast Fourier Transform (FFT) is conducted for the processed data. Figure 3.14 (d) shows the result of FFT analysis exhibits strong peak at 2.8 Hz. This is the one of observational evidences that on-off variations of PAs are composed of more rapid variations in the frequency range of a few Hz. This result is consistent with that in Chapter 2.

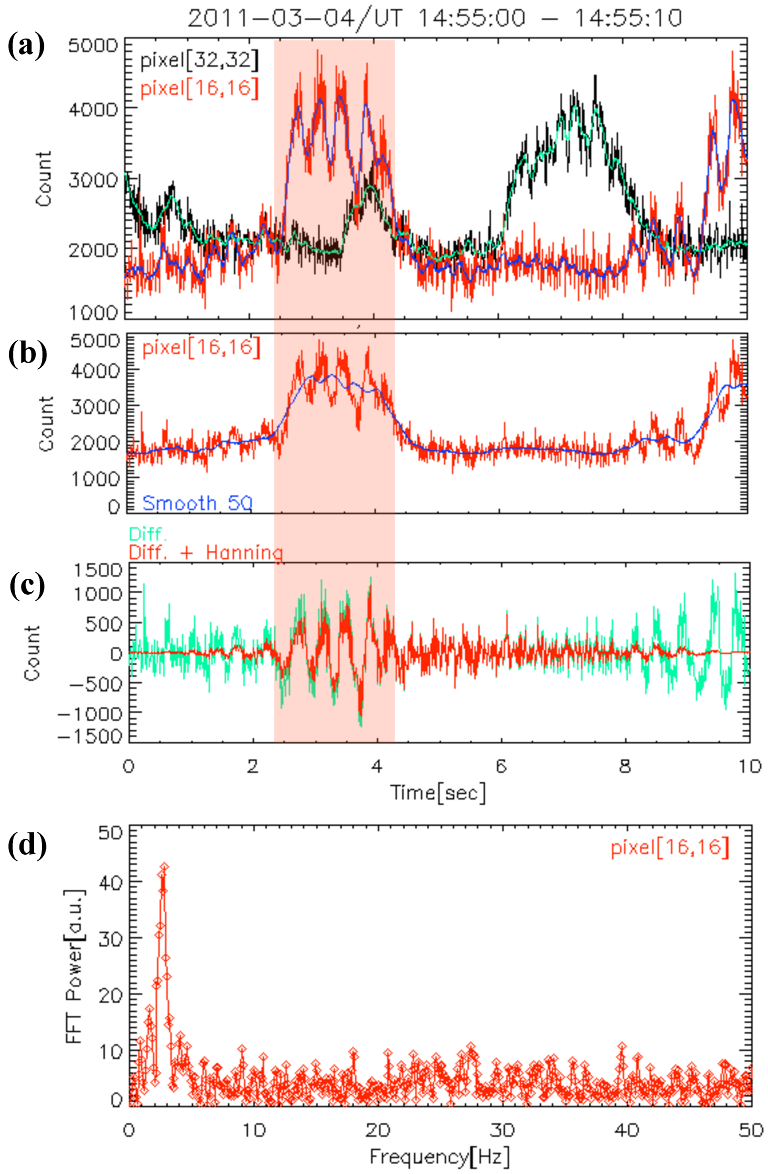

Figure 3.14: (a) Auroral variations as a function of time for the period as shaded by light red in Figure 3.13 (c). (b) A blue line shows slow variations of 0.5s-averaged data. (c) A light green line shows the rapid variations obtained by subtracting long-term variations from original data. A red line indicated the data obtained by multiplying the component of the rapid variations by a function of Hanning window (a red line). (d) The result of FFT analysis is shown.

3.2.2 Event study on March 4th, 2011

We present the further result of an event study on March 4th, 2011. Time-shifted interplanetary conditions to the magnetopause provided by OMNI-2 database and indices of geomagnetic disturbance (*Dst* and *AE*) between 1st and 4th March 2011 are shown in Figure 3.15. IMF Bz component considerably fluctuated between -15 and 15 nT on 1st

March, and a magnetic storm with the minimum *Dst* index of -60 nT was recorded. The storm recovery phase still remained on 4th March. *Dst* index remained at -20 and -10 nT due to the fluctuating IMF Bz. During this period "storm-time" substorms had occurred many times. We focused on the substorm around 11:00 UT with duration of about 2 hours and magnitude of 800 nT in *AE* index. All-sky camera data of THEMIS ground observations indicated that the breakup of this substorm was located in eastern Alaska, surrounded by Gakona, Whitehorse, and Inuvik. The data obtained from THEMIS probe D and E are also available to monitor the magnetosphere in the morning sector. These probes were located at 11 Re near the magnetic equator around 11:00 UT, though about MLT 3-4 h (3-4 h east from the longitude of PFRR). Although they were not conjugate with the FOV of any instruments at PFRR during the period, probe E observed intermittent energy-time dispersion structures of electrons, likely to be associated with injections during the day. Figure 3.16 of (e) and (f) show that a hot electron population between 1 and 10 keV was present at the inner edge of the plasma sheet and the electron density fluctuated irregularly during the substorm around 11:00 UT.

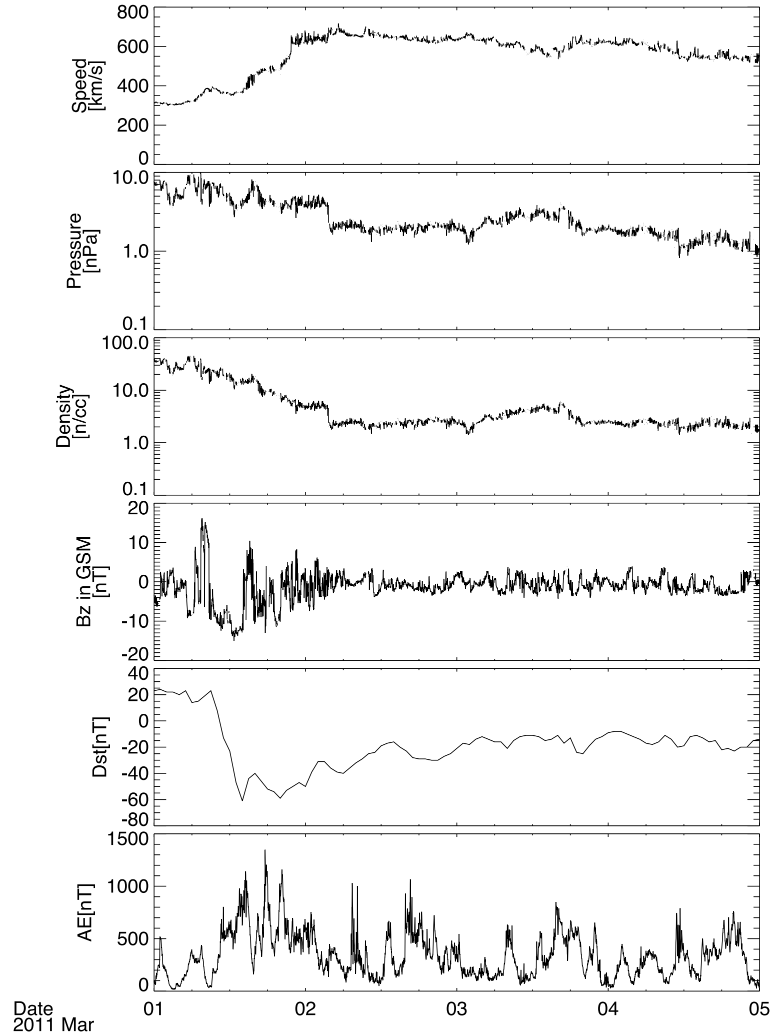

Figure 3.15: Summary plots of time-shifted solar wind and IMF parameters (solar wind speed, pressure, density, and Bz component in GSM), *Dst* and *AE* indices, as a function of time between 1st and 4th March 2011.

Local geomagnetic activities at PFRR remained relatively high during the day. A summary plot of IMF Bz component, *Dst* and *AE* with geomagnetic field variations measured by the magnetometer at PFRR as a function of time on March 4th are shown in Figure 3.17. This figure shows that a sudden decrease of 500 nT in the H-component

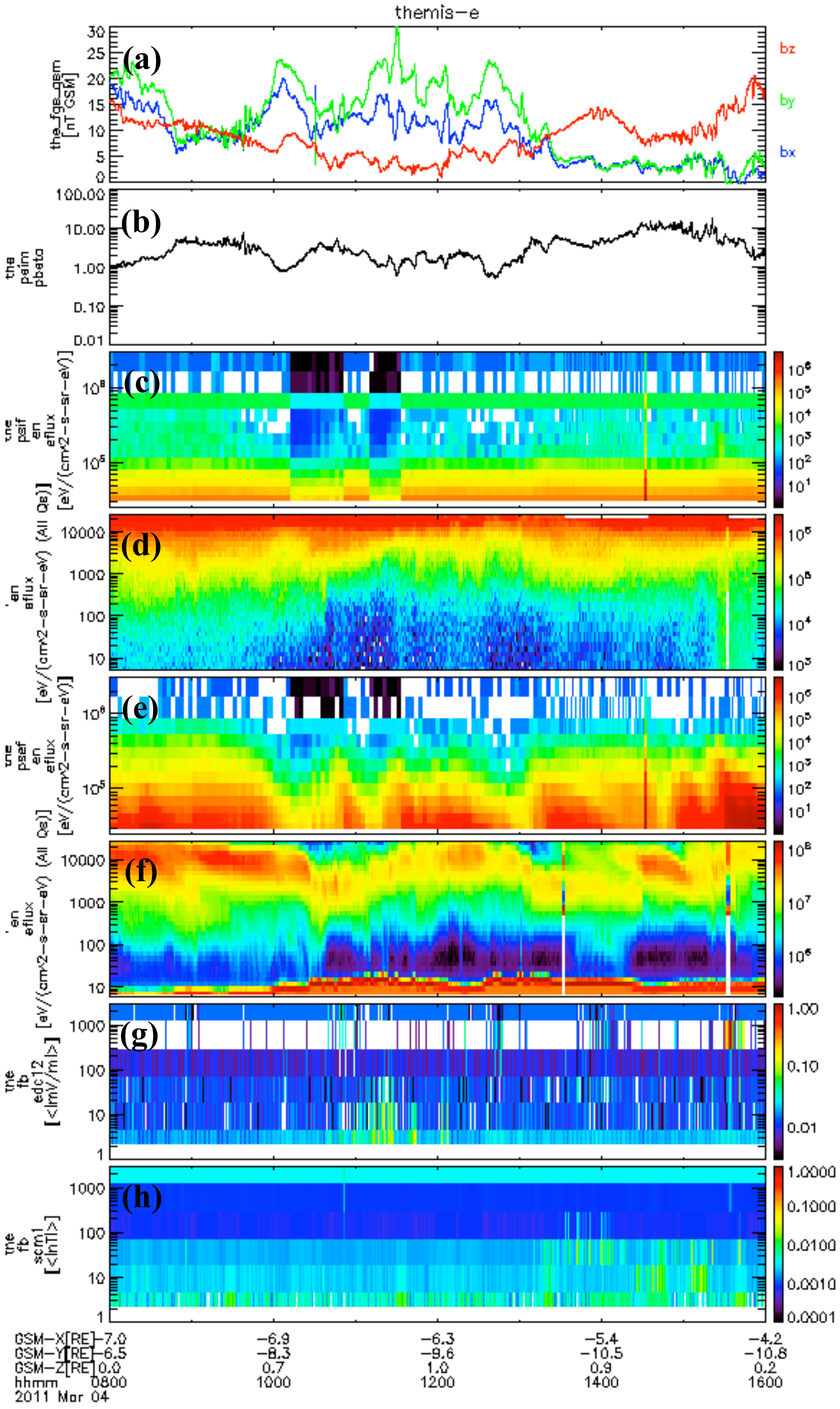

Figure 3.16: A summary plot of in-situ observations by the THEMIS-E probe showing (a) magnetic field variations in GSM coordinate in the range from 0 to 30 nT, (b) plasma-β estimated from the in-situ measurements, (c-d) ion energy flux ranges from 25 keV to 3 MeV measured by Solid State Telescope, and that ranges from 5 eV to 25 keV measured by Electrostatic Analyzer, (e-f) electron energy flux in the same format as (c-d), (g-h) electric and magnetic field variations range from 1 Hz to 3 kHz, respectively.

occurred around 10:40 UT, and simultaneously *AE* index increased up to 800 nT. Here, Figures 3.18(a) and (b) are auroral keograms at four wavelengths obtained from a meridian spectrograph at PFRR from 05:00 to 15:00 UT and from 10:00 to 12:00 UT, respectively. As shown in Figure 3.18(a) relatively dim aurora existed in the north from 05:00 UT. More intensified aurora with its luminosity over 15 kR at 557.7 nm appeared after 10:00 UT, but it did not seem to develop an aurora breakup as seen in Figure 3.18(b). Aurora expansion was clearly seen at 557.7 nm and 427.8 nm starting at 10:40 UT. After the breakup, the next aurora expansion was identified around 11:30 UT. High auroral activities on that day continued until 13:30 UT. Figure 3.19 shows both the temporal thin arc at aurora break up at 10:40 UT and PAs which covered the field of view at PFRR at 11:00 UT. These image data were obtained from the all-sky panchromatic camera and the EMCCD camera. Note that both instruments were pointing to the local zenith and the magnetic zenith ($\approx$ the elevation angle of 77°) existed in the image obtained from the EMCCD camera. Here, PAs began to appear in the south at 10:50 UT, and a variety of PAs continued until sunrise. Around 11:00 UT, in the early recovery phase of the substorm, a group of PAs with north-south extended band structures moved southward and was gradually folded. Spatial and temporal evolution of these PAs is shown in Figure 3.20. Large-scale structures moved southward while being compressed and extended eastward. It is also noted that stable black regions characterized as low auroral intensities laid in the vicinity of these PAs structures. PAs with typical patchy structures started to appear mainly around 11:40 UT, and drifted eastward. The enhancement of ELF waves from 1 to 10 Hz was seen only at the breakup at 10:40 UT. Around 11:00 UT the activity became weak, and there was no clear correspondence between ELF waves and PAs. In addition, no whistler mode wave activity in the frequency range around 500 Hz was seen during this period. However, since several possibilities such as ionization of E and D layers, reflections in the ionosphere, and artificial noise around PFRR will mask the whistler mode waves on the ground, we do not rule out whistler mode waves being related to this PA event.

The results presented here are derived from the analysis of PAs between 11:00 and 11:01 UT. During this period, three different pulsating patches existed in the FOV of the EMCCD camera that we labeled as PA1 with a shape similar to a boomerang, PA2 in southeast, and a relatively small PA3 in northeast. They were clearly separated by boundaries characterized as no auroral emissions. All patches gradually moved south while losing their distinct shapes. In the last part of the period, PA1 did not keep its boomerang-like structure, and it was composed of a cluster of patchy structures after 11:00:40. PA2 and PA3 sometimes merged with each other, and the boundary was not as discrete as that between PA1 and other patches. The most part of PA2 moved outside of the FOV and the southern part of PA3 was completely merged with PA2 in the last 30 seconds of this period. We conducted the FFT analysis for 2-D image data as a function of time. The number of pixels is 64 × 64, and pixel [0, 0] corresponds to the bottom pixel on the left side. Auroral intensities as a function of time on pixel [32, 32] and [16, 16] for every 10th frame between 11:00:00 and 11:00:20 are shown in Figure 3.21(a) (a total of 200 samples each). The FFT power as a function of frequency for the two pixels is shown in Figure 3.21(b). We estimated the frequency at the single peak with a power greater than 80 [a.u.] for each pixel. As a result, we obtained the period map shown in Figure 3.21(c). It should be noted that PA1-3 gradually moved southward in the FOV of the EMCCD camera. After several test analyses, we concluded that a 20-s of data window was the most appropriate for detecting periods of PAs and separating both temporal and spatial variations. In addition, PA1-3 gradually lost their own shapes after 11:00:20, and the period map between 11:00:00 and 11:00:20 showed the shapes of PA1-3 the most sharply. Note that the EMCCD image data just does not exist for 20 seconds before 11:00 UT due to the data transferring and data recording. As shown in Figure 3.21(c), three patches had specific periods in the range of 4-7 seconds. Additionally, these patches with different periods coexisted very close to each other . The boundaries surrounding PAs were not seen in Figure 3.21(c) because the ambient patches were not stable but slightly moving, the

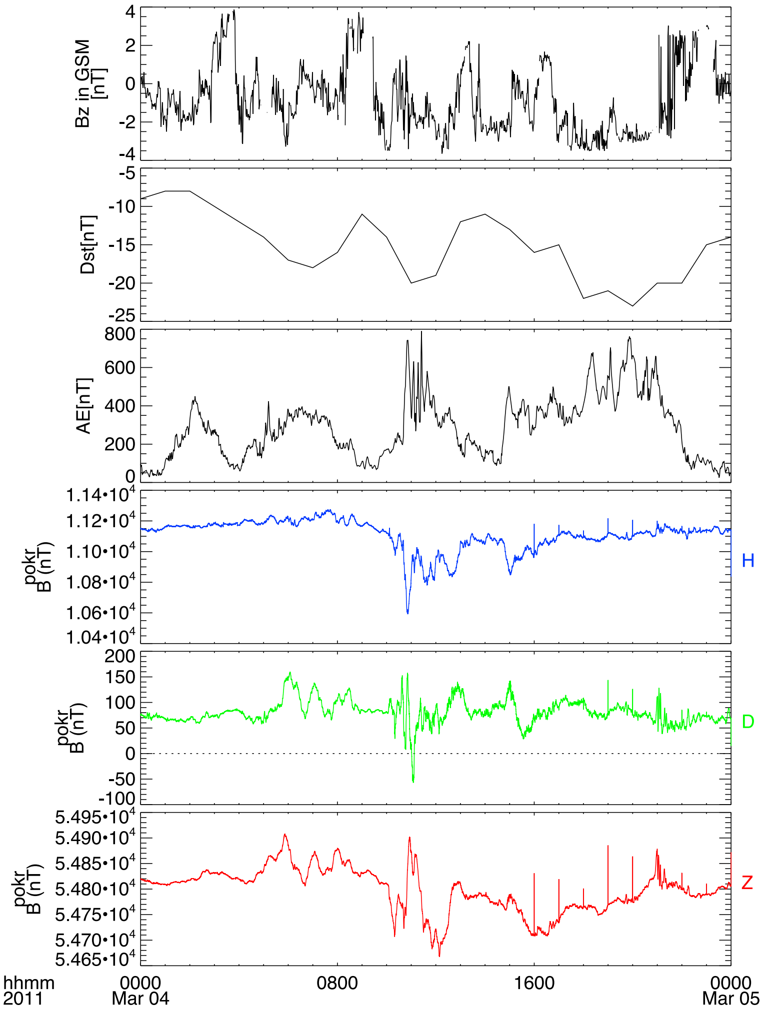

Figure 3.17: A summary plot of time-shifted IMF Bz component, *Dst*, *AE* index, and geomagnetic fields variations (H, D, and Z components) obtained from a magnetometer at Poker Flat Research Range, as a function of time on 4th March 2011.

boundaries can be estimated to be 5-8 km wide on the basis of images from the EMCCD camera.

In addition, we have carried out the FFT analysis for a shorter data window of 1000 frames (10-seconds duration) to detect a few Hz modulations of PAs. Auroral intensity variations on pixel [32, 32] and [10, 35] between 11:00:10 UT and 11:00:20 UT are shown in Figure 3.22(a). Note that saw-toothed modulations were clearly identified in the data at pixel [10, 35] in the on-phase enhancement around 11:00:14 UT, and they may be considered as typical a few Hz modulations. To investigate the characteristics of these modulations in detail, FFT analysis was conducted and the result is shown in Figure 3.22(b). There was a sharp peak at 1.50 Hz, with a narrow frequency width of about 0.30 Hz. Another peak was also found at about 4.00 Hz, but no dominant frequency modulations existed in the frequency range higher than 5.00 Hz. Similar to Figure 3.21 (c), the power maps for PA modulations in the frequency range of 0.10-3.00 Hz are shown in Figure 3.23, and it is the first attempt to visualize the spatial distribution of modulation power in this frequency range. The position of boomerang-like PA1 showed a slight difference between Figure 3.21 (c) and Figure 3.23. We obtained Figure 3.21(c) from the FFT analysis for 20-s of data between 11:00:00 UT and 11:00:20 UT, whereas only the last 10 seconds of the same data was used for Figure 3.23. We can consider that PA1 expanded eastward and PA2 shrank in the latter part of the 20 seconds, as the frequency maps of

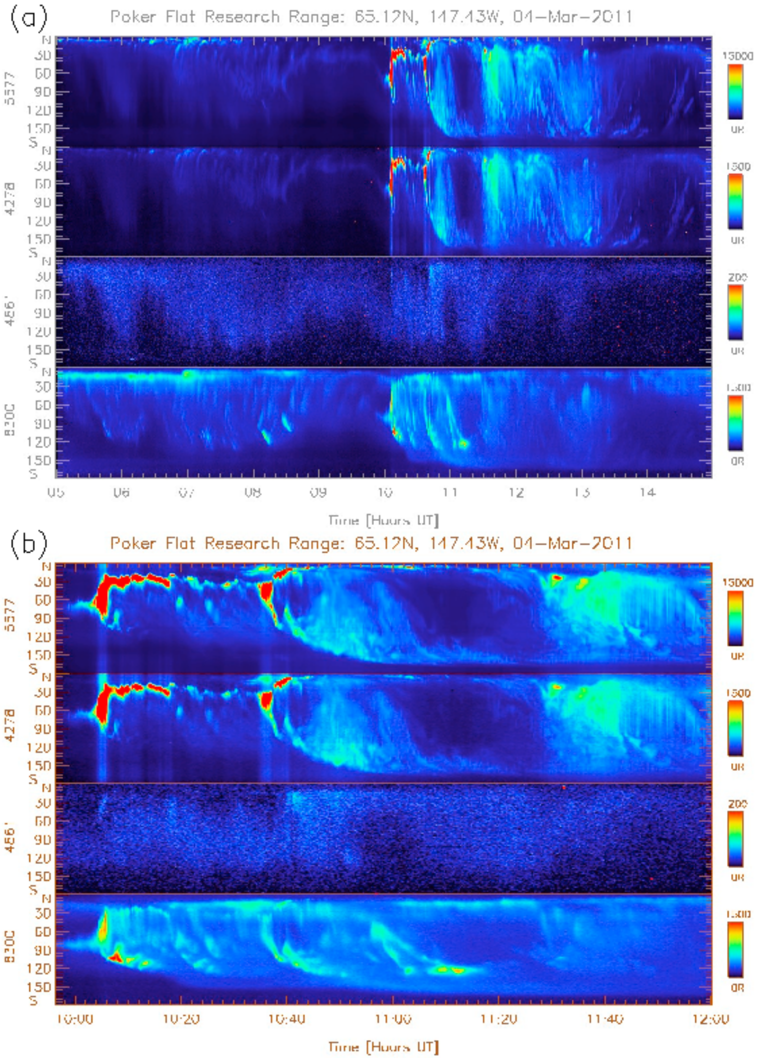

Figure 3.18: Two keograms obtained from a meridian spectrograph with four wavelengths of 557.7, 427.8, 486.1, and 630.0 nm installed at PFRR (a) from 05:00 to 15:00 UT and (b) from 10:00 to 12:00 UT, respectively.

0.20 and 0.30 Hz show. Each patch showed more complicated spatial structures in Figure 3.23 compared with Figure 3.22(c). PA1 had strong modulations in the frequency range from 1.40 and 1.70 Hz. These estimated frequencies were consistent with original waveforms on pixel [10, 35], in particular, around 11:00:15 UT. While 1.40-1.70 Hz modulations almost covered the patch of PA1, a strong peak about 2-3 times greater than background level also existed locally around pixel [10, 35]. Here, PA2 seemed to be not uniform but composed of sub-structures as spots or arc segments. While strong modulations were seen as a few spots in PA2 for 1.3-1.5 Hz, they also appeared along the edge of the patch of PA2 for lower frequencies of 0.50-0.80 Hz. Moreover, PA2 had fast variations around 2.4 Hz, but PA3 seemed to have no strong modulations faster than 1.00 Hz during this period.

To examine whether the estimated peak frequencies and the distributions are reasonable, we calculated the coherence between temporal variations at each pixel with applying the FFT analysis. For the variation as a function of time $f_i(t)$, the Fourier Transform formula can be written as

$$F_i(\omega) = \frac{1}{2\pi}\int_{-\infty}^{\infty} f_i(t)e^{-i\omega t}dt \tag{3.1}$$

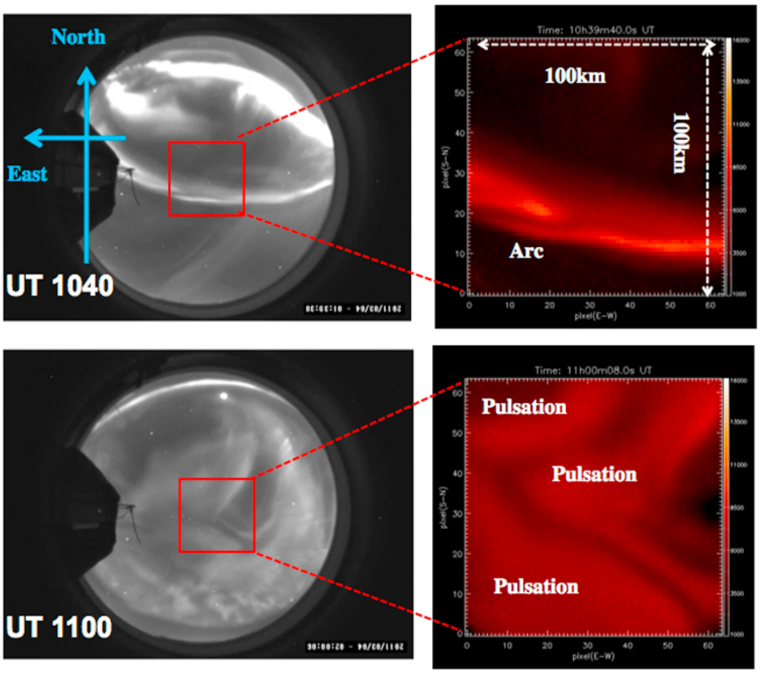

Figure 3.19: Two sets of all-sky panchromatic images and wide FOV filtered images obtained from the EMCCD camera around 10:40 UT and 11:00 UT, respectively. Red squares in all-sky images correspond to the FOV of the EMCCD camera (49 × 49°). The color scale of the EMCCD images indicates calibrated counts between 1000 and 16000.

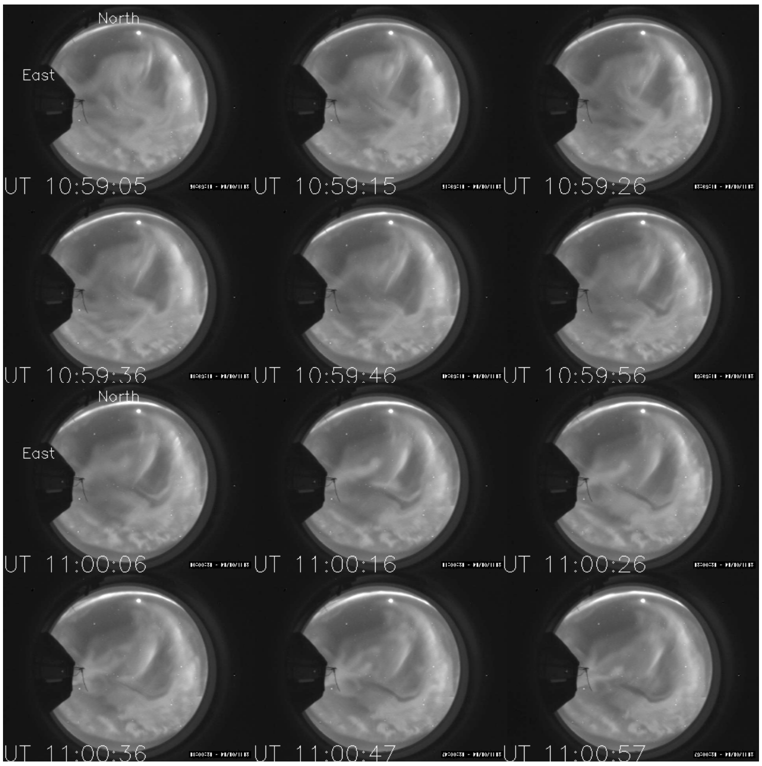

Figure 3.20: Sequence of all-sky panchromatic images captured at 10-s intervals from 10:59:05 UT to 11:00:57 UT. Top and left sides in images correspond approximately to geomagnetic north and east, respectively. Large-scale auroral structures with pulsations propagated southward while being compressed gradually. Black regions existed between adjacent aurora structures.

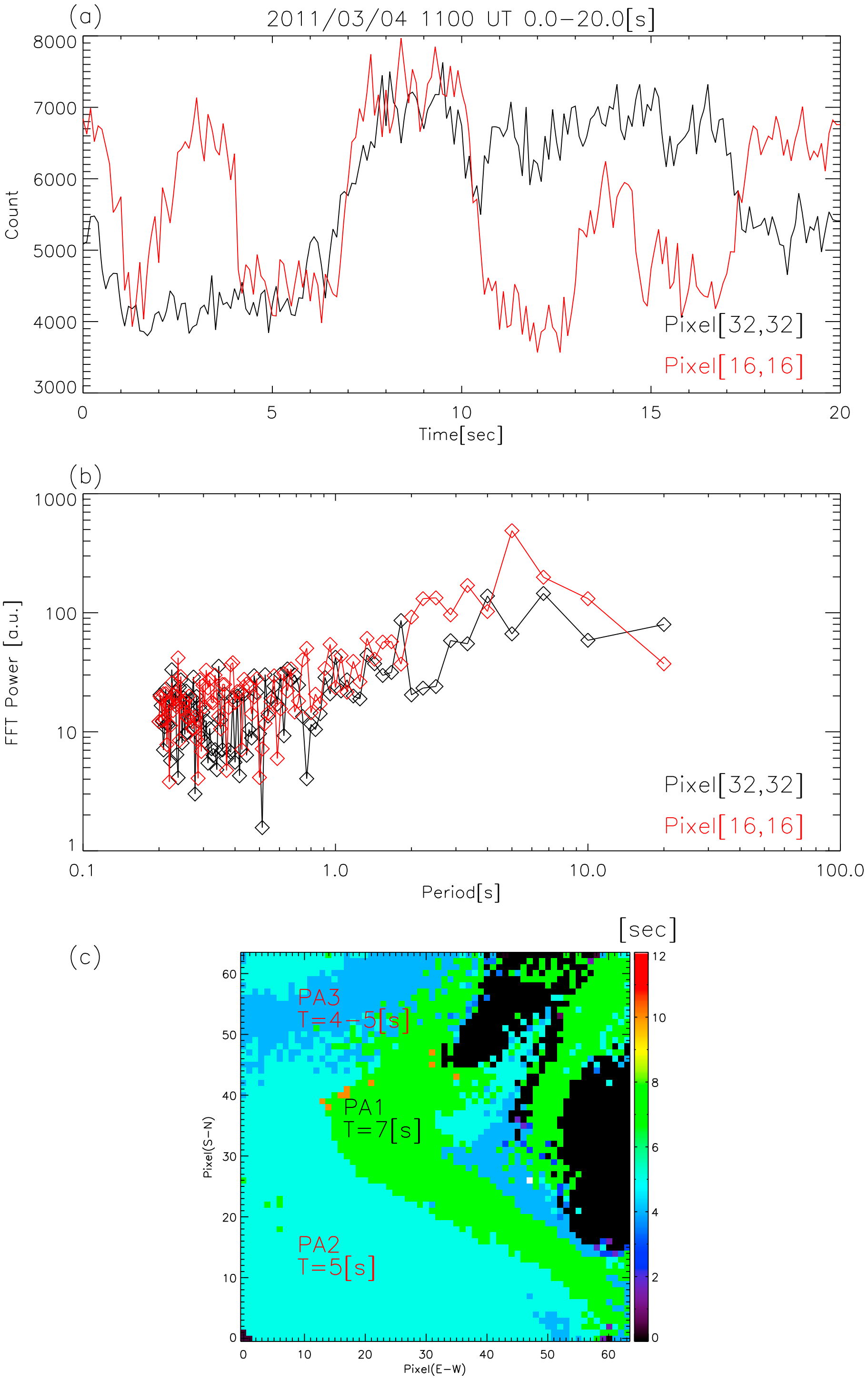

Figure 3.21: (a) Auroral intensities as a function of time on pixels at [32, 32] (black) and [16, 16] (red) for every 10th frame between 11:00:00 UT and 11:00:20 UT (a total of 200 samples each). (b) Results of FFT analysis for temporal variations as shown in (a). Two power spectra for pixels at [32, 32] and [16, 16] had peaks at 7 and 5 seconds, respectively. The spectrum of the pixel at [32, 32] had also secondary peak at 4 seconds. (c) A map shows the peak frequency of power spectra for all pixels estimated from the data during the period between 11:00:00 and 11:00:20. Color scale corresponds to periods from 0 to 12 seconds, and the pixels with peaks of FFT power greater than 80.0 [a.u.] only are plotted.

The cross spectrum, $S_{ij}(\omega)$, can be given by

$$S_{ij}(\omega) = \lim_{T\to\infty} \frac{2\pi}{T} F_i^*(\omega) F_j(\omega) = K_{ij}(\omega) - iQ_{ij}(\omega) \tag{3.2}$$

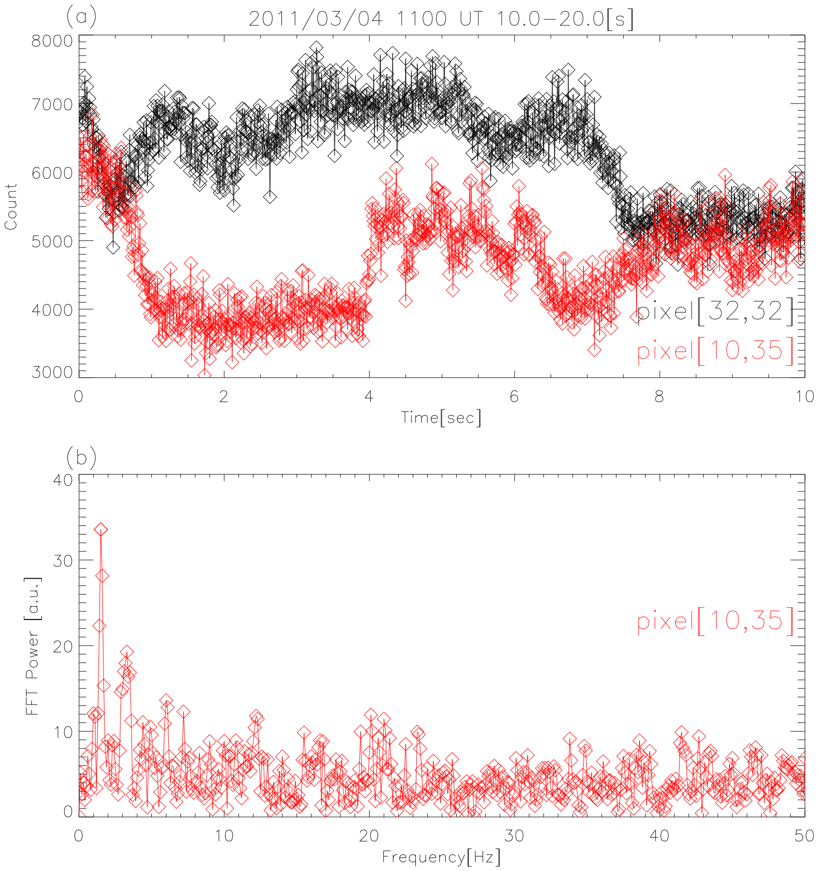

Figure 3.22: (a) Auroral intensity variations as a function of time for pixels at [32, 32] (black) and [10, 35] (red) between 11:00:10 UT and 11:00:20 UT. Full time resolution data of 100 Hz are used in this plot. (b) Results of FFT analysis for temporal variations for pixel [10, 35]. A sharp peak at 1.50 Hz, with a narrow frequency bandwidth of about 0.30 Hz, is clearly seen, and this peak corresponds to saw-toothed feature seen between 11:00:14 UT and 11:00:16 UT. A secondary peak was also seen at about 4.00 Hz, and no dominant peak was evident in the frequency range higher than 5.00 Hz.

If $i = j$, then cross spectrum equals the power spectrum of function $f_i(t)$. Using a cross spectrum, we can obtain the following coherence $coh_{ij}^2(\omega)$ and $\phi_{ij}^2(\omega)$ phase between two pixels:

$$coh_{ij}^2(\omega) = \frac{|S_{ij}(\omega)|^2}{|S_{ii}(\omega)||S_{jj}(\omega)|} = \frac{Q_{ij}^2(\omega) + K_{ij}^2(\omega)}{|S_{ii}(\omega)||S_{jj}(\omega)|} \tag{3.3}$$

$$\phi_{ij}^2(\omega) = \arctan\left(\frac{Q_{ij}(\omega)}{K_{ij}(\omega)}\right) \tag{3.4}$$

Indices i and j represent the basis and arbitrary pixel, respectively. To improve the signal-to-noise ratio each image was re-binned with 2 × 2 pixels. The coherence maps in the same format as Figure 3.23 are shown in Figure 3.24. Note that we set the pixel at [10, 35] as the reference which has a strong 1.5-Hz modulation (corresponding to the pixel at [5, 17] in 2 × 2 ensemble average). This result shows the coherence of two different types of temporal variations, corresponding to pulsations ($<$ 1.00 Hz) and modulations ($>$ 1.00 Hz). The low-frequency components between 0.20 and 0.60 Hz seemed to have high coherency in all PA1-3. However, the coherency of high-frequency components around 1.50 Hz was enhanced in only PA1 while variations around 2.4 Hz inside PA2 were not so coherent. Moreover, Figure 3.25 shows the phase maps derived from the cross spectrum analysis where the bins with $coh_{ij}^2(\omega)$ less than 0.50 are ignored and not plotted. We can focus on the different temporal scales of pulsations and modulations in Figure 3.25. For

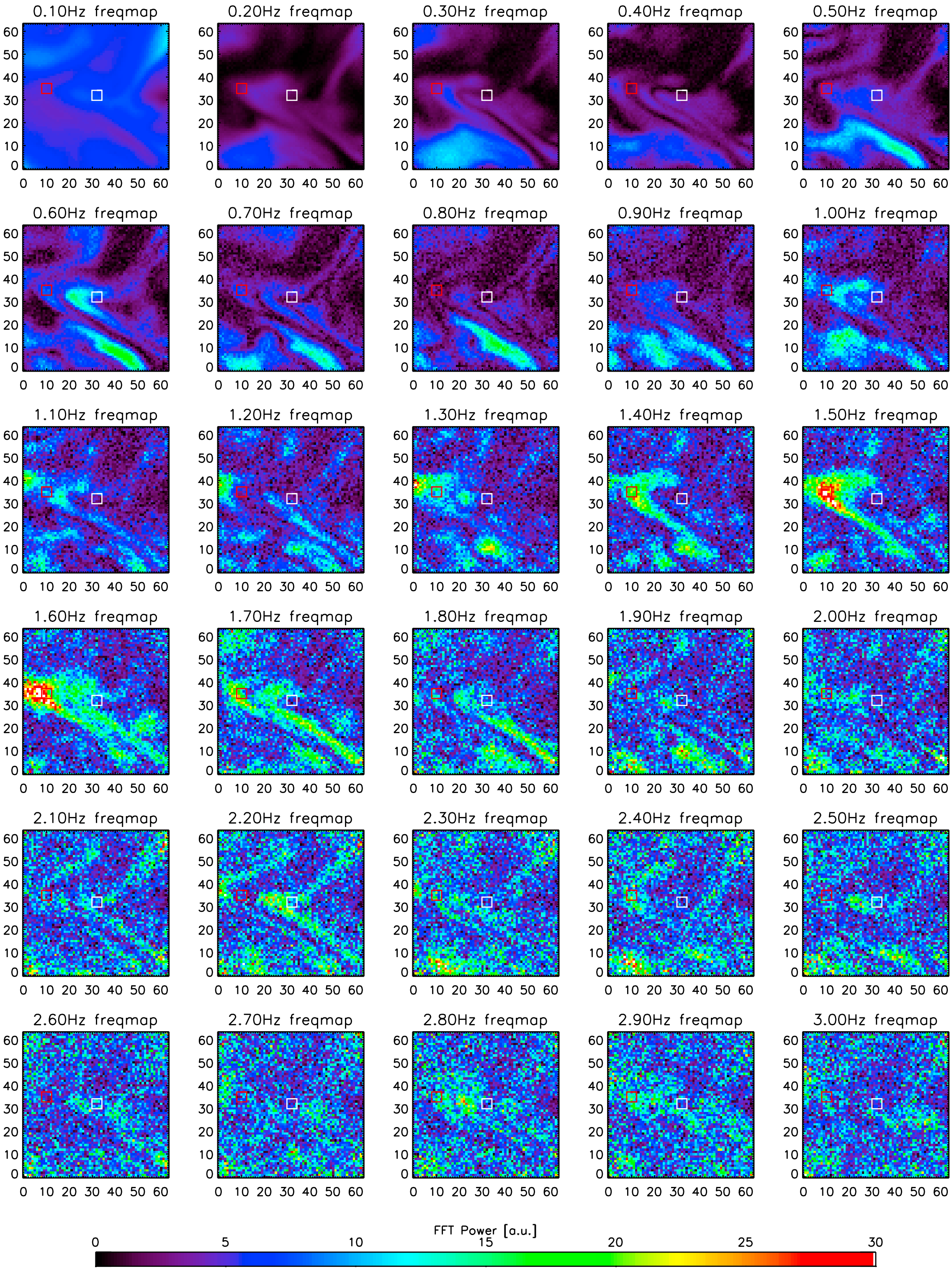

Figure 3.23: Modulation powers of PA variations between 0.10 and 3.00 Hz plotted onto the image area of our EMCCD camera. Red and white square in each power map represent the position of pixel [32, 32] and [10, 35], respectively. Color scale is from 0 to 30 [a.u.]. Between 1.40 and 1.70 Hz, the modulations are distributed inside boomerang-like PA1.

examples of pulsations, the phase maps of both 0.20 and 0.30 Hz clearly indicate auroral pulsations propagated westward inside PA2 and PA3 during this 10-s period because their phases advanced continuously westward in both PA2 and PA3. On the other hand, PA1 had more complicated phase differences inside, and it seemed to consist of two structures with different phases in the range of frequency between 0.20 and 0.60 Hz. Furthermore, phase jumps existed at the boundaries between three PAs, in particular in the phase maps of 0.20, 0.30, 0.50, and 0.70 Hz. In contrast, the phase map for the most dominant modulation frequency at 1.5 Hz showed that PA1 had almost the same phase all over the patch and other PAs did not have coherent modulations.

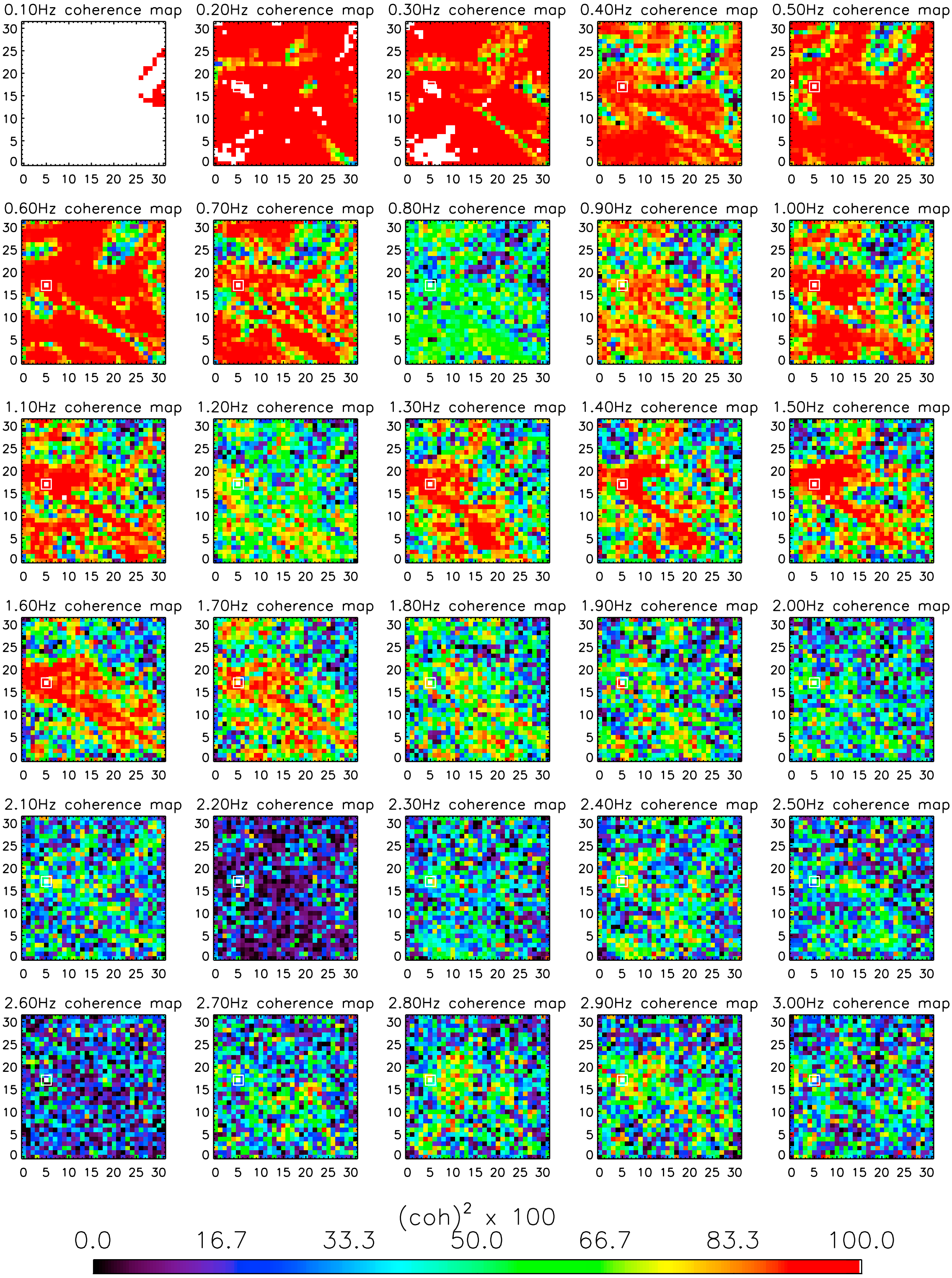

Figure 3.24: Coherency maps in the same format as those in Figure 3.23. Color scale represents coherency between basis and arbitrary pixels from 0.0 to 100.0 (× 100). Number of pixels is changed into 32 × 32, due to 2 × 2 ensemble averages.

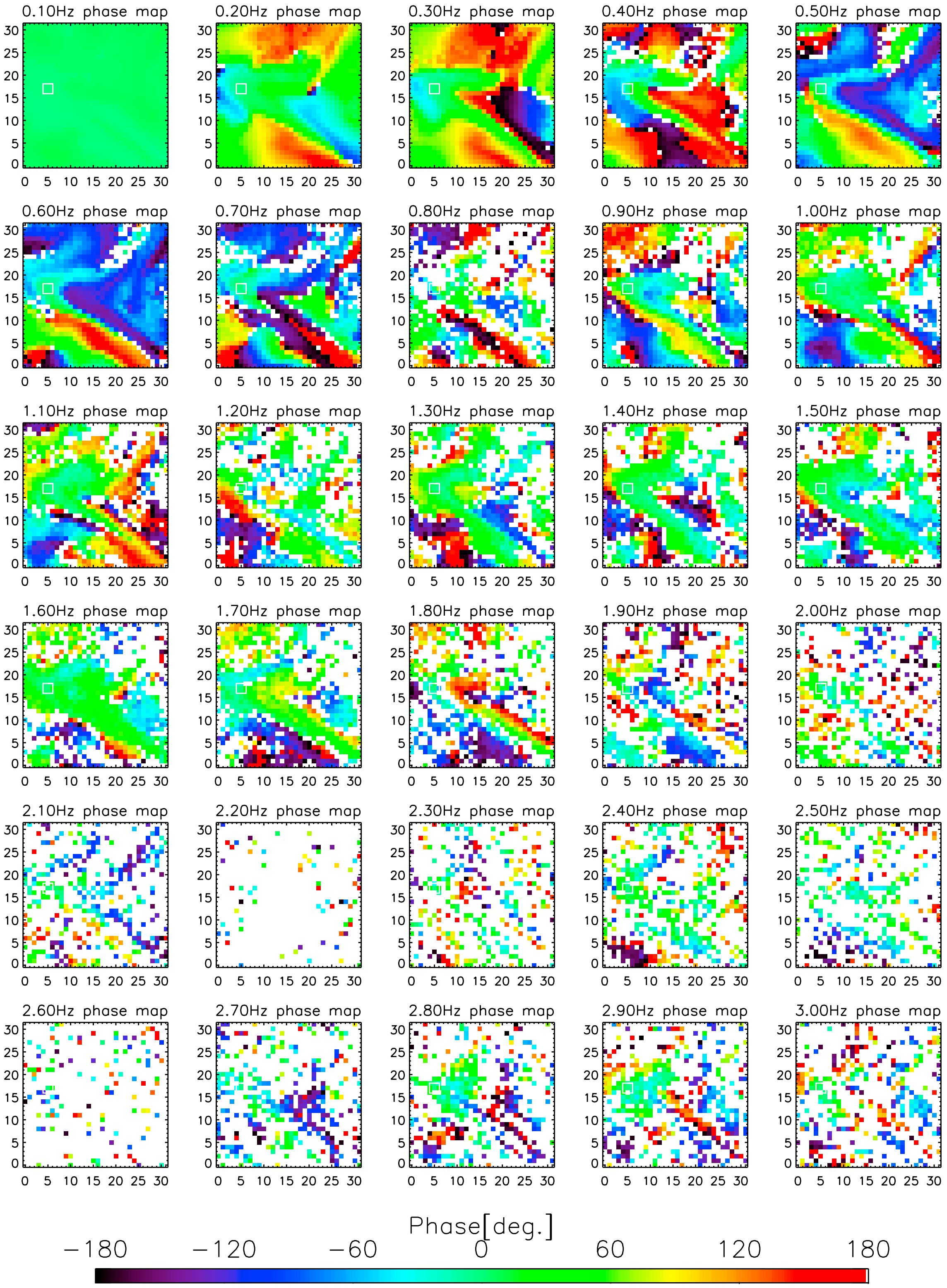

Figure 3.25: Phase maps in the same format as those in Figure 3.23. Color scale represents phase difference between basis and arbitrary pixels from -180 to 180 degrees. White squares corresponds to the basis pixel in this analysis. Pixels with coherency less than 0.50 are not plotted.

While the modulations around 1.5 Hz inside PA1 were almost in phase, low-frequency variations inside PA1-3 seemed to propagate in particular directions with clear wavefronts. To investigate the detail of dynamics inside the pulsating patches, we estimated the propagation velocities for each frequency map from the phase difference between an arbitrary pixel and adjacent ones. The propagation velocity as a function of frequency, ω, can be estimated as below.

$$V_{pro,ij}(\omega) = \frac{d_0\omega}{\delta\phi_{ij}(\omega)} \tag{3.5}$$

Here, d_0 and $\delta\phi_{ij}(\omega)$ are distance and phase difference between the adjacent pixels, respectively. In this analysis, we ignored any phase difference under 2.0 degrees and regarded it as homogeneous. The phase maps shown in Figures 3.26(a), (b) and (c) are the same as those of 0.2, 0.3, and 0.5 Hz as in Figure 3.25, overplotted with propagation velocity vectors by black arrows on each pixel. Note that the length of the arrows was normalized in each frequency phase map. We find from equation 3.5 that the error in propagation velocities $V_{pro,ij}$ is proportional to the error in $\delta\phi_{ij}(\omega)$ and inversely proportional to the square of $\delta\phi_{ij}(\omega)$. It means that when small $\delta\phi_{ij}(\omega)$ is obtained, i.e., $V_{pro,ij}$ is large, the error in $V_{pro,ij}$ cannot be neglected. Thus, we excluded $V_{pro,ij}$ in case that the error is larger than the half of absolute value of $V_{pro,ij}$. $V_{pro,ij}$ had large errors particularly in the large propagation velocities over 100 km/s. We can see dominant flows in the northwest direction with speeds of 50-120 km/s around pixel [12, 5] in Figure 3.26. The estimated velocity was reliable because these propagation velocities inside PA2 seemed to be "a convergent motion", which is resulted from the coherent phase differences. The velocities tended to become very low in the region closer to the boundary between PA1 and PA2. The flows changed the direction along the boundary in the vicinity of the boundary and reversal flows also appeared. In addition, the estimated velocities just on the boundaries were no more than 2 km/s at the ionosphere. These boundaries with low velocities clearly corresponded to those seen in raw images. It is evident on PA2 that convergent flows clearly existed inside the patch PA2, and that the velocities near the boundaries became extremely low.

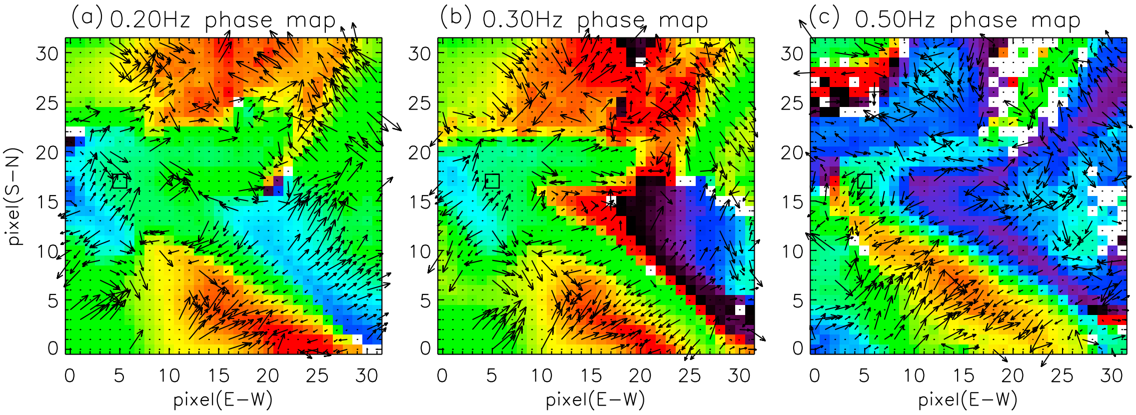

Figure 3.26: Phase maps in the same format as those in Figure 3.25 for frequencies of 0.2, 0.3, and 0.5 Hz. Estimated propagation velocities of each frequency component are over-plotted onto the maps. Note that the velocities indicated by black arrows are normalized in each phase map. Black squares represent the position of the basis pixel for cross spectrum analysis. We can see dominant flows to the northwest directions in the three frequencies inside of PA2. The velocities tended to become very low, closer to the boundary of PA1 and PA2.

Discussion

As shown in Figure 3.21(c), PA1-3 presented here had different periods between 4 and 7 seconds although the PAs coexisted in the amall 100 × 100 km scale at the auroral altitude of 110 km. We should note that PA1-3 observed by the EMCCD camera were a part of large scale auroral structure in the spatial scale of a few hundred km identified by the all-sky imager. The periods of PA1-3 partially corresponded to bounce periods of 5-25 keV electrons estimated with a realistic magnetic field model of *Tsyganenko and Sitnov.* [2005], and they were equal to 2.3-5.1 seconds. However, the result showed that the periods of the three adjacent PAs differed, suggesting that the periodicity cannot simply be attributed to the bounce periods. Past theoretical studies mentioned other generation mechanisms of PAs, such as pitch angle scattering resulted from perturbations of energetic particle flux or cold plasma density inside a pulsating patch [*Davidson and Chiu*, 1987; *Davidson*, 1990; *Demekhov and Trakhtengerts*, 1994] and a time interval of particle supply into a flux tube [*Demekhov and Trakhtengerts*, 1994]. A recent study showed that perturbations of cold plasma density were observed simultaneously with enhancements of whistler mode chorus waves [*Li et al.*, 2011], and these variations of plasma density, in particular density depletions, were thought to play an essential role in the generation of PAs. In addition, the spatial scale of pulsating patch, that is "coherent area" at the magnetic equator, was estimated to extend over 500 km [*Haque et al.*, 2011], and to be typically 5000 km [*Nishimura et al.*, 2011]. The typical scale of the patch presented here can be estimated to be 2000 km at the equator inferred from the scale of PA1 in the ionosphere, and it is comparable with the other estimations based on in situ observations.

There is also a possibility that patches PA1-3, in particular on PA1, were composed of spatial fine-scale structures of cold plasma in the magnetosphere since there is a cluster of small patchy structures or arc segments and a strong modulation spot inside PA1 as seen in Figure 3.23. Such spatial characteristics may bring us the key to solve the remaining problems about generation process of PAs. We need in-situ observations as well as theoretical studies concerning on the plasma characteristics in the spatial scale smaller than a thousand km in the magnetosphere to discuss the generation mechanisms and spatio-temporal characteristics of PAs. We should also consider active ionospheric processes [e.g., *Stenbaek-Nielsen*, 1980; *Hosokawa et al.*, 2008] such as the polarization electric field in the vicinity to a patchy structure in our future studies.

PA1-3 were transient phenomena that altered their shapes, propagated southward, and passed by the FOV of our EMCCD camera with in a minute. Such PAs, i.e., those with band structures or arc segments in many cases, were typically observed in other events of our observations. Concerning PAs with patchy structures, *Fujii et al.* [1987] suggested that pitch angle scattering by some waves results in conjugacy of patchy PAs in the both hemisphere. *Su et al.* [2009] suggested that the electron pancake distribution develops over a few hours and effective pitch angle scattering by whistler mode chorus results in generations of diffuse auroras. Therefore, PA with patchy structure in the late recovery phase of substorm probably be closely associated with the temporal evolution of electron distribution functions and excitation of whistler mode chorus.

On the other hand, the characteristics of PAs in the early recovery phase of substorm that we presented here as PA1-3 are still unknown for the most part, including the generation mechanisms and morphology. For example, one of the causes for the morphology was suggested to be the modification of the electric field in the ionosphere [*Hosokawa et al.*, 2010a]. In addition to the ionospheric feedback, highly structured diffuse auroras in the non-patch shape with a spatial scale of a few km were suggested to be a result of interchange instability in the magnetosphere [*Ebihara et al.*, 2010]. A Rayleigh-Taylor type instability was also expected to be cause the finger-like patches [*Shiokawa et al.*, 2010]. According to these resent suggestions, the spatial structures of PA1-3 may be determined by a balance between magnetic tensions and plasma pressures. In particular, the boomerang-like shape of PA1 is possibly explained by the model proposed by *Shiokawa et al.* [2010]. We suppose that the force balances between the pressure gradient and the magnetic tension on the west edge of PA1 perturbed the surface on the side and then, a polarization electric field in the north-south direction would be generated. The E × B drift force, which resulted from this electric field and ambient magnetic field, was expected to develop the boomerang-like shape with both the north and south parts extending to the west. However, it should be noted that the magnetospheric footprints of PA1-3 were located earthward compared to the case of *Shiokawa et al.* [2010] and strong magnetic tension generally prevents the development of the instability.

Another candidate is a azimuthally spaced auroral forms (AAF) have recently been considered as ionospheric phenomena of kinetic ballooning/interchange instability [*Elphinstone et al.*, 1995; *Uritsky et al.*, 2009]. However, they are auroral signatures in the "pre-onset" of substorms. Typical longitudinal mode number of such preexisting auroral arcs ranged from 100 to 300 [*Liang et al.*, 2008], and it is in agreement with the spatial scale of our observed pulsating patches. We should note that energy stored in the stretched magnetotail with a deep Bz minimum, which drives ballooning instability, may be released after breakup. It means that applications of AAF to our observations are not so simple. Whether they occur before or after breakup, local plasma pressures in the magnetic equator can be thought to play an important role in the formation of complicated PA structures and they also possibly contribute to generate the intermittent precipitation in the early recovery phase of substorms.

Our optical measurements with 100-Hz sampling revealed that the enhanced modulations were generated at well-defined frequencies with small bandwidths. One insight presented in this study is that there were no strong modulations from 5.00 Hz up to 50.0 Hz (Nyquist frequency). If whistler mode chorus generates electron precipitation that causes PAs through cyclotron resonance, the modulations can be regarded as an interval between subsequent chorus elements. Indeed, a number of in situ observations showed that whistler mode chorus consisted of a sequence of chorus elements with repetition periods between a few tens and hundreds of ms [e.g., *Santolik et al.*, 2003; *Trakhtengerts et al.*, 2004]. The simulations of *Nunn et al.* [2009] demonstrated that the intervals between chorus elements varied considerably from a few hundreds ms to one second due to changes in ambient electron density and the pitch angle of magnetospheric electrons. Therefore, if the electron density at the magnetic equator was stable during the on-phase of PA (typically $\sim$ 10 seconds), it is reasonable to expect that the modulation will be identified as a single and sharp peak frequency.

We presented, for the first time, the modulation power maps of pulsating patches derived from ground-based optical measurements. Modulation around 1.5 Hz is distributed over the patchy structure of PA1, while PA2 and 3 have no enhancements. Our observations indicate that patch PA1 is small, compared to PA2 and PA3. This observational fact is consistent with the previous result that patches with small structures tend to fluctuate with higher frequencies [*Samara and Michell*, 2010]. In addition, as shown in Figures 3.24 and 3.25, strongly modulated variations at the frequency of 1.5 Hz were seen only in the center of PA1, although PA1 showed the coherency of modulation over the entire patchy structure. This result demonstrates that strong modulations of PAs are not distributed uniformly inside the patch but exist locally. Here, we found that PA2 and PA3 in the FOV of our EMCCD camera corresponded to the edges of their large-scale structures seen by our all-sky camera. Thus, this may be also why both PA2 and 3 had no strong modulations and coherency in the frequency around 1.5 Hz.

Finally, Figure 3.27 shows the occurrence profiles of propagation velocities for three different frequencies of 0.2, 0.3, and 0.5 Hz as well as a sum of the three profiles to demonstrate the range and the occurrence peak of the estimated velocity distributions. We should note that each bin contains the ambiguities of propagation velocities with a few to almost a 50 percent error resulting from methodology. In particular, the errors reached 40 percent for velocities greater than 130 km/s. Figure 3.27 also demonstrates that the velocity profile for a lower frequency had no high velocity components over 100 km/s. Most observed velocities of all the profiles showed almost similar occurrence maximized around 20-30 km/s at altitude 110 km. These low velocity populations of 20-30 km/s corresponded to those in the vicinity to boundaries, and the populations in the range accounted for 32%

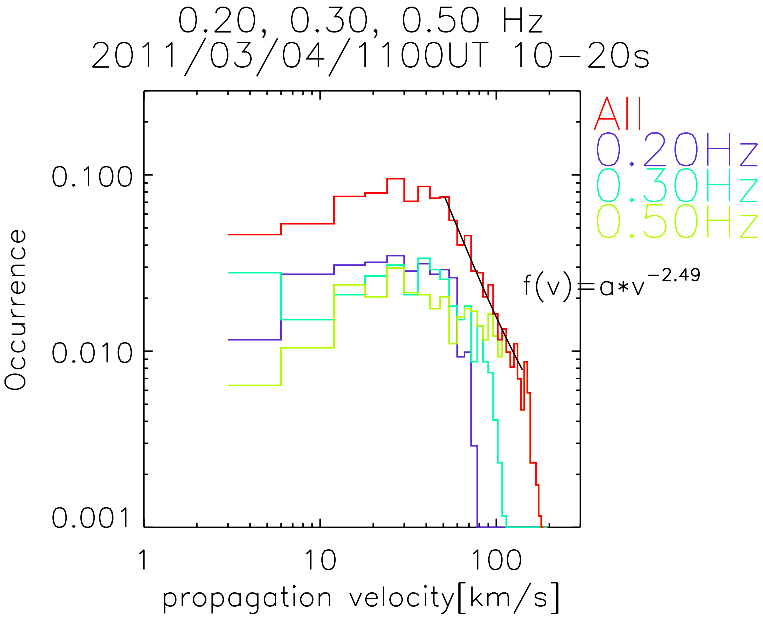

Figure 3.27: Occurrence profiles of propagation velocities at the frequency of 0.2, 0.3, 0.5 Hz, and a sum of the three profiles are shown. The low velocity populations of 20-30 km/s corresponded to those in the vicinity to boundaries, and the populations in the range accounted for 32% of the speed profiles for the sum of 0.2, 0.3, and 0.5 Hz. A group of propagation velocities, as seen inside PA2, corresponded to about 50-120 km/s and these accounted for 37%. The profile of propagation velocities for the sum of three frequencies can be fitted with a power law function, and the best-fit power law index is -2.49.

of the speed profiles for the sum of 0.2, 0.3, and 0.5 Hz. A group of propagation velocities, as seen inside PA2, corresponded to about 50-120 km/s and these accounted for 37%. As shown in Figure 3.27, the profile of propagation velocities for the sum of three frequencies can be fitted with a power law function, and the best-fit power law index is -2.49. The estimated propagation velocities in the range of 50-120 km/s were almost consistent with the apparent extent of the movement of the auroral patches reported in the previous study [*Yamamoto and Oguti*, 1982]. However, they were much faster than the drift velocities of pulsating patches due to magnetospheric convection [*Nakamura and Oguti*, 1987]. If we assume that the flux tube is an equipotential, estimated propagation velocities of 50-120 km/s were equal to 1200-2700 km/s in the magnetic equator.

One interesting insight is that the estimated propagation velocities are almost equal to the Alfven speed in the magnetic equator at $L \sim 6$. Since we regard them as flows in the perpendicular directions to the field line, they must be the waves that can propagate across the ambient magnetic field. One of plausible candidates is compressional components of ULF waves. In particular, compressional waves in the range of Pc4-5 pulsations have been expected to modulate seed electron fluxes for the generation of whistler mode chorus [*Kokubun et al.*, 1977; *Kremser et al.*, 1981; *Sarris et al.*, 2007]. Recently, ground-based observations demonstrated simultaneous modulations of particle precipitation and whistler mode chorus driven by the 2.0 mHz compressional component of Pc5 poloidal geomagnetic pulsations [*Manninen et al.*, 2010]. In situ observations suggested that compressional Pc4-5 pulsations with an anti-correlation between the density and the magnetic field played an important role in modulating chorus waves on a timescale of tens of seconds to a few minutes, which overlapped with typical timescales of PA [*Li et al.*, 2011b]. *Liang et al.* [2010] also demonstrated that the spatial distributions of PA patches showed an azimuthal "wavelength" of $\sim$ 6000 km consistent with that of the ULF waves. However, the shortest wavelength estimated by our observations is $\sim$ 2000 km, corresponding to the length of PA1 in the longitudinal direction. ULF waves with different wavelength should have different oscillation period of the flux tube, which may indirectly cause the different periods of the PAs. In conclusion, we suggest the scenario that compressional waves, which propagated inside the patch, contributed to change the growth rates of whistler mode chorus via modulations of the field line intensity or the cold plasma intensity and caused intermittent precipitation associated with PA.

Key findings

Based on the ground-based optical observation using an EMCCD camera with wide a FOV (49 × 49°) and a high sampling rate of 100 frames/s, outstanding spatial and temporal characteristics of PAs were presented. We focused on transient PA phenomena in the early recovery phase of the substorm. The results of Section 3.2.2 are summarized as follows:

1. A large-scale auroral structure ($\sim$ a few hundreds km), which consisted of a group of pulsating patches (50-100 km), propagated southward and it was gradually compressed and extended eastward in the early recovery phase of the substorm at 11:00 UT, on 4th March 2011. It is also noted that clear and stable boundaries with a width of 5-8 km existed between each pulsating patch.

2. Three independent pulsating patches with different periods from 4 to 7 seconds were observed in the FOV of 100 ×100 km at the altitude of 110 km. The periodicity seemed to be not consistent with the electron bounce motion. The typical scale of the patch was estimated to be 2000 km in the magnetic equator, and it is comparable with the estimations based on recent in-situ observations.

3. We investigated in detail the modulations of PAs in the frequency range higher than 1.0 Hz. The results revealed that the modulation had a peak frequency around 1.5 Hz, with a narrow frequency width of 0.30 Hz. Additionally, there was no strong modulation above 5.0 Hz. This is probably because plasma parameters in the magnetosphere related to the generation process of the fine-scale structures of precipitation, i.e. the modulations, such as electron density were stable in the short term ($\sim$ 10 seconds).

4. Strong modulation around 1.5 Hz was not distributed uniformly inside the PA1 structure but existed locally as a spot in PA1. On the other hand, the adjacent PA2 and PA3 had no strong modulation and coherency in the frequency around 1.5 Hz. This work showed for the first time such two-dimensional distributions of modulation power.

5. Coherence and phase maps obtained from the cross spectrum analysis revealed that the modulations around 1.5 Hz inside PA1 were almost in phase, and that the low frequency variations from 0.2 to 0.5 Hz inside PA1-3 propagated as a group of flows with consistent directions. The estimated fast flow velocities inside PA2 ranged from 50 to 120 km/s at the auroral altitude. They were corresponding to the horizontal velocities between 1800 and 2700 km/s at the magnetic equator, and almost equal to the Alfven speed at $L \sim 6$. The result suggests that compressional waves may drive control the growth rates of whistler mode waves, which can generate precipitation associated with PA, and drive the dynamics inside a patch.

3.2.3 Event study on December 1st, 2011

Here, another event of PAs on December 1st, 2011 is presented. Figure 3.28 shows the time-shifted solar wind and IMF parameters, geomagnetic fluctuations, and auroral intensity measured by the photometer as a function of time. High solar wind velocity of 500 km/s and *Dst* index of about -20 nT continued during this day. Sudden negative excursion of IMF Bz component and decrease in dynamic pressure are seen from 12:00 UT. At the same time, *AE* index rapidly increased and reached 350 nT. In addition, the three components of geomagnetic field observed at PFRR showed simultaneous rapid changes, which suggested a substorm occurred close to PFRR. Second panel from the bottom in Figure 3.28 shows auroral intensity variations for the wavelengths of N_2 1st positive band (650-700 nm), N_2 emission line at 670.5 nm, and atomic Oxygen emission line at 844.6 nm emission. The intensity of N_2 670.5 nm emission was estimated from N_2 1st positive band based on the result of *Whiter et al.* [2012]. Aurora activity over PFRR increased once around 10:40 UT, however, it did not develop to an aurora breakup. A typical aurora breakup occurred simultaneously with *AE* index and geomagnetic field around 12:00 UT, and PAs appeared at 12:20 UT. The bottom panel in Figure 3.28 shows the ratio between intensity of N_2 670.5 nm emission line and O 844.6 nm emission line. The ratio showed the minimum less than 1.0 just after 12:00 UT, which implies that energetic-electrons precipitated during this period (described later in detail).

We show successive images taken by the all-sky panchromatic camera at a 6-s interval in Figure 3.29. The period of Figure 3.29 is from12:19:44 UT to 12:21:28 UT during the beginning of recovery phase of the substorm moentioned above (roughly 20 minutes after the auroral breakup). Although the sky was covered with wispy clouds during this period, an meso-scale auroral patch structure in meso scale was identified in the region indicated by a red square superimposed on the image at 12:20:21 UT. This auroral structure gradually moved southward, however, we did not confirm its pulsation because of the insufficient temporal resolution of the all-sky camera ($\sim$ 6 seconds). Figure 3.30 shows successive images taken by the EMCCD camera from 12:20:10 UT to 12:20:29 UT. It is noted that the images are displayed at an interval of 1 second, and top and right of the image are the magnetic north and east direction. From the EMCCD camera data, the aurora patch did not move southward simply and gradually but also oscillated back and forth like a pendulum, and sometimes split into sub-structures. Figures 3.31 (a) and (b) are the images obtained from the EMCCD camera during the period from 12:20:15.4 UT to 12:20:15.6 UT in the same format as Figure 3.30. Figure 3.31 (c) is auroral temporal variations on the two pixel, indicated with stars in light green and blue, from 12:20:10 UT to 12:21:10 UT. We find that the temporal variations of aurora luminosity were not uniform even inside the one patch. Figure 3.31 shows the spatial distribution of dominant periods estimated from the FFT analysis with a color scale corresponding to the period of 0-30 seconds. The whole patch can be divided a few micro-structures characterized by different periods, i.e., different temporal variations, and typical periods for this 1 minute data ranged from 7.8 to 10 seconds.

The temporal variations of this pulsating patch observed by the photometer showed a different aspect. Figure 3.32 indicates the temporal variations of auroral intensities of N_2 1st positive band (650-700 nm), N_2 emission line at 670.5 nm, and O emission line at 844.6 nm during the period from 12:18:00 to 12:23:00 UT and from 12:20:10 UT to 12:21:10 UT. The periods shaded in gray represent the "switch-on" phase of the PA. The temporal variation of emission line at N_2 1st positive band in Figure 3.32 (b) was similar to that observed with the EMCCD camera (shown in Figure 3.31 (c)), however, there are slight differences between them due to the filter bandwidths of the two instruments. The ratio between N_2 670.5 nm emission line and O 844.6 nm emission line reached about 0.60 during on-phase, which suggested the PA was generated by electron precipitation with

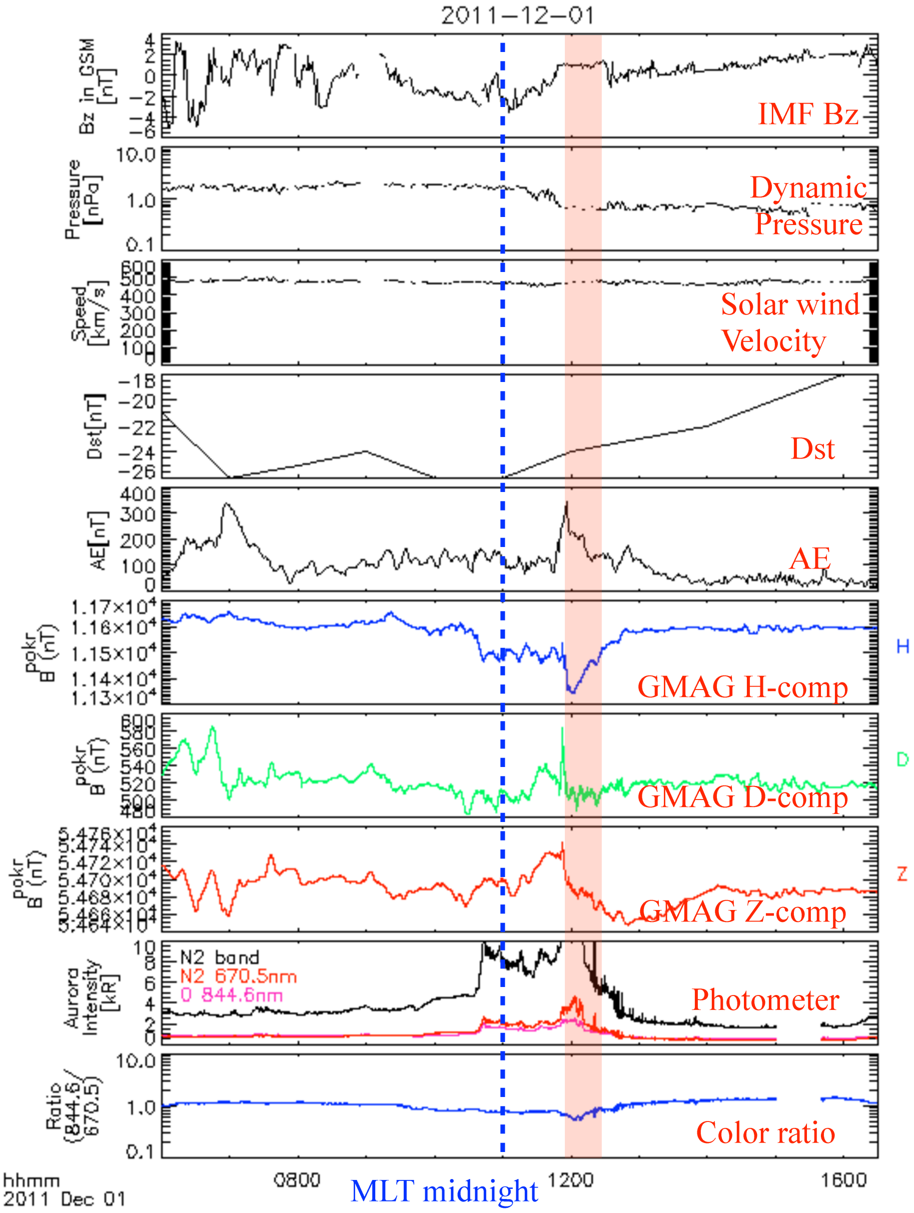

Figure 3.28: Time-shifted solar wind and IMF parameters (IMF Bz, dynamic pressure, and solar wind velocity), geomagnetic variations (*Dst*, *AE*, Geomagnetic field H, D, and Z components) and auroral intensities measured by the photometer as a function of time on December 1st, 2011.

energy of approximately 10 keV [*Ono and Morishima*, 1994.].

The pulsating patch also had rapid temporal variations as shown in Figure 3.33. Top panels in Figure 3.33 are aurora intensities at two selected pixels as a function of time from 12:20:10 UT to 12:20:20 UT, and from 12:20:25 to 12:20:35 UT. Red lines indicate the temporal variations for the pixel [32,5], corresponding to southern part of the patch. We can see clear internal modulations within large scale of on-phase variation during both periods. In the F-t spectrum derived by the FFT analysis for the data during these periods, the strong peaks were identified at the frequencies of 3.0 Hz in (a) and 2.9 Hz in (b) . One more insight is that the rapid variations were excited not in the whole patch structure but in the sub-structure of the patch. Additionally, this sub-structure with the modulation frequency at about 3.0 Hz was almost overlapped with the sub-structure indicated in Figure 3.31 (d). This result shows the possibility that one pulsating patch consists of a few sub-structures in which rapid variations are strongly excited.

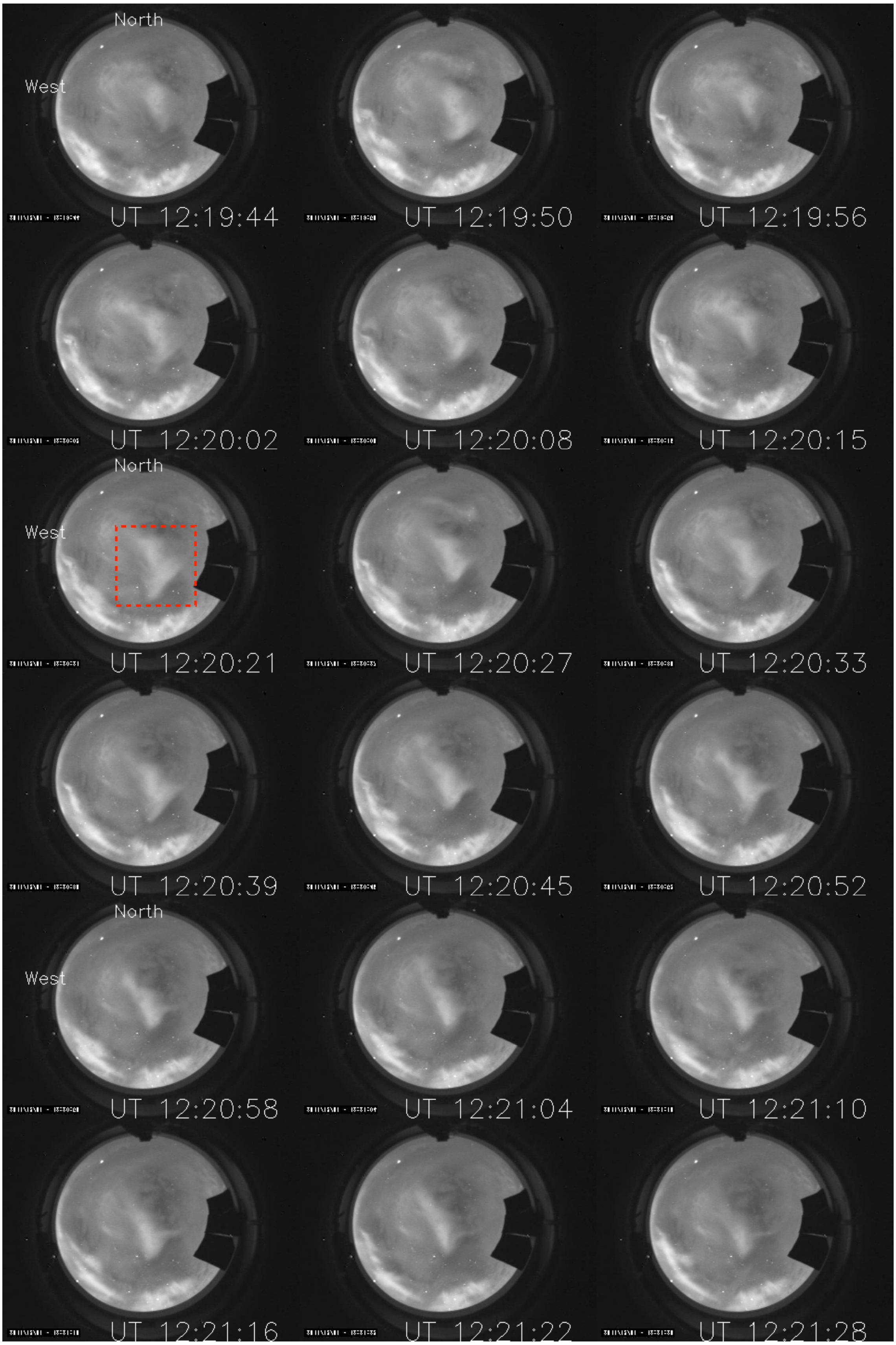

Figure 3.29: Successive images of the all-sky camera at an 6-s intervals from 12:19:44 UT to 12:21:28 UT on 1st December, 2011

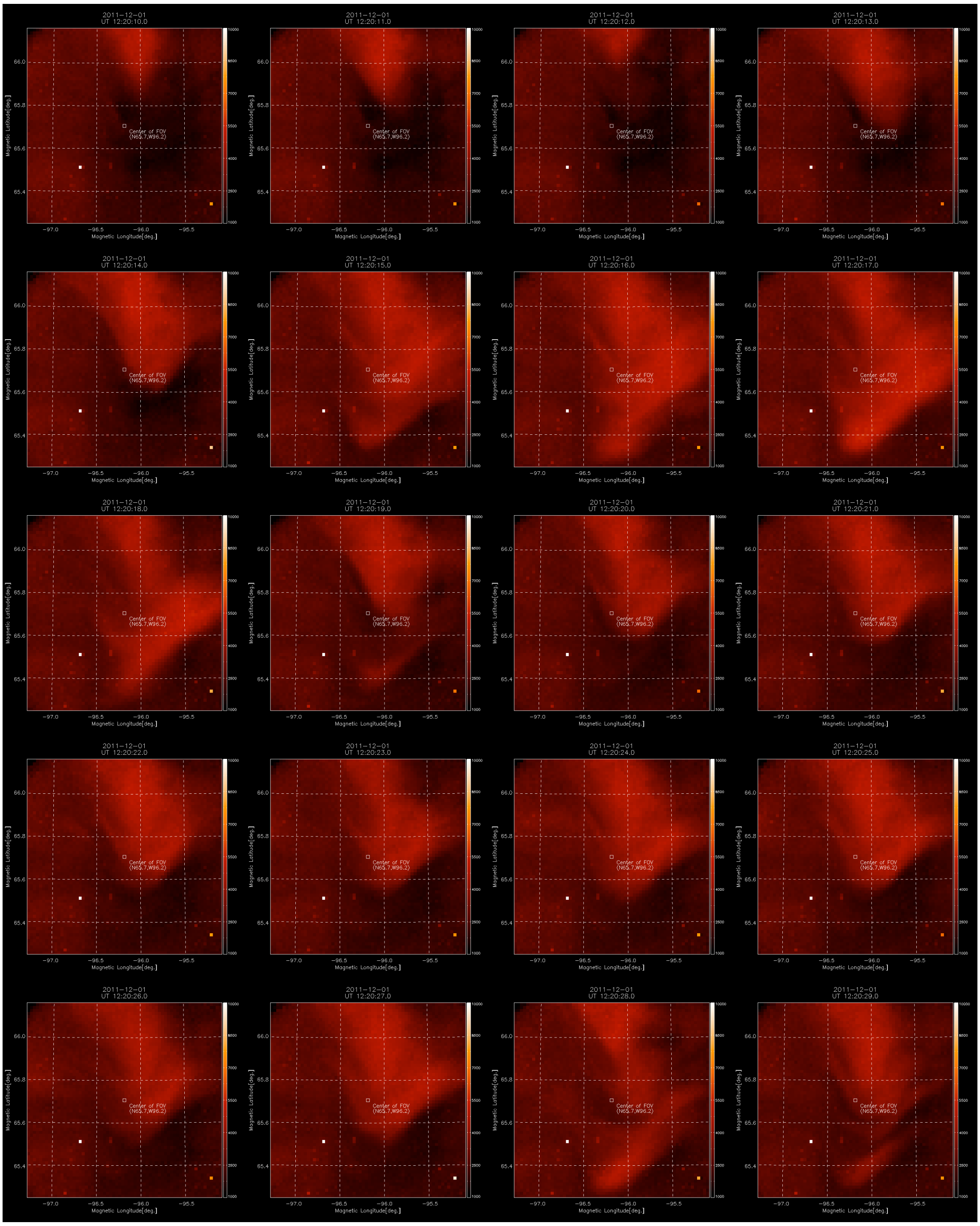

Figure 3.30: Successive images of the EMCCD camera at an interval of 1 second from 12:20:10 UT to 12:20:29 UT. Each image is obtained by averaging 10 images taken with 100 Hz sampling to gain S/N. A color scale is from 1000 to 10000 counts. The FOV corresponds to the horizontal scale of 110 × 110 km, and top and right are the magnetic north and east directions, respectively. White broken horizontal and vertical lines represent magnetic latitudes (66.0°, 65.8°, 65.6°, and 65.4°) and longitudes (-97.0°, -96.5°, -96.0°, and -95.5°), respectively.

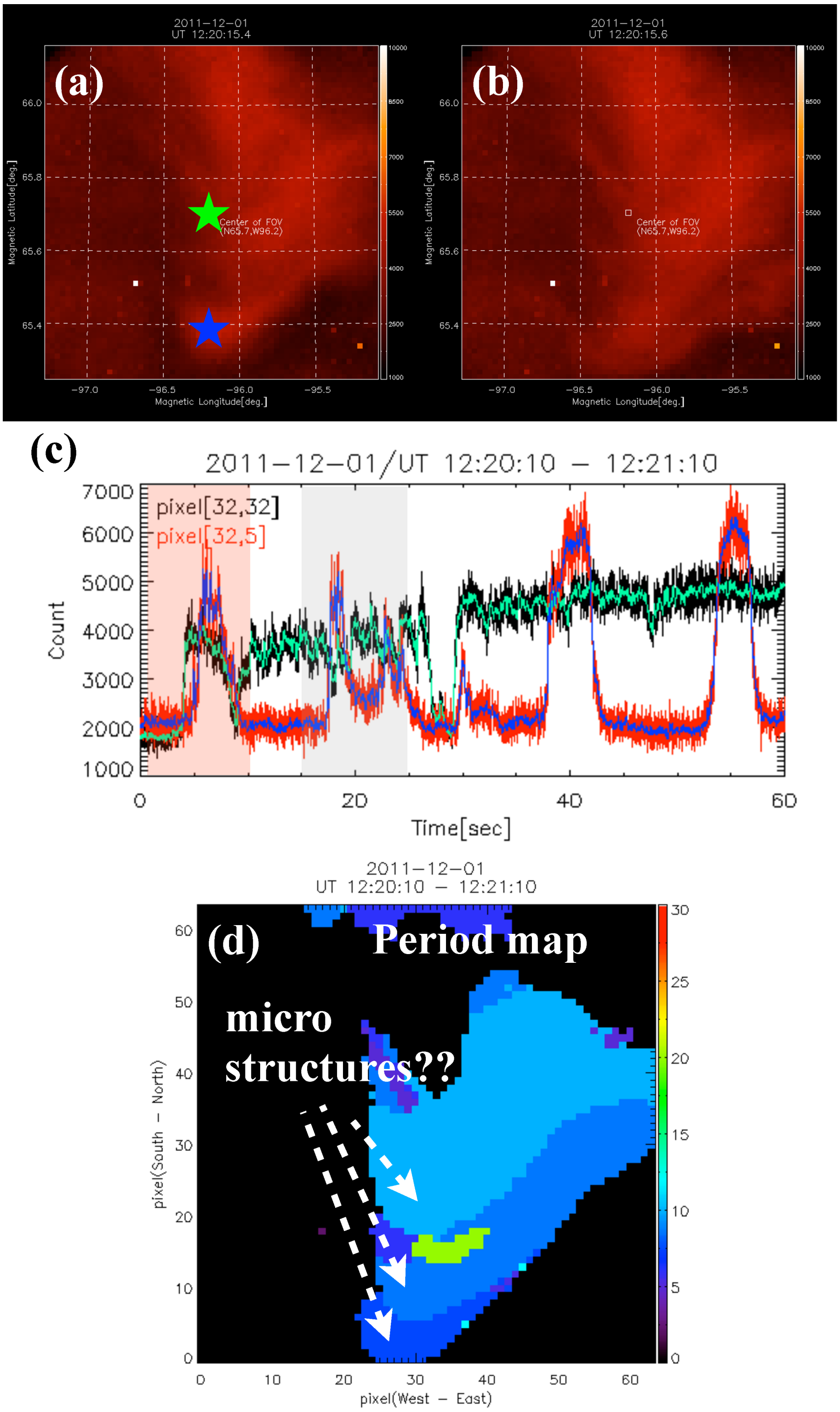

Figure 3.31: (a) and (b) Examples of the EMCCD camera image data at 12:20:15.4 UT and at 12:20:15.6 UT in the same format as Figure 3.30. (c) Temporal variations of auroral intensity on the two pixel, indicated with stars in light green and blue in Figure 3.31. (d) Spatial distribution of dominant periods estimated with the FFT analysis with a color scale for the period ranges of 0-30 seconds.

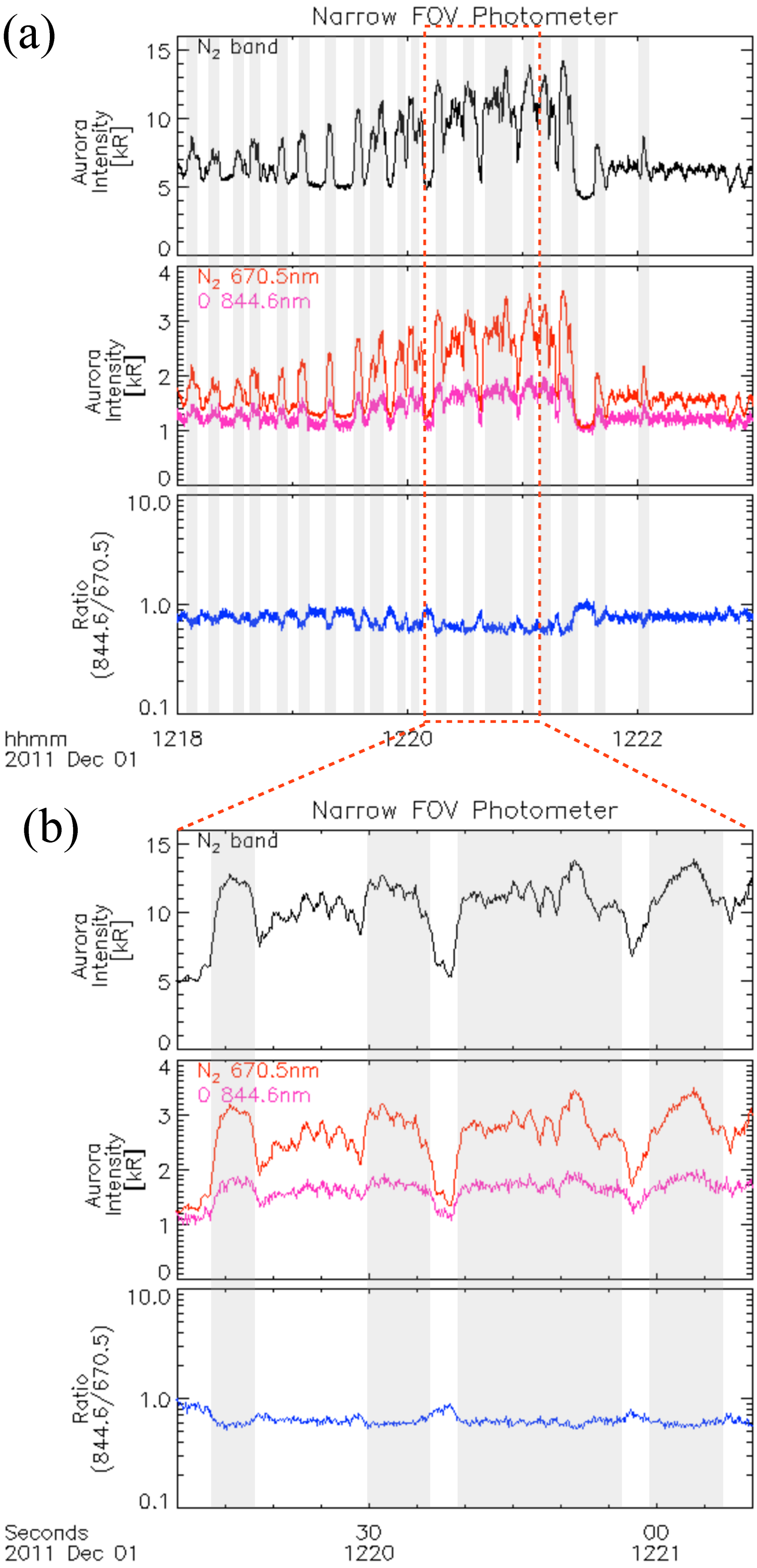

Figure 3.32: (a) Temporal variations of auroral intensities for N_2 1st positive band (650-700 nm), N_2 emission line at 670.5 nm, and O emission line at 844.6 nm, and the ratio between intensities of the N_2 emission line and the O emission line during the period from 12:18:00 UT to 12:23:00 UT. The periods shaded in gray represent the “switch-on” phase of pulsations. (b) The same plots as (a) but during the period from 12:20:10 UT to 12:21:10 UT.

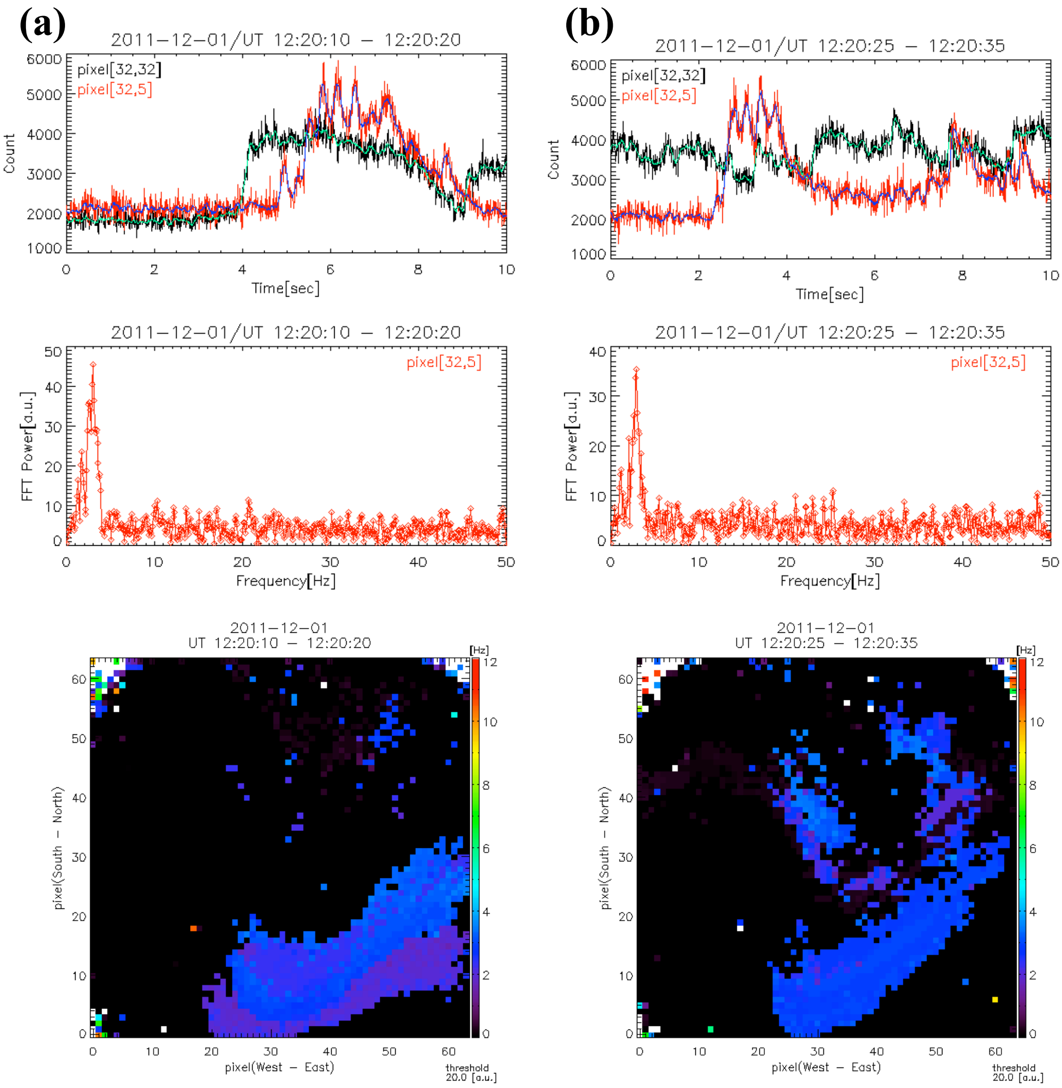

Figure 3.33: (Top) Auroral intensity variations at two selected pixels as a function of time (a) from 12:20:10 UT to 12:20:20 UT, and (b) from 12:20:25 UT to 12:20:35 UT in the same format of Figure 3.14. (Middle) F-t spectrum for the same periods (a) and (b), exhibiting the peak power frequencies of 3.0 and 2.9 Hz, respectively. (Bottom) Spatial distributions of the peak frequency for the rapid variations on each pixel with a color scale from 0 to 12 Hz. Pixels where peak power is less than 20.0 [a.u.] are not plotted.

Since the FFT analysis needs data with enough long finite time window ($\sim$ 10 seconds, in our cases) to detect a peak frequency, it is difficult to understand the temporal evolution of the sub-structure with about 3.0 Hz modulations. Thus, we performed principal component analysis, which is well-known in meteorology and oceanography, to try to pick coherent structures and temporal variations of them out image data during specific periods. The principle of this analysis is shown here. We assume $\mathbf{W}$, a matrix with P-column and N-row ($P \leq N$) written as

$$\mathbf{W} = \begin{pmatrix} a_{11} & \cdots & a_{1P} \\ \cdot & \cdots & \cdot \\ \cdot & \cdots & \cdot \\ a_{N1} & \cdots & a_{NP} \end{pmatrix} \tag{3.6}$$

Here, P is the number of the data point such as the number of pixels, and N is the number of the time series data for time duration of observation.“*Covariance matrix*” for“$\mathbf{W}$” can be calculated as follows

$$\mathbf{V} = \frac{1}{N}{}^t\mathbf{W}\mathbf{W} = \begin{pmatrix} \sigma_{11} & \cdots & \sigma_{1P} \\ \cdot & \cdots & \cdot \\ \cdot & \cdots & \cdot \\ \sigma_{N1} & \cdots & \sigma_{NP} \end{pmatrix} \tag{3.7}$$

Next, we conduct“Eigenvalue decomposition” for “$\mathbf{V}$” written as $\mathbf{VX} = \mathbf{X}\Lambda$, where

$$\mathbf{X} \;=\; \begin{pmatrix} x_{11} & \cdots & x_{1P} \\ \cdot & \cdots & \cdot \\ \cdot & \cdots & \cdot \\ x_{P1} & \cdots & x_{PP} \end{pmatrix} \tag{3.8}$$

$$\Lambda \;=\; \begin{pmatrix} \lambda_{11} & 0 & \cdots & 0 \\ 0 & \lambda_{22} & \cdots & \cdot \\ \cdot & \cdots & \ddots & 0 \\ 0 & \cdots & 0 & \lambda_{PP} \end{pmatrix} \tag{3.9}$$

$\mathbf{X}$ is the matrix composed of P-plex eigenvectors, and the eigenvector, $\vec{X_k}$, has the eigenvalue of λ_{kk} ($\lambda_{11} > \lambda_{22} > \cdots > \lambda_{PP}$). $\vec{X_k}$ shows the spatial structure in two-dimensional plane defined by P-plex elements. Percentage of explained variance for $\vec{X_k}$ can be derived as $\lambda_{kk}/\sum_{k=1}^{P}\lambda_{kk}$, and it represents how much dominant in matrix $\mathbf{W}$ the spatial structure defined by each eigenvector is. Additionally, time coefficients $\vec{T_k}$ can be obtained from projecting eigenvector $\vec{X_k}$ onto $\mathbf{W}$.

$$\vec{T_k} = \begin{pmatrix} t_{1k} \\ t_{2k} \\ \vdots \\ t_{Nk} \end{pmatrix} = \mathbf{W} \begin{pmatrix} x_{1k} \\ x_{2k} \\ \vdots \\ x_{Pk} \end{pmatrix} = \mathbf{W}\vec{X_k} \tag{3.10}$$

The time coefficients $\vec{T_k}$ is composed of N-plex elements corresponding to the time axis of data, and it represent similarity between the spatial pattern of $\vec{X_k}$ and a snapshot of $\mathbf{W}$ at a specific time. Using the equation 3.10, we also obtain the relationship among $\mathbf{W}$, $\vec{X_k}$, and $\vec{T_k}$ as follows

$$\mathbf{W} = \sum_{k=1}^{P} \vec{T_k} \cdot {}^t\vec{X_k} \tag{3.11}$$

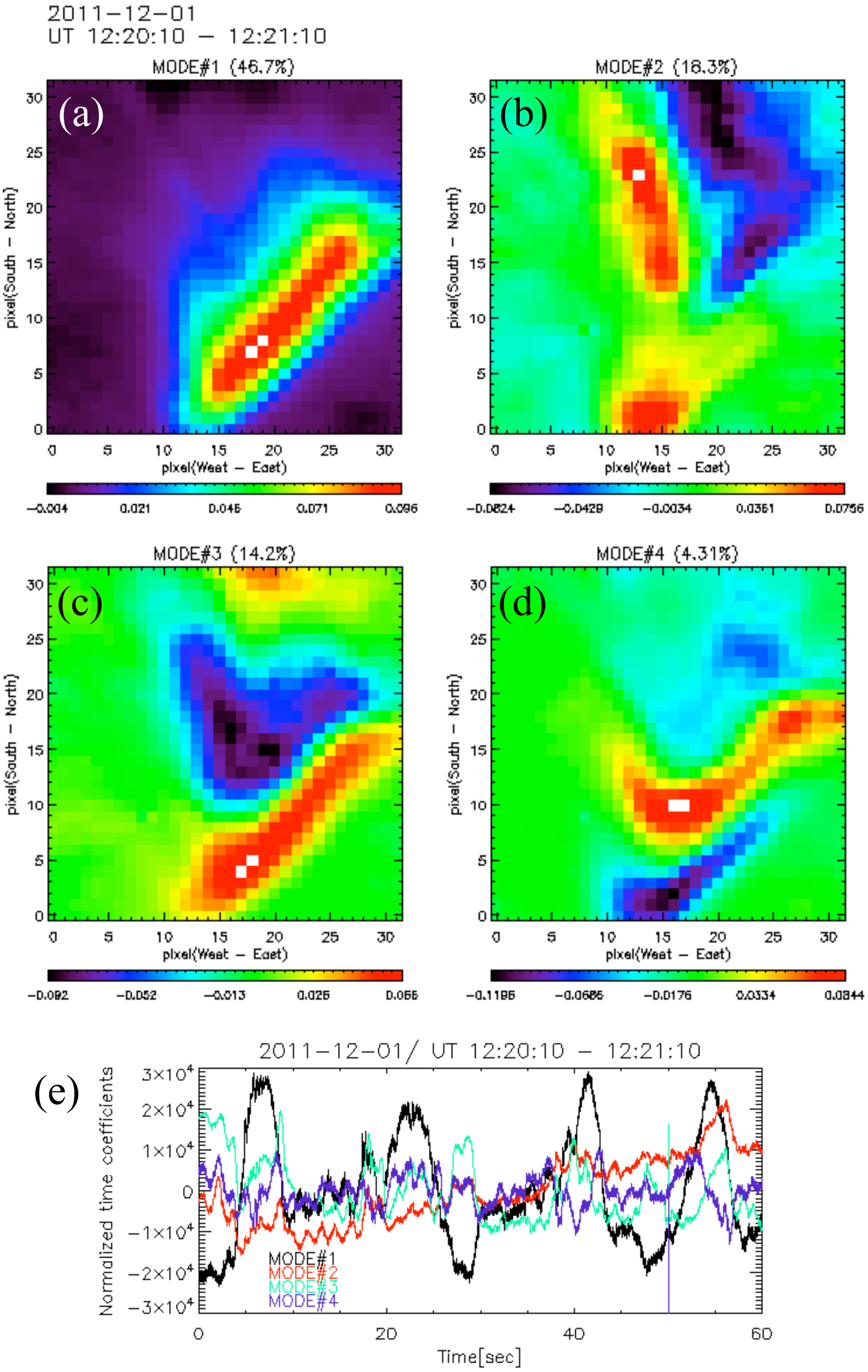

Figure 3.34: (a)-(d) Spatial distributions for most dominant four modes. Color scales show the deviations from the mean counts for each bin during this period. (e) Temporal variations of time coefficients for each mode obtained from the principal component analysis for the EMCCD data between 12:20:10 UT and 12:21:10 UT.

The equation 3.11 simply shows that two-dimensional data as a function of time can be expressed by the sum of the product of each eigenvector and each time coefficient, corresponding to spatial structures and temporal variations of them.

Figure 3.34 shows spatial structures for dominant four modes and the temporal variations of time coefficients for each mode obtained from the principal component analysis for the EMCCD data between 12:20:10 UT and 12:21:10 UT. The image data used in Figures

3.34 (a-d) were re-bined with 2 × 2 pixels to simplify the calculation. It should be noted that color scale indicates the deviations from the mean counts for each bin during this period. Percentage of explained variances for four dominant modes were 46.7%, 18.3%, 14.2% and 4.31%, respectively. While the structure shown in Figure 3.34 (a) is quite similar to the whole patch structure, the structures of Figure 3.34 (b-d) demonstrate that the whole structure consists of sub-structures. This result is consistent with that of the FFT analysis as shown in 3.33. Figure 3.34 (e) is the normalized time coefficients as a function of time for the dominant four mode. A black line represents the time coefficient for mode 1, which shows the temporal variation with a large amplitude and large time scale of ∼ 10 seconds. It strongly suggests that mode 1 agrees well with large-scale pulsation concerning not only on the spatial distribution but also on the temporal characteristics. The coefficients for modes 2-4 indicate the characteristics of the sub-structures, which show spiky signatures with small amplitudes compared with those for mode 1. Therefore, we conclude that the spatial and temporal characteristics of the PA can be distinguished by the principal component analysis. However, this analysis cannot well resolve movements of structures like propagation, since it assumes that spatially stable structures only constitute original data: in general, a propagation of structures appears as structures of two modes with the almost same percentages of explained variance. Thus, the structures for the mode 2-4 are probably be regarded as one group with the total percentages of the explained variances of 36.8%. Since the sum of percentages were almost comparable to that of mode 1, the contribution of mode 2-4 for the total variances is not negligible, however, the spatial and temporal characteristics of mode 2-4 are totally different with those of mode 1. In addition, the spatial structures defined by each mode should be independent of each other both spatially and temporally as shown in Figure 3.34. It implies that the whole structure with on-off pulsations and sub-structures with rapid variations can be generated by different processes or different effects of a process.

We summarize the cross-scale properties of the PA in this event as follows. This pulsating patch clearly exhibited temporal variations to be categorized into two types: a large-scale on-off pulsation (7.8-10 seconds) and internal modulations excited in on-phase with a frequency of about 3.0 Hz. Additionally, the enhancements of such modulations were seen in the sub-structures rather than in the whole patch. The principal component analysis revealed that the patch structure was switched to the sub-structures in a few times as shown in Figure 3.34 (e). In other words, the sub-structures did not continue to exist but seemed to appear spontaneously. However, the sum of percentages of explained variances of sub-structures was almost comparable to that of the whole patch structure, which means the contributions of both patch and sub-structures to total temporal variances were also comparable.

Table 3.4: Cross-scale properties of the PA obtained from the FFT analysis and the principal component analysis for the case on December 1st, 2011

	patch structure	sub-structure
temporal variations	7.8-10 seconds	about 3.0 Hz
waveforms	on-off pulsation	spiky modulation
mode	1	2-4
percentage of explained variance	46.7%	36.8%
typical spatial scale	1450 km[1]	782 km[1]
minimum scale	—	414 km[1]
motions	southward propagation	back and forth

Table 3.4 summarize the typical spatial scale estimated with the principal component analysis. Figure 3.35 shows the distribution histograms as a function of variance for the

---

[1] At the magnetic equator.

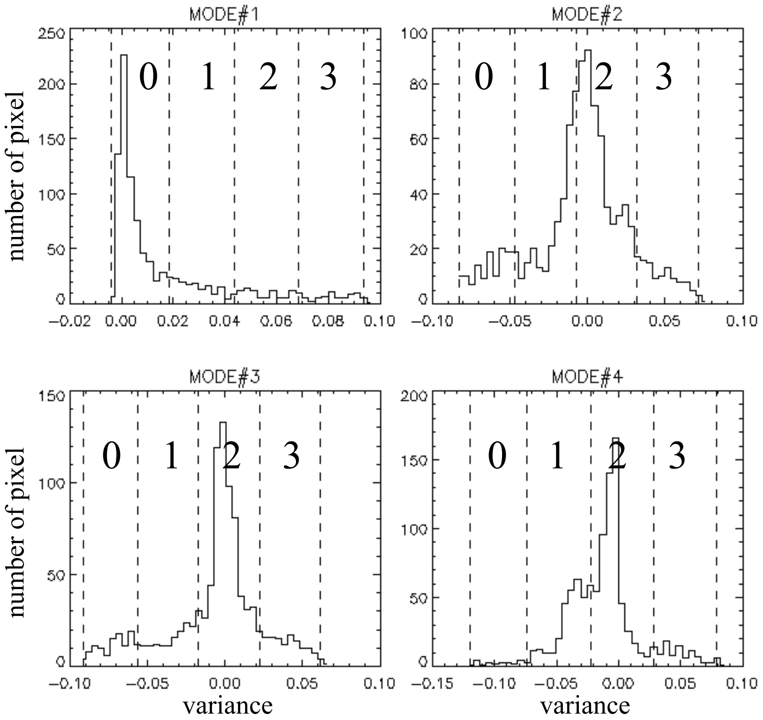

Figure 3.35: Histograms of the variances for spatial structures of modes 1-4, and these histograms can be categorized into four groups separated by vertical black dashed lines.

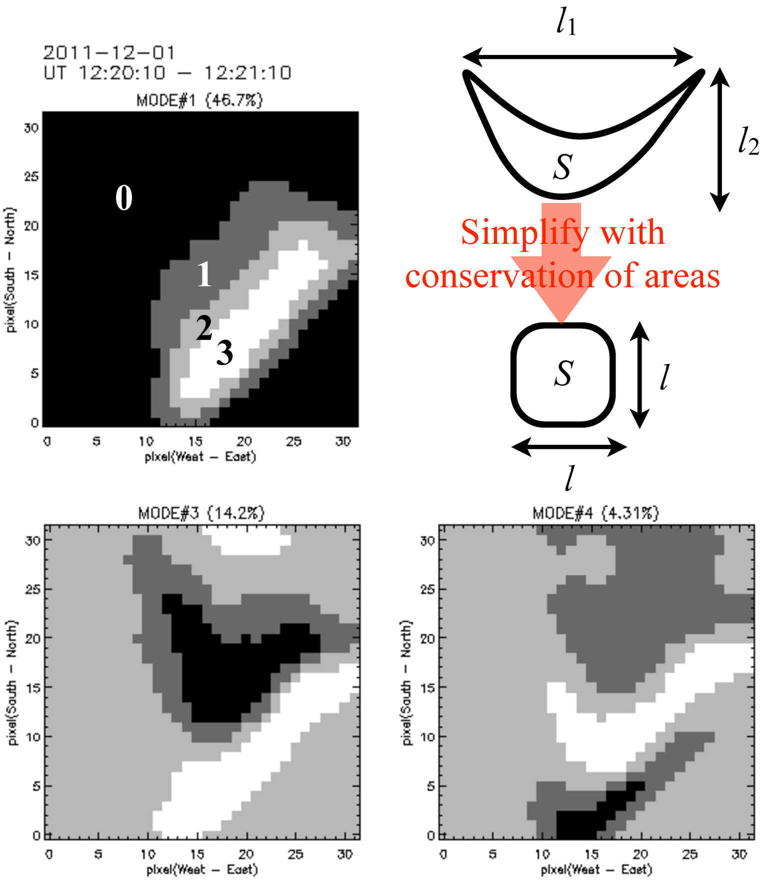

Figure 3.36: Quadnary images for mode 1, 3 and 4 obtained from the histograms in Figure 3.35 . A schematic illustration shows the estimation of typical length of structure (the detail is described in the context).

spatial structures in mode 1-4, and after several test analyses it was found that these histograms can be categorized into four groups separated by vertical black dashed lines. Based on the four groups, the variance maps in Figure 3.34 are converted into "quadnary" images (Figure 3.36). We can estimate the area of structure with counting the number of pixels that constitute the structure of interest in the quadnary images. It should be noted that the typical spatial scale is simply the root of the area. The minimum spatial scale or the width of the structures in a horizontal plane is also important information when one considers whichever effect, MHD or kinetic, maintains the structures [*Ebihara et al.*, 2010]. The minimum width of sub-structures was estimated to be about 410 km at the magnetic equator in this event, which suggests the sub-structures were mainly maintained by MHD forces because the local proton gyro radius[1] was $\approx$ 100 km. However, we cannot exclude that kinetic effects, such as ion finite Larmor radius effects, may contribute to form these complicated sub-structures because the minimum scale is close to local proton gyro radius [*Hiraki and Sakaguchi*, 2010]. It may be related to the kinetic effect that the sub-structures showed back and forth motions like a pendulum inside the patch. On the other hand, the whole patch structure gradually moved southward i.e., earthward in the magnetosphere, and it is consistent with the global convection pattern around the midnight MLT sector. Since it was suggested that PA in the early recovery phase can be related to Fermi-type accelerations at the dipolarization front [*Nakajima et al.*, 2011], the characteristics such as the on-off pulsation and the patch structure seen in our observation data may result from the generation process associated with Fermi-type accelerations. In-situ data by satellites is quite useful to evaluate the generation process in the source region. However, THEMIS spacecrafts (probe A, D and E) were unfortunately located around noon during this period, and no in-situ observational evidence supporting this scenario has been found yet. In future study, we should investigate the generation process of sub-structures of PA based on observation data in detail to understand why rapid modulations are excited only in the sub-structures.

3.2.4 Statistical analysis

In Section 3.2.3, we presented the cross-scale properties of the PA observed on December 1st, 2011. Such properties of PAs have been hardly reported in previous studies, and therefore, a statistical study on the properties is quite valuable to understand the generation mechanisms and basic plasma processes. We carried out multiple events study using the dataset obtained from our ground-based observations with the analysis methods described in Sections 3.2.2 and 3.2.3. First, a typical case study used for statistics is shown as an example. Figure 3.37 is the time-shifted solar wind parameters, geomagnetic fluctuations as a function of time on February 19th, 2012. Dst index reached down to about -60 nT at 04:00 UT and gradually increased afterward, and therefore this day corresponded to the recovery phase at a magnetic storm. IMF Bz component fluctuated considerably until 08:00 UT, and the disturbances was in AE index and geomagnetic variations are clearly seen during this period. After 08:00 UT, IMF Bz mostly varied around zero nT, and the geomagnetic activities relatively decreased. An isolated substorm suddenly occurred around 12:00 UT and AE index increased rapidly to 500 nT. During this period shaded by red, we observed active aurora associated with the substorm by our ground-based instruments, and typical PAs appeared 3 hours after the substorm onset as indicated by a red broken line.

Figure 3.38 shows a summary plot of the data analysis on the PA event occurred around 14:56 UT. Figure 3.38 (a) and (b) show temporal variations of auroral intensity from 14:56:00 UT to 14:57:00 UT and from 14:56:30 UT to 14:56:40 UT, respectively. Similar to the case study given in the previous section, we identify the rapid modulations

---

[1] The energy of proton is assumed to be 10 keV.

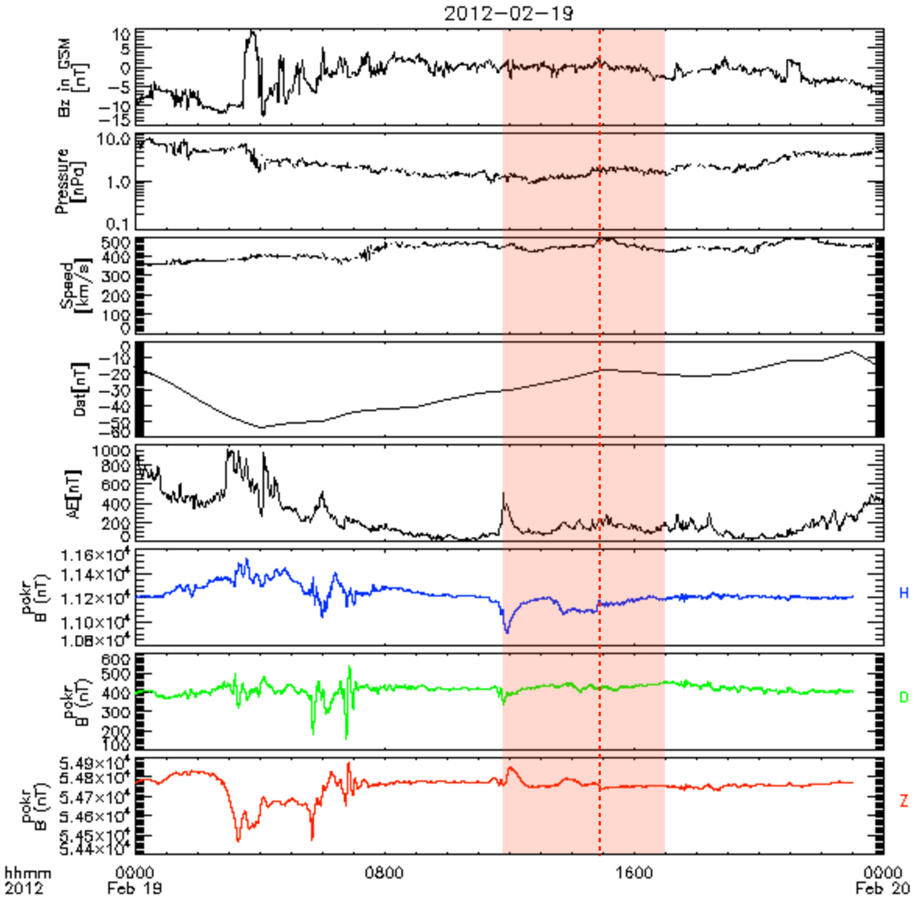

Figure 3.37: Time-shifted solar wind and IMF parameters (IMF Bz, Dynamic pressure, and Solar wind velocity) and geomagnetic fluctuations (*Dst*, *AE*, Geomagnetic field H, D, and Z components) as a function of time on February 19th, 2012.

involved with large scale pulsation during on-phase in Figure 3.38 (b). Figure 3.38 (c) is a F-t spectrum obtained from the FFT analysis on the temporal variations of the data indicated by the red line in Figure 3.38 (b), and it shows maximum of modulation power at a frequency of 1.8 Hz. Figure 3.38 (d) and (e) are variance maps for the mode 1 and 2 obtained from the principal component analysis on the data from 14:56:00 UT to 14:57:00 UT. Typical spatial scales of the main structure and sub-structure seen in mode 1 and 2 are estimated to be 2000 and 900 km. Figure 3.38 (f) is a period map that shows the on-off pulsation periods plotted onto each pixel with a color scale ranges from 0 to 30 seconds. The auroral patch structure which is seen on the left, had the period ranges from 5.0 to 7.8 seconds. Finally, Figure 3.38 (g) is a frequency map that shows the modulation frequency plotted onto each pixel with a color scale ranges 0 to 6 Hz, which demonstrates that 2.0 Hz variation was dominant during this period. It is also noted that the variance maps for the modes 1 and 2 are well agreed with the pulsating period and the modulation maps, respectively. This PA differs from the two events described in the previous sections in that it appeared in the late recovery phase of substorm. Our all-sky camera data demonstrates that a cluster of patch, including the patch in Figure 3.38, were moving eastward drift with developing their complicated structures. PFISR also conducted continuous observations[1] with 4 radar pulses during this period. The data shows that enhancement of electron density in the ionospheric D and E regions at the altitude range of 80-150 km around 15:00 UT, which suggests electron precipitation with energy larger than 10 keV occurred

---

[1] IPY17 - Long duration measurements in support of the International Polar Year, from 2012-02-19 07:53:33 to 2012-03-03 06:00:05

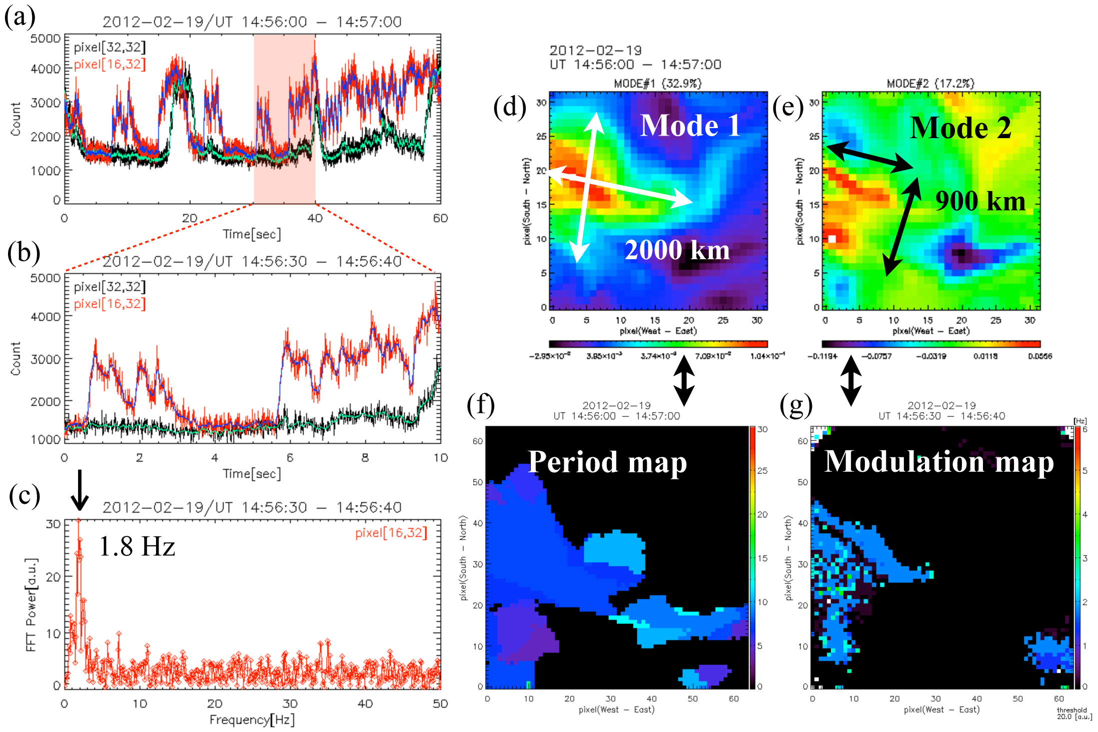

Figure 3.38: (a) and (b) Temporal variations of auroral intensity obtained form the EMCCD camera from 14:56:00 UT to 14:57:00 UT and from 14:56:30 UT to 14:56:40 UT on February 19th, 2012. (c) F-t spectrum obtained from the FFT analysis on the data indicated by the red line in (b) It is evident that a dominant peak is seen at 1.8 Hz. (d) and (e) Variance maps for the mode 1 and 2 obtained from the principal component analysis on the the data from 14:56:00 UT to 14:57:00 UT. See text for the detail. (f) Period map that shows the long-term on-off period plotted with a color scale ranges from 0 to 30 seconds. The map is obtained from the data between 14:56:00 UT and 14:57:00 UT. (g) Frequency map that shows the dominant modulation frequency on each pixel with a color scale ranges from0 to 6 Hz. The map is obtained from the data between 14:56:30 UT and 14:56:40 UT.

during this period. The plasma drift velocity measured with PFISR ranged 300 to 600 m/s mostly in the eastward direction, which is consistent with the auroral drift motion seen in our all-sky image data.

We statistically stored the cross-scale properties of PA using long-term and continuous observations, not depending on whether they appeared in the early recovery phase or the late recovery phase of substorm. From 10-minutes observation data taken with the EMCCD camera, we estimated the cross-scale property. The aurora that exhibited clearly the cross-scale property was counted as one PA. This is because 10 minutes data can be thought be enough to identify individual patch passing through or disappearing in the FOV of the EMCCD camera. The specific purposes of statistical analysis on the cross-scale property are summarized as follows:

- To obtain the typical spatial and temporal scales of sub-structures and rapid modulations,
- To understand the temporal evolutions for a few hour focusing on the characteristics of individual patch.
- To investigate the relationship among the parameters of cross-scale properties for PA,

Since there is a few observational report focusing on small-scale and rapid variations (faster than 1 second), it should be necessary to estimate their typical scales. In addition to the cross-scale properties, we suggest that it is worth investigating when a PA appears and how long it varies associated with a substorm. It has been well understood that the morphology of PAs is drastically changed depending on a substorm phase [e.g., *Røyrvik and Davis*, 1977], and therefore we expect meso-small scale structures and rapid variations also have substorm dependence. Furthermore, it is interesting to investigate the relationship among the properties of PAs, such as on-off periods and modulation frequencies, and so on. Although *Samara and Michell.* [2010] reported such relationship on a case study, we discuss the detailed relationship in statistics. Here, the PA events used for statistical analysis are listed in Table 3.5. A total number of the PAs were 53. $^{\mathrm{first}}$hh:mm and $^{\mathrm{last}}$hh:mm were determined when first and last PAs appeared during a period of auroral activity related to the substorm in the right column. The substorm onset was defined when an aurora breakup and sudden negative excursion of geomagnetic variations in H-component simultaneously happened at PFRR. As Table 3.5 shows, the substorm onset sometimes occurred in a few times on the same day, and the magnitudes of *AE* indices widely ranged 100 to 1000 nT. A weak correlation was seen between *AE* index and the number of PAs events with a correlation coefficient of 0.33.

Table 3.5: Dataset used for the statistical analysis in this study. Individual PA and substorm event was identified using the data obtained from the EMCCD camera, the all-sky camera, and the magnetometer. $^{\mathrm{first}}$hh:mm and $^{\mathrm{last}}$hh:mm are determined when the first and last PAs appeared in the FOV of the EMCCD camera during a auroral activities period related to the substorm in the right column. The substorm onset was defined when an aurora breakup and sudden negative excursion of geomagnetic variations in H-component simultaneously happened at PFRR.

YYYY-MM-DD	$^{\mathrm{first}}$hh:mm - $^{\mathrm{last}}$hh:mm	# samples	related substorm (*AE* index)
2011-12-01	12:20	1	12:00 (350 nT)
2012-01-01	13:24	1	12:10 (230 nT)
2012-01-03	15:03	1	13:20 (400 nT)
2012-01-16	14:08	1	11:50 (800 nT)
2012-01-16	16:50	1	14:20 (400 nT)
2012-01-17	14:27 - 15:06	4	12:30 (100 nT)
2012-01-20	14:05	1	12:00 (100 nT)
2012-01-21	11:50 - 12:50	3	11:50 (1000 nT)
2012-01-22	15:51	1	12:00 (700 nT)
2012-01-29	11:45	1	10:30 (100 nT)
2012-02-13	12:55 - 13:37	3	12:45 (550 nT)
2012-02-15	15:22	1	14:50 (700 nT)
2012-02-19	14:56 - 15:40	6	11:50 (500 nT)
2012-02-20	09:19 - 09:29	2	08:10 (800 nT)
2012-02-20	11:14 - 12:15	4	10:40 (500 nT)
2012-02-20	14:21 - 15:41	4	13:30 (550 nT)
2012-03-01	09:45 - 12:01	12	09:10 (100 nT)
2012-03-01	12:38 - 15:23	7	12:30 (500 nT)

Figure 3.39 shows four histograms for the cross-scale properties in the observed PAs: (a) frequencies of modulation, (b) on-off periods, (c) spatial length of large-scales of patchy or band structure, and (d) spatial length of small-scales sub-structure. The Frequency range of the observed modulations were from 1.5 to 3.3 Hz, and it is almost consistent with well-known 3±1 Hz modulations [*Røyrvik and Davis*, 1977]. The frequency of modulations was slightly concentrated in the range between 2.0 and 2.5 Hz, however, the distributions seems to be almost flat. It should be noted that the frequency of modulations was quite stable in each auroral event through the observations in most cases as shown in Figure

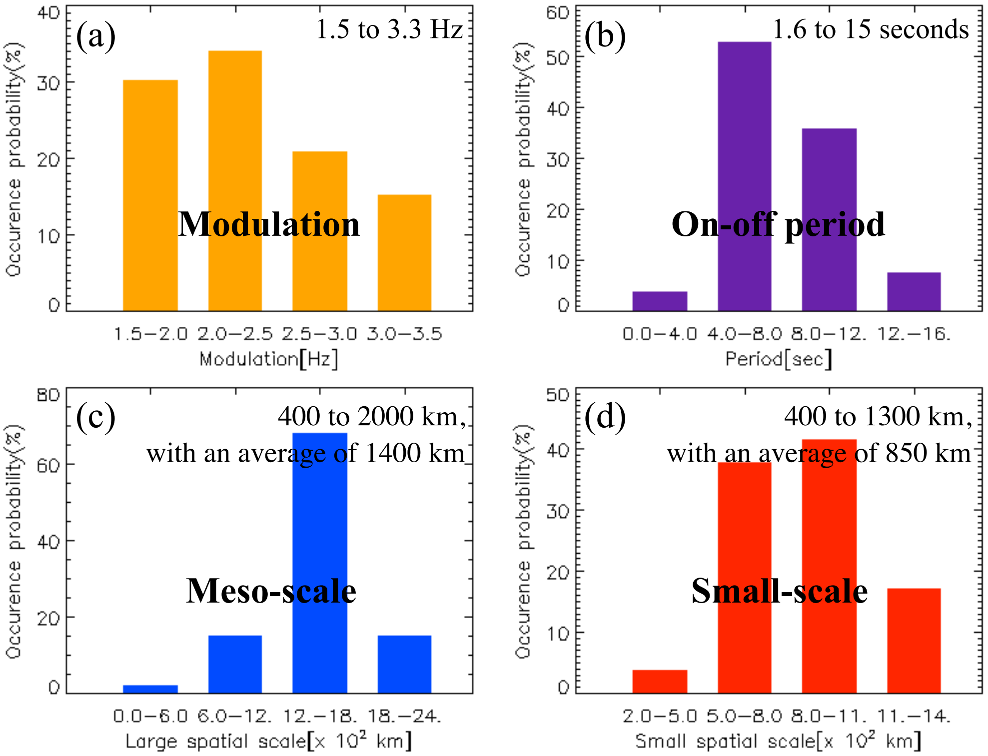

Figure 3.39: Four histograms for cross-scale properties of observed PAs: (a) frequencies of modulation, (b) on-off periods, (c) large spatial scales of patchy or band structures, and (d) small scales of sub-structures.

3.33 showed. The observed on-off periods ranged from 1.6 to 15 seconds, and the PAs with the period shorter than 10 seconds accounted for 72% of the total. Spatial length of large-scales whole structures ranged from 400 to 2000 km[1], with an average of km. On the other hand, the spatial length of small-scales sub-structures were estimated to be from 400 to 1300 km, with an average scale of 850 km. In addition, the ratio of the large spatial to the small spatial scale of each PA ranged from 1.0 to 3.6. Its average of the ratio was 1.7, which means the area of the sub-structure was typically one-third of the area of the whole structure. The sub-structures inside a whole structure were not clearly identified in only four cases, in which the spatial lengths of whole structures were estimated to be 400, 720, 730, and 1200 km. These lengths are relatively small compared with a typical lengths of the large scales, and they are included in the bottom of 19% of total.

Next, we investigated the temporal variations of cross-scale properties. Figure 3.40 (a) and (b) show the relationships between the cross-scale properties (modulation frequency, spatial length of large-scale and small-scale structures) and the time lags from the onset timings of related substorm. Figure 3.40 (c) and (d) also show the UT dependence on the cross-scale properties. The frequency of modulation slightly correlated to the time lag with a correlation coefficient of -0.32, however, there was no clear correlation between the modulation frequency and UT (C.C. = -0.18). Therefore, the modulations of PAs seem to depend on the time lags, i.e., the substorm phases, although the dependence is likely to be low. On the other hand, there was no clear relationship between both large-scale and small-scale structures and the time lag or UT. Additionally, the on-off period also seemed to have no evident dependence with the coefficient of -0.04 and -0.14.

Finally, Figure 3.41 shows the relationship between among the cross-scale properties and auroral intensity. Since the auroral intensity plays a role of good proxy for downward energy flux of electrons, it is possible to directly compare the spatial and temporal proper-

---

[1] The FOV of the EMCCD camera corresponds to 2500 km at the magnetic equator.

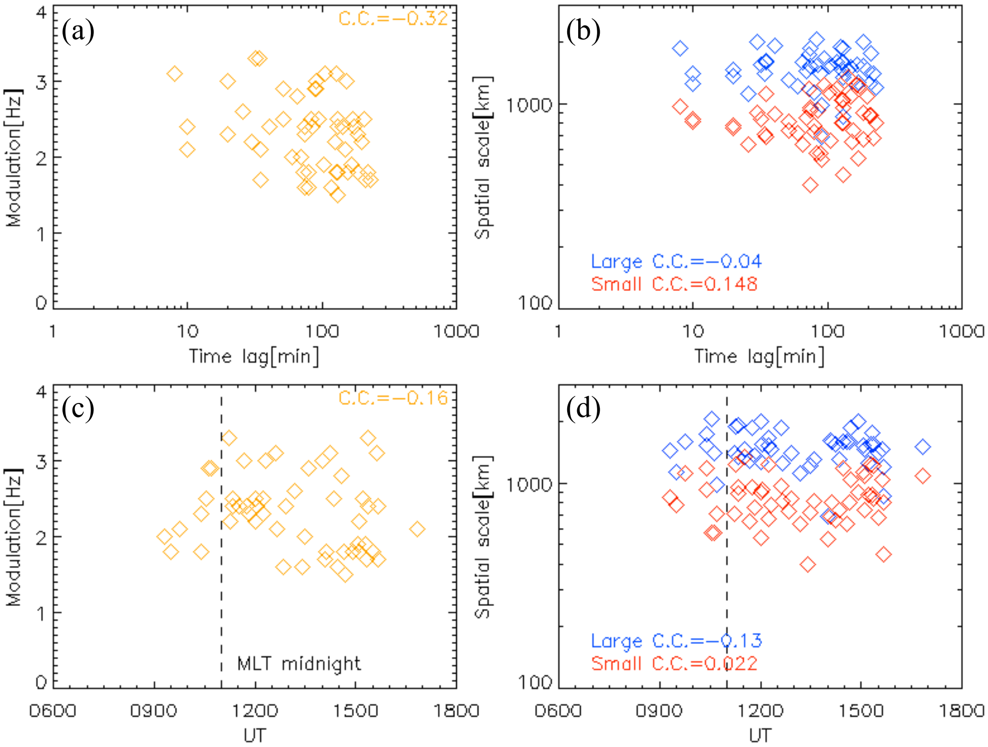

Figure 3.40: (a) and (b) Relationships between the cross-scale properties (modulation frequency, spatial length of large-scale and small-scale structures) and the time lags from the onset timings of related substorm. (c) and (d) UT dependence on the cross-scale properties.

ties with the precipitating electron energy on individual PA. Figure 3.41 (a) and (b) shows the dependence of the frequencies of modulation and the on-off periods to the aurora intensity. The correlation coefficient between the frequency of modulation and the auroral intensity is 0.52, suggesting relatively strong positive correlation, while the modulation frequency had large variances when the aurora intensity increased. On the other hand, the correlation coefficient between the on-off period and the aurora intensity was almost 0. Figure 3.41 (c) and (d) are the scatter plots of the frequencies of modulation and the on-off periods versus the spatial lengths. It was reported that the frequency of the pulsations correlates to the intensity of the aurora, with brighter aurora containing higher frequencies [*Samara and Michell.* 2010]. Our statistical result agreed well with that in *Samara and Michell.* [2010], however, the on-off pulsations periods did not correlate to auroral intensities. It was also previously mentioned that the scale size of the structures relates to the frequency of the pulsations, with the smaller structures occurring with higher frequency pulsations [*Samara and Michell*, 2010]. In our result, we find that the small-spatial scale sub-structures had a slight negative correlation with the on-off pulsation period with the coefficient of -0.16 (in Figure 3.41 (d)) and the modulation frequency with the coefficient of -0.19 (in Figure 3.41 (c)). Interestingly, large-scale spatial structure had no correlation with temporal variations of the on-off periods and the modulation frequencies, which suggests that spatial scale of sub-structures may be related to temporal variations of PAs rather than that of a whole patch. In addition, we found the weak correlation between the modulation frequency and the on-off period with the coefficient of 0.18 (not shown in Figure 3.41).

Discussion

Here, the results based on statistical analysis are discussed in detail. We successfully detected the rapid variations of PAs (∼ 3 Hz) using the ground-based EMCCD camera

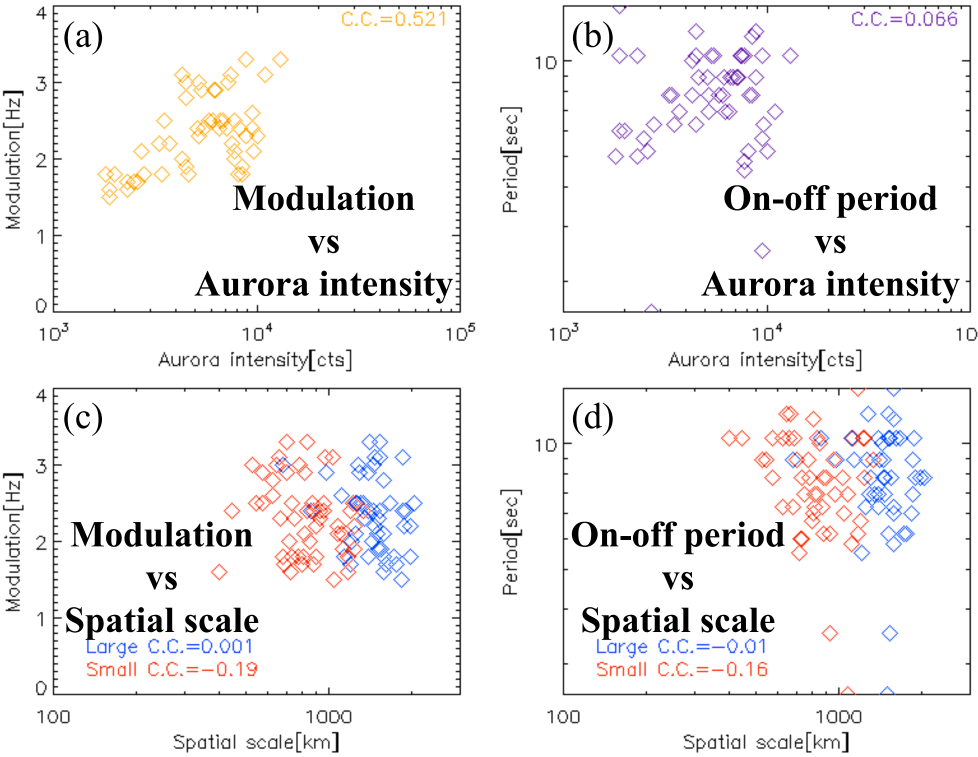

Figure 3.41: (a) and (b) Scatter plots of the frequencies of modulation, and the on-off periods versus the aurora intensities. (c) and (d) Same as (a) and (b) but for spatial lengths of large-scale and small-scale structures.

with a high-sampling rate of 100 Hz, and showed the statistical characteristics of these rapid variations for the first time, to author's knowledge. It demonstrates that frequency of modulations ranged from 1.5 to 3.3 Hz and they were slightly concentrated on the frequency range between 2.0 and 2.5 Hz. These observational facts are almost consistent with 3 ± 1 Hz modulations reported by ground-based measurements [*Røyrvik and Davis*, 1977; *Samara and Michell*, 2010] and by in-situ measurements at low-altitudes [e.g., *Bryant et al.*, 1971; *Sandahl et al.*, [1980]; *Sato et al.*, 2004]. However, in-situ measurement data of whistler mode chorus at the magnetic equator demonstrated that the repetition periods of chorus elements, which is associated with the frequency of modulations shows a wide frequency range. Figure 3.42 shows distribution of time intervals between chorus elements as seen by Cluster [*Trakthengerts et al.*, 2004]. Probability density of time interval between the chorus elements increase with shorter intervals, and its distribution can be fitted with a power-law function as indicated by a black solid line. This result implies that the modulations of downward electron flux with higher frequency at a few tens of Hz can occur, and therefore, by definition, such more rapid variations can be expected to measure with enough temporal resolutions. Actually, *Samara and Michell.* [2010] suggested that the temporal variations existed in the frequency range up to 15 Hz although they were not obtained with a sufficient signal-to-noise ratio. *Kataoka et al.* [2012] recently found out very rapid fluctuations of 20-30 msec superimposed on pulsations beyond the ULF range by a high-speed camera with a temporal resolution of 500 frames per second. In their work two hypotheses based on wave-particle interactions at the equator and fast modulations in the magnetosphere-ionosphere coupled region were suggested and discussed. However, the hypotheses still remain an open question. Although any strong modulations in the frequency range higher than about 3 Hz were not identified in our study, we consider the TOF effect that is plausible to explain th reason why strong modulations with frequency higher than 3 Hz are difficult to be detect. Figure 3.43 shows the numerical simulation for

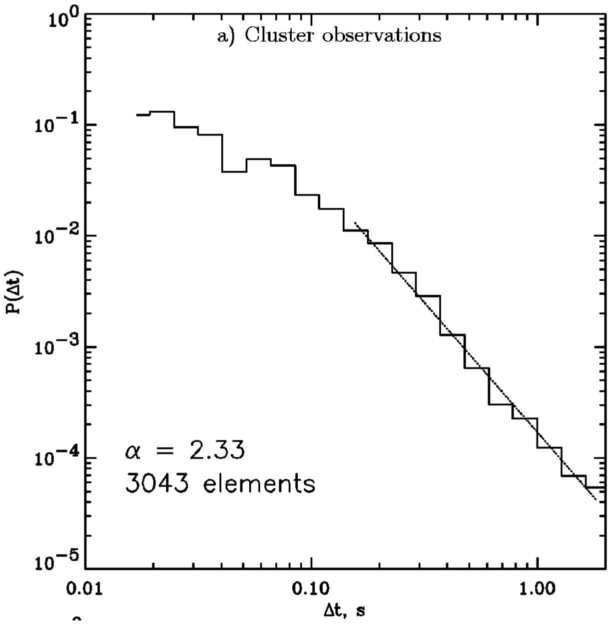

Figure 3.42: Distribution of time intervals between chorus elements as seen by Cluster. On-off intermittency manifests itself by the power-law behavior of the distribution, $P \propto (\Delta t)^{-\alpha}$ [*Trakthengerts et al.*, 2004]

micro-burst type precipitations [*Saito et al.*, 2012]. Top panels in Figure 3.43 show simplified model of whistler mode chorus elements at the magnetic equator with time intervals of 3 and 10 Hz inputted into their calculations. Middle panels in Figure 3.43 demonstrate the count rates of 1 MeV precipitation resulting from the cyclotron resonance with chorus elements propagating along a field line, which is agreed well with modulated pulsation observed with our EMCCD camera. While the count rate of precipitating electrons for 3-Hz chorus elements exhibits spiky modulations clearly, we cannot identify no strong modulations in the case for 10 Hz intervals due to the TOF effect discussed in the Chap-

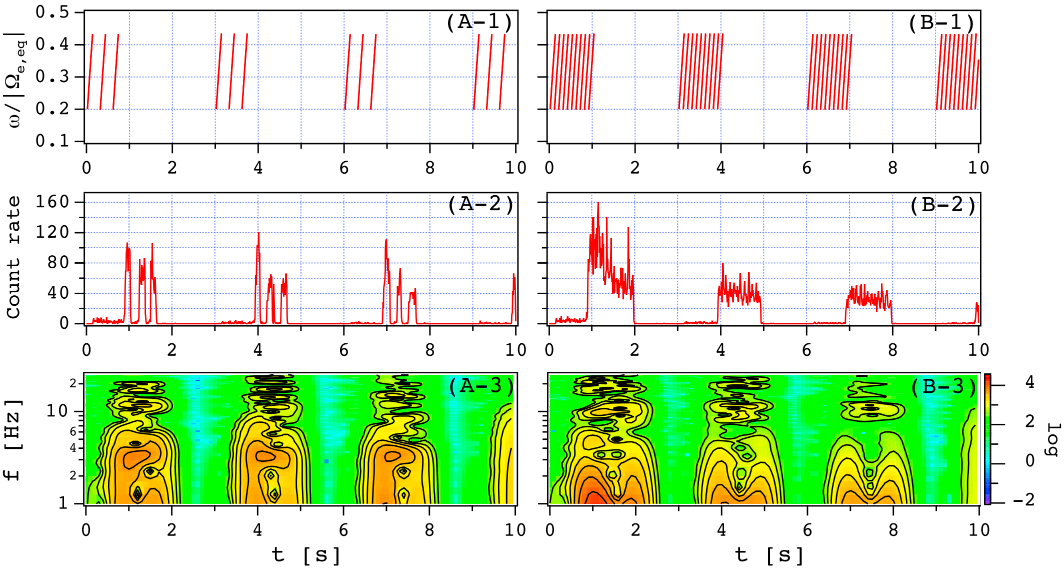

Figure 3.43: (top) Frequency spectra of applied whistler chorus at the equator (labeled by 1), (middle) count rates of precipitated 1 MeV electrons per 10 msec (labeled by 2) at $L^* = 6$ in the dipole magnetic field by using GEMSIS-RBW simulations, and (bottom) dynamic frequency spectra of the count rates (labeled by 3) for simulations (left) A and (right) B [*Saito et al.*, 2012].

ter 2. Actually, the F-t spectrum of the the count rates for 10-Hz chorus elements in the bottom panel of Figure 3.43 does not necessarily exhibit a single and strong peak of modulation around 10 Hz. It is easy to expect that temporal variations in actual PAs is more complicated because they are generated not mono-energetic precipitations but ones with energy ranges a few to a few tens of keV. We suggest from the result of *Saito et al.* [2012] that the TOF effect should be taken into account in the modulation frequency, in particular, higher than 3 Hz, when one analyzes the data obtained from ground-based instruments and low-altitude satellites. Therefore, we cannot exclude the possibility that rapid variations in the frequency range higher than 3 Hz have been neglected in our analysis process. A realistic TOF model, which includes propagation of chorus elements and resonant energy dependence along a field line, is needed to understand rapid modulations seen in the data obtained from ground-based optical instruments.

On the other hand, the quasi 3-Hz modulations identified in our study would be regarded as a reliable proxy of wave-particle interactions based on the simulation result of *Saito et al.* [2012]. Hereafter we focus on quasi 3-Hz modulations and discuss in the context of generation mechanisms of temporal variations of PA. One of important insights in our statistical analysis is that the frequency of modulations showed relatively strong correlation to the auroral intensity with the correlation coefficient of 0.52, which implies that the modulation frequency increases with larger downward energy flux of electrons. We examine this characteristics in the context of wave-particle interactions between electron and a chorus element. Here, the frequency of modulation can be considered an inverse of time interval between two chorus elements as shown in Figure 3.44, and the time interval, t_m is equal to a sum of duration time for one chorus emission with a rising tone, t_0, and quiet time, t_1. Therefore, we obtain a simple equation for frequency of modulation, f_m, as follow:

$$f_m = \frac{1}{t_m} = \frac{1}{t_0 + t_1} \tag{3.12}$$

If t_1 is the same temporal scale as t_0, then $t_m = 2t_0$, and we obtain

$$f_m = \frac{1}{t_m} \approx \frac{1}{2t_0} \tag{3.13}$$

Therefore, it is expected that the modulation frequency is inversely proportional to the duration time of one chorus emission with a frequency drift.

Based on the nonlinear wave growth theory of whistler mode chorus, the frequency sweep rate can be derived from the second-order resonance condition as follows [*Omura et al.*, 2008]:

$$\frac{\partial \omega}{\partial t} = \frac{0.4\delta}{\gamma\xi}\frac{V_{\perp 0}}{c}\frac{\omega}{\Omega_e}\left(1 - \frac{V_R}{V_g}\right)^{-2}\frac{B_W}{B_0}\Omega_e^2 \tag{3.14}$$

where $\delta^2 = (1+\xi^2)^{-1}$, $\gamma = [1-(v_\parallel^2 + v_\perp^2)/c^2]^{-1/2}$, c is the speed of light, $v_\parallel$ and $v_\perp$ are parallel and perpendicular velocity coponent of an electron, $\xi^2 = \omega(\Omega_e - \omega)/\omega_{pe}^2$, ω_{pe} is the electron plasma frequency, $V_{\perp 0}$ is an average value of $v_\perp$ of the initial velocity distribution of energetic electrons at the magnetic equator, the electron cyclotron frequency $\Omega_e = eB_0/m_0$, e and m_0 are the charge and the rest mass of electron, B_0 is the background magnetic field, V_R is the resonance velocity, V_g is the group velocity, and B_W is the amplitude of the wave magnetic field. The equation 3.14 suggests that the frequency sweep rate of chorus elements can be regarded as a function of the amplitude of the magnetic field. The dependence of the frequency sweep rate was demonstrated by a numerical simulation by *Katoh and Omura* [2011]. Since the range of frequency sweep, ω_0, is almost constant, a relationship between the modulation frequency and the amplitude of the wave magnetic field can be written as

$$f_m \approx \frac{1}{2t_0} \propto \frac{\omega_0}{t_0} \approx \frac{\partial \omega}{\partial t} \propto B_W \tag{3.15}$$

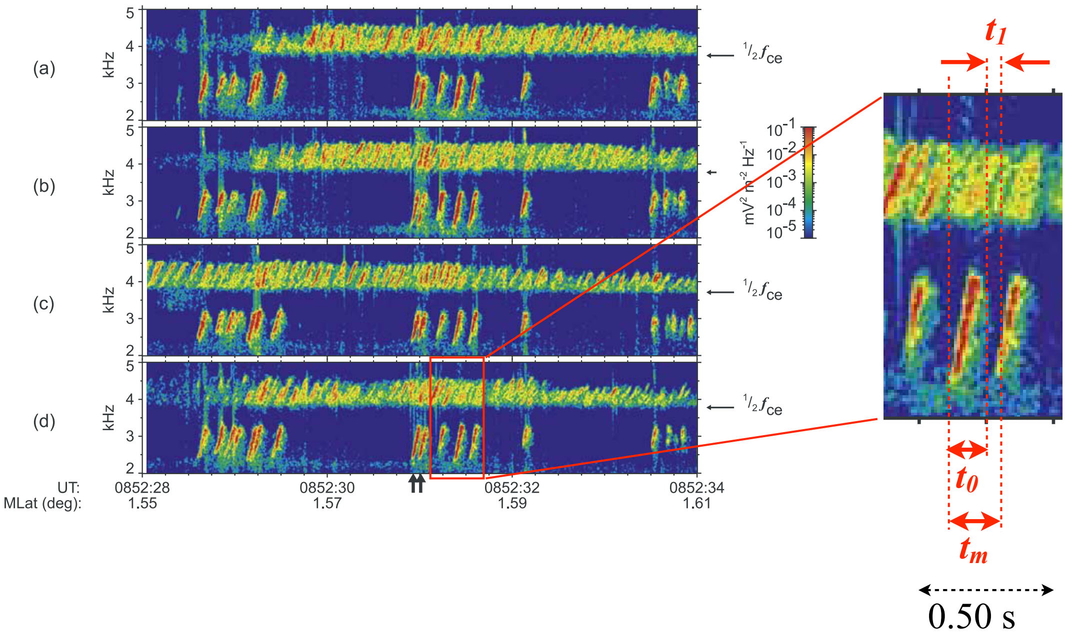

Figure 3.44: (Left) Power spectrograms of electric field fluctuations recorded by the WBD instruments on the Cluster satellites on 18 April 2002 after 0852:28 UT [*Santolik et al.*, 2003]. (Right) Expanded F-t spectrum showing the repetition of chorus elements in detail, which is corresponding to modulations seen in precipitation and auroral intensity.

In addition, whistler mode chorus with large wave amplitudes is expected to generate significant pitch-angle scattering of energetic electrons [*Hikishima et al.*, 2010]. The electrons lose their free energy stored as anisotropy and consequently they start precipitating along the field line into the upper-atmosphere. Therefore, we can consider that the aurora intensity is closely related to the wave amplitude. Combining the relation with the equation of 3.15, the correlation between the modulation frequency and the aurora intensity is explained qualitatively. Therefore, the modulation frequency is thought to behavior as a proxy of the activity of wave-particle interactions. Similarly, the frequency of modulation is expected to correlate to AE index since the whistler mode chorus with large amplitudes probably appear in the early recovery phase when AE index is relatively large [e.g., *Meredith et al.*, 2003]. However, we obtained the clear correlation between the modulation frequency and the aurora intensity rather than that with AE index. It is well known that AE index is a proxy of the global ionospheric currents at high-latitudes. On the other hand, coherent chorus emissions are typically generated in the region with the spatial size of a few thousands of km at the equator [*Santolik et al.*, 2003; *Nishimura et al.*, 2011]. Therefore, the wave-particle interaction should directly be related to th aurora intensity of individual auroral structure, and it would not be related to AE index.

To evaluate the observed modulation frequency quantitatively, we calculated the sweep rate of a whistler mode chorus element from the equation of 3.14. Table 3.6 shows the plasma parameters used in the calculation of the frequency sweep rate of a whistler mode chorus element. In the calculation, we used the realistic parameters assuming dipole magnetic filed at L-value 6.4 and cold plasma density of 0.50, 1.0, and 3.0 [cm^{-3}] which correspond to ω_{pe}/Ω_e of 1.9, 2.7, and 4.7. Since intense chorus emission were frequently observed in the regions where ω_{pe}/Ω_e less than 5 [*Li et al.*, 2010], our assumption is thought to be reasonable. ω was assumed to be 0.30 Ω_e, and the sweep rate was regarded as the constant during the frequency sweep. $V_{\perp 0}$ was set to be 0.26c by reference to [*Hikishima et al.*, 2008], and B_W was a variable ranging from 1 to 100 pT. The calculated frequency sweep rates are also shown in Table 3.6 and the sweep rates for the amplitude larger than 10 pT were roughly consistent with the result of in-situ observations, 8 kHz/s [*Santolik et*

Table 3.6: Plasma parameters used in the calculation for the frequency sweep rate of a whistler mode chorus element based on non linear wave growth theory [*Omura et al.*, 2008]. The calculated frequency sweep rates are also shown in the bottom row.

Background magnetic filed intensity $B_0 = 118$ [nT]		
Electron energy $E = 20$ [keV]		
Gamma factor $\gamma = 1.02$		
Cold electron density [cm^{-3}]		
0.50	1.0	3.0
ω_{pe}/Ω_e		
1.9	2.7	4.7
Resonant velocity V_R		
-0.12c	-0.064c	-0.021c
Sweep rate df/dt [kHz/s]		
0.16-0.16 $\times$ 10^2	0.38-0.38 $\times$ 10^2	1.4-1.4 $\times$ 10^2

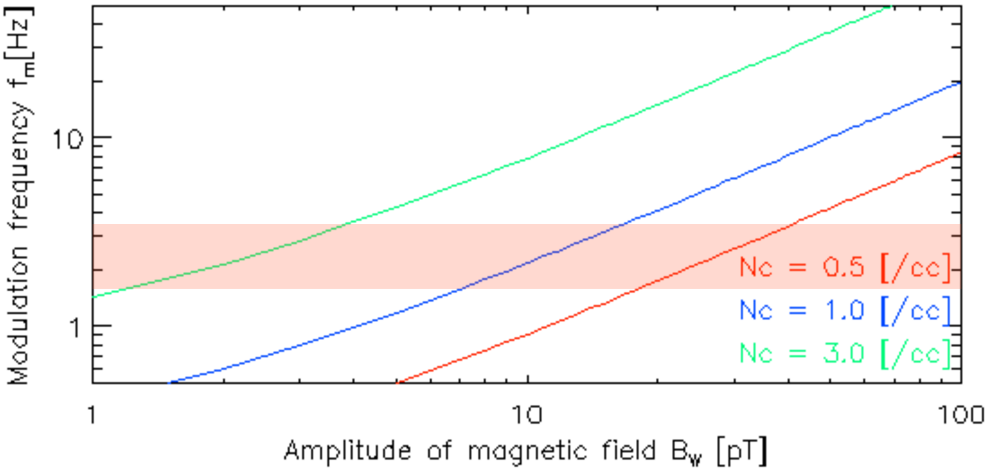

Figure 3.45: Estimated modulation frequency for temporal variations of PA intensity as a function of an amplitude of magnetic filed component of whistler mode chorus wave. The calculation of the modulation frequency was conducted based on the sweep rates of whistler mode chorus wave in non linear wave growth theory of *Omura et al.* [2008]. The region indicated by red shade is corresponding to the observed modulation frequency ranges from 1.5 to 3.3 Hz in 53 PA events in present study.

al., 2008]. Next, we assumed the frequency range of the sweep, ω_0, were from 0.20 Ω_e to 0.50 Ω_e, and the duration of whistler mode chorus element, t_0, was estimated. Finally, the modulation frequency of PA intensity variations can be calculated using the relation of $f_m = 1/2t_0$. Here, Figure 3.45 shows the estimated modulation frequency of PA intensity variations as a function of the amplitude of magnetic field component of whistler mode chorus. The region indicated by red shade is corresponding to the observed modulation frequency ranges from 1.5 to 3.3 Hz in 53 PA events in present study. If the cold plasma density ranges from 0.50 to 1.0 cm^{-3}, the observed modulation frequency ranges can be obtained with the amplitude of whistler mode chorus from 10 pT to a few tens of pT. Although this amplitude is one order of magnitude smaller than the typical amplitudes of a few hundreds pT when whistler chorus elements are observed [*Santolik et al.*, 2003], the observed modulation frequency in this study would be explained numerically by non linear wave growth theory. However, a few subjects, such as quiet time of a chorus emission t_1 and the frequency sweep range ω_0, still remain for the quantitatively understanding of the relationship between the modulation frequency and the frequency sweep rate of whistler mode chorus.

In contrast to the rapid variations, the on-off pulsations periods showed no significant correlations with any of the other cross-scale properties and auroral intensity. For example, the on-off periods did not correlate to the aurora intensity at all[1]. One may simply suppose that the on-off periods can have a negative correlation to the aurora intensity according to the same reason as modulations. Our result suggests that the on-off periods should be determined by the balance of a variety of factors, and therefore, they didn't exhibit simple correlation with other parameters. The wave amplitude is probably one of many factors to determine the on-off periods, and other factors should additionally be taken into account: a long-term variation of the cold plasma density [*Liang et al.*, 2010; *Li et al.*, 2011] such as compressional waves in the range of Pc3-5, a spatial size of a flux tube, and a drift velocity of an energetic electrons [e.g., *Demekhov and Tarkthengerts*, 1994; *Trakthengerts et al.*, 2004]. Since a typical traveling time for full bounce motion of a chorus element is estimated to be 6-7 seconds at $L = 6.4$ [*Ozaki et al.*, 2012], the duration time of on-phase may be related to this time scale.

Our observations with the EMCCD camera revealed that the whole structures of PAs often consisted of a few sub-structures with minimum horizontal width of 10-20 km at the auroral altitudes close to a proton gyro radius. However, no obvious relationship among large and small spatial scale lengths and other properties of PAs were found in the statistical analysis. The candidates of instabilities that can develop such complicated meso- and small-spatial structures include kinetic ballooning instability [*Elphinstone et al.*, 1995; *Liang et al.*, 2008; *Uritsky et al.*, 2009], Rayleigh-Taylor type instability [*Shiokawa et al.*, 2010], and interchange instability [*Ebihara et al.*, 2010]. We suggest that kinetic effects play an important role in developing highly-structured auroras because of their spatial small-scales. In particular, *Hiraki and Sakaguchi.* [2010] demonstrated with a reduced MHD model simulation including the ion and electron inertia effects that a dual-scale patchy structure (about 10 km scale) with finger-like structures (2-5 km scale) can develop under low-β plasma conditions. It is also consistent with the observational fact that shows the occurrence of whistler mode chorus wave frequently at the low-β region called as 'density depletion' in the post-midnight region [*Li et al.*, 2011]. Therefore in-situ observation of plasma β and the horizontal structure of a flux tube is essential to investigate and discuss quantitatively the process of developing meso- and small-scale structures in PAs. However, it is beyond the scope of our current study, which has no in-situ data to compare.

In addition to the cross-scale structures of PAs, we showed that the rapid modulations tended to occur in the sub-structures of PA. Although it is roughly consistent with recent result based on ground-based observations [*Samara and Michell*, 2010], no clear correlations between the modulation frequency and the spatial size of the structures was found statistically. It would still remain an open question why the rapid variations, i.e., a series of fine-scale precipitation of energetic electrons are excited only in the sub-structures of a flux tube and should be addressed in near future. However many numerical experiments for non linear wave growth and micro-burst have been conducted in a 1-D simulation space. Therefore, the visualization of wave-particle interactions and related instabilities based on a high-speed optical imaging technique is quite useful for further understanding about the cross-scale properties of space plasma in the inner magnetosphere.

Key findings

We presented a case study on a PA event in Section 3.2.3 and showed statistical characteristics of the cross-scale properties in 3.2.4 for the first time. The PA observed on 1st December, 2011 exhibited the typical cross-scale structures in space and time. On the statistical analysis, the cross-scale properties were investigated on 53 events during

---

[1] The correlation coefficient was small (0.067)

the period from December 1st, 2011 to March 1st, 2012. The key findings of Section 3.2.3 and Section 3.2.4 can be summarized as follows:

1. A southward propagating aurora patch observed on 1st December, 2011 exhibited the typical meso-scale structures composed of a few sub-structures with clear 3.0-Hz temporal modulations superimposed on on-off pulsations of the period of 8-10 seconds. The characteristic energy of precipitating electrons generating this aurora patch was roughly estimated to be 10 keV.

2. While the large-spatial scale of the whole patch was estimated to be 1500 km mapped onto the magnetic equator, the spatial scale of the sub-structure was 800 km. In addition, the strong 3.0-Hz modulations superimposed on on-phase of pulsation were excited only in the sub-structures.

3. The minimum width of sub-structures was estimated to be 410 km at the magnetic equator. This fact suggests that the sub-structures would be mainly maintained by MHD forces. However, a kinetic effect, such as ion finite Larmor radius effects, may also contribute to form the complicated sub-structures [*Hiraki and Sakaguchi*, 2010], because the minimum scale was still close to local proton gyro radius $\approx$ 100 km.

4. Observed modulation frequency ranged from 1.5 to 3.3 Hz, and it is almost consistent with well-known 3 ± 1 Hz modulations in previous studies [*Røyrvik and Davis*, 1977]. The occurrence probability was slightly concentrated on the frequency range between 2.0 and 2.5 Hz, although its peak was not evident.

5. Any strong modulations were not seen in frequency range higher than about 3 Hz in our study, although recent result obtained from ground-based observations showed rapid variations in higher frequency range of 10-30 Hz. We suggest that the electron TOF effect should be taken into account for the rapid variations higher than 3 Hz.

6. The frequency of modulation showed relatively strong correlation to auroral intensities with the correlation coefficient of 0.52, and it can be explained with a non linear wave growth theory suggesting that higher modulation frequency with larger wave amplitude of whistler mode chorus. Further quantitative understanding of the relation will be addressed in future study.

7. In contrast to the rapid modulations, the on-off pulsations showed no significant correlations with any of other properties of PA. This results imply that the on-off periods may be determined by the balance of a variety of factor. In addition to the wave-particle interactions corresponding to loss rate of electrons in a flux tube, long-term variations of the cold plasma density caused by compressional mode waves would play more important role in control wave-particle interactions in the temporal scale of the on-off pulsation periods. A spatial size on the flux tube and a drift velocity of an energetic electron, i.e., production rate of energetic electrons may additionally be taken into account [e.g., *Demekhov and Tarkthengerts*, 1994; *Trakthengerts et al.*, 2004].

8. The enhancement of rapid variations was seen inside sub-structures in many cases. However, no clear correlations between the modulation frequency and the spatial size of the whole and sub-structures were found statistically. The reason still remains an open question and should be addressed to investigate in near future. The visualization of wave-particle interactions and related instabilities with a high-speed imaging technique is quite useful on further study.

Chapter 4

Discussion

We demonstrated the cross-scale properties of PAs based on observations using the Reimei satellite and the EMCCD camera in Chapter 2 and Chapter 3, respectively. The temporal properties can be explained by two different time-scale process: wave-particle interactions between electrons and whistler mode chorus waves based on non linear wave growth theory and long-term external processes controlling on-off pulsations. In Chapter 4, we propose a possible generation mechanism of PAs that explains the spatial and temporal cross-scale properties as a summary of Chapter 2 and Chapter 3. We should also note that not all of observed PAs did exhibit rapid variations superimposed on on-phase. This fact suggests that the generation of PA is not only one, and other processes contribute to the generation. Here, the other plausible generation mechanism is also discussed, and we propose specific future plans to clarify unsolved problems.

4.1 A proposed generation mechanism

The statistical result in this study showed that the on-off periods did not correlate at all to the aurora intensity as a proxy of wave-particle interactions. It implies that the on-off periods are generated by other plasma process with time-scale in the range of a few sec to a few tens of sec. On the other hand, the rapid modulations which would be related directly to non linear wave growth have shorter time scales, because pitch angle scattering is so effective that electron flux is drastically decreased within a short repetition periods less than 1 second [*Hikishima et al.*, 2010]. Such micro-scale electron precipitation with the short-term duration occurs repeatedly and spontaneously, as long as the cyclotron resonance condition on a non linear wave growth is satisfied in a flux tube. In other words, on-off switchings of the resonance condition may cause on-off pulsations composed of more rapid variations associated with the micro-scale electron precipitations. Figure 4.1 is a schematic illustration for the plausible on-off generation mechanism resulting from long-term cold plasma density variations in a flux tube or intermittent supply of energetic electrons into a flux tube.

We consider that temporal variations of cold plasma density is the more plausible process for on-off pulsations by the following reasons. One is that the Reimei observations demonstrated that trapped energetic electrons were existed continuously at the Reimei altitude during the period of on-off pulsation, although intermittent downward electrons were observed synchronizing with on-off pulsation (for example Figure 2.9). Another is that compressional mode waves may also play an important role in driving the dynamics inside a patch as described in Section 3.2.2. Thus, temporal variations of cold plasma density due to compressional mode waves can be regarded as a key driver for not only the horizontal dynamics inside a patch but also temporal on-off pulsations.

As one of conclusions in this study, we show the Figure 4.2, which is a schematic illustration for the generation process of PAs driven and controlled by a variety of phenomena

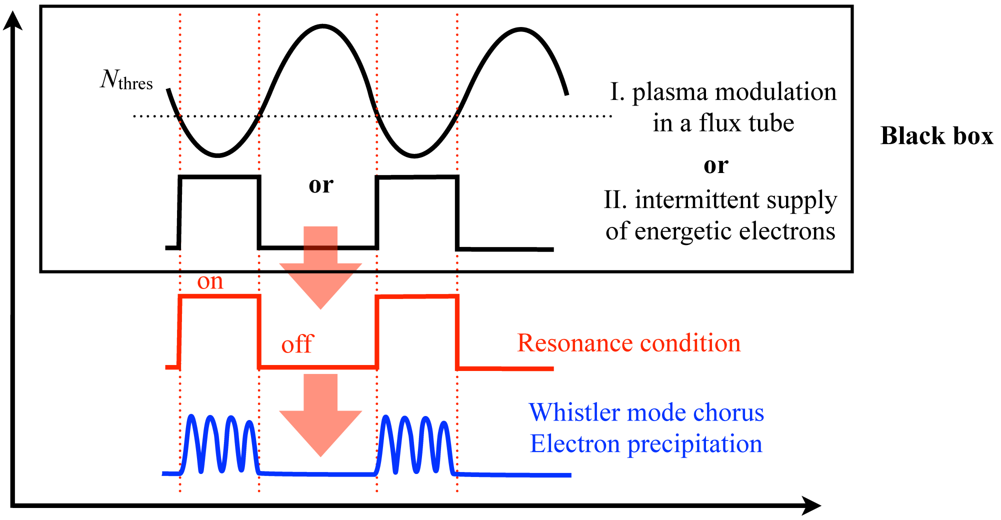

Figure 4.1: A schematic illustration of triggering process of on-off pulsation: long-term cold plasma density variations in a flux tube or intermittent supply of energetic electrons into a flux tube.

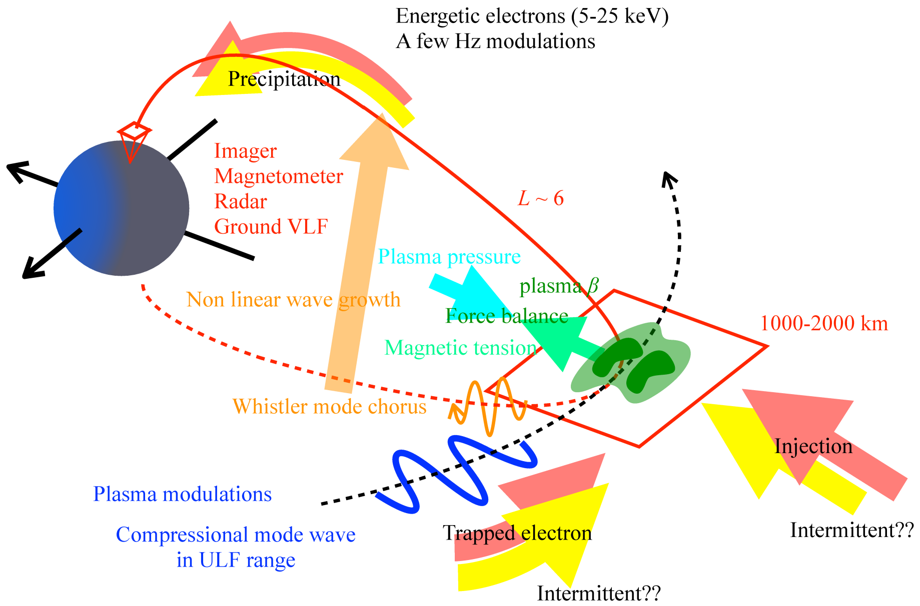

Figure 4.2: A schematic illustration showing a generation mechanism of PAs proposed in Chapter 3 based on the ground-based observations with the EMCCD camera with 100-Hz sampling rate.

in the magnetosphere. The FOV of the EMCCD camera corresponds to an area of 2400 × 2400 km at the magnetic equator. A group of energetic electron with energy ranges from a few to a few tens of keV are supplied into a flux tube with a drift velocity. The electrons with sufficient anisotropy immediately excite whistler mode chorus element with a time scale less than 1 second based on non linear wave growth theory, and the electrons are almost simultaneously scattered into small pitch angles. The electrons scattered into a local loss cone result the fine-scale electron precipitation corresponding to one chorus element with a duration time of several hundreds of milli-seconds. As long as the supply of fresh electrons into the flux tube continues or the cyclotron resonance conditions are changed by temporal variations of cold plasma density due to compressional mode waves, the chorus elements, i.e., the micro-scale precipitations of electrons, are generated repeatedly. Consequently, the on-phase of PA modulated at the frequency of a few-Hz can be observed with ground-based optical instruments. Expanding a scope of the property in equatorial plane, a compressional mode wave may control the dynamics inside a patch, such as expansion-contraction and streaming, via modulation of the flux tube. Force balance between magnetic tension and plasma pressure triggers the development of complicated spatial patch structures governed by instabilities taking into account kinetic effects on a time scale longer than a few minutes.

This model for the generation process give us comprehensive understandings of the cross-scale properties of PA in space and time. Quantitative evaluation of the model combined with simultaneous ground-based and in-situ observations would be an essential in near future. In addition, this scenario focuses on only the PA events exhibiting the rapid modulations. However, there were certainly PA events where the rapid modulations were not identified in our analyses. Unsolved issues such as a generation mechanism of PA without any modulations and future plans to address the issues are given in the following sections.

4.2 Remaining issues

4.2.1 Other possible mechanisms

Based on the two approaches, the Reimei satellite and the EMCCD camera, we suggested that the plausible generation mechanism of PAs is cyclotron resonance between electrons and whistler mode chorus waves, and non linear wave growth effect particularly plays an important role in generating superimposed rapid variations on the on-off pulsation. However, we only analyzed and discussed the PA events that show clear energy-time dispersions of downward electrons (in Chapter 2) and rapid variations in on-phase (in Chapter 3). It was reported that a 3 ± 1 Hz modulation appeared in more than 50% of all PAs in the midnight and morning sectors [*Røyrvik and Davis*, 1977]. On the other hand, it seems that the occurrence probability by our ground-based observations is slightly higher than *Røyrvik and Davis.* [1977] on an empirical basis. Anyway, PAs without exhibiting the 3-Hz modulation are not negligible, and the discussion about generation mechanisms of PAs should include the reason why PAs sometimes do not contain the rapid variations. Here, we consider two possibilities as follows: one is the TOF effect already mentioned in Section 3.2.4, another is the contribution of other generation mechanisms such as cyclotron resonance with ECH waves [*Liang et al.*, 2010]. The first possibility is a difficult issue, because we cannot determine whether modulations are neglected or not existed only by current analysis methods due to the electron TOF effect. If PAs without any modulation actually exist, the other proposed mechanisms would contribute: ECH waves, a quasiperiodic oscillation of the field-aligned E field, and Fermi-type acceleration. Among the mechanisms, we consider that the contribution of ECH wave is most plausible, because ECH wave is expected to generate the on-off pulsation of PA based on the same logic our proposed scenario [*Liang et al.*, 2010]. In contrast, the other two mechanisms seem to have no logical explanations for generation processes of the on-off pulsations. ECH wave has been regarded as one of main contributors to diffuse auroras so far [*Kennel et al.*, 1970; *Horne et al.*, 2003; *Sergienko et al.*, 2008]. Although it is difficult for ECH waves to effectively scatter electrons with high energies over a few keV into loss cone [*Horne and Thorne*, 2000; *Horne et al*, 2003; *Ni et al.*, 2008], *Liang et al.* [2010] demonstrated that ECH wave would resonate electrons with tens of keV in the high L-shell regions at $L \sim 11$. Therefore, the possibility that ECH contributed to PAs cannot be excluded for the case without any rapid modulations, even though our observation site of PFRR is located at L of 6.4. The relationship between PAs and ECH waves should be investigated further particularly for the case showing no rapid variations.

4.2.2 MLT dependence

It is well known that the morphology of PAs is changed drastically with substorm phases [e.g., *Røyrvik and Davis*, 1977]. However, the precise relationship between generation mechanisms of PAs and substrom phases has not been discussed yet in the past studies. We discuss here the MLT dependence on PAs since the substorm phases would be roughly related to MLT statistically. Although THEMIS observations demonstrated that the generation process of whistler mode chorus has the MLT dependence on the global scale roughly divided into midnight to dawn sector and dawn to noon sector [*Li et al.*, 2011] as shown in Figure 4.3, the precise variations of chorus generation process inside the midnight to dawn sector (indicated by "DD" in Figure 4.3) is not fully understood. In the present study, we showed the statistical result on 29 events that the estimated cold plasma density increased in the midnight region compared to that at later MLTs in Chapter 2 (Figure 2.19). In contrast, the statistics based on the total 53 cases using ground-based observation data did not show any significant correlations among the properties of PAs, MLT and time lag since substorm onset, except for the weak negative correlations between modulation frequency and the time lag (Figure 3.40). From the results in Chapter 2 and Chapter 3 mentioned above, we conclude that the properties of PAs such as the on-off repetition period, modulation frequency, and spatial scale of their structures generally don't persist for long-term durations on the scale of a few hours. This may be because these properties are directly affected by meso- or micro scale irregular plasma environment rather than global scale environment as discussed in Chapter 3. To understand the MLT dependence on the generation mechanisms of PAs (whistler mode chorus wave, etc.) quantitatively, further simultaneous in-situ and ground-based observations are needed in the future.

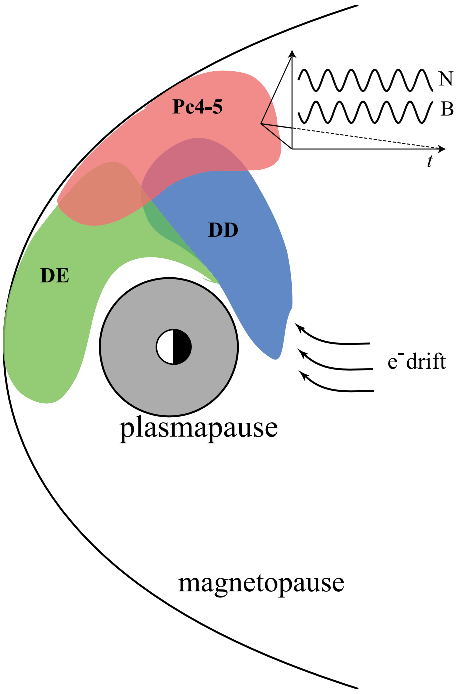

Figure 4.3: A schematic illustration showing the global distribution of chorus modulation associated with three different mechanisms in the equatorial magnetosphere. Red, blue and green regions represent chorus modulation relevant to compressional Pc4-5 pulsations with an anti-correlation between the density and the magnetic field (shown next to the red region), density depletions (DD), and density enhancements (DE) respectively [*Li et al.*, 2011].

Temporal evolutions of the morphology of PAs were frequently seen by our ground-based observations: generally, chaotic patches transiently appear after an aurora breakup, multiple bands extended in the east-west direction (omega bands) drift eastward, and finally a cluster of patches are seen getting close to dawn. These characteristics are also reported in the past studies and widely accepted [*Untiedt and Baumjohann*, 1993]. These evolutions are probably relevant to the global structure of auroral oval and convection pattern in the magnetosphere. In addition, the developments of highly-complicated auroral patch seem to be related to meso-scale plasma environment such as the plasma density and the force balance between the magnetic tensions and the plasma pressures. The complicated patchy structures were developing typically near dawn on time scale of a few to a few tens minutes in many cases. It is suggested that ionospheric electric filed contributes to the forming of small-scale finger structures in patches [*Hosokawa et al*, 2010a; *Shiokawa et al.*, 2010], therefore, direct comparison to local 2-D convection pattern is one of effective methods for further understanding of development of complicated patchy structures and instabilities that triggers the forming process.

4.3 Future plans

4.3.1 Coordinated observation with in-situ measurements in the magnetosphere

Simultaneous ground-based and in-situ observations are essential for investigations into the generation mechanism of PAs. However, we have not yet found any in-situ observation in the magnetosphere to directly compare with the Reimei or the EMCCD camera data. Imaging observations with both high-sensitivity and high-sampling rate (> 100 Hz) coordinated with in-situ measurements are necessary for understanding the precise relationship between the 3-Hz modulation (micro-scale precipitation of electrons) and the whistler mode chorus element. Such approach is also quite useful for investigations into the driver of auroral dynamics inside a patch and temporal development of highly-structured patches. Therefore, we propose specific research agenda to be made in future as follows:

- One-to-one correspondence between the 3-Hz modulation (micro-scale precipitation) and the whistler mode chorus element.
- Meso- and small-scale plasma perturbation and spatial structure of plasma inside a flux tube, which corresponds to aurora patch and highly-structured auroral shapes.
- Identification of the PA events related to ECH waves, field-aligned potential, and Fermi-type acceleration, and their statistical characteristics such as occurrence probability and location.

In particular, there is no high-time resolution data demonstrating the relationship between the 3-Hz modulation of auroral intensity and the whistler mode chorus elements due to low resolution wave data. Therefore, the first agenda is crucially important to the proposed generation mechanism proposed in this present study. Practical difficulties arise on a huge amount of accumulated data, rare conjunction opportunity between a ground-based instruments and a satellite, and high-data sampling rate. Especially, the high sampling rate particularly requires sufficient data processing speed on hardwares. If the data processing speed is not enough, one has to set low spatial resolutions, i.e., insufficient number of pixel-binning. Consequently, FOV becomes relatively narrow by necessity in order to keep the sufficient spatial resolution. Improvement of hardwares such as data writing speed and complementary observation using all-sky imager will be a solution for to the difficulties. In addition, it is quite useful to develop networked ground-based instruments in the simultaneous observations coordinated with the satellites such as the Van Allen Probes (launched on August 30, 2012) and Japanese geospace exploration project, “The

Energization and Radiation in Geospace (ERG)" (will be launched on December, 2015). For example of the network, a imaging array composed of high-time resolution imagers will give us a great opportunity to the precise investigation based on the simultaneous ground-based and in-situ observations.

4.3.2 Coordinated observation with remote sensing of the ionosphere

Recent radar experiment enable us to measure three-dimensional ionospheric plasma parameters. PFISR is configured to volumetric imaging of ionospheric parameters with a typical time resolution of 2 min [*Semeter et al.*, 2010]. Although the fine-scale structures of discrete aurora that appear frequently at an auroral breakup were investigated with a great interest in the context of their relationship to kinetic or inertial Alfven waves, no applications of three-dimensional imaging of ionospheric plasma to the spatial structures of PAs has been performed yet. Here, possible applications are given as follows from results of present study:

- Direct comparison between the sub-structures inside a whole patchy structure of PA and the spatial distribution of electron density.
- Relationship of local plasma drift velocity to the temporal development of complicated patchy structures.
- Observation of electron density enhancement in the D region of the ionosphere, as an evidence of energetic electron precipitations ($>$ a few tens of keV).

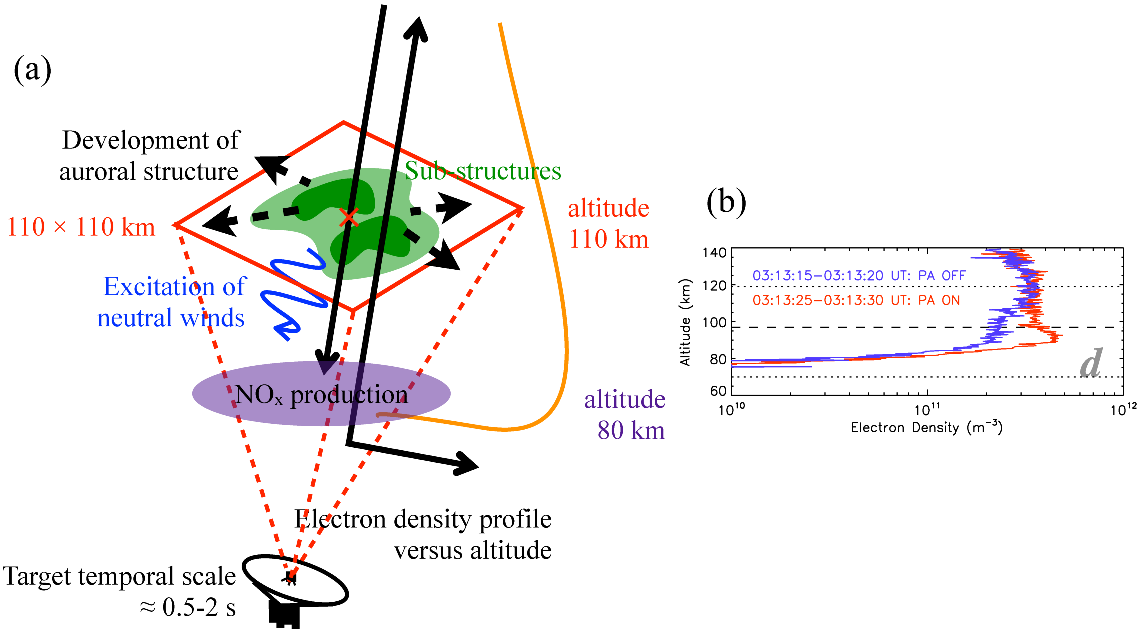

Figure 4.4: (a) A schematic illustration showing the configuration of ground-based observations coordinated with an incoherent scattering radar and the science targets. (b) Altitude profile of the electron density at the times of "on" (red) and "off" (blue) phase of the pulsating aurora [*Hosokawa et al.*, 2010b].

Figure 4.4 (a) shows a schematic illustration for the configuration of ground-based observation coordinated with an incoherent scattering radar. It is noticed that current time resolution of experiments with PFISR would be much lower than typical on-off pulsations (a few to 20 seconds). Although *Semeter et al.*, [2010] mentioned that 30-second resolution would be expected in future experiments with PFISR, it seems to be still insufficient to measure the on-off variations. Considering on the measurement of ionospheric parameters related to the sub-structures and 3-Hz modulations, a further improvement of radar capability is required, and European Incoherent Scattering radar-3D (EISCAT 3D) will bring us an opportunity to investigate the subject. Although the spatial resolution of current global MHD simulation for M-I coupling is generally insufficient for meso- and small-scales temporal and spatial variations of PAs, a regional simulation plays important role in understanding the small-scale phenomena, combined with data from the high-sampling remote sensing of the ionosphere. The EISCAT radar demonstrated ionization layer appearing in the D regions during the period of on-phase of PA as shown in Figure 4.4 (b) [e.g., *Wahlund et al.*, 1989; *Hosokawa et al.*, 2010b], which implies electron precipitation at energy of 20-40 keV occurred in the PA events. Such energetic electron may be generated by quite similar process to that of microburst, and it is valuable to examine whether microbust (precipitating electrons with a few hundreds keV to MeV) occurs simultaneously with PAs.

Finally, we refer to mesosphere-thermosphere-ionosphere (MTI) coupling through the electron precipitation responsible to PAs. Energetic particle precipitation can contribute directly to the heating of ionospheric plasma and neutral atmosphere, and the heating subsequently excites dynamics to transport momentum as neutral winds perturbations in the lower-thermoshere and even in the middle atmosphere. Actually, the excitation of vertical neutral wind associated with Joule heating in the E region was observed with appearance of PAs [*Oyama et al.*, 2010]. It is also suggested that relativistic electron precipitation with energy of several MeV is quite effective for generating NOx, which is important for the loss process of O_3 in mesosphere and stratosphere [*Turunen et al.*, 2009] (Figure 4.5), although the energy is larger than two magnitudes of that of precipitating electrons related to PAs. Therefore, we conclude that important and interesting physical process for solar-terrestrial environment, such as neutral-plasma interactions, still remains unsolved in this field, i.e., the middle atmosphere.

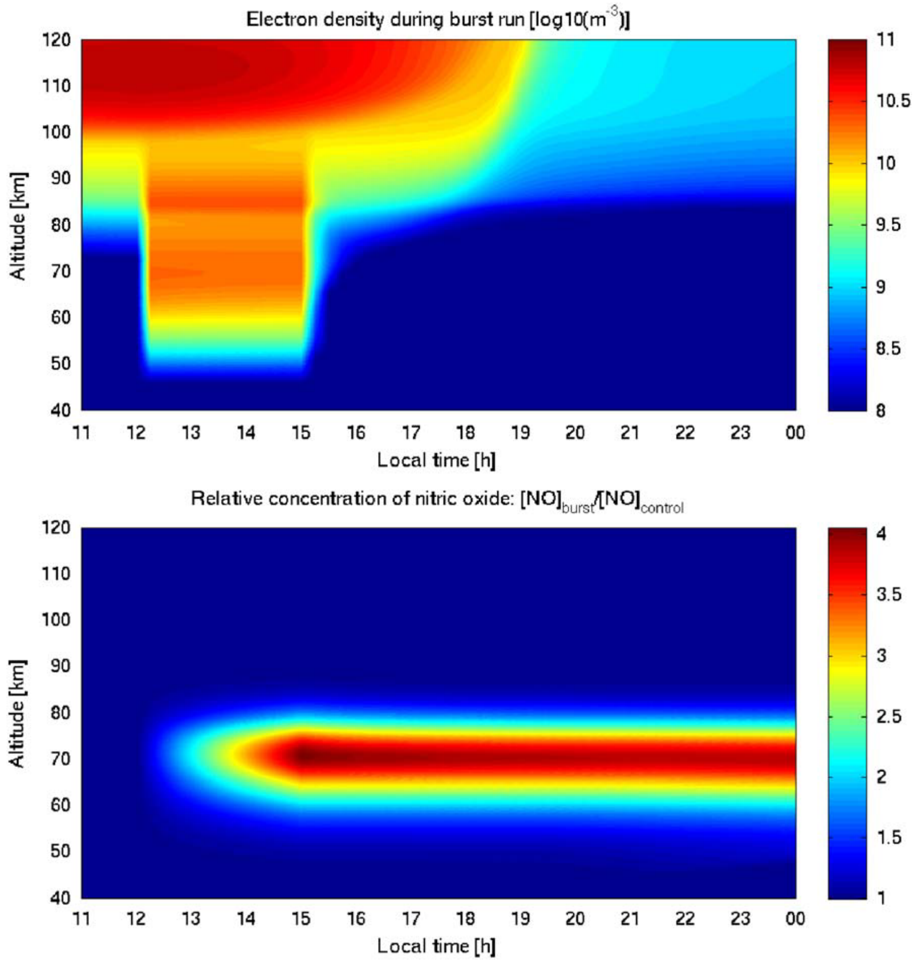

Figure 4.5: The effect of a 3 h long burst of relativistic electron precipitation on electron number density (upper panel) and NOx (bottom panel) levels using the precipitating fluxes measured in the bounce loss cone at L = 3.5-4 by the Upper Atmosphere Research Satellite on 18 May 1992 (*Gaines et al.*, [1995]). The spectrum of the relativistic electron is very hard, containing significant fluxes at energies as high as 5 MeV [*Turunen et al.*, 2009].

Chapter 5

Concluding remarks

This study has revealed the spatial and temporal cross-scale properties of pulsating aurora (PA) with several analysis methods and distinctive data obtained with the two different but complementary observations: the Reimei satellite and the ground-based EMCCD camera with a high sampling rate. Based on the observational evidences, we proposed the plausible generation mechanism for PA properties including the rapid modulations, small-scale structures (10-30 km), and the dynamics inside a patch.

Firstly we showed the electron precipitations causing PA, with energy-time dispersion and short-term duration less than 1 second, using the data from simultaneous image-particle observations by the Reimei satellite. Applying the two TOF analysis models to 29 PA events, we investigated the generation process of the electron precipitations and identified the source region of the electrons. The main results of this study are as follows:

1. The source region obtained from the standard TOF model (TOF-A) was distributed almost continuously in magnetic latitude ranges from -20 to 50°. On the other hand, the source regions obtained from the new TOF model (TOF-B), which takes into account the interaction electron and whistler mode wave [*Miyoshi et al.*, 2010], ranged from the magnetic equator to low-latitudinal region ($\sim$ -11°).
2. The source regions obtained from the TOF-B analysis generally corresponded to the regions in which whistler mode chorus waves are frequently observed in the previous studies, suggesting that the micro-scale precipitation of electrons caused by the cyclotron resonance with propagating whistler mode waves is a plausible mechanism for the production of PAs.

To expand our scope of the investigation on the property of PA, the ground-based optical observation using an EMCCD camera with wide a FOV ($49 \times 49°$) and a high sampling rate of 100 frames/s was carried out during the period from November 2010 to March 2011 and from November 2011 to March 2012. We focused on meso- and small-scale PAs appeared at the early recovery phase of the substorm on March 4, 2011, and outstanding spatial and temporal characteristics of the PAs were presented. The results of this case study are summarized as follows:

3. Three independent pulsating patches (PA1-3) with different periods from 4 to 7 seconds were observed in the FOV of 100 ×100 km at the altitude of 110 km. The periodicity seemed to be not consistent with the electron bounce motion. The typical scale of the patch was estimated to be 2000 km mapped on the magnetic equator, and it is comparable with the estimations based on recent in-situ observations. It is also noted that clear and stable black boundaries with a width of 5-8 km existed between each pulsating patch.

4. We examined the modulations of PAs in the frequency range higher than 1.0 Hz and their spatial distributions in detail. The results revealed that the modulation had a peak frequency around 1.5 Hz, with a narrow frequency width of 0.30 Hz. In addition, the dominant modulation at the frequency 1.5 Hz was not distributed uniformly in a whole PA1 structure but existed locally as a spot in PA1. On the other hand, the adjacent PA2 and PA3 had no dominant modulation and coherency at the frequency around 1.5 Hz.

5. Coherence and phase maps obtained from the cross spectrum analysis revealed that the modulations around 1.5 Hz inside PA1 were almost in phase, and that the low frequency variations from 0.2 to 0.5 Hz inside PA1-3 propagated as a group of flows with consistent directions. The estimated fast flow velocities inside PA2 ranged from 50 to 120 km/s at the auroral altitude. They were corresponding to the horizontal velocities between 1800 and 2700 km/s mapped on the magnetic equator, and almost equal to the Alfven speed at $L \sim 6$. The result suggests that compressional waves may drive control the growth rates of whistler mode waves, which can generate precipitation associated with PA, and drive the dynamics inside a patch.

Further, We presented a case study on the PA showing the cross-scale properties of PA in space and time on the 1st December, 2011 as follow:

6. A southward propagating aurora patch observed on 1st December, 2011 exhibited the typical meso-scale structures composed of a few sub-structures. The temporal variations of the PA contained clear 3.0-Hz temporal modulations superimposed on on-off pulsations of the period of 8-10 seconds. The characteristic energy of precipitating electrons generating this aurora patch was roughly estimated to be 10 keV.

7. While the large-spatial scale of the whole patch was estimated to be 1500 km mapped onto the magnetic equator, the spatial scale of the sub-structure was 800 km. In addition, the dominant 3.0-Hz modulations were excited only in the sub-structures.

8. The minimum width of sub-structures was estimated to be 410 km at the magnetic equator. On the other hand local proton gyro radius was estimated to be smaller (≈ 100 km) than the width, which suggests that the sub-structures would be mainly maintained by MHD forces. However, a kinetic effect, such as ion finite Larmor radius effects, may also contribute to form the complicated sub-structures [*Hiraki and Sakaguchi*, 2010], because the minimum scale was still close to local proton gyro radius.

On the statistical analysis, the cross-scale properties were investigated on 53 events during the period from December 1st, 2011 to March 1st, 2012. The key findings of the results can be summarized as follows:

9. Observed modulation frequency ranged from 1.5 to 3.3 Hz, and it is almost consistent with well-known 3 ± 1 Hz modulations in previous studies [*Røyrvik and Davis*, 1977]. The occurrence probability was slightly concentrated on the frequency range between 2.0 and 2.5 Hz, although its peak was not evident.

10. Any strong modulations were not seen in frequency range higher than about 3 Hz in present study, which may suggest that the TOF of electron makes the time-smoothing effect on the rapid variations higher than 3 Hz.

11. The frequency of modulation showed relatively strong correlation to auroral intensities with the correlation coefficient of 0.52, and it can be explained with a non linear

wave growth theory suggesting that higher modulation frequency with larger wave amplitude of whistler mode chorus.

12. In contrast to the rapid modulations, the on-off pulsations showed no significant correlations with any of other properties of PA. This results imply that the on-off periods may be determined by the balance of a variety of factor. In addition to the wave-particle interactions corresponding to loss rate of electrons in a flux tube, long-term variations of the cold plasma density caused by compressional mode waves would play more important role in control wave-particle interactions in the temporal scale of the on-off pulsation periods. A spatial size on the flux tube and a drift velocity of an energetic electron, i.e., production rate of energetic electrons may additionally be taken into account [e.g., *Demekhov and Tarkthengerts*, 1994; *Trakthengerts et al.*, 2004].

13. The enhancement of rapid variations was seen inside sub-structures in many cases. However, no clear correlations between the modulation frequency and the spatial size of the whole and sub-structures were found statistically. The reason still remains an open question and should be addressed to investigate in near future.

Finally, we propose a possible generation mechanism of PAs that explains the spatial and temporal cross-scale properties presented in this study. A group of energetic electron with energy ranges from a few to a few tens of keV are supplied into a flux tube with a drift velocity. The electrons with sufficient anisotropy immediately excite whistler mode chorus element with a time scale less than 1 second based on non linear wave growth theory, and the electrons are almost simultaneously scattered into small pitch angles. The electrons scattered into a local loss cone result the fine-scale electron precipitation with a duration time of several hundreds of milli-seconds. As long as the supply of fresh electrons into the flux tube continues or the cyclotron resonance conditions are changed by temporal variations of cold plasma density due to compressional mode waves, both the chorus elements and the fine-scale precipitations of electrons are generated repeatedly. Consequently, the on-phase of PA modulated at the frequency of a few-Hz can be observed with ground-based optical instruments. Expanding a scope of the property in equatorial plane, a compressional mode wave may control the dynamics inside a patch, such as expansion-contraction and streaming, via modulation of the flux tube. Force balance between magnetic tension and plasma pressure triggers the development of complicated spatial patch structures governed by instabilities taking into account kinetic effects on a time scale longer than a few minutes.

This model for the generation process give us comprehensive understandings of the cross-scale properties of PA in space and time. Quantitative evaluation of the model combined with simultaneous ground-based and in-situ observations would be an essential, and the visualization of wave-particle interactions and related instabilities with a high-speed imaging technique is quite useful for further understandings of microscopic space plasma physics including PAs.

References

Akasofu, S.-I. (1976), Recent progress in studies of DMSP auroral photographs, *Space Sci. Rev., 19*, 169-215, doi:10.1007/BF00215692.

Akasofu, S.-I. (1981), Energy coupling between the solar wind and the magnetosphere, *Space Sci. Rev., 28*, 111.

Anderson, K. A., and D. W. Milton (1964), Balloon observations of X rays in the auroral zone, *J. Geophys. Res., 69*(21), 4457.

Asamura, K., D. Tsujita, H. Tanaka, Y. Saito, T. Mukai, and M. Hirahara (2003), Auroral particle instrument onboard the INDEX satellite, *Adv. Space Res., 32*, 375-378.

Asamura, K., C. C. Chaston, Y. Itoh, M. Fujimoto, T. Sakanoi, Y. Ebihara, A. Yamazaki, M. Hirahara, K. Seki, Y. Kasaba, and M. Okada (2009), Sheared flows and small-scale Alfven wave generation in the auroral acceleration region, *Geophys. Res. Lett., 36*, L05105, doi:10.1029/2008GL036803.

Bortnik, J., R. M. Thorne, and N. P. Meredith (2007), Modeling the propagation characteristics of chorus using CRRES suprathermal electron fluxes, *J. Geophys. Res., 112*, A08204, doi:10.1029/2006JA012237.

Bortnik, J., R. M. Thorne, and N. P. Meredith (2008), The unexpected origin of plasmaspheric hiss from discrete chorus emissions, *Nature, 452*(7183), 62-66, doi:10.1038/nature06741.

Boström, R. (1964), A model of the auroral electrojets, *J. Geophys. Res., 69*, 4983-4999.

Bryant, D. A., G. M. Courtier, and G. Bennett (1971), Equatorial modulation of electrons in a pulsating aurora, *J. Atmos. Terr. Phys., 33*, 859-867, doi:10.1016/0021-9169(71)90086-9.

Carpenter, D. L., and R. R. Anderson (1992), An ISEE/Whistler model of equatorial electron density in the magnetosphere, *J. Geophys. Res., 97*, 1097-1108.

Chum, J., O. Santolík, A. W. Breneman, C. A. Kletzing, D. A. Gurnett, and J. S. Pickett (2007), Chorus source properties that produce time shifts and frequency range differences observed on different Cluster spacecraft, *J. Geophys. Res., 112*, A06206, doi:10.1029/2006JA012061.

Davidson, G. T. (1990), Pitch-angle diffusion and the origin of temporal and spatial structures in morningside aurorae, *Space Sci. Rev., 53*, 45-82.

Davidson, G. T., and Y. T. Chiu (1987), A nonlinear model of wave-particle interactions in the trapped radiation belts: Auroral pulsation solutions, *Geophys. Res. Lett., 14*(11), 1166-1169, doi:10.1029/GL014i011p01166.

Demekhov, A. G., and V. Y. Trakhtengerts (1994), A mechanism of formation of pulsating aurorae, *J. Geophys. Res., 99*, 5831-5841.

Ebihara, Y., T. Sakanoi, K. Asamura, M. Hirahara, and M. F. Thomsen (2010), Reimei observation of highly structured auroras caused by nonaccelerated electrons, *J. Geophys. Res., 115*, A08320, doi:10.1029/ 2009JA015009.

Elphinstone, R. D., et al. (1995), Observations in the vicinity of substorm onset: Implications for the substorm process, *J. Geophys. Res., 100*(A5), 7937-7969, doi:10.1029/94JA02938.

Frey, H. U., et al. (2010), Small and meso-scale properties of a substorm onset auroral arc, *J. Geophys. Res., 115*, A10209, doi:10.1029/ 2010JA015537.

Fujii, R., N. Sato, T. Ono, H. Fukunishi, T. Hirasawa, S. Kokubun, T. Araki and T. Saemundsson (1987), Conjugacies of pulsating auroras by all-sky TV observations, *Geophys. Res. Lett., 14*, 115-118.

Gaines, E. E., D. L. Chenette, W. L. Imhof, C. H. Jackman, and J. D. Winningham (1995), Relativistic electron fluxes in May 1992 and their effect on the middle atmosphere, *J. Geophys. Res., 100*, 1027-1033.

Gustavsson, B., J. Lunde, and E. M. Blixt (2008), Optical observations of flickering aurora and its spatiotemporal characteristics, *J. Geophys. Res., 113*, A12317, doi:10.1029/2008JA013515.

Haerendel, G. (2007), Auroral arcs as sites of magnetic stress release, *J. Geophys. Res., 112*, A09214, doi:10.1029/2007JA012378.

Hallinan, T. J., et al. (1998), Spectra of type-B red lower borders, *J. Geophys. Res., 103*, 11,635-11,640, doi:10.1029/97JA03459.

Hansen, H. J., and W. J. Scourfield (1990), Associated ground-based observations of optical aurorae and discrete whistler waves, *J. Geophys. Res., 95*(A1), 233-239, doi:10.1029/JA095iA01p00233.

Hardy, D. A., W. J. Burke, and E. Villalon (1990), Electron dispersionevents in the morningside auroral zone and their relationship with VLFemissions, *J. Geophys. Res., 95*(A5), 6451-6466.

Haque, N., U. S. Inan, T. F. Bell, J. S. Pickett, J. G. Trotignon, and G. Facskó (2011), Cluster observations of whistler mode ducts and banded chorus, *Geophys. Res. Lett., 38*, L18107, doi:10.1029/2011GL049112.

Hikishima, M., Y. Omura, and D. Summers (2010), Microburst precipitation of energetic electrons associated with chorus wave generation, *Geophys. Res. Lett., 37*, L07103, doi:10.1029/2010GL042678.

Hiraki, Y., and K. Sakaguchi (2010), Formation of fingerlike structures in fragmentation of small-scale patchy aurora, *J. Geophys. Res., 115*, A12253, doi:10.1029/2010JA015623.

Horne, R. B., and R. M. Thorne (2000), Electron pitch angle diffusion by electrostatic electron harmonic waves: The origin of pancake distributions, *J. Geophys. Res., 105*, 5391.

Horne, R. B., R. M. Thorne, N. P. Meredith, and R. R. Anderson (2003), Diffuse auroral electron scattering by electron cyclotron harmonic and whistler mode waves during an isolated substorm, *J. Geophys. Res., 108*, 1290, doi:10.1029/2002JA009736.

Hosokawa, K., A. Kadokura, N. Sato, S. E. Milan, M. Lester, G. Bjornsson, and Th. Saemundsson (2008), Electric field modulation behind pulsating aurora, *J. Geophys. Res., 113*, A11322, doi:10.1029/2008JA013601.

Hosokawa, K., Y. Ogawa, A. Kadokura, H. Miyaoka, and N. Sato (2010), Modulation of ionospheric conductance and electric field associated with pulsating aurora, *J. Geophys. Res., 115*, A03201, doi:10.1029/ 2009JA014683

Hosokawa, K., and Y. Ogawa (2010), Pedersen current carried by electrons in auroral Dregion, *Geophys. Res. Lett., 37*, L18103, doi:10.1029/2010GL044746.

Imhof, W. L., H. D. Voss, J. Mobilia, D. W. Datlowe, E. E. Gaines, J. P. McGlennon, and U. S. Inan (1992), Relativistic electron microbursts, *J. Geophys. Res., 97*(A9), 13,829.

Jones, S. L., M. R. Lessard, K. Rychert, E. Spanswick, and E. Donovan (2011), Large-scale aspects and temporal evolution of pulsating aurora, *J. Geophys. Res., 116*, A03214, doi:10.1029/2010JA015840.

Johnstone, A. D. (1983), The mechanism of pulsating aurora, *Ann. Geophys., 1*, 397-410.

Kataoka, R., Y. Miyoshi, D. Hampton, T. Ishii, and H. Kozako (2012), Pulsating aurora beyond the ultra-low-frequency range, *J. Geophys. Res., 117*, A08336, doi:10.1029/2012JA017987.

Katoh, Y., and Y. Omura (2007), Computer simulation of chorus wave generation in the Earth's inner magnetosphere, *Geophys. Res. Lett., 34*, L03102, doi:10.1029/2006GL028594.

Katoh, Y., and Y. Omura (2011), Amplitude dependence of frequency sweep rates of whistler mode chorus emissions, *J. Geophys. Res., 116*, A07201, doi:10.1029/2011JA016496.

Kennel, C. F., and H. E. Petscheck, (1966), Limit on stably trapped particle fluxes, *J. Geophys. Res., 71*, 1-28.

Kennel, C. F., F. L. Scarf, R. W. Fredricks, J. H. Mcghee, and F. V. Coroniti (1970), VLF electric field observations in the magnetosphere, *J. Geophys. Res., 75*, 6136-6152.

Kivelson, M. G., and C. T Russell (1995), *Introduction to Space Physics*, Cambridge Univ. Press, New York.

Kokubun, S., M. G. Kivelson, R. L. McPherron, C. T. Russell, and H. I. West Jr. (1977), Ogo 5 observations of Pc 5 waves: Particle flux modulations, *J. Geophys. Res., 82*(19), 2774-2786, doi:10.1029/ JA082i019p02774.

Kremser, G., A. Korth, J. A. Fejer, B. Wilken, A. V. Gurevich, and E. Amata (1981), Observations of quasi-periodic flux variations of energetic ions and electrons associated with Pc 5 geomagnetic pulsations, *J. Geophys. Res., 86*(A5), 3345-3356, doi:10.1029/JA086iA05p03345

Li, W., R. M. Thorne, V. Angelopoulos, J. Bortnik, C. M. Cully, B. Ni, O. LeContel, A. Roux, U. Auster, and W. Magnes (2009a), Global distribution of whistler-mode chours waves observed on the THEMIS spacecraft, *Geophys. Res. Lett., 36*, L09104, doi:10.1029/2009GL037595.

Li, W., R. M. Thorne, V. Angelopoulos, J. W. Bonnell, J. P. McFadden, C. W. Carlson, O. LeContel, A. Roux, K. H. Glassmeier, and H. U. Auster (2009b), Evaluation of whistler-mode chorus intensification on the nightside during an injection event observed on the THEMIS spacecraft, *J. Geophys. Res., 114*, A00C14, doi:10.1029/2008JA013554.

Li, W., et al. (2010), THEMIS analysis of observed equatorial electron distributions responsible for the chorus excitation, *J. Geophys. Res., 115*, A00F11, doi:10.1029/2009JA014845.

Li, W., J. Bortnik, R. M. Thorne, Y. Nishimura, V. Angelopoulos, and L. Chen (2011), Modulation of whistler mode chorus waves: 2. Role of density variations, *J. Geophys. Res., 116*, A06206, doi:10.1029/ 2010JA016313.

Liang, J., E. F. Donovan, W. W. Liu, B. Jackel, M. Syrjasuo, S. B. Mende, H. U. Frey, V. Angelopoulos, and M. Connors (2008), Intensification of preexisting auroral arc at substorm expansion phase onset: Wave-like disruption during the first tens of seconds, *Geophys. Res. Lett., 35*, L17S19, doi:10.1029/2008GL033666.

Liang, J., et al. (2010), THEMIS observations of electron cyclotron harmonic emissions, ULF waves, and pulsating auroras, *J. Geophys. Res., 115*, A10235, doi:10.1029/2009JA015148.

Lorentzen, K. R., J. B. Blake, U. S. Inan, and J. Bortnik (2001), Observations of relativistic electron microbursts in association with VLF chorus, *J. Geophys. Res., 106*(A4), 6017.

Lyons, L. R. (1974), Pitch angle and energy diffusion coefficients from resonant interactions with ion-cyclotron and whistler waves, *J. Plasma Phys., 12*, 417.

Lyons, L. R., H. E. J. Koskinen, J. Blake, A. Egeland, M. Hirahara, M. Øieroset, P. E. Sandholt, and K. Shiokawa (1999), Processes leading to plasma losses into the high-latitude atmosphere, *Space Sci. Rev., 88*, 85.

Manninen, J., N. G. Kleimenova, O. V. Kozyreva, and T. Turunen (2010), Pc5 geomagnetic pulsations, pulsating particle precipitation, and VLF chorus: Case study on 24 November 2006, *J. Geophys. Res., 115*, A00F14, doi:10.1029/2009JA014837.

Mende, S. B., H. U. Frey, M. Lampton, J.-C. Gérard, B. Hubert, S. Fuselier, J. Spann, R. Gladstone, and J. L. Burch (2001), Global observations of proton and electron auroras in a substorm, *Geophys. Res. Lett., 28*, 1139-1142, doi:10.1029/2000GL012340.

Meredith, N. P., R. B. Horne, and R. R. Anderson (2001), Substorm dependence of chorus amplitudes: Implications for the acceleration of electrons to relativistic energies, *J. Geophys. Res., 106*, 13165-13178.

Meredith, N. P., R. B. Horne, R. M. Thorne, and R. R. Anderson (2003), Favored regions for chorus-driven electron acceleration to relativistic energies in the Earth’s outer radiation belt, *Geophys. Res. Lett., 30*(16), 1871, doi:10.1029/ 2003GL017698.

Meredith, N. P., R. B. Horne, R. M. Thorne, and R. R. Anderson (2009), Survey of upper band chorus and ECH waves: Implications for the diffuse aurora, *J. Geophys. Res., 111*, A07218, doi:10.1029/2009JA014230.

Miyoshi, Y., A. Morioka, T. Obara, H. Misawa, T. Nagai, and Y. Kasahara (2003), Rebuilding process of the outer radiation belt during the 3 November 1993 magnetic storm: NOAA and Exos-D observations, *J. Geophys. Res., 108*(A1), 1004, doi:10.1029/2001JA007542.

Miyoshi, Y., Y. Katoh, T. Nishiyama, T. Sakanoi, K. Asamura, and M. Hirahara (2010), Time of flight analysis of pulsating aurora electrons, considering wave-particle interactions with propagating whistler mode waves, *J. Geophys. Res., 115*, A10312, doi:10.1029/2009JA015127.

Nakajima, A., et al. (2012), Electron and wave characteristics observed by the THEMIS satellites near the magnetic equator during a pulsating aurora, *J. Geophys. Res., 117*, A03219, doi:10.1029/2011JA017066.

Nakamura, R., and T. Oguti (1987), Drifts of auroral structures and magnetospheric electric fields, *J. Geophys. Res., 92*(A10), 11,241-11,247, doi:10.1029/JA092iA10p11241.

Nemzek, R. J., R. Nakamura, D. N. Baker, R. D. Belian, D. J. McComas, M. Thomsen, and T. Yamamoto (1995), The relationship between pulsating auroras observed from the ground and energetic electrons and plasma density measured at geosynchronous orbit, *J. Geophys. Res., 100*, 23935-23944.

Ni, B., R. M. Thorne, Y. Shprits, and J. Bortnik (2008), Resonant scattering of plasma sheet electrons by whistler-mode chorus: contribution to diffuse aurora precipitating, *Geophys. Res. Lett., 35*, L11106, doi:10.1029/2008GL034032.

Nishimura, Y., et al. (2010), Identifying the driver of pulsating aurora, *Science, 330*, 81-84.

Nishimura, Y., et al. (2011), Multievent study of the correlation between pulsating aurora and whistler mode chorus emissions, *J. Geophys. Res., 116*, A11221, doi:10.1029/2011JA016876.

Nunn, D., O. Santolík, M. Rycroft, and V. Trakhtengerts (2009), On the numerical modelling of VLF chorus dynamical spectra, *Ann. Geophys., 27*, 2341-2359, doi:10.5194/angeo-27-2341-2009.

O'Brien, T. P., and M. B. Moldwin (2003), Empirical plasmapause models from magnetic indices, *Geophys. Res. Lett., 30*(4), 1152, doi:10.1029/2002GL016007.

Obuchi, Y., T. Sakanoi, A. Yamazaki, T. Ino, S. Okano, Y. Kasaba, M. Hirahara, Y. Kanai, and N. Takeyama (2008), Initial observations of auroras by the multispectral auroral camera on board the Reimei satellite, *Earth Planets Space, 60*, 827-835.

Oguti, T., S. Kokubun, K. Hayashi, K. Tsuruda, S. Machida, T. Kitamura, O. Saka, and T. Watanabe (1981), Latitudinally propagating on-off switching aurorae and associated geomagnetic pulsations: A case study of an event of February 20, 1980, *Can. J. Phys., 59*, 1131-1136.

Omura, Y., Y. Katoh, and D. Summers (2008), Theory and simulation of the generation of whistler-mode chorus, *J. Geophys. Res., 113*, A04223, doi:10.1029/2007JA012622.

Omura, Y., M. Hikishima, Y. Katoh, D. Summers, and S. Yagitani (2009), Nonlinear mechanisms of lower-band and upper - band VLF chorus emissions in the magnetosphere, *J. Geophys. Res., 114*, A07217, doi:10.1029/ 2009JA014206.

Ono, T., and K. Morishima (1994), Energy parameters of precipitating auroral electrons obtained by using photometric observations, *Geophys. Res. Lett., 21*, 261-264.

Oyama, S., K. Shiokawa, J. Kurihara, T. T. Tsuda, S. Nozawa, Y. Ogawa, Y. Otsuka, and B. J. Watkins (2010), Lower-thermospheric wind fluctuations measured with an FPI during pulsating aurora at Tromsø, Norway, *Ann. Geophys., 28*, 1847-1857, doi:10.5194/angeo-28-1847-2010.

Ozaki, M., et al. (2012), Observed correlation between pulsating aurora and chorus waves at Syowa Station in Antarctica: A case study, *J. Geophys. Res., 117*, A08211, doi:10.1029/2011JA017478.

Pedersen, T., E. Mishin, and K. Oksavik (2007), Observations of structured optical emissions and particle precipitation equatorward of the traditional auroral oval, *J. Geophys. Res., 112*, A10208, doi:10.1029/2007JA012299.

Reeves, G. D. (2007), Radiation Belt Storm Probes: A new mission for space weather forecasting, *Space Weather, 5*, S11002, doi:10.1029/2007SW000341.

Røyrvik, O., and T. N. Davis (1977), Pulsating aurora: Local and global morphology, *J. Geophys. Res., 82*, 4720-4740.

Saito, H., Y. Masumoto, T. Mizuno, A. Miura, M. Hashimoto, H. Ogawa, S. Tachikawa, T. Oshima, A. Choki, H. Fukuda, M. Hirahara, and S, Okano (2001), INDEX: Piggy-back satellite for aurora observation and technology demonstration, *Acta Astronautica, 48*, 723-735.

Saito, S., Y. Miyoshi, and K. Seki (2010), A split in the outer radiation belt by magnetopause shadowing: Test particle simulations, *J. Geophys. Res., 115*, A08210, doi:10.1029/2009JA014738.

Saito, S., Y. Miyoshi, and K. Seki (2012), Relativistic electron microbursts associated with whistler chorus rising tone elements: GEMSIS-RBW simulations, *J. Geophys. Res., 117*, A10206, doi:10.1029/2012JA018020.

Sakanoi, T., S. Okano, Y. Obuchi, T. Kobayashi, M. Ejiri, K. Asamura, and M. Hirahara (2003), Development of the multi-spectral auroral camera onboard the INDEX satellite, *Adv. Space Res., 32*, 379-384.

Samara, M., and R. G. Michell (2010), Ground-based observations of diffuse auroral frequencies in the context of whistler mode chorus, *J. Geophys. Res., 115*, A00F18, doi:10.1029/2009JA014852.

Samara, M., R. G. Michell, K. Asamura, M. Hirahara, D. L. Hampton, and H. C. Stenbaek-Nielsen (2010), Groundbased observations of diffuse auroral structures in conjunction with Reimei measurements, *Ann. Geophys., 28*, 873-881, doi:10.5194/angeo-28-873-2010.

Sandahl, I., L. Eliasson, and R. Lundin (1980), Rocket observations of precipitating electrons over a pulsating aurora, *Geophys. Res. Lett., 7*, 309-312.

Santolík, O., D. A. Gurnett, J. S. Pickett, M. Parrot, and N. Cornilleau-Wehrlin (2003), Spatio-temporal structure of storm-time chorus, *J. Geophys. Res., 108*, 1278, doi:10.1029/2002JA009791.

Santolík, O., D. A. Gurnett, J. S. Pickett, M. Parrot, and N. Cornilleau-Wehrlin (2005a), Central position of the source region of storm-time chorus, *Planet. Space Sci., 53*, 299-305, doi:10.1016/j.pss.2004.09.056.

Santolík, O., E. Macúšová, K. H. Yearby, N. Cornilleau-Wehrlin, and H. S. C. K. Alleyne (2005b), Radial variation of whistler-mode chorus: First results from the STAFF/DWP instrument onboard the Double Star TC 1 spacecraft, *Ann. Geophys., 23*, 2937-2942.

Santolík, O., E. Macúšová, E. E. Titova, B. V. Kozelov, D. A. Gurnett, J. S. Pickett, V. Y. Trakhtengerts, and A. G. Demekov (2008), Frequencies of wave packets of whistler-mode chorus inside its source region: A case study, *Ann. Geophys., 26*, 1665-1670, doi:10.5194/angeo-26-1665-2008.

Sarris, T. E., T. M. Loto’ aniu, X. Li, and H. J. Singer (2007), Observations at geosynchronous orbit of a persistent Pc4-5 geomagnetic pulsation and energetic electron flux modulations, *Ann. Geophys., 25*, 1653-1667, doi:10.5194/angeo-25-1653-2007.

Sato, N., M. Morooka, K. Minatoya, and T. Saemundsson (1998), Nonconjugacy of pulsating auroral patches near L=6, *Geophys Res Lett, 25*(20), 3755.

Sato, N., D. M. Wright, Y. Ebihara, M. Sato, Y. Murata, H. Doi, T. Saemundsson, S. E. Milan, M. Lester, and C. W. Carlson (2002), Direct comparison of pulsating aurora observed simultaneously by the FAST satellite and from the ground at Syowa, *Geophys. Res. Lett., 29*(21), 2041, doi:10.1029/2002GL015615.

Sato, N., D. M. Wright, C. W. Carlson, Y. Ebihara, M. Sato, T. Saemundsson, S. E. Milan, and M. Lester (2004), Generation region of pulsating aurora obtained simultaneously by the FAST satellite and a Syowa-Iceland conjugate pair of observations, *J. Geophys. Res., 109*, A10201, doi:10.1029/2004JA010419.

Scourfield, M. W. J., and N. R. Parsons (1969), Auroral pulsations and flaming-Some initial results of a cinematographic study using an image intensifier, *Planet. Space Sci., 17*, 1141.

Semeter, J., M. Zettergren, M. Diaz, and S. Mende (2008), Wave dispersion and the discrete aurora: New constraints derived from high-speed imagery, *J. Geophys. Res., 113*, A12208, doi:10.1029/2008JA013122.

Semeter, J., T. W. Butler, M. Zettergren, C. J. Heinselman, and M. J. Nicolls (2010), Composite imaging of auroral forms and convective flows during a substorm cycle, *J. Geophys. Res., 115*, A08308, doi:10.1029/2009JA014931.

Sergienko, T., I. Sandahl, B. Gustavsson, L. Andersson, U. Brändström, and Å. Steen (2008), A study of fine structure of diffuse aurora with ALIS-FAST measurements, *Ann. Geophys., 26*, 3185-3195.

Sheeley, B. W., M. B. Moldwin, H. K. Rassoul, and R. R. Anderson (2001), An empirical plasmasphere and trough density model: CRRES observations, *J. Geophys. Res., 106*, 25631-25641.

Shiokawa, K., A. Nakajima, A. Ieda, K. Sakaguchi, R. Nomura, T. Aslaksen, M. Greffen, and E. Donovan (2010), Rayleigh-Taylor type instability in auroral patches, *J. Geophys. Res., 115*, A02211, doi:10.1029/2009JA014273.

Stenbaek-Nielsen, H. C., E. M. Wescott, and R. W. Peterson (1973), Pulsating auroras over conjugate areas, *Antarct. J. U. S., 8*, 246-247.

Stenbaek-Nielsen, H. C. (1980), Pulsating aurora: The importance of the ionosphere, *Geophys. Res. Lett., 7*(5), 353-356, doi:10.1029/ GL007i005p00353.

Stenbaek-Nielsen, H. C., T. J. Hallinan, D. L. Osborne, J. Kimball, C. Chaston, J. McFadden, G. Delory, M. Temerin, and C. W. Carlson (1998), Aircraft observations conjugate to FAST: Auroral arc thicknesses, *Geophys. Res. Lett., 25*, 2073-2076.

Su, Z., H. Zheng, and S. Wang (2009), Evolution of electron pitch angle distribution due to interactions with whistler mode chorus following substorm injections, *J. Geophys. Res., 114*, A08202, doi:10.1029/ 2009JA014269.

Swenson, G. R., R. L. Raidern, S.C. Solomon, and S. Ananth (1998), Imaging spectrometry for 2 dimensional characterization of auroral emissions, *Appl. Opt., 37*, 5740-5770.

Trakhtengerts, V.Y., (1999). A generation mechanism for chorus emissions. *Ann. Geophys. 17*, 95-100.

Trakhtengerts, V. Y., A. G. Demekhov, E. E. Titova, B. V. Kozelov, O. Santolík, D. Gurnett, and M. Parrot (2004), Interpretation of Cluster data on chorus emissions using the backward wave oscillator model, *Phys. Plasmas, 11*, 1345-1351, doi:10.1063/1.1667495.

Tsuruda, K., S. Machida, T. Oguti, S. Kokubun, K. Hayashi, T. Kitamura, O. Saka, and T. Watanabe (1981), Correlations between the very low frequency chorus and pulsating aurora observed by low-light-level television at L-4.4, *Can. J. Phys., 59*, 1042-1048.

Tsyganenko, N. A. (2002a), A model of the near magnetosphere with a dawn-dusk asymmetry: 1. Mathematical structure, *J. Geophys. Res., 107*(A8), 1179, doi:10.1029/2001JA000219.

Tsyganenko, N. A. (2002b), A model of the near magnetosphere with a dawn-dusk asymmetry: 2. Parameterization and fitting to observations, *J. Geophys. Res., 107*(A8), 1176, doi:10.1029/2001JA000220.

Tsyganenko, N. A., H. J. Singer, and J. C. Kasper (2003), Storm-time distortion of the inner magnetosphere: How severe can it get?, *J. Geophys. Res., 108*(A5), 1209, doi:10.1029/2002JA009808.

Tsyganenko, N. A., and M. I. Sitnov (2005), Modeling the dynamics of the inner magnetosphere during strong geomagnetic storms, *J. Geophys. Res., 110*, A03208, doi:10.1029/2004JA010798.

Turunen, E., P. T. Verronen, A. Seppälä, C. J. Rodger, M. A. Clilverd, J. Tamminen, C. F. Enell, and T. Ulich (2009), Impact of different precipitation energies on NOx generation in the middle and upper atmosphere during geomagnetic storms, *J. Atmos. Sol. Terr. Phys., 71*, 1176-1189, doi:10.1016/j.jastp.2008.07.005.

Untiedt, J., and W. Baumjohann (1993), Studies of polar current systems using the IMS Scandinavian magnetometer array, *Space Sci. Rev., 63*, 245-390.

Uritsky, V. M., J. Liang, E. Donovan, E. Spanswick, D. Knudsen, W. Liu, J. Bonnell, and K. H. Glassmeier (2009), Longitudinally propagating arc wave in the pre-onset optical aurora, *Geophys. Res. Lett., 36*, L21103, doi:10.1029/2009GL040777.

Yaegashi, A., T. Sakanoi, R. Kataoka, K. Asamura, Y. Miyoshi, M. Sato, and S. Okano (2011), Spatial-temporal characteristics of flickering aurora as seen by high-speed EMCCD imaging observations, *J. Geophys. Res., 116*, A00K04, doi:10.1029/2010JA016333.

Yamamoto, T. (1988), On the temporal fluctuations of pulsating auroral luminosity, *J. Geophys. Res., 93*, 89-7-911.

Yamamoto, T., and T. Oguti (1982), Recurrent fast motions of pulsating auroral patches. 1: A case study on optical and quantitative characteristics during a slightly active period, *J. Geophys. Res., 87*(A9), 7603-7614, doi:10.1029/JA087iA09p07603.

Yau, A. W., B. A. Whalen, and D. J. McEwen (1981), Rocket-borne measurements of particle pulsation in pulsating aurora, *J. Geophys. Res., 86*, 5673-5681.

Wahlund, J., H. Opgenoorth, and P. Rothwell (1989), Observation of thin auroral ionization layers by ElSCAT in connection with pulsating aurora, *J. Geophys. Res., 94*, 17,223-17,233, doi:10.1029/JA094iA12p17223.

Wallis, D. D., J. R. Burrows, M. C. Moshupi, C. D. Anger, and J. S. Murphree (1979), Observations of particles precipitating into detached arcs and patches equatorward of the auroral oval, *J. Geophys. Res., 84*(A4), 1347-1360, doi:10.1029/JA084iA04p01347.

Watanabe, M., A. Kadokura, N. Sato, and T. Saemundsson (2007), Absence of geomagnetic conjugacy in pulsating auroras, *Geophys. Res. Lett., 34*, L15107, doi:10.1029/2007GL030469.

Whiter, D. K., B. S. Lanchester, B. Gustavsson, N. Ivchenko, J. M. Sullivan, and H. Dahlgren (2008), Small scale structures in flickering aurora, *Geophys. Res. Lett., 35*, L23103, doi:10.1029/2008GL036134.

Whiter, D. K., B. S. Lanchester, B. Gustavsson, N. Ivchenko, and H. Dahlgren (2010), Using multispectral optical observations to identify the acceleration mechanism responsible for flickering aurora, *J. Geophys. Res., 115*, A12315, doi:10.1029/2010JA015805.

Whiter, D. K., B. S. Lanchester, T. Sakanoi, and K. Asamura (2012), Estimating high-energy electron fluxes by intercalibrating Reimei optical and particle measurements using an ionospheric model, *J. Atmos. Terr. Phys., 89*, 8-17, doi:10.1016/j.jastp.2012.06.014.

Obuchi, Y. (2008), Study on dynamics of black aurora based on simultaneous optical and particle observations by REIMEI satellite, Doctor thesis, Tohoku University.